



Ashton, Thomas E. (2016) *Microwave-assisted synthesis and local analyses of positive insertion electrodes for Li-ion batteries*. PhD thesis.

<http://theses.gla.ac.uk/7856/>

Copyright and moral rights for this work are retained by the author

A copy can be downloaded for personal non-commercial research or study, without prior permission or charge

This work cannot be reproduced or quoted extensively from without first obtaining permission in writing from the author

The content must not be changed in any way or sold commercially in any format or medium without the formal permission of the author

When referring to this work, full bibliographic details including the author, title, awarding institution and date of the thesis must be given

Enlighten:Theses  
<http://theses.gla.ac.uk/>  
theses@gla.ac.uk

Microwave-assisted synthesis and local  
analyses of positive insertion electrodes for  
Li-ion batteries

Thomas E. Ashton, M. Sci.

Submitted in the fulfilment of the requirements for the Degree of  
Doctor of Philosophy

School of Chemistry  
College of Science and Engineering  
University of Glasgow

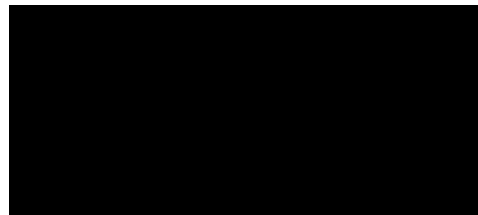


Supervisor:  
Dr. S. A. Corr

6TH JANUARY 2017

I am aware of and understand the University's policy on plagiarism and I certify that this assignment is my own work, except where indicated by referencing, and that I have followed the good academic practices noted by the University of Glasgow.

Signed:



Thomas E. Ashton

## Abstract

Efficient energy storage holds the key to reducing waste energy and enabling the use of advanced handheld electronic devices, hybrid electric vehicles and residential energy storage. Recently, Li-ion batteries have been identified and employed as energy storage devices due to their high gravimetric and volumetric energy densities, in comparison to previous technologies. However, more research is required to enhance the efficiency of Li-ion batteries by discovering electrodes with larger electrochemical discharge capacities, while maintaining electrochemical stability. The aims of this study are to develop new microwave-assisted synthesis routes to nanostructured insertion cathodes, which harbor a greater affinity for lithium extraction and insertion than bulk materials. Subsequent to this, state-of-the-art synchrotron based techniques have been employed to understand structural and dynamic behaviour of nanostructured cathode materials during battery cell operation. In this study, microwave-assisted routes to  $\alpha$ -LiFePO<sub>4</sub>, VO<sub>2</sub>(B), V<sub>3</sub>O<sub>7</sub>, H<sub>2</sub>V<sub>3</sub>O<sub>8</sub> and V<sub>4</sub>O<sub>6</sub>(OH)<sub>4</sub> have all been developed. Muon spin relaxation has shown that the presence of  $\beta$ -LiFePO<sub>4</sub> has a detrimental effect on the lithium diffusion properties of  $\alpha$ -LiFePO<sub>4</sub>, in agreement with first principles calculations. For the first time,  $\alpha$ -LiFePO<sub>4</sub> nanostructures have been obtained by employing a deep eutectic solvent reaction media showing near theoretical capacity (162 mAh g<sup>-1</sup>). Studies on VO<sub>2</sub>(B) have shown that the discharge capacity obtained is linked to the synthesis method. Electrochemical studies of H<sub>2</sub>V<sub>3</sub>O<sub>8</sub> nanowires have shown outstanding discharge capacities (323 mAh g<sup>-1</sup> at 100 mA g<sup>-1</sup>) and rate capability (180 mAh g<sup>-1</sup> at 1 A g<sup>-1</sup>). The electrochemical properties of V<sub>4</sub>O<sub>6</sub>(OH)<sub>4</sub> have been investigated for the first time and show a promising discharge capacity of (180 mAh g<sup>-1</sup>). Lastly, *in situ* X-ray absorption spectroscopy has been utilised to track the evolution of the oxidation states in  $\alpha$ -LiFePO<sub>4</sub>, VO<sub>2</sub>(B) and H<sub>2</sub>V<sub>3</sub>O<sub>8</sub>, and has shown these can all be observed dynamically.

## Acknowledgements

There are many people that I would like to thank throughout the course of this PhD, least of all the wasps that decided to inhabit my bedroom windowsill, and took part in the Great Battle of Inchlee Street in the summer of 2014. These were closely followed by the two rats I found in my kitchen bin after a weekend away. Luckily, their rigidity aided their disposal. Oh, and the man that enjoyed flicking matchsticks at me while I waited for the bus. Sticks and stones may break my bones, but at least my liver will outlast yours.

Thanks to my brother for launching Weetabix at the kitchen ceiling in the morning when we were young, and blaming it on me. Physics in action, and the prowess of discovery. Thank you to my sister Emma, niece Jessica, nephew Albert (and unknown nibbling number three) for their patient understanding of their Brother and Uncle, respectively. Thanks to my Mum and Dad for giving me everything I have needed to get to this point in life, and supporting me wholly in every decision.

Thanks to my friends from Kent University and home for all the fun we've had together. Unfortunately, I'm *so* popular I won't be able to list you all, but you know who you are. I'd also like to thank Dr. Bob Faller-Fritsch and Dr. Franklin Human who taught me the sciences at Rutlish High School, and first got me interested in chemistry.

Thank you to Dr. Hugh Flowers, your knowledge of analytical chemistry, overabundance of green beans, skill at the Metro puzzles helped scientifically, gastronomically and, genuinely. Thank you to Ying "Jenny" Zheng for introducing me to Chinese hotpot, and exchanging Confucius quotes (I still think mine were better). Thank you to Dr. Stephen Sproules for his expertise in electronic effects, and ceaseless bombardment of film and TV quotes. Thanks to Cailean McLeod for having a name that's really hard to spell, let alone pronounce, and for good talks over even better whisky. Thank you to the muon group at ISIS, specifically Dr. Peter Baker for his Gregorian chants, photographs of frogs and support with muon spin relaxation.

Thank you to the Corr Group, you are all great researchers that will go far and have been a good group to be around. Specifically I would like to thank Marco Amores. You've been a great friend and I will miss our arguments over every single, small aspect of all possible subjects, even if we were wrong. I'd also like to thank our Supervisor, Dr. Serena Corr for

her unyielding help and support. None of this work would have been possible without your determination. A very special thank you to Mr. Michael Beglan. Being a part of team Beglan was an honour and a privilege, and I'll miss having the best ever, white, male, Scottish technician, on Floor 5 of the Joseph Black Building, around.

Finally I'd like to thank my girlfriend, Liv, who has put up with me for 4 years (only god knows why). I couldn't have done it without you.

# Contents

<b>List of abbreviations</b>	<b>vi</b>
<b>List of Figures</b>	<b>xxii</b>
<b>List of Tables</b>	<b>xxiv</b>
<b>1 Introduction</b>	<b>1</b>
1.1 Lithium ion batteries . . . . .	2
1.1.1 Tailoring voltage in Li-ion electrodes . . . . .	6
1.1.2 $\alpha$ -LiFePO <sub>4</sub> as an insertion electrode . . . . .	7
1.1.3 Enhancing capacity in Li-ion insertion electrodes . . . . .	10
1.1.4 Multiple electron transfer in vanadium oxides . . . . .	12
1.2 Lithium intercalation and diffusion in insertion electrodes . . . . .	14
1.2.1 Mechanism of lithium intercalation in insertion electrodes . . . . .	14
1.2.2 Mechanism of lithium diffusion in insertion electrodes . . . . .	16
1.3 Methods for analysing Li <sup>+</sup> diffusion mechanics . . . . .	18
1.3.1 Traditional methods for analysing Li <sup>+</sup> diffusion mechanics . . . . .	18
1.3.2 Muon spin relaxation as a Li <sup>+</sup> diffusion probe . . . . .	19
1.3.3 Muon spin relaxation of Li-ion intercalation electrodes . . . . .	21
1.4 Nanostructured insertion electrodes . . . . .	22
1.5 Synthetic routes to nanostructured insertion electrodes . . . . .	24
1.5.1 Solid state synthesis . . . . .	24
1.5.2 Hydrothermal and solvothermal synthesis . . . . .	24
1.5.3 Microwave synthesis . . . . .	25
1.5.4 Preparation of metal oxides by microwave-assisted synthesis . . . . .	29
1.5.5 Preparation of vanadium oxide materials by microwave-assisted approaches . . . . .	31
1.5.6 Preparation of olivine phosphate materials by microwave-assisted approaches . . . . .	32

1.6	Summary of aims and objectives . . . . .	34
<b>2</b>	<b>Experimental methods</b>	<b>35</b>
2.1	Microwave synthesis . . . . .	35
2.1.1	Preparation of $\text{LiFePO}_4$ polymorphs in polyol media . . . . .	35
2.1.2	Preparation of $\text{LiFePO}_4$ polymorphs in ionic liquids . . . . .	35
2.1.3	Preparation of $\text{LiFePO}_4$ polymorphs in deep eutectic solvents . . . . .	36
2.1.4	Preparation of $\text{VO}_2$ (B) and $\text{V}_3\text{O}_7$ . . . . .	37
2.1.5	Microwave-assisted reduction of $\text{V}_2\text{O}_5$ in isopropanol (IPA) . . . . .	38
2.1.6	Microwave-assisted preparation of $\text{H}_2\text{V}_3\text{O}_8$ . . . . .	38
2.1.7	Microwave-assisted preparation of $\text{V}_4\text{O}_6\text{O}(\text{OH})_4$ . . . . .	39
2.2	Solvothermal preparation of $\text{VO}_2$ (B) . . . . .	39
2.3	Chemical lithiation of $\text{H}_2\text{V}_3\text{O}_8$ . . . . .	39
2.4	Flame photometry . . . . .	41
2.5	Carbon coating of $\text{LiFePO}_4$ . . . . .	41
2.6	Fourier transform infrared spectroscopy . . . . .	42
2.7	Powder X-ray diffraction . . . . .	42
2.8	Scanning electron microscopy . . . . .	44
2.9	Galvanostatic cycling with potential limitation . . . . .	44
2.10	Cyclic voltammetry . . . . .	45
2.11	Preparation of electrochemical half cells . . . . .	45
2.12	X-ray absorption spectroscopy . . . . .	46
2.12.1	Preparation of <i>ex situ</i> samples . . . . .	50
2.12.2	Preparation of <i>in situ</i> AMPIX cells . . . . .	50
2.13	Muon spin relaxation . . . . .	51
2.13.1	Preparation of $\mu\text{SR}$ samples . . . . .	53
<b>3</b>	<b>Microwave-assisted polyol and ionothermal synthesis of <math>\text{LiFePO}_4</math> polymorphs</b>	<b>54</b>
3.1	Introduction . . . . .	54
3.2	Microwave spectroscopy of polar and ionic liquids . . . . .	55
3.3	Microwave-assisted preparation of $\text{LiFePO}_4$ in polyol media . . . . .	57

3.3.1	Synthesis and characterisation of $\alpha$ -LiFePO <sub>4</sub> in polyol media . . . . .	59
3.3.2	Synthesis and characterisation of $\alpha$ -LiFePO <sub>4</sub> in ethylene glycol . . . . .	60
3.4	Heat treatment of $\beta$ -LiFePO <sub>4</sub> to produce phase pure $\alpha$ -LiFePO <sub>4</sub> . . . . .	65
3.5	Microwave-assisted preparation of $\alpha$ -LiFePO <sub>4</sub> in ionic liquid . . . . .	67
3.6	Preparation of LiFePO <sub>4</sub> polymorphs for local studies . . . . .	70
3.6.1	Larger scale synthesis of LiFePO <sub>4</sub> polymorphs . . . . .	70
3.6.2	Electron microscopy of LiFePO <sub>4</sub> polymorphs . . . . .	71
3.6.3	Electrochemical characterisation of LiFePO <sub>4</sub> polymorphs . . . . .	72
3.7	Muon spin relaxation of LiFePO <sub>4</sub> polymorphs . . . . .	73
3.8	<i>In situ</i> XANES of LiFePO <sub>4</sub> polymorphs . . . . .	78
3.9	<i>In situ</i> EXAFS of $\alpha$ -LiFePO <sub>4</sub> . . . . .	83
3.10	Conclusions . . . . .	88
<b>4</b>	<b>Deep eutectic solvents as media for microwave-assisted synthesis</b>	<b>90</b>
4.1	Preparation of $\alpha$ -LiFePO <sub>4</sub> in diethylene glycol, tetraethylene glycol and glycerol based eutectics . . . . .	91
4.1.1	Synthesis and characterisation of $\alpha$ -LiFePO <sub>4</sub> prepared in (di)ethaline, (tetra)ethaline and glyceline . . . . .	93
4.2	Microwave heating of ethaline . . . . .	95
4.3	Ethaline mediated microwave-assisted synthesis of $\alpha$ -LiFePO <sub>4</sub> . . . . .	97
4.3.1	Structural characterisation of ethaline mediated $\alpha$ -LiFePO <sub>4</sub> . . . . .	97
4.4	Effect of choline chloride concentration on ethaline mediated microwave-assisted synthesis of $\alpha$ -LiFePO <sub>4</sub> . . . . .	101
4.4.1	Effect of salt concentration on microwave heating properties in 1:3 ethaline and 2:3 ethaline . . . . .	101
4.4.2	Synthesis and characterisation of $\alpha$ -LiFePO <sub>4</sub> 1:3 ethaline . . . . .	102
4.4.3	Electrochemical analysis $\alpha$ -LiFePO <sub>4</sub> of 1:3 ethaline . . . . .	103
4.4.4	Synthesis and characterisation of $\alpha$ -LiFePO <sub>4</sub> 2:3 ethaline . . . . .	105
4.5	Synthesis and characterisation of $\alpha$ -LiFePO <sub>4</sub> in tetramethylammonium chloride based DES . . . . .	118
4.6	Conclusions . . . . .	122

<b>5</b>	<b>Microwave-assisted synthesis of vanadium oxides for lithium ion batteries</b>	<b>124</b>
5.1	Attempted reduction of $V_2O_5$ in isopropanol . . . . .	127
5.1.1	Electrochemical characterisation of $V_3O_7$ . . . . .	131
5.2	Synthesis and characterisation of $VO_2(B)$ nanostructures . . . . .	132
5.2.1	Electrochemical characterisation of $VO_2(B)$ nanostructures . . . . .	135
5.3	<i>In situ</i> X-ray absorption spectroscopy of $VO_2(B)$ nanostructures . . . . .	138
5.4	Microwave-assisted synthesis of $VO_2(B)$ in binary solvent systems . . . . .	141
5.4.1	Microwave-assisted synthesis of $VO_2(B)$ in formaldehyde and ethylene glycol (EG) . . . . .	141
5.4.2	Electrochemical characterisation of $VO_2(B)$ synthesised in formaldehyde and ethylene glycol . . . . .	142
5.4.3	Microwave-assisted synthesis of $VO_2(B)$ in formaldehyde and diethylene glycol . . . . .	143
5.4.4	Electrochemical characterisation of $VO_2(B)$ synthesised in formaldehyde and diethylene glycol (DEG) . . . . .	147
5.5	Microwave-assisted synthesis of $VO_2(B)$ in formaldehyde with PVP . . . . .	148
5.5.1	Electrochemical characterisation of $VO_2(B)$ synthesised in formaldehyde in the presence of PVP . . . . .	150
5.6	Conclusions . . . . .	151
<b>6</b>	<b>Microwave-assisted synthesis of vanadium oxyhydroxides cathodes</b>	<b>153</b>
6.1	Introduction . . . . .	153
6.2	Preparation and investigation of $V_4O_6(OH)_4$ . . . . .	156
6.2.1	Synthesis and characterisation of $V_4O_6(OH)_4$ . . . . .	156
6.2.2	XANES analyses of $V_4O_6(OH)_4$ . . . . .	157
6.2.3	Electrochemical analyses of $V_4O_6(OH)_4$ . . . . .	158
6.3	Preparation and investigation of $H_2V_3O_8$ . . . . .	159
6.3.1	Synthesis and characterisation of $H_2V_3O_8$ . . . . .	159
6.3.2	Electrochemical analysis of $H_2V_3O_8$ . . . . .	163
6.4	$Li^+$ diffusion in $Li_{0.4}H_2V_3O_8$ . . . . .	166
6.4.1	Chemical lithiation of $H_2V_3O_8$ . . . . .	167

6.4.2	Investigation of Li <sup>+</sup> diffusion in Li <sub>0.4</sub> H <sub>2</sub> V <sub>3</sub> O <sub>8</sub> by muon spin relaxation .	169
6.5	<i>In situ</i> XAS of H <sub>2</sub> V <sub>3</sub> O <sub>8</sub> . . . . .	172
6.6	Conclusions . . . . .	178
<b>7</b>	<b>Conclusions and Future Work</b>	<b>180</b>
7.1	Summary of conclusions . . . . .	180
7.2	Future work . . . . .	181
<b>8</b>	<b>Appendices</b>	<b>183</b>
	<b>Bibliography</b>	<b>183</b>

## List of abbreviations

AC - Alternating current

b.p. - Boiling point

$B_{LF}$  - Longitudinal magnetic field

ChCl - Choline chloride

CV - Cyclic voltammetry

$D_{Li}$  - Lithium diffusion coefficient

DC - Direct current

DEG - Diethylene glycol

DES - Deep eutectic solvent

DMC - Dimethylcarbonate

DMSO - Dimethylsulfoxide

$E_{we}$  - Working electrode potential

$E_a$  - Activation energy

EC - Ethylene carbonate

EG - Ethylene glycol

EMIM-TFMS - 1-ethyl-3-methylimidazolium trifluoromethanesulfonate

EMIM-TFSI - 1-ethyl-3-methylimidazolium bis(trifluorosulfonylimide)

EXAFS - Extended X-ray absorption fine structure

FTIR - Fourier transform infrared

FWHM - Full width half maximum

GCPL - Galvanostatic cycling with potential limitation

GITT - Galvanostatic intermittent titration technique

Gly - Glycerol

HCHO - Formaldehyde

HOMO - Highest occupied molecular orbital

ICSD - International crystal structure database

IPA - Isopropyl alcohol (propan-2-ol)

LD50 - Lethal dose 50

Li-ion - Lithium ion  
LUMO - Lowest occupied molecular orbital  
MEM - Minimum entropy method  
MET - Multiple electron transfer  
NMR - Nuclear magnetic resonance  
NPD - Neutron powder diffraction  
OCV - Open circuit voltage  
PEDOT - Poly(3,4-ethylenedioxythiophene)  
PTFE - Polytetrafluoroethylene  
PVP - Polyvinylpyrrolidone  
PXRD - Powder X-ray diffraction  
RPM - Revolutions per minute  
SEI - Solid electrolyte interphase  
SEM - Scanning electron microscopy  
tan $\delta$  - Loss tangent  
TEG - Tetraethylene glycol  
TMAC - Tetramethylammonium chloride  
 $V_{oc}$  - Open circuit voltage  
XANES - X-ray absorption near-edge spectroscopy  
XAS - X-ray absorption spectroscopy  
 $\mu$ SR - Muon spin relaxation

## List of Figures

1.1	Volumetric and gravimetric energy density of different available energy storage devices. Li-ion batteries offer one of the highest potential, safe sources of energy density currently available. Adapted with permission from Reference 1. Copyright (2001) Nature. . . . .	2
1.2	Schematic of a Li-ion battery showing the movement of Li <sup>+</sup> and electrons during electrochemical discharge between the anode (graphite) and the cathode (LiCoO <sub>2</sub> ) through the electrolyte. The Li <sup>+</sup> and electrons take separate pathways between the electrodes, and this process is reversible on electrochemical charging. . . . .	3
1.3	Schematic of the energy levels involved in electrochemical cycling of a Li-ion cell. . . . .	5
1.4	Operating voltage of iron oxide and polyanionic iron compounds showing an increase in potential with increasing electronegativity of the polyanion. . . . .	7
1.5	Crystal structure of <i>Pnma</i> structured $\alpha$ -LiFePO <sub>4</sub> . The primary direction of Li <sup>+</sup> diffusion is along <i>b</i> -axis through 1D channels in the [0 1 0] direction. . . . .	8
1.6	Lithium diffusion pathway in $\alpha$ -LiFePO <sub>4</sub> calculated by (a) neutron powder diffraction minimum entropy method (MEM) showing the nuclear distribution of Li (blue). Adapted with permission from Reference 20. Copyright (2008) Science. (b) First principles calculations showing one dimensional diffusion along the <i>b</i> -axis ([010] direction). Adapted with permission, from Reference 21. Copyright (2005) American Chemical Society. . . . .	9
1.7	Capacity and voltage from <i>ab initio</i> calculations for olivine phosphates containing various metals, in various oxidation states. The dashed red line represents the safe voltage limit imposed by current organic electrolytes. Reprinted with permission from Reference 37. Copyright (2011) American Chemical Society. . . . .	11
1.8	Structure of V <sub>2</sub> O <sub>5</sub> showing the intercalation of Li <sup>+</sup> between the layers of VO <sub>5</sub> square-based pyramidons (V <sup>5+</sup> ). . . . .	13

1.9	Galvanostatic cycling profile of an intercalation electrode that undergoes one redox reaction. A solid-solution region is observed at the start and the end of the two-phase redox plateau. The maximum possible $\text{Li}^+$ concentration to form lithium deficient material is denoted as $y'$ and the minimum required concentration to form a $\text{Li}^+$ rich solid-solution is denoted as $y''$ . . . . .	17
1.10	Two types of diffusion can occur in solid-state materials, vacancy and interstitial diffusion. Vacancy diffusion (1.a) shows the movement of a structural ion such as $\text{O}^{2-}$ from one lattice site to a neighbouring vacancy (1.b). Figure 2.a shows interstitial diffusion of an ion in a lattice from an interstitial site to a neighbouring interstitial site (2.b). . . . .	18
1.11	Structures of (a) the lithium nitride anode material $\text{Li}_3\text{N}$ , (b) the layered oxide cathode material $\text{LiCoO}_2$ and (c) the garnet structured solid-state electrolyte $\text{Li}_6\text{MLa}_2\text{Nb}_2\text{O}_{12}$ . It can be seen that these materials can accommodate the intercalation of $\text{Li}^+$ into their open structures. . . . .	19
1.12	Distribution of (a) the lithium diffusion coefficient ( $D_{\text{Li}}$ ) and (b) the activation energy ( $E_a$ ) of this process for $\alpha\text{-LiFePO}_4$ . It can be seen that there is large difference in reported values between the techniques. <sup>21,28,49–58</sup> . . . . .	20
1.13	Conventional heating in an oil-bath (a) versus microwave-assisted heating (b) shows rapid heating, unhindered by the vessel walls after just 60 s of irradiation. Reproduced from Reference 113 with permission from Elsevier publishing. . . . .	26
1.14	Schematic showing the difference behaviour of ionic and polar substances irradiated with microwaves. Dipolar molecules (1a, 1b, 1c) undergo a polarisation mechanism, whereas ionic molecules (2a, 2b) experience a much stronger conduction mechanism. . . . .	27
2.1	Concentration of lithium in washings from the chemical lithiation of $\text{H}_2\text{V}_3\text{O}_8$ taken ever 50 mL. A rapid decrease is observed in Li concentration up until 750 mL where the concentration becomes constant. . . . .	40

2.2	(a) Core electron excitations in XAS are named by the electronic level from which they originate (K, L, M). (b) The Bohr atomic model showing the various electronic levels. The binding energy of the electrons is greater, closer to the nucleus. . . . .	47
2.3	K-edge XAS spectrum collected for $V_2O_5$ . The feature labelled A is the pre-edge and B the rising edge. Inset is a diagram showing the electronic transitions that give rise to features A and B. . . . .	48
2.4	(a) Real space plot of EXAFS data, peaks in $ \chi(R) $ can be attributed to separate contributions from interatomic distances (inset). (b) Schematic describing coordination shells in a material. (c) Schematic describing the wave behaviour of the scattering and absorbing atoms. Constructive and destructive interference can occur when the outgoing and incoming waves interact. . . .	49
2.5	Schematic showing the construction of electrochemical cells for <i>in situ</i> X-ray absorption spectroscopy (XAS). . . . .	51
3.1	Microwave spectroscopy of polyol (ethylene glycol) and ionic (EMIM-TFMS) media. The real (a) and imaginary (b) permittivities describe the microwave absorbance and the incoming radiation to heat energy conversion respectively. The dashed line indicates the synthetic frequency of 2.45 GHz. . . . .	56
3.2	Average power consumption of EG, DEG and TEG heated by microwave irradiation. Exponential relationships are observed in all cases with lower maintenance power observed as polyol chain length increases. . . . .	57
3.3	PXRD patterns of syntheses conducted in EG, DEG and TEG at 220 °C for 3 hours. Mixed phases of <i>Pnma</i> ( $\alpha$ , Reference 31) and <i>Cmcm</i> ( $\beta$ , Reference 181) structured $LiFePO_4$ are observed with impurities of $Li_3PO_4$ (*) and an unidentified impurity phase ( $\circ$ ). . . . .	59
3.4	PXRD of products prepared by a microwave-assisted route in ethylene glycol for 1 h. Peak positions for <i>Pnma</i> structured $\alpha$ - $LiFePO_4$ are shown at the top of the data taken from Reference 31. . . . .	60

3.5	PXRD of products prepared by a microwave-assisted route in ethylene glycol for 3 h. Peak positions for <i>Pnma</i> structured $\alpha$ -LiFePO <sub>4</sub> are shown at the top of the data taken from Reference 31. . . . .	61
3.6	PXRD of products prepared by a microwave-assisted route in ethylene glycol for 5 h. Peak positions for <i>Pnma</i> structured $\alpha$ -LiFePO <sub>4</sub> are shown at the top of the data taken from Reference 31. . . . .	62
3.7	(a) Rietveld refinement of EG_LFP_250 <i>Pnma</i> structured $\alpha$ -LiFePO <sub>4</sub> (Reference pattern taken from Reference 31. Calculated Rietveld parameters for EG_LFP_250 are shown in Table 3.2. (b) SEM of $\alpha$ -LiFePO <sub>4</sub> exhibiting a large size distribution with particles typically between 200 nm and 300 nm in diameter. . . . .	63
3.8	PXRD pattern of a mixed $\alpha/\beta$ -LiFePO <sub>4</sub> sample heat treated in a tube furnace under an Ar atmosphere at 600 °C for 2 hours showing conversion of the $\beta$ - to $\alpha$ -LiFePO <sub>4</sub> with a small unidentified impurity noted (*). . . . .	65
3.9	(a) PXRD after 15 min and 45 min of microwave irradiation. (b) 15 min and 45 min samples were dried, resuspended in EG and irradiated for 15 min and 45 min further respectively yielding phase pure $\alpha$ -LiFePO <sub>4</sub> . . . . .	66
3.10	(a) SEM image of mixed phase $\alpha/\beta$ -LiFePO <sub>4</sub> prepared after 15 min of microwave irradiation of stoichiometric ratios of FeC <sub>2</sub> O <sub>4</sub> · 2 H <sub>2</sub> O and LiH <sub>2</sub> PO <sub>4</sub> in EG at 220 °C. (b) SEM image of the same sample after 15 min of further irradiation in EG showing that morphology is preserved after conversion to pure $\alpha$ -LiFePO <sub>4</sub> . . . . .	67
3.11	Chemical structure of the two ionic liquids investigated for microwave-assisted ionothermal synthesis of $\alpha$ -LiFePO <sub>4</sub> . . . . .	67
3.12	Power consumption of two ionic liquids, EMIM-TFMS (blue) and EMIM-TFSI (red). The exponential relationship between temperature, and power consumption is almost identical in both cases. . . . .	68

3.13 PXRD patterns for irradiation of a stoichiometric mixture of $\text{FeC}_2\text{O}_4 \cdot 2\text{H}_2\text{O}$ and $\text{LiH}_2\text{PO}_4$ in either EMI-TFMS or EMI-TFSI, including impurity phases of $\text{Li}_3\text{PO}_4$ and $\text{Fe}_2\text{PO}_5$ . Reference patterns are taken from Reference 31 and 181 for $\alpha$ - and $\beta$ - $\text{LiFePO}_4$ respectively. . . . .	69
3.14 X-ray diffraction patterns of pure $\alpha$ - $\text{LiFePO}_4$ and $\beta$ - $\text{LiFePO}_4$ with Reference patterns taken from Reference 31 ( $\alpha$ ) and 181 ( $\beta$ ). . . . .	70
3.15 Dual phase Rietveld refinement of the mixed $\alpha$ -/ $\beta$ - $\text{LiFePO}_4$ . Reference patterns are taken from Reference 31 and 181 for $\alpha$ - $\text{LiFePO}_4$ and $\beta$ - $\text{LiFePO}_4$ respectively. . . . .	71
3.16 Scanning electron microscopy images taken of (a) $\alpha$ - $\text{LiFePO}_4$ , (b) $\alpha$ -/ $\beta$ - $\text{LiFePO}_4$ and (c) $\beta$ - $\text{LiFePO}_4$ synthesised by a microwave assisted solvothermal route exhibiting different morphologies depending on the synthetic route employed. . . . .	72
3.17 (a) First galvanostatic cycle with potential limitation between 2.2 V and 4 V of $\text{LiFePO}_4$ polymorphs at C/10. (b) Discharge capacity of $\text{LiFePO}_4$ polymorphs over 20 cycles at C/10. . . . .	73
3.18 Raw muon spin relaxation data collected at three fields (0 G, 5 G and 10 G) for $\alpha$ - $\text{LiFePO}_4$ at 200 K fit with a dynamic Kubo-Toyabe model. . . . .	74
3.19 Raw muon spin relaxation data for (a) $\beta$ - $\text{LiFePO}_4$ at 200 K and (b) $\beta$ - $\text{LiFePO}_4$ at 400 K fit with a dynamic Kubo-Toyabe model. It is observed that a good fit can only be obtained at higher temperatures. . . . .	75
3.20 Temperature dependence of fluctuation rate ( $\nu$ ) for $\alpha$ - $\text{LiFePO}_4$ (a) and $\alpha$ -/ $\beta$ - $\text{LiFePO}_4$ (c) and field distribution width ( $\Delta$ ) for $\alpha$ - $\text{LiFePO}_4$ (b) and $\beta$ - $\text{LiFePO}_4$ (d). . . . .	76
3.21 Crystal structures of (a) $\alpha$ - $\text{LiFePO}_4$ , space group $Pnma$ , and (b) $\beta$ - $\text{LiFePO}_4$ , space group $Cmcm$ . . . . .	77
3.22 Arrhenius plot of the lithium diffusion coefficient of $\alpha$ - $\text{LiFePO}_4$ and $\alpha$ -/ $\beta$ - $\text{LiFePO}_4$ calculated from Equation 3.3. . . . .	78

3.23 (a) Normalised <i>ex situ</i> Fe K-edge X-ray absorption near edge spectra (XANES) of $\alpha$ -LiFePO <sub>4</sub> , mixed $\alpha/\beta$ -LiFePO <sub>4</sub> prepared by a microwave-assisted route and standards containing Fe <sup>2+</sup> (FeO) and Fe <sup>3+</sup> (Fe(NO <sub>3</sub> ) <sub>3</sub> ). The pre-edge (A) and rising edge (B) show a shift to lower energy with decreasing oxidation state. (b) Second derivative of the normalised XANES spectra over the pre-edge region shows minima corresponding to contributions from Fe <sup>2+</sup> t <sub>2g</sub> and e <sub>g</sub> orbitals. . . . .	79
3.24 B3LYP DFT simulation of the Fe K-edge spectrum expected for $\alpha$ -LiFePO <sub>4</sub> . The two low energy features arise from the core 1s to 3d (t <sub>2g</sub> and e <sub>g</sub> ) orbitals and a high energy incline from 1s to 4+np excitations. . . . .	80
3.25 (a) Normalised <i>in situ</i> Fe K-edge XAS of $\alpha$ -LiFePO <sub>4</sub> prepared by a microwave-assisted route during electrochemical charging (Li <sup>+</sup> deintercalation). The pre-edge (A) and rising edge (B) shift to lower energy as Li <sup>+</sup> is removed from the structure. (b) The second derivative of the pre-edge shows an increase in Fe <sup>3+</sup> and a decrease in Fe <sup>2+</sup> as Li <sup>+</sup> is deintercalated. . . . .	81
3.26 (a) Normalised <i>in situ</i> Fe K-edge XAS of $\alpha/\beta$ -LiFePO <sub>4</sub> prepared by a microwave-assisted route during electrochemical charging (Li <sup>+</sup> deintercalation). The pre-edge (A) and rising edge (B) shift to lower energy as Li <sup>+</sup> is removed from the structure. (b) The second derivative of the pre-edge shows an increase in Fe <sup>3+</sup> and a decrease in Fe <sup>2+</sup> as Li <sup>+</sup> is deintercalated. . . . .	82
3.27 Raw data and EXAFS fit of $\alpha$ -LiFePO <sub>4</sub> to <i>Pnma</i> structured LiFePO <sub>4</sub> . 31 Two features are observed for the Fe-O radial distances (2.0 Å) and Fe-P (3.2 Å). . . . .	83
3.28 Raw data and EXAFS fit of $\alpha$ -Li <sub>0.77</sub> FePO <sub>4</sub> to <i>Pnma</i> structured FePO <sub>4</sub> taken from Reference 31. Two features are observed for the Fe-O radial distances at 1.8 Å and 2.2 Å and two for Fe-P radial distances at 2.5 Å and 3.1 Å. . . . .	85
3.29 The average interatomic distance of Fe-O and Fe-P calculated from EXAFS data collected for $\alpha$ -Li <sub>x</sub> FePO <sub>4</sub> shows a small decrease with decreasing Li <sup>+</sup> concentration. $\alpha$ -Li <sub>1</sub> FePO <sub>4</sub> was fit with a <i>Pnma</i> structured $\alpha$ -LiFePO <sub>4</sub> standard while all other concentrations were fit with a <i>Pnma</i> FePO <sub>4</sub> standard taken from Reference 31. . . . .	87

4.1	Chemical structure of choline chloride (ChCl). . . . .	90
4.2	(a) Average power required to maintain a given temperature for 4 ml of (di)ethaline and (tetra)ethaline irradiated with microwaves ( $\nu = 2.45$ GHz). (b) Average power required to maintain a given temperature for 4 ml of glyceline or Gly irradiated with microwaves ( $\nu = 2.45$ GHz). . . . .	92
4.3	PXRD patterns collected for $\alpha$ -LiFePO <sub>4</sub> syntheses conducted in a 1:2 molar ratio of ChCl and either DEG [(di)ethaline] or TEG [(tetra)ethaline] for 3 h at 220 °C. $\alpha$ -LiFePO <sub>4</sub> and an impurity of Li <sub>3</sub> PO <sub>4</sub> (*) is obtained in both cases. . . . .	93
4.4	PXRD of products obtained from the microwave-assisted synthesis of $\alpha$ -LiFePO <sub>4</sub> in a 1:2 ChCl:Gly after 3 h of irradiation. $\alpha$ -LiFePO <sub>4</sub> and an impurity of Li <sub>3</sub> PO <sub>4</sub> (*) is obtained at all temperatures. . . . .	94
4.5	Power consumption versus temperature of pure ethylene glycol and ethaline in the CEM Discover SP microwave synthesiser ( $\nu = 2.45$ GHz). . . . .	95
4.6	FTIR spectra of choline chloride and ethylene glycol and the mixture of the two (ethaline). The solvent shows good chemical stability upon heating to temperatures required for microwave-assisted synthesis of $\alpha$ -LiFePO <sub>4</sub> nanoparticles. . . . .	96
4.7	PXRD patterns for products obtained after 1 h microwave-assisted solvothermal preparation in ethaline and expected reflections for $\alpha$ -LiFePO <sub>4</sub> . <sup>31</sup> Impurity peaks from Li <sub>3</sub> PO <sub>4</sub> are observed below 250 °C. . . . .	97
4.8	PXRD patterns for products obtained after 3 h microwave-assisted solvothermal preparation in ethaline and expected reflections for $\alpha$ -LiFePO <sub>4</sub> . <sup>31</sup> Impurity peaks from Li <sub>3</sub> PO <sub>4</sub> are observed below 240 °C. . . . .	98
4.9	PXRD patterns for products obtained after 5 h microwave-assisted solvothermal preparation in ethaline and expected reflections for $\alpha$ -LiFePO <sub>4</sub> . <sup>31</sup> Impurity peaks from Li <sub>3</sub> PO <sub>4</sub> are observed below 220 °C. . . . .	99
4.10	SEM images of $\alpha$ -LiFePO <sub>4</sub> prepared in 1:2 ethaline after 5h of $\mu\lambda$ irradiation at (a) 220 °C and (b) 230 °C. . . . .	100

4.11 Average power required to maintain a temperature of 4 ml of 1:3 ethaline or 2:3 ethaline with microwave irradiation ( $\nu = 2.45$ GHz) showing an increase in both cases versus the results for 1:2 ethaline. . . . .	101
4.12 (a) PXRD $\alpha$ -LiFePO <sub>4</sub> synthesised in a 1:3, ChCl:EG molar mixture. Below 230 °C an impurity of Li <sub>3</sub> PO <sub>4</sub> is observed (*). (b) Rietveld refinement of PXRD data collected for $\alpha$ -LiFePO <sub>4</sub> prepared in 1:3 ethaline at 230 °C and 240 °C after 3 h of microwave irradiation ( $\nu = 2.45$ GHz). A good fit to the ICSD literature pattern is observed in both cases. <sup>31</sup> . . . . .	102
4.13 SEM images of $\alpha$ -LiFePO <sub>4</sub> prepared in 1:3 ethaline at (a) 230 °C and (b) 240 °C after 3 h of microwave irradiation ( $\nu = 2.45$ GHz). . . . .	103
4.14 (b) First charge and discharge cycle from GCPL of carbon coated $\alpha$ -LiFePO <sub>4</sub> synthesised in 1:3 ethaline at 240 °C. Cycling was carried out at a C/10 rate between 2.2 V and 4 V. (b) GCPL of $\alpha$ -LiFePO <sub>4</sub> synthesised in 1:3 ethaline for 3 h at 240 °C at increasing rates. . . . .	104
4.15 (a) PXRD of $\alpha$ -LiFePO <sub>4</sub> prepared in 2:3 ethaline after 1 h of microwave irradiation ( $\nu = 2.45$ GHz). Peaks from an impurity of Li <sub>3</sub> PO <sub>4</sub> are denoted by *. (b) Rietveld refinement of PXRD data collected for $\alpha$ -LiFePO <sub>4</sub> prepared in 2:3 ethaline at 230 °C and 240 °C after 1 h of microwave irradiation ( $\nu = 2.45$ GHz). A good fit to the ICSD literature pattern is observed in both cases. . .	105
4.16 (a) PXRD patterns collected for the synthesis of $\alpha$ -LiFePO <sub>4</sub> in 2:3 ethaline after 3 h of microwave irradiation ( $\nu = 2.45$ GHz). Phase pure $\alpha$ -LiFePO <sub>4</sub> is obtained at all temperatures with peak broadening observed with decreasing temperature. (b) Rietveld refinement of PXRD data collected for $\alpha$ -LiFePO <sub>4</sub> prepared in 2:3 ethaline at 200 °C and 240 °C after 3 h of microwave irradiation ( $\nu = 2.45$ GHz). A good fit to the ICSD literature pattern is observed in both cases. <sup>31</sup> . . . . .	106
4.17 SEM images of $\alpha$ -LiFePO <sub>4</sub> prepared in 2:3 ethaline after 3 h of irradiation at (a) 200 °C, (b) 210 °C, (c) 220 °C, (d) 230 °C and (e) 240 °C. . . . .	108

4.18 (a) PXRD patterns collected for the synthesis of $\alpha$ -LiFePO <sub>4</sub> in 2:3 ethaline after 5 h of microwave irradiation ( $\nu = 2.45$ GHz). Phase pure $\alpha$ -LiFePO <sub>4</sub> is obtained at all temperatures with peak broadening observed with decreasing synthesis temperature. (b) Rietveld refinement of PXRD data collected for $\alpha$ -LiFePO <sub>4</sub> prepared in 2:3 ethaline at 200 °C and 230 °C after 5 h of microwave irradiation ( $\nu = 2.45$ GHz). A good fit to the ICSD literature pattern is observed in both cases. <sup>31</sup> . . . . .	109
4.19 SEM images of $\alpha$ -LiFePO <sub>4</sub> prepared in 2:3 ethaline at (a) 200 °C, (b) 210 °C, (c) 220 °C and (d) 230 °C. . . . .	110
4.20 PXRD of $\alpha$ -LiFePO <sub>4</sub> prepared in 2:3 ethaline at 200 °C, 220 °C and 240 °C after carbon coating with sucrose and annealing at 700 °C. Phase purity of the <i>Pnma</i> structured $\alpha$ -LiFePO <sub>4</sub> is retained in all samples. . . . .	111
4.21 (a) First charge and discharge cycle from GCPL of carbon coated $\alpha$ -LiFePO <sub>4</sub> synthesised in 2:3 ethaline after 3 h of microwave irradiation at 200 °C, 220 °C and 240 °C. Cycling was carried out at a C/10 rate between 2.2 V and 4 V. (b) GCPL of carbon coated $\alpha$ -LiFePO <sub>4</sub> synthesised in 2:3 ethaline for 3 h between 2.2 V and 4 V. The rate capability shows that the 240 °C has a superior discharge capacity at all rates compared to 200 °C. . . . .	112
4.22 PXRD of $\alpha$ -LiFePO <sub>4</sub> prepared in 2:3 ethaline at 200 °C, 220 °C and 240 °C post-cycling. The <i>Pnma</i> structure of $\alpha$ -LiFePO <sub>4</sub> is retained in all samples with the evolution of FePO <sub>4</sub> (*) due to irreversible Li <sup>+</sup> deintercalation. . . . .	113
4.23 Chemical structure of tetramethylammonium chloride (TMAC). . . . .	118
4.24 (a) PXRD patterns collected for samples synthesised in 1:2 EG:TMAC media after 3 h of microwave irradiation ( $\nu = 2.45$ GHz) at 200 °C, 210 °C, 220 °C and 230 °C. Phase pure $\alpha$ -LiFePO <sub>4</sub> is obtained at all temperatures showing peak broadening with decreasing temperature. (b) Rietveld refinement of PXRD data collected for $\alpha$ -LiFePO <sub>4</sub> prepared in 1:2 TMAC at 200 °C and 230 °C after 3 h of microwave irradiation ( $\nu = 2.45$ GHz). A good fit to the ICSD literature pattern is observed in both cases. <sup>31</sup> . . . . .	119

4.25 SEM images collected for $\alpha$ -LiFePO <sub>4</sub> prepared in 1:2 TMAC:EG after 3 h of microwave irradiation ( $\nu = 2.45$ GHz) at (a) 200 °C, (b) 210 °C, (c) 220 °C and (d) 230 °C. . . . .	121
4.26 GCPL of carbon coated $\alpha$ -LiFePO <sub>4</sub> synthesised in TMAC based DES at 200 °C, 210 °C, 220 °C and 230 °C showing superior discharge rates with decreasing synthesis temperature. . . . .	122
5.1 Relative abundance of redox metals in the Earth's crust versus iron. Inset is a zoomed view of the 3 <sup>rd</sup> to 17 <sup>th</sup> most abundant redox metals. . . . .	124
5.2 Crystal structure of bronze phase VO <sub>2</sub> (B) (space group <i>C12/m1</i> ) showing an open framework, ideal for Li <sup>+</sup> intercalation. Vanadium atoms are shown in blue and oxygen atoms in orange. The VO <sub>6</sub> polyhedra are also in blue. . . . .	125
5.3 (a) PXRD of the sample prepared in isopropanol. A transformation to phase pure V <sub>3</sub> O <sub>7</sub> , space group <i>C12/c1</i> , is observed after heating. (b) Rietveld refinement after annealing at 400 °C in Ar with no preferred orientation showing a poor fit to V <sub>3</sub> O <sub>7</sub> taken from Reference 220. (c) Rietveld refinement after applying preferred orientation along the [ <i>n</i> 0 0] direction showing an excellent fit. . . . .	127
5.4 (a) PXRD data of V <sub>3</sub> O <sub>7</sub> prepared by a microwave-assisted route emphasising the difference in peak intensity compared to an ICSD standard diffraction pattern for bulk V <sub>3</sub> O <sub>7</sub> taken from Reference 220. (b) Crystal structure of V <sub>3</sub> O <sub>7</sub> showing planes corresponding to the (-1 1 1) (red), (-6 0 2) (green) and (6 0 0) (violet) planes. . . . .	128
5.5 SEM of V <sub>3</sub> O <sub>7</sub> after annealing at 400 °C for 1 h at low (a) and high (b) magnification showing a sheets tens of $\mu\text{m}$ in diameter approximately 100 nm in thickness. . . . .	129
5.6 (a) Galvanostatic cycling of V <sub>3</sub> O <sub>7</sub> at 100 mA g <sup>-1</sup> between 1.5 V and 3.75 V. (b) Discharge capacity of V <sub>3</sub> O <sub>7</sub> over 20 cycles shows a large initial loss. . . . .	131

5.7	PXRD of products from solvothermal (48 h reaction [VO <sub>2</sub> (B)_ST]) and microwave-assisted (1 h [VO <sub>2</sub> (B)_MW_1h], 3h [VO <sub>2</sub> (B)_MW_3h] and 6 h [VO <sub>2</sub> (B)_MW_6h] reactions) reduction of V <sub>2</sub> O <sub>5</sub> by 37% formaldehyde solution. All samples can be indexed to phase-pure VO <sub>2</sub> (B) (space group <i>C12/m1</i> ). <sup>223</sup> Increased peak broadening is observed in VO <sub>2</sub> (B)_MW_ <i>nh</i> samples with decreased irradiation time. . . . .	133
5.8	Scanning electron microscopy of VO <sub>2</sub> (B) prepared after 1 h [VO <sub>2</sub> (B)_MW_1h] (a), 3 h [VO <sub>2</sub> (B)_MW_3h] (b) and 6 h [VO <sub>2</sub> (B)_MW_6h] (c) of microwave-irradiation. (d) SEM image of VO <sub>2</sub> (B) prepared by conventional solvothermal routes after 48 h of heating [VO <sub>2</sub> (B)_ST]. Multimicron length rods are observed in VO <sub>2</sub> (B)_ST compared to sub-micron length rods from the VO <sub>2</sub> (B)_MW_ <i>nh</i> samples. . . . .	134
5.9	Cyclic voltammetry of VO <sub>2</sub> (B)_MW_3h between 1.6 V and 3.6 V at a rate of 0.1 mV s <sup>-1</sup> showing two peaks corresponding to the the oxidation and reduction processes arising from the V <sup>4+</sup> /V <sup>3+</sup> redox couple. . . . .	135
5.10	Galvanostatic cycling with potential limitation profile from the first discharge-charge cycle of VO <sub>2</sub> (B)_ST and VO <sub>2</sub> (B)_MW_3h from 1.8 V to 3.8 V at a C/10 rate. It is observed that VO <sub>2</sub> (B)_MW_3h is able to intercalate more Li <sup>+</sup> per formula unit than the VO <sub>2</sub> (B)_ST sample. . . . .	136
5.11	Discharge capacities of the VO <sub>2</sub> (B)_ST and VO <sub>2</sub> (B)_MW_3h samples at rates increasing from C/10 to 10C. The GCPL was conducted between 1.8 V and 3.8 V. . . . .	137
5.12	XAS spectra collected on the vanadium K-edge of vanadium standards V <sup>3+</sup> (V <sub>2</sub> O <sub>3</sub> ), V <sup>4+</sup> (VC) and V <sup>5+</sup> (V <sub>2</sub> O <sub>5</sub> ), and of VO <sub>2</sub> (B)_ST, VO <sub>2</sub> (B)_MW3h <i>ex situ</i> . . . . .	138
5.13	Normalised <i>in situ</i> XAS collected on the vanadium K-edge during electrochemical discharge of (a) VO <sub>2</sub> (B)_MW_3h and (c) VO <sub>2</sub> (B)_ST. The shift in photon energy to lower eV with increasing Li <sup>+</sup> content is indicative of the V <sup>4+</sup> to V <sup>3+</sup> oxidation state change. (b) and (d) show the first derivative of (a) and (c) respectively. . . . .	140

5.14 PXRD for the solvothermal reduction of $V_2O_5$ by formaldehyde:EG solvent media. Phase pure $VO_2(B)$ is obtained where the EG content of the solvent is smaller than than 3 ml. . . . .	142
5.15 SEM of $VO_2(B)$ nanostructures prepared in formaldehyde:EG binary solvent mixtures of (a) 4 ml:1 ml and (b) 3 ml:2 ml. . . . .	143
5.16 (a) First cycle GCPL of $VO_2(B)$ synthesised in formaldehyde:DEG ratios of 4 ml:1 ml (blue), 3 ml:2 ml (violet) and 2 ml:3 ml (red). (b) Discharge capacity over 20 cycles for $VO_2(B)$ synthesised in formaldehyde:DEG ratios of 4:1 (blue) and 3:2 (violet) showing a good capacity retention of 95 % and 96 % respectively. . . . .	144
5.17 PXRD patterns for the solvothermal reduction of $V_2O_5$ by formaldehyde:DEG solvent media. Increasing the volume of DEG decreases the intensity of the <i>hkl</i> (002) and (003) plane peaks at $29^\circ$ and $44^\circ 2\theta$ respectively. . . . .	145
5.18 SEM of $VO_2(B)$ nanostructures prepared in formaldehyde:DEG binary solvent mixtures of (a) 4.5 ml:0.5 ml,(b) 4 ml:1 ml, (c) 3.5 ml:1.5 ml, (d) 3 ml:2 ml, (e) 2 ml:2 ml and (f) 2 ml:3 ml. All samples exhibit a nanorod morphology, and some exhibit hierarchical structures. . . . .	146
5.19 (a) First cycle galvanostatic cycling profiles of $VO_2(B)$ synthesised in formaldehyde:DEG ratios of 4 ml:1 ml (blue) and 3 ml:2 ml (violet). (b) Discharge capacity over 20 cycles for $VO_2(B)$ synthesised in formaldehyde:DEG ratios of 4:1 (blue) and 3:2 (violet) showing excellent capacity retentions of 95 % and 96 %, respectively. . . . .	147
5.20 SEM images of $VO_2(B)$ prepared in the presence of (a) 1 mg, (b) 2.5 mg and (c) 5 mg of PVP. (d) PXRD patterns of $VO_2(B)$ synthesised by microwave-assisted reduction of $V_2O_5$ in formaldehyde solution in the presence of PVP. Increasing the amount of PVP leads to a decrease in the (002) and (003) plane peak intensities. . . . .	149

5.21 (a) First cycle profile for the galvanostatic cycling of VO <sub>2</sub> (B) prepared in the presence of 1 mg of PVP by microwave-assisted solvothermal reduction in formaldehyde between 3.8 V and 1.8 V at a rate of C/10. The half-cell exhibits the intercalation of 0.8 Li <sup>+</sup> per formula unit (capacity of 258 mAh g <sup>-1</sup> ). The material shows excellent capacity retention over 11 cycles (b) with a capacity retention of 98 %.	150
5.22 Electrochemical capacity of VO <sub>2</sub> (B) samples synthesised by various methods showing improvements on capacity can be made by specific modification of the solvent system or addition of a PVP additive.	152
6.1 Crystal structures of (a) VOOH and (b) H <sub>2</sub> V <sub>3</sub> O <sub>8</sub> . Both compounds exhibit open frameworks ideal for Li <sup>+</sup> intercalation. H atoms are omitted.	155
6.2 (a) PXRD pattern collected for synthetic V <sub>4</sub> O <sub>6</sub> (OH) <sub>4</sub> and a reference pattern for the material taken from Reference 248. (b) shows the transformation during reduction from the V <sub>2</sub> O <sub>5</sub> structure to V <sub>4</sub> O <sub>6</sub> (OH) <sub>4</sub> (Häggite) structured material.	156
6.3 SEM (a) showing a typical particle of V <sub>4</sub> O <sub>6</sub> (OH) <sub>4</sub> approximately 10 μm in diameter. EDX mapping of vanadium in the sample shown in blue (b) indicates a homogenous distribution across the particle.	157
6.4 XANES spectra collected for V <sub>4</sub> O <sub>6</sub> (OH) <sub>4</sub> prepared by a microwave assisted method, and standards of V <sup>4+</sup> [VO(acac) <sub>2</sub> ] and V <sup>5+</sup> [V <sub>2</sub> O <sub>5</sub> ].	158
6.5 Galvanostatic cycling profiles (a) of V <sub>4</sub> O <sub>6</sub> (OH) <sub>4</sub> at a rate of 100 mA g <sup>-1</sup> and the respective charge and discharge capacities as a function of cycle number (b).	159
6.6 (a) Microwave-assisted reactions carried out in 2 ml:2 ml and 3 ml:1 ml IPA:H <sub>2</sub> O showing no reduction of the V <sub>2</sub> O <sub>5</sub> reagent. The reference pattern for <i>Pmmnz</i> structured V <sub>2</sub> O <sub>5</sub> is take from Reference 253.(b) Rietveld refinement of H <sub>2</sub> V <sub>3</sub> O <sub>8</sub> prepared in 1 ml:3 ml, H <sub>2</sub> O:IPA and (c) with preferential orientation applied along the [0 0 1] direction. Refinement was performed using H <sub>2</sub> V <sub>3</sub> O <sub>8</sub> diffraction data from Reference 243.	160

6.7	(a) SEM image of $\text{H}_2\text{V}_3\text{O}_8$ nanowires and (b) the $\text{H}_2\text{V}_3\text{O}_8$ crystal structure showing the preferential growth along the $b$ -axis ( $[0\ 0\ 1]$ direction) from Rietveld analysis. . . . .	162
6.8	(a) CV of $\text{H}_2\text{V}_3\text{O}_8$ between 4 V and 0.1 V showing irreversible loss of redox features and close to no electrochemical activity after 15 cycles. The large peak at 0.5 V corresponds to the formation of the SEI layer. (b) CV of $\text{H}_2\text{V}_3\text{O}_8$ between 1.5 V and 4 V showing good reversibility of the redox behaviour. . .	163
6.9	(a) Galvanostatic cycling of $\text{H}_2\text{V}_3\text{O}_8$ between 1.5 V and 3.75 V versus $\text{Li}/\text{Li}^+$ at $100\ \text{mA}\ \text{g}^{-1}$ . (b) Excellent stability of the charge and discharge capacities is observed after 20 cycles, with a retention of 98 % and 95 % respectively, inset shows the cycling performance at faster rates. . . . .	165
6.10	GCPL of $\text{H}_2\text{V}_3\text{O}_8$ nanowires between 3.75 V and 1.5 V at a constant current of $1000\ \text{mA}\ \text{g}^{-1}$ . . . . .	166
6.11	(a) Rietveld refinement of $\text{Li}_{0.4}\text{H}_2\text{V}_3\text{O}_8$ prepared by chemical lithiation of $\text{H}_2\text{V}_3\text{O}_8$ nanowires using $\text{H}_2\text{V}_3\text{O}_8$ diffraction data from Reference 243. Numerical parameters for the refinement can be seen in Table 8.2. (b) SEM image of $\text{Li}_{0.4}\text{H}_2\text{V}_3\text{O}_8$ showing that the overall nanowire morphology is preserved but with a reduction length due to grinding in a pestle and mortar. . . . .	168
6.12	Raw muon data collected at 300 K showing a relaxation in the positron decay asymmetry with increasing time. Applying larger longitudinal fields sequentially decouples the muon decay from paramagnetic $\text{V}^{4+}$ . . . . .	169
6.13	(a) Muon spin relaxation measurements performed on $\text{Li}_x\text{H}_2\text{V}_3\text{O}_8$ show temperature dependence of the fluctuation rate, $\nu$ , beginning at $180\ ^\circ\text{C}$ . (b) The field distribution width, $\Delta$ , remains a relative constant suggesting the behaviour of $\nu$ can be wholly attributed to the diffusion of $\text{Li}^+$ . (c) Activation energy calculated from an Arrhenius plot over the thermally activated region. . . . .	171
6.14	<i>Ex situ</i> XAS of $\text{H}_2\text{V}_3\text{O}_8$ prepared by a microwave-assisted route and vanadium standards $\text{V}_2\text{O}_3$ ( $\text{V}^{3+}$ ), VC ( $\text{V}^{4+}$ ) and $\text{V}_2\text{O}_5$ ( $\text{V}^{5+}$ ) . . . . .	172

6.15 <i>In situ</i> normalised XAS spectra over the XANES region of $\text{H}_2\text{V}_3\text{O}_8$ during electrochemical lithiation showing an increasing shift in the edge energy to lower eV with increasing $\text{Li}^+$ concentration due to the reduction of $\text{V}^{5+}$ in $\text{H}_2\text{V}_3\text{O}_8$ . . . . .	173
6.16 B3LYP pre-edge calculation for the $\text{H}_2\text{V}_3\text{O}_8$ asymmetric unit and experimental data showing the expected energies for the 3 V sites. Both $\text{V}^{5+}$ environments overlap at high energy while $\text{V}^{4+}$ is at lower energy. . . . .	174
6.17 Second derivative of the pre-edge feature for $\text{H}_2\text{V}_3\text{O}_8$ as an increasing concentration of $\text{Li}^+$ is inserted showing separate contributions from $\text{V}^{5+}$ (5470.4 eV) and $\text{V}^{4+}$ (5469.2 eV). . . . .	175
6.18 Pre-edge fits using two Lorentzian functions with centroids fixed at 5470.4 eV ( $\text{V}^{5+}$ ) and 5469.2 eV ( $\text{V}^{4+}$ ) and an arc tangent function to account for contributions from the rising edge of (a) $\text{H}_2\text{V}_3\text{O}_8$ and (b) $\text{Li}_2\text{H}_2\text{V}_3\text{O}_8$ . . . . .	177
6.19 Scan number versus peak area for the two contributions to the pre-edge from $\text{V}^{5+}$ and $\text{V}^{4+}$ in $\text{H}_2\text{V}_3\text{O}_8$ . It is observed that $\text{V}^{5+}$ decreases while $\text{V}^{4+}$ increases indicating a change in the relative concentration upon $\text{Li}^+$ insertion. . . . .	177
8.1 Histogram of particle width for $\text{H}_2\text{V}_3\text{O}_8$ prepared by a microwave-assisted solvothermal route. . . . .	184
8.2 Histogram of particle width for chemically lithiated $\text{Li}_{0.4}\text{H}_2\text{V}_3\text{O}_8$ prepared by a microwave-assisted solvothermal route. . . . .	185

## List of Tables

1.1	A comparison of common solvents and their physical properties as candidates for solvents for microwave syntheses. . . . .	28
2.1	Investigated salts and hydrogen bond donors (HBD) for deep eutectic mixtures.	37
3.1	Values of the exponential fits to maintenance power studies in Figure 3.2. . .	58
3.2	Calculated Rietveld refinement parameters from the PXRD patterns of $\alpha$ -LiFePO <sub>4</sub> prepared in EG at 250 °C for 5 h. . . . .	64
3.3	Calculated EXAFS parameters for nanostructured $\alpha$ -Li <sub>1</sub> FePO <sub>4</sub> fit to data from a bulk sample of $\alpha$ -LiFePO <sub>4</sub> taken from Reference 31. . . . .	84
3.4	Calculated EXAFS parameters for nanostructured $\alpha$ -Li <sub>0.77</sub> FePO <sub>4</sub> fit to data from a bulk sample of FePO <sub>4</sub> taken from Reference 31. . . . .	86
4.1	Composition of DES mixtures Type I, II, III and IV reproduced from Reference 193. All contain metals except which may contaminate synthesis of $\alpha$ -LiFePO <sub>4</sub> except type III. . . . .	91
4.2	Calculated Rietveld refinement parameters from the PXRD patterns of $\alpha$ -LiFePO <sub>4</sub> prepared in 1:3 ethaline after 3 h of microwave irradiation (textnu = 2.45 GHz) at 230 and 240 °C. . . . .	114
4.3	Calculated Rietveld refinement parameters from the PXRD patterns of $\alpha$ -LiFePO <sub>4</sub> prepared in 2:3 ethaline after 1 h of microwave irradiation (textnu = 2.45 GHz) at 230 and 240 °C. . . . .	115
4.4	Calculated Rietveld refinement parameters from the PXRD patterns of $\alpha$ -LiFePO <sub>4</sub> prepared in 2:3 ethaline after 3 h of microwave irradiation (textnu = 2.45 GHz) at 200 °C and 240 °C. . . . .	116
4.5	Calculated Rietveld refinement parameters from the PXRD patterns of $\alpha$ -LiFePO <sub>4</sub> prepared in 2:3 ethaline after 5 h of microwave irradiation (textnu = 2.45 GHz) at 200 °C and 240 °C. . . . .	117
4.6	Calculated Rietveld refinement parameters from the PXRD patterns of $\alpha$ -LiFePO <sub>4</sub> prepared in 1:2 TMAC:EG at 200 °C and 230 °C for 5 h. . . . .	120

5.1	Calculated Rietveld refinement parameters from PXRD data collected for $V_3O_7$ annealed at 400 °C for 1 h with preferred orientation along [n 0 0] compared to the reference to the pattern taken from Reference 220. . . . .	130
5.2	Calculated crystallite domain sizes from the Scherrer broadening in PXRD of $VO_2(B)$ prepared by solvothermal and microwave-assisted methods in Figure 5.7. . . . .	132
6.1	Calculated Rietveld refinement parameters from the powder XRD pattern of $Li_{0.4}H_2V_3O_8$ prepared by chemical lithation of $H_2V_3O_8$ with reference to the pattern taken from Reference 243. . . . .	161
8.1	Rietveld refinement parameters for the dual-phase refinement in Figure 3.15 from Figure 3.15. . . . .	186
8.2	Calculated Rietveld refinement parameters from the powder XRD pattern of $Li_{0.4}H_2V_3O_8$ prepared by chemical lithation of $H_2V_3O_8$ with reference to the pattern taken from Reference . . . . .	187

## Chapter 1: Introduction

With the realisation that fossil fuel resources are finite and our global population ever growing, focus has turned towards renewable, sustainable technologies. In particular, developments in efficient storage methods will slow down the rate at which fossil fuel reserves are depleted by reducing waste energy, and also ensure effective use of the energy harvested from emerging green technologies, such as wind and solar. Figure 1.1 shows the energy density of current energy storage technologies. Lithium ion (Li-ion) batteries offer a promising energy storage solution with higher energy densities compared to lead-acid (used primarily in automobiles) and Ni-Cd (used primarily in power tools). The increased volumetric and gravimetric energy density in Li-ion batteries mean that less material can be used to give a similar energy output, compared to other technologies. This allows for lighter cells or smaller cells to be developed, making them ideal for portable electronic applications.

The demand for power sources in electric vehicles has increased dramatically in recent years with many companies making significant investments, such as Honda ©, Toyota ©, Nissan © and Tesla Motors ©. By replacing conventional petrol based motor vehicles with electric vehicles, harmful exhaust emissions could also be reduced and is a current, global concern in major cities. Several companies have also invested in domestic energy storage units, such as the Tesla Powerwall © and the Samsung Energy Storage System ©. These advances in technology make domestic solar panels more attractive, allowing the generation of solar energy during the day to use at night when there is no sunlight. Local power storage could also limit the energy losses from long range electricity transfer around national grids. Through the use of these systems the amount of fossil fuels burned will also decrease, generating less CO<sub>2</sub> and CO. These gases are considered to be a contributing factor to global warming, and limiting their release into the atmosphere would help to alleviate this effect.<sup>2</sup>

Investing research into Li-ion batteries presents an exciting opportunity to advance our current electronic technologies, and promote clean energy, and efficient storage of electricity.

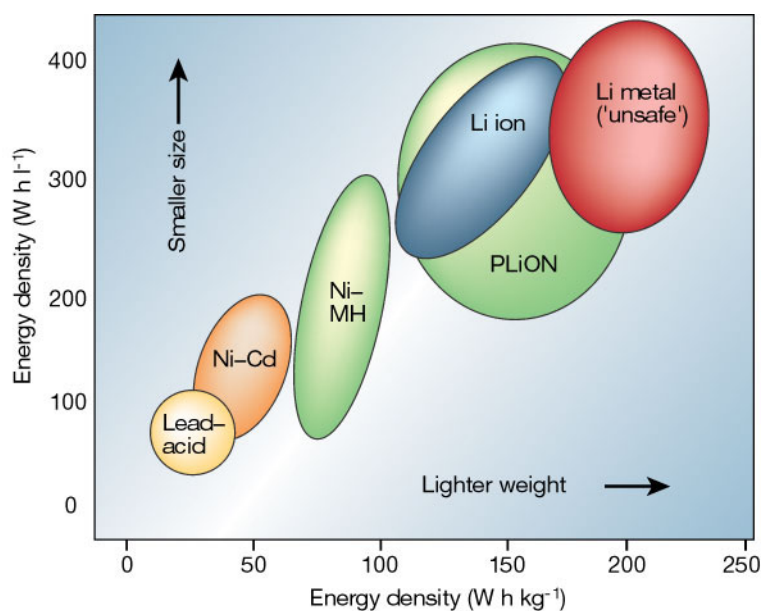


**Figure 1.1:** Volumetric and gravimetric energy density of different available energy storage devices. Li-ion batteries offer one of the highest potential, safe sources of energy density currently available. Adapted with permission from Reference 1. Copyright (2001) Nature.

## 1.1 Lithium ion batteries

Li-ion batteries have been of increasing interest as they provide a route to rechargeable storage of electrochemical energy. Li-ion batteries consist of three main parts, a cathode, an anode and an electrolyte, Figure 1.2.

The anode is a material with a low reduction potential versus  $\text{Li}/\text{Li}^+$  which is able to accommodate  $\text{Li}^+$  during electrochemical charging. Anode materials typically undergo either conversion reactions, such as  $\text{SnO}_2$ , forming separate phases of Sn and  $\text{Li}_2\text{O}$  upon reduction ( $1494 \text{ mAh g}^{-1}$ ), or intercalation reactions, such as graphite, where  $\text{Li}^+$  ions are inserted between the layers of graphite.<sup>3,4</sup> Most commonly, graphite is used as the anode due to severe concerns with volumetric expansion in metal oxide conversion anodes.  $\text{SnO}_2$  for instance experiences large capacity losses after extended cycling due to 420 % volumetric expansion upon incorporation of  $\text{Li}^+$ , leading to pulverisation of the particles.<sup>5</sup>

The cathode in a  $\text{Li}^+$  ion battery is a material with a high reduction potential versus  $\text{Li}/\text{Li}^+$  and accepts  $\text{Li}^+$  upon electrochemical discharge. Typically, layered or channeled materi-

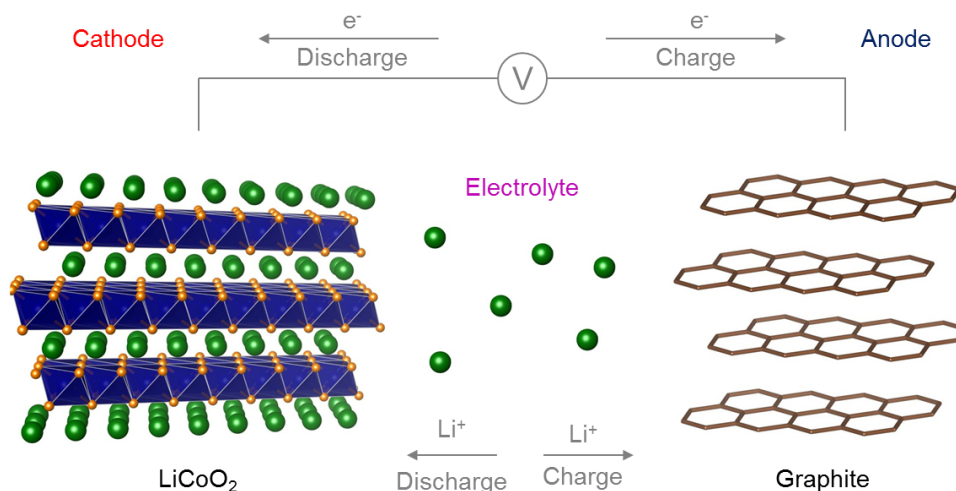


**Figure 1.2:** Schematic of a Li-ion battery showing the movement of  $\text{Li}^+$  and electrons during electrochemical discharge between the anode (graphite) and the cathode ( $\text{LiCoO}_2$ ) through the electrolyte. The  $\text{Li}^+$  and electrons take separate pathways between the electrodes, and this process is reversible on electrochemical charging.

als have been employed as intercalation electrodes due to their limited volumetric expansion upon cycling, although some examples of conversion cathodes exist in the literature.<sup>6</sup>  $\text{LiCoO}_2$  is a prominent Li-ion insertion cathode and possesses a layered structure (Figure 1.2).  $\text{LiCoO}_2$  operates at a voltage of 4 V versus  $\text{Li}/\text{Li}^+$  and exhibits a discharge capacity of  $180 \text{ mAh g}^{-1}$ .<sup>7</sup>

The electrolyte is often comprised of a lithium salt in an organic solvent such as  $\text{LiPF}_6$  in a mixture of dimethyl carbonate and ethylene carbonate, and conducts the  $\text{Li}^+$  charge from the two electrodes. The electrolyte should possess a high ionic conductivity and extremely low electronic conductivity to force the electrons around an external circuit through an electrical output. If the electrons were to travel through the electrolyte, the discharging process would happen spontaneously, and could not be controlled.

To summarise, upon charging  $\text{Li}^+$  are extracted from the cathode ( $\text{LiCoO}_2$ ) and diffuse through the electrolyte to the anode (graphite). The movement of  $\text{Li}^+$  instigates the simultaneous movement electrons through the external circuit to preserve charge balance. When this occurs, the  $\text{Co}^{3+}$  atoms in  $\text{LiCoO}_2$  are oxidised to  $\text{Co}^{4+}$  due to the loss of one electron. This process is described in Equation 1.1, where G represents the graphite anode.



Fundamentally, these reactions occur due to a potential difference existing between the two electrodes. This is where it is more energetically favourable for one of the electrodes to be reduced, and one to be oxidised. This relationship can be evaluated using the free-energy of the redox reaction in Equation 1.2.

$$\Delta G^{\circ} = -nFE^{\circ} \quad (1.2)$$

$\Delta G^{\circ}$  is the change in free energy,  $n$  is the number of electrons,  $F$  is the Faraday constant and  $E^{\circ}$  is the potential. If  $\Delta G^{\circ}$  is negative then the redox reaction will proceed spontaneously, and the potential energy can be harvested. However, if  $\Delta G^{\circ}$  is positive then no reaction will occur, since the lowest energy state has already been achieved. The movement of electrons through the external circuit is what allows energy to be harvested from the cell.

Investigating these dynamics further, Figure 1.3 shows a schematic of the relative electron energies of the electrodes and the electrolyte. The anode (reductant, blue) and cathode (oxidant, red) are separated by the ionically conducting, and electronically insulating electrolyte (grey). The work functions of the anode and the cathode are denoted as  $\Phi_A$  and  $\Phi_C$  respectively. The work function is the minimum energy required to remove an electron from an atom, and thus oxidise it. The values of  $\Phi_A$  and  $\Phi_C$  are also proportional to their respective electrochemical potentials,  $\mu_A$  and  $\mu_C$ . The difference between  $\mu_A$  and  $\mu_C$  provides the operating voltage, or open circuit voltage ( $V_{OC}$ ) of the cell according to Equation 1.3.

$$V_{OC} = \mu_A - \mu_C \quad (1.3)$$

For a battery cell to possess thermodynamic stability, careful pairing of the electrodes with a suitable electrolyte is required.  $E_g$  is the energy window between the HOMO and LUMO of the electrolyte. Thermodynamic stability can be achieved by ensuring both  $\mu_A$  and  $\mu_C$  lie within the  $E_g$  window, leading to preferential reduction or oxidation of the electrodes, rather than the electrolyte. If  $\mu_A$  is higher than the LUMO of the electrolyte, the electrolyte will be reduced during electrochemical discharge. In addition, if the energy of  $\mu_C$  is lower than the HOMO of the electrolyte, the electrolyte will be oxidised during electrochemical

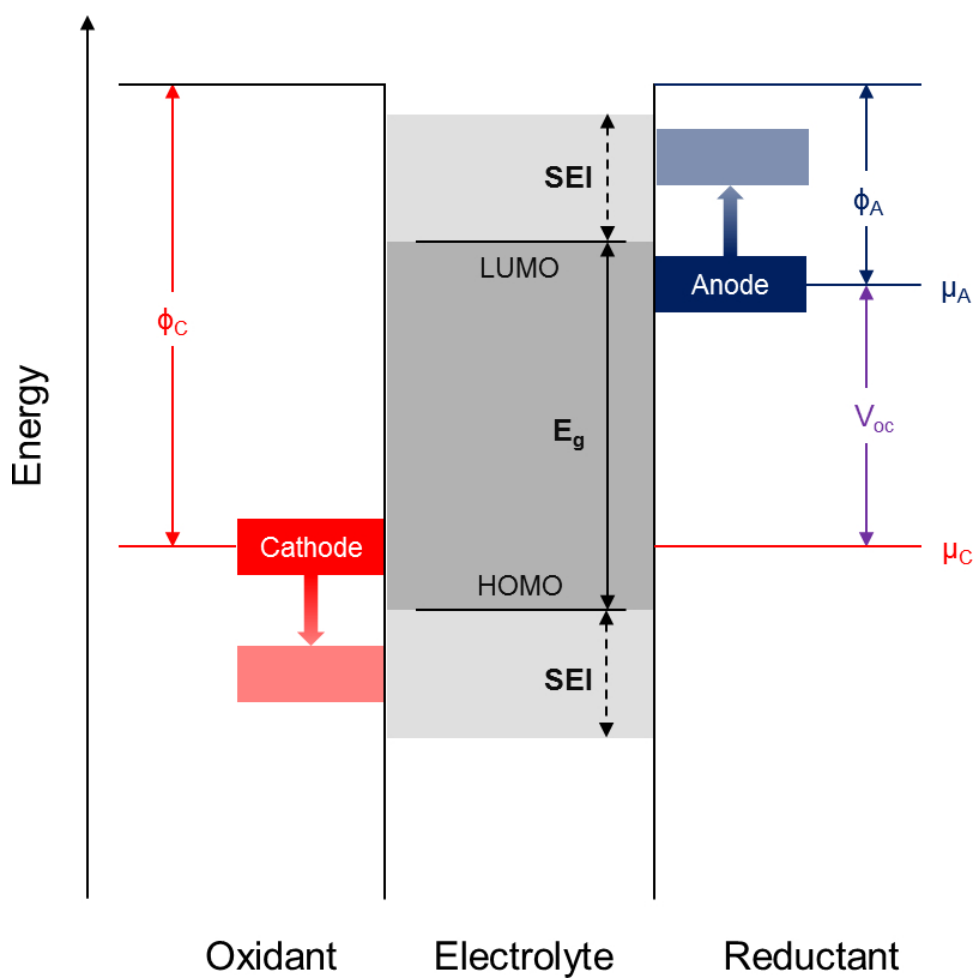


**Figure 1.3:** Schematic of the energy levels involved in electrochemical cycling of a Li-ion cell.

charging. However, if  $\mu_A$  is only slightly higher than the LUMO or  $\mu_C$  slightly lower than the HOMO a passivation layer may be formed between the electrode and the electrolyte. This occurs by consuming some of the electrolyte through oxidation or reduction to form a solid/electrolyte-interphase (SEI) on the surface of the electrodes.

For some materials, such as the cathode material  $\text{LiCoO}_2$ ,  $\mu_C$  is semi-compatible with liquid electrolytes. This is due  $\mu_C$  shifting to a lower energy during  $\text{Li}^+$  extraction, causing to the  $\text{Co}3d$  valence band in  $\text{LiCoO}_2$  to overlap with the  $\text{O}2p$  band of the electrolyte.<sup>8</sup> When more than half of the  $\text{Li}^+$  ions are removed from  $\text{LiCoO}_2$  during electrochemical charging in a cell, thermodynamic stability is lost and the electrolyte rapidly degrades, releasing  $\text{O}_2$ .<sup>9</sup> This is a key concern in cathode development, as oxygen evolution in battery cell can lead to chemical fires through combustion of the flammable electrolytes. Concern has also been raised over the toxicity ( $\text{LD}_{50} = 150$  and  $500 \text{ mg kg}^{-1}$ ) and limited availability of cobalt.<sup>10,11</sup> Similarly, the  $\mu_A$  of lithium metal which has an extremely high capacity ( $3860 \text{ mAh g}^{-1}$ ) lies above the LUMO of all currently known liquid electrolytes.<sup>12</sup> To overcome these challenges, it is essential to tailor  $\mu_A$  and  $\mu_C$  of the electrodes to compliment  $E_g$  while retaining high electrochemical capacities and highest possible voltages.

### 1.1.1 Tailoring voltage in Li-ion electrodes

Much research has been devoted to improving the electrochemical behaviour of transition metal redox couples to harvest the most energy in Li-ion electrodes. The most prominent example is the  $\text{Fe}^{3+}/\text{Fe}^{2+}$  redox couple. As iron is a cheap, abundant, environmentally benign metal, it is an attractive alternative to cobalt. However, iron oxides such as  $\text{Fe}_2\text{O}_3$  and  $\text{Fe}_3\text{O}_4$  show poor electrochemical stability, hindering the reinsertion of lithium after repeated charge and discharge cycles.<sup>13</sup> Further research has found that by substituting oxygen ligands with polyanions such as  $\text{SO}_4^{2-}$  and  $\text{SiO}_4^{3-}$  not only increases the electrochemical stability, but can lower the Fermi energy level of the  $\text{Fe}^{3+}/\text{Fe}^{2+}$  redox couple, increasing the cell potential.<sup>14,15</sup> This occurs due to the inductive effect. An increase in electronegativity of the polyanion increases the electron-withdrawing effect experienced by the Fe-O bond. This decreases the covalent nature of the Fe-O bond and decreases the redox energy. This reduction in energy increases the gap between the  $\text{Li}/\text{Li}^+$  and  $\text{Fe}^{2+}/\text{Fe}^{3+}$  redox energies, which

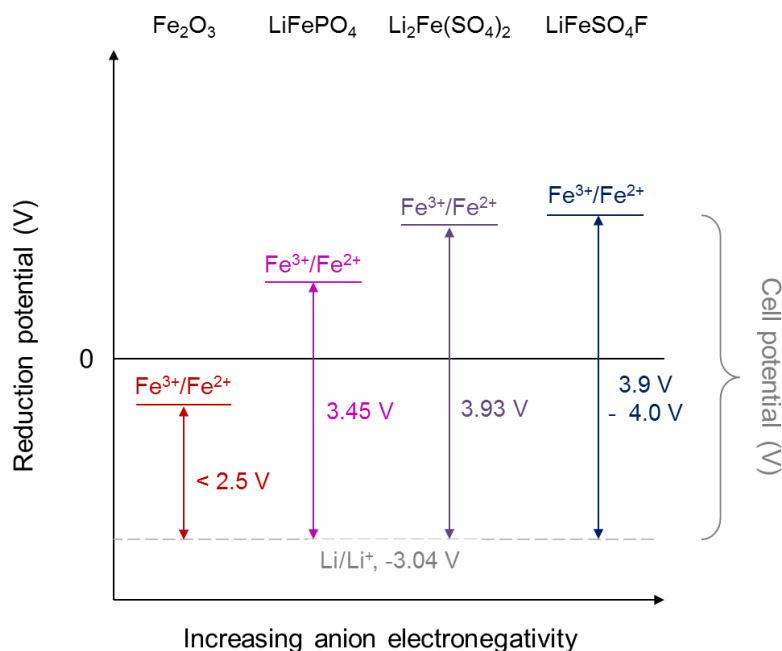


**Figure 1.4:** Operating voltage of iron oxide and polyanionic iron compounds showing an increase in potential with increasing electronegativity of the polyanion.

in turn decreases the  $\mu_C$  of the  $\text{Fe}^{3+}/\text{Fe}^{2+}$  redox couple. Figure 1.4 shows the effect of increasingly electronegative anions on the chemical potential of the  $\text{Fe}^{2+}/\text{Fe}^{3+}$  redox couple. The highest observed electrochemical potentials have been observed in sulfate based iron compounds.  $\text{Li}_2\text{Fe}(\text{SO}_4)_2$  can achieve a redox potential of 3.93 V versus  $\text{Li}/\text{Li}^+$  and is only bested by triplite structured  $\text{LiFeSO}_4\text{F}$ , which has shown the highest  $\text{Fe}^{3+}/\text{Fe}^{2+}$  redox couple to date of 3.9-4 V versus  $\text{Li}/\text{Li}^+$ .<sup>16</sup> Furthermore,  $\text{LiFeSO}_4\text{F}$  only exhibits a volumetric change of 0.6%.<sup>17</sup> However, the fluorination has not been exclusively linked to the inductive effect, and only exhibits a reversible capacity of  $85\text{ mAh g}^{-1}$ , though this can be improved to  $105\text{ mAh g}^{-1}$  with the addition of carbon nanotubes to increase the electronic conductivity.<sup>18</sup>

### 1.1.2 $\alpha$ - $\text{LiFePO}_4$ as an insertion electrode

Tailoring of the redox potential has also given rise to the highly attractive olivine phosphates. Olivine phosphate materials ( $\text{LiMPO}_4$ ; space group  $Pnma$ ) are an interesting class of compounds for positive insertion electrodes due to their structural stability, reversible intercalation of positive ionic species, and ease of metal site doping to modify electrochemical characteristics. Continued development of positive insertion electrodes for Li-ion batteries

has led to the investigation of olivine structured  $\alpha$ -LiFePO<sub>4</sub>, which exhibits a lower operating voltage of 3.45 V versus Li<sup>+</sup>/Li than LiCoO<sub>2</sub>, but a competitive theoretical capacity of 170 mAh g<sup>-1</sup>.<sup>19</sup> Olivine  $\alpha$ -LiFePO<sub>4</sub> is comprised of iron and lithium atoms occupying octahedral sites (M(1) and M(2) respectively) and phosphorus atoms occupying tetrahedral sites. The crystal structure of  $\alpha$ -LiFePO<sub>4</sub> can be seen in Figure 1.5.

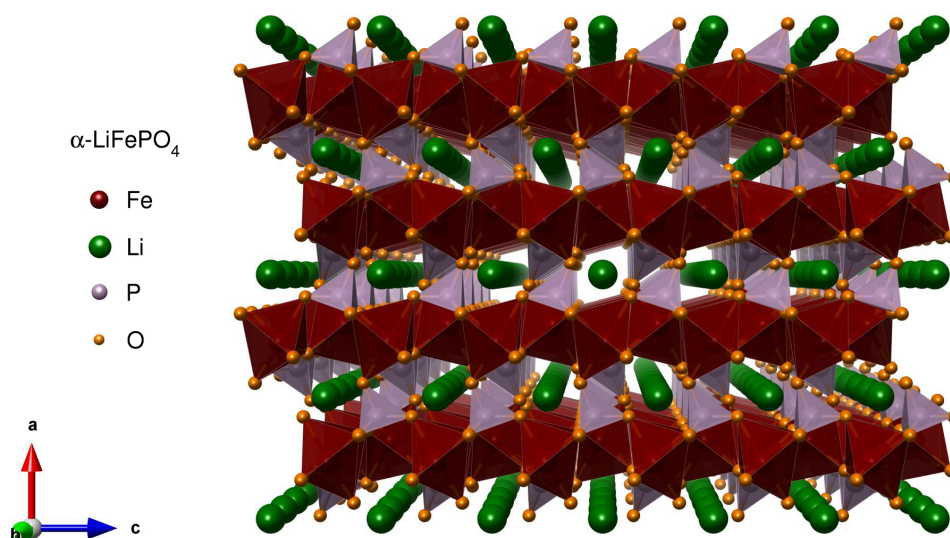


**Figure 1.5:** Crystal structure of *Pnma* structured  $\alpha$ -LiFePO<sub>4</sub>. The primary direction of Li<sup>+</sup> diffusion is along *b*-axis through 1D channels in the [0 1 0] direction.

The FeO<sub>6</sub> octahedra are corner-sharing along the *bc* plane, while LiO<sub>6</sub> octahedra are edge-sharing along the *b*-axis. An FeO<sub>6</sub> octahedron shares edges with two LiO<sub>6</sub> octahedra and one PO<sub>4</sub> tetrahedron. PO<sub>4</sub> tetrahedra share edges with one FeO<sub>6</sub> octahedron and two LiO<sub>6</sub> octahedra. The structural arrangement of  $\alpha$ -LiFePO<sub>4</sub> forms 1D tunnels along the *b*-axis ([0 1 0] direction) which is thought to be the primary pathway for Li<sup>+</sup> diffusion. This has been visualised both experimentally and from first principles calculations (Figure 1.6).<sup>20,21</sup> The reversible intercalation of Li<sup>+</sup> in to and out of  $\alpha$ -LiFePO<sub>4</sub> operates through the Fe<sup>2+</sup>/Fe<sup>3+</sup> redox couple, at a potential of 3.45 V versus Li/Li<sup>+</sup> according to:



It has been noted that the voltage observed is higher than that of iron oxides. The increase in the redox potential can be explained by two major influences. Firstly, an inductive effect instigated by electronically withdrawing PO<sub>4</sub><sup>3-</sup>, dampening the covalency of the Fe-O

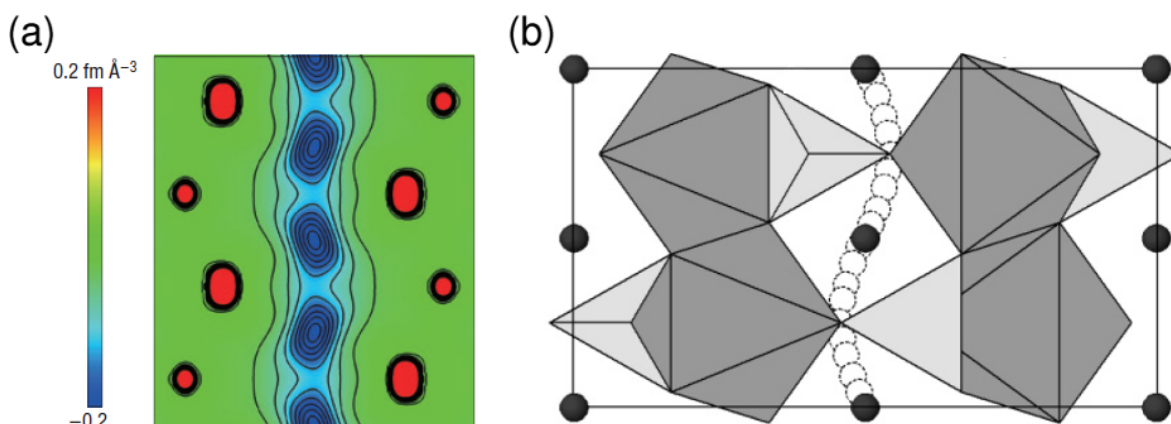


**Figure 1.6:** Lithium diffusion pathway in  $\alpha$ -LiFePO<sub>4</sub> calculated by (a) neutron powder diffraction minimum entropy method (MEM) showing the nuclear distribution of Li (blue). Adapted with permission from Reference 20. Copyright (2008) Science. (b) First principles calculations showing one dimensional diffusion along the  $b$ -axis ([010] direction). Adapted with permission, from Reference 21. Copyright (2005) American Chemical Society.

bonds. This causes oxygen to form stronger bonds with P and reduces the energy required for reduction to occur at the Fe site.<sup>19</sup> Secondly, the Madelung electric fields at the cation site are stronger in  $\alpha$ -LiFePO<sub>4</sub> than in the oxides. This is due to extensive edge sharing of FeO<sub>6</sub> polyhedra leading to higher cation-cation Coulomb repulsions. This effect has been shown to increase the  $V_{OC}$  in  $\alpha$ -LiFePO<sub>4</sub>, relative to iron phosphates with less or no edge sharing.<sup>22</sup> The trade-off with this increased voltage is that PO<sub>4</sub><sup>3-</sup> limits the electronic conductivity of  $\alpha$ -LiFePO<sub>4</sub>. For this reason  $\alpha$ -LiFePO<sub>4</sub> is usually coated with carbon to increase the electronic conductivity.<sup>23</sup>

The actual mechanism for lithium diffusion through  $\alpha$ -LiFePO<sub>4</sub> is still not fully understood. One of the prevailing theories is the core-shell model. The rate determining step for diffusion in the core-shell model is hypothesised to be the reduction in size of the FePO<sub>4</sub>/LiFePO<sub>4</sub> interface during Li<sup>+</sup> insertion.<sup>24</sup> As lithium is reinserted into the structure, the surface area of the FePO<sub>4</sub> decreases, lowering the amount of lithium that can pass through the interface. This means that the current cannot be sustained and leads to a lower reversible capacity at higher current densities. Due to this fact, it was proposed that more lithium could be reversibly extracted and reinserted into materials with smaller particle sizes, such as nanoparticles.<sup>25</sup> This effect has been observed experimentally, where nanoparticles of

$\alpha$ -LiFePO<sub>4</sub> of decreasing size show better rate capability.<sup>26</sup> Therefore tailoring a synthetic route to access nanostructured  $\alpha$ -LiFePO<sub>4</sub> is vital to improving electrochemical performance. Another model for diffusion is the domino-cascade model. The domino-cascade model contradicts the core-shell model in that the nucleation for one phase happens within the other, and that this delithiation is fast.<sup>27</sup> This creates multiple sites of lithium diffusion, rather than the shrinking core of the core-shell model.

As diffusion of Li<sup>+</sup> through  $\alpha$ -LiFePO<sub>4</sub> is a rapid 1D process along the *b* axis by which the Li<sup>+</sup> hops from one interstitial site to the next, structural defects could dramatically decrease the performance of these materials.<sup>20,28</sup> There have also been studies to show that lattice contraction upon delithiation leading to a volumetric change of 7%.<sup>29</sup> The shrinkage of diffusion paths could lead to impeded lithium ion reinsertion, as the ions effectively have smaller tunnels to pass through after leaving and/or travelling through the  $\alpha$ -LiFePO<sub>4</sub>. Other studies have suggested these changes are still small enough to avoid major degradation of the charge capacity and also compensate for volume changes experienced by carbon anodes.<sup>30–32</sup> Structural changes in LiFePO<sub>4</sub> have shown to be overcome by doping small amounts of other metal ions such as Mn, Co and Zn.<sup>33–35</sup> The addition of different ions can bring more stability to the structure, allowing it to experience less volumetric loss during electrochemical cycling. Furthermore, fast cycling of  $\alpha$ -LiFePO<sub>4</sub> has been shown to reduce the structural changes by capturing metastable phases upon delithiation and leading to an increased lifetime.<sup>36</sup> Limitations on Li<sup>+</sup> diffusion can be evaluated by looking at the activation energy ( $E_a$ ) of Li<sup>+</sup> diffusion and diffusion coefficient ( $D_{Li}$ ).

### 1.1.3 Enhancing capacity in Li-ion insertion electrodes

Although  $\alpha$ -LiFePO<sub>4</sub> shows outstanding electrochemical properties, its modest theoretical capacity is its main limitation. Equation 1.5 can be used to calculate theoretical capacity ( $Q$ , mAh g<sup>-1</sup>) of an electrode, where *n* is the number of moles of electrons involved in the charge/discharge, *F* is the Faraday constant and *M* is the molecular mass of the electrode material. *Q* can be increased by either decreasing *M*, or increasing *n*. One tactic to decrease *M* is to employ a lighter redox metal such as Ti, V, Cr or Mn which would increase the theoretical capacity. However, the best possible result that could be achieved by this method

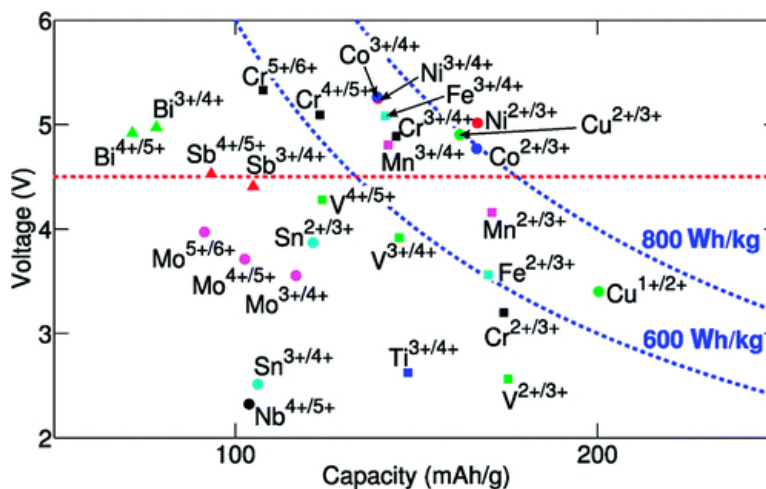


**Figure 1.7:** Capacity and voltage from *ab initio* calculations for olivine phosphates containing various metals, in various oxidation states. The dashed red line represents the safe voltage limit imposed by current organic electrolytes. Reprinted with permission from Reference 37. Copyright (2011) American Chemical Society.

would be replacing Fe with Ti. This would only provide a 5 % reduction in mass of the electrode (based on a theoretical  $\text{LiTiPO}_4$ ) and a similar increase in the capacity. Another tactic is to employ lighter anions (such as  $\text{O}^{2-}$ ), however as discussed previously this may dramatically affect the stability and decrease  $\mu_{\text{C}}$  of the cathode below the electrolyte HOMO. One further option is to use material containing a redox metal which has multiple oxidation states, whose  $\mu_{\text{C}}$  lie within the  $E_{\text{g}}$  range of the electrolyte. Figure 1.7 shows values of voltage and capacity derived from *ab initio* calculations of olivine phosphates containing various metals.

It can be seen that employing a metal that can only undergo one oxidation state change is a prominent limitation in capacity, such as Co or Fe. By choosing a material with multiple oxidation state changes, the amount of  $\text{Li}^+$  intercalated,  $n$ , can be increased per formula unit. This in turn increases  $Q$ , and is commonly referred to as multiple electron transfer (MET) Metals capable of undergoing MET include Cr, Mo, and W (not shown in Figure 1.7). Each has been investigated with varying electrochemical properties.

$$Q = \frac{nF}{3.6 \times M} \quad (1.5)$$

$\text{WO}_3$  has been investigated as a  $\text{Li}^+$  intercalation cathode and is able to harbor 1.2  $\text{Li}^+$

per formula unit.<sup>38</sup> However, due to the high atomic mass of W, this limits the capacity to just 150 mAh g<sup>-1</sup>. Molybdates have been studied with stoichiometries ranging between MoO<sub>2</sub> and MoO<sub>3</sub>.<sup>39</sup> It was found that Mo<sub>17</sub>O<sub>47</sub> possesses the best electrochemical performance, intercalating up to 1.2 Li<sup>+</sup> per formula unit.

Chromium oxides Cr<sub>2</sub>O<sub>3</sub>, CrO<sub>2</sub>, Cr<sub>5</sub>O<sub>12</sub>, Cr<sub>2</sub>O<sub>5</sub>, Cr<sub>6</sub>O<sub>15</sub> and Cr<sub>3</sub>O<sub>8</sub> have also been investigated as potential cathode materials.<sup>40</sup> Studies have shown that as the average oxidation state in the cathodes increases from Cr<sub>2</sub>O<sub>3</sub> (3+) to Cr<sub>3</sub>O<sub>8</sub> (5<sup>1</sup>/<sub>3</sub>+) a consistent increase in capacity is also observed. This is due to reduction being possible in the higher oxidation state Cr, leading to intercalation of larger amounts of Li<sup>+</sup>. Furthermore, amorphous Cr<sub>3</sub>O<sub>8</sub> has shown full reversible reduction of the Cr<sup>6+</sup> down to Cr<sup>3+</sup>, allowing the intercalation of over 6 Li<sup>+</sup> per formula unit (2 Li<sup>+</sup> per Cr).<sup>41</sup> However, concern over the toxicity of Cr<sup>6+</sup> has severely hampered interest in these materials. Furthermore, the red dashed line in Figure 1.7 indicates the voltage considered safe for conventional electrolytes, which Cr<sup>5+/6+</sup> and Cr<sup>4+/5+</sup> exceed.

MET capable cathodes present themselves as an interesting opportunity to enhance the capacity of Li<sup>+</sup> insertion cathodes, but there is still scope to explore other metals that exhibit this behaviour with better electrochemical performance which do not exceed safe voltage limits.

#### 1.1.4 Multiple electron transfer in vanadium oxides

Vanadium oxides offer a unique opportunity to incorporate a redox active metal into an Li<sup>+</sup> insertion cathode and access oxidation states of V<sup>5+</sup> to V<sup>3+</sup>, all within the E<sub>g</sub> window of common organic electrolytes. Referring to Figure 1.7, V is presented as a "Goldilocks" transition metal, with all oxidation states below the safe limit, whilst retaining a reasonably high voltage and low mass. The structural flexibility of vanadates allows for a great number of materials, theoretically capable of intercalating more than 1 Li<sup>+</sup> per V.<sup>42</sup> In order of O:V ratio, these include V<sub>6</sub>O<sub>13</sub>, V<sub>4</sub>O<sub>9</sub>, V<sub>7</sub>O<sub>16</sub>, V<sub>3</sub>O<sub>7</sub>, V<sub>12</sub>O<sub>29</sub>, V<sub>9</sub>O<sub>22</sub> and V<sub>2</sub>O<sub>5</sub>. However, there are only limited reports on a select few of these materials. This is mainly caused by the oxidation state chemistry being so flexible that vanadates are often obtained with impurity phases, and require precise tailoring of the reaction conditions. This is a major challenge

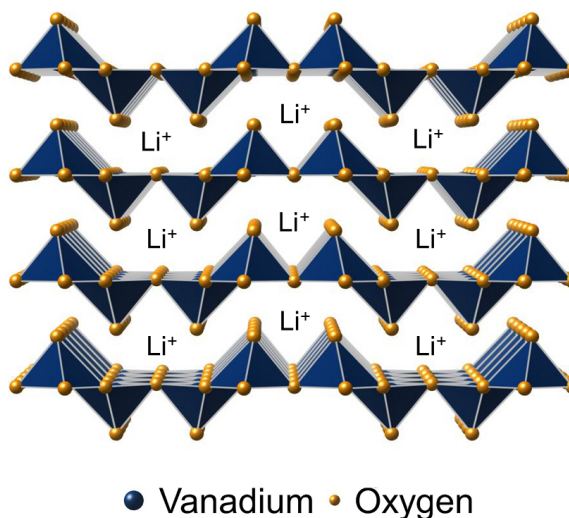


**Figure 1.8:** Structure of  $V_2O_5$  showing the intercalation of  $Li^+$  between the layers of  $VO_5$  square-based pyramids ( $V^{5+}$ ).

with vanadates and still requires more investigation.

$V_2O_5$  has been the most widely investigated to date due to its outstanding theoretical capacity of  $589 \text{ mAh g}^{-1}$  upon insertion of 4  $Li^+$ , upon full reduction from  $V^{5+}$  to  $V^{3+}$ .  $V_2O_5$  is also very easy to obtain, as it can be prepared in an ambient atmosphere due to all the vanadium atoms being in the highest possible oxidation state,  $V^{5+}$ . Figure 1.8 shows the layered structure of  $V_2O_5$ , which accommodates  $Li^+$  between the layers.

However, studies have shown that this theoretical capacity is unobtainable, as insertion of 4  $Li^+$  leads to irreversible capacity loss due to major structural changes and is only capable of reversibly intercalating 2  $Li^+$  per formula unit (one  $Li^+$  per V).<sup>43</sup> Even though  $V_2O_5$  is limited to the insertion of 2  $Li^+$ , it still exhibits a reversible and stable capacity of  $240 \text{ mAh g}^{-1}$ , and still attractive for Li-ion cathode applications. However, other studies have shown sluggish  $Li^+$  diffusion kinetics and significant structural changes discourage the development of  $V_2O_5$  as a insertion cathode material.<sup>44,45</sup>

$V_6O_{13}$  has also been investigated as a potential intercalation cathode with a theoretical capacity of  $417 \text{ mAh g}^{-1}$ , corresponding to the intercalation of 8  $Li^+$  atoms per formula unit. This occurs due to the presence of 4  $V^{4+}$  and 2  $V^{5+}$  per formula unit. Experimentally,  $V_6O_{13}$  shows a theoretical capacity of  $200 \text{ mAh g}^{-1}$ , at a rate of  $100 \text{ mA g}^{-1}$ .<sup>46</sup> This capacity corresponds to the reversible intercalation of 3.8  $Li^+$  (0.63  $Li^+$  per V). This lower capacity

has been explained by the voltage window over which the measurements were conducted (3.2 V to 2.0 V) not being large enough to capitalise on the full reduction down to  $V^{3+}$ . Further studies have shown that increasing this window down to 1 V is detrimental to the operation of the electrode, and the reversible intercalation quickly fades from the theoretical 8  $\text{Li}^+$  per formula unit to just 1  $\text{Li}^+$  per formula unit over 100 cycles.<sup>47</sup>

Lastly,  $V_3O_7$  has been investigated as an MET insertion cathode, possessing 2  $V^{5+}$  and 1  $V^{4+}$  and a theoretical capacity of  $506 \text{ mAh g}^{-1}$ . Experimental investigations of  $V_3O_7$  have found an initial capacity of  $200 \text{ mAh g}^{-1}$ , corresponding to the insertion of 2  $\text{Li}^+$  per formula unit ( $\frac{2}{3} \text{ Li}^+$  per V).<sup>48</sup> However, this capacity quickly fades to around  $150 \text{ mAh g}^{-1}$  after 10 cycles (3.5 V and 1.5 V), due to irreversible structural changes upon  $\text{Li}^+$  intercalation.

To summarise, although MET capable vanadates may be used to access high capacities theoretically, more work is required to obtain higher experimental capacities. This could be achieved by either (a) stabilising the initial capacities of existing compounds or (b) developing new synthetic routes to single phase, alternative vanadate materials.

## 1.2 Lithium intercalation and diffusion in insertion electrodes

Although voltage and capacity are important attributes of intercalation electrodes, ultimately the electrochemical behaviour in these materials is governed by one factor,  $\text{Li}^+$  mobility. If  $\text{Li}^+$  are unable to move there will be no electrochemical activity, or if the kinetics of the  $\text{Li}^+$  movement are slow, faster charge and discharge rates will suffer increasing capacity losses. Therefore it is of the utmost importance that  $\text{Li}^+$  diffusion mechanics in intercalation materials are understood, although this can be a challenging endeavour. Firstly, the mechanics of  $\text{Li}^+$  mobility are discussed, and can be separated into two processes, intercalation and diffusion.

### 1.2.1 Mechanism of lithium intercalation in insertion electrodes

$\text{Li}^+$  intercalation occurs when a  $\text{Li}^+$  ion enters into an interstitial site in an electrode at the Fermi energy level of the host material, determined by the valence band. This behaviour is mediated by a change in the oxidation state of a transition metal, to balance the overall charge upon insertion of a positive  $\text{Li}^+$  ion (e.g.  $M^{3+}$  to  $M^{2+}$ ). During electrochemical cycling, intercalation materials can accommodate increasing amounts of lithium in two ways, (a) by

forming a solid-solution and (b) by forming two discrete phases. In the solid-solution regime the electrode is dominated by Nernst-like behaviour, where insertion  $\text{Li}^+$  occurs primarily due to a concentration difference. This behaviour can be summarised by the Nernst equation:

$$E_{\text{we}} = E^{\circ} + \frac{RT}{nF} \ln \frac{a_{\text{Ox}}}{a_{\text{Red}}} \quad (1.6)$$

where  $E_{\text{we}}$  is the working electrode potential,  $E^{\circ}$  is the reduction potential of the working electrode,  $R$  is the gas constant,  $T$  is the temperature in K,  $n$  is the number of moles of electrons involved in the redox process,  $F$  is the Faraday constant, and  $a_{\text{Ox}}$  and  $a_{\text{Red}}$  are the chemical activities of the oxidised electrode species and reduced electrode species respectively. As the concentration of reduced species in the cathode increases,  $E_{\text{we}}$  becomes logarithmically smaller. As  $\text{Li}^+$  ions are initially inserted, the intercalation electrode forms a solid solution and a single lithiated phase. For a simple metal oxide this could be written as:



At a given point the material may reach a critical concentration where a solid-solution cannot be maintained, leading to the evolution of two distinct lithium rich, and lithium deficient phases, a two-phase system:



where  $y'$  is the maximum amount of  $\text{Li}^+$  accommodated into the lithium deficient solid solution, and  $y''$  is the minimum amount of  $\text{Li}^+$  required for the lithium rich solid solution to form. At this point, structural factors inhibit the concentration dominated intercalation. The difference between  $y'$  and  $y''$  is known as the miscibility gap, which is the concentration range over which a solid-solution cannot be sustained. As increasing amounts of  $\text{Li}^+$  are inserted into the two-phase system, the relative concentration of  $\text{Li}_{y''}\text{MO}$  also increases. This continues until the two-phase system is saturated with  $\text{Li}^+$ , and all  $\text{Li}_{y'}\text{MO}$  has been converted to  $\text{Li}_{y''}\text{MO}$ . From this point, a new solid-solution is formed:



This solid-solution continues until the material is saturated and no more reduction can occur in the transition metal. During electrochemical delithiation this entire process is reversed, and leads to the typical plateaued hysteresis profile observed in electrochemical cycling (Figure 1.9).

The solid-solution regions lie at the beginning and end of the profiles where rapid change in the voltage occurs over small changes in  $[\text{Li}^+]$ , and the two-phase reaction occurs over the plateau region. These observations occur in intercalation materials that undergo a single oxidation state change. In materials that undergo multiple oxidation state changes upon  $\text{Li}^+$  insertion there is a plateau region for each redox reaction, separated by solid-solution region.

### **1.2.2 Mechanism of lithium diffusion in insertion electrodes**

Solid state diffusion can occur by two routes, interstitial or substitutional diffusion. For an ion to diffuse it must possess enough energy to cross the diffusion barrier. The quantity of energy required is known as the activation energy ( $E_a$ ) of diffusion. If an ion does possess energy greater than the  $E_a$  of diffusion, it may be displaced from its original position to a neighbouring position. In intercalation electrodes, interstitial diffusion is the primary diffusion mechanism as most  $\text{Li}^+$  occupy interstitial sites. Interstitial diffusion is also less energetically costly, as no ionic bonds between the  $\text{Li}^+$  and neighbouring atoms are required to be broken for the  $\text{Li}^+$  to diffuse.

$\text{Li}^+$  can occur at and even below room temperature. The process of  $\text{Li}^+$  diffusion is also thermally activated, meaning that as temperature increases, the diffusion becomes faster. This is due to more thermal energy being supplied to the  $\text{Li}^+$ , increasing the probability that the  $\text{Li}^+$  will have enough energy to jump from one site to the next. This behaviour has been investigated by many methods, but the accuracy of these measurements remains a key concern.

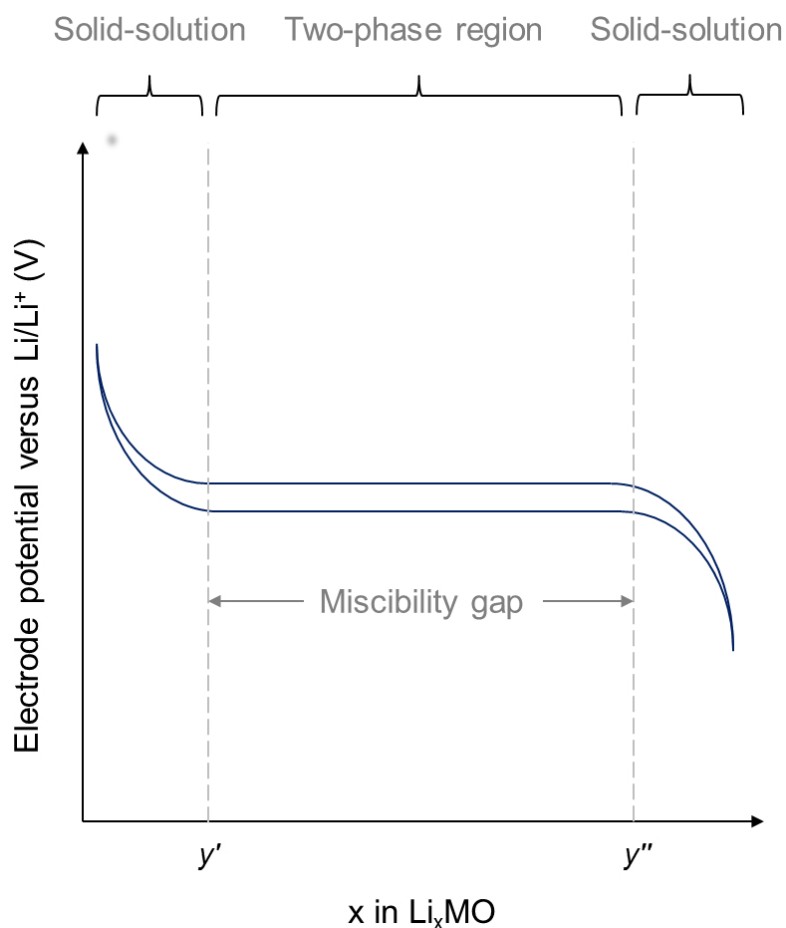


**Figure 1.9:** Galvanostatic cycling profile of an intercalation electrode that undergoes one redox reaction. A solid-solution region is observed at the start and the end of the two-phase redox plateau. The maximum possible  $\text{Li}^+$  concentration to form lithium deficient material is denoted as  $y'$  and the minimum required concentration to form a  $\text{Li}^+$  rich solid-solution is denoted as  $y''$ .

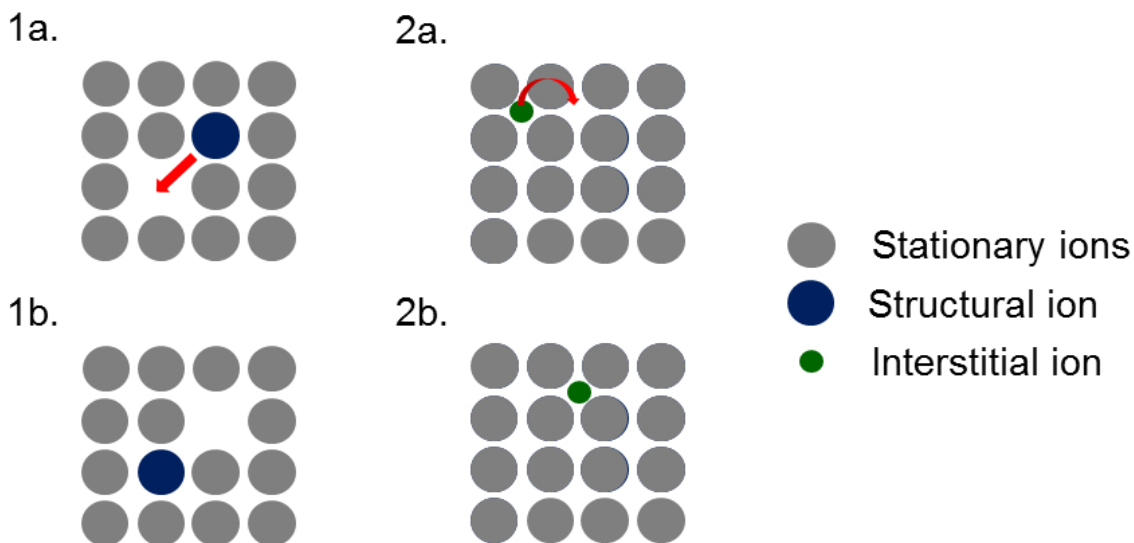


**Figure 1.10:** Two types of diffusion can occur in solid-state materials, vacancy and interstitial diffusion. Vacancy diffusion (1.a) shows the movement of a structural ion such as  $O^{2-}$  from one lattice site to a neighbouring vacancy (1.b). Figure 2.a shows interstitial diffusion of an ion in a lattice from an interstitial site to a neighbouring interstitial site (2.b).

### 1.3 Methods for analysing $Li^+$ diffusion mechanics

#### 1.3.1 Traditional methods for analysing $Li^+$ diffusion mechanics

Examples of the varied structural architectures can be seen in Figure 1.11, showing (a) the layered oxide cathode  $LiCoO_2$ , (b) a  $Li_3N$  nitride anode and (c) a garnet structured solid-state electrolyte  $Li_6MLa_2Nb_2O_{12}$ . It is apparent that hindering the transit of  $Li^+$  through these materials will have adverse affects on the electrochemical performance, since rechargeable materials rely on the free movement of these ions between the electrodes.

$Li^+$  diffusion characteristics, such as the diffusion coefficient ( $D_{Li}$ ) and activation energy ( $E_a$ ) are important considerations for optimised electrochemical performance in Li-ion batteries. However, the values obtained for these parameters can vary dramatically depending on the experimental technique employed. For example,  $Li^+$  ion diffusion in  $\alpha$ - $LiFePO_4$  has been studied using a range of methods including theoretical calculations, AC and DC impedance analysis, galvanostatic intermittent titration techniques (GITT), Mössbauer spectroscopy and  $Li^+$  nuclear magnetic resonance (NMR). A summary of values obtained from these methods

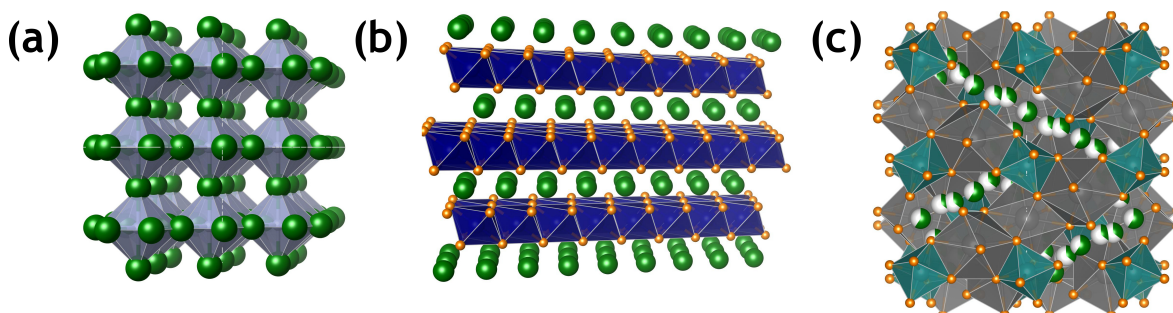


**Figure 1.11:** Structures of (a) the lithium nitride anode material  $\text{Li}_3\text{N}$ , (b) the layered oxide cathode material  $\text{LiCoO}_2$  and (c) the garnet structured solid-state electrolyte  $\text{Li}_6\text{MLa}_2\text{Nb}_2\text{O}_{12}$ . It can be seen that these materials can accommodate the intercalation of  $\text{Li}^+$  into their open structures.

for the cathode material  $\alpha\text{-LiFePO}_4$  can be seen in Figure 1.12 and the broad distribution of values obtained for  $D_{\text{Li}}$  and  $E_a$  are apparent, between and even within techniques.

There may be a number of reasons for such large differences between measurement techniques. For example, AC and DC impedance are subject to interference from grain boundaries, and if the measurements are taken using a complete cell rather than just the single component the accuracy of the results will vary depending on the experimental set-up.<sup>49–51,55</sup> Regarding  $\text{Li}^+$  NMR, the timescale on which measurements take place are not fast enough to measure the some rates at which  $\text{Li}^+$  diffusion occurs, and the associated interactions may also be masked by magnetic ions in the lattice.<sup>59</sup>

Since many of these techniques look at bulk influences, any difference in crystalline domain size will change the observed  $\text{Li}^+$  diffusion mechanics since it takes into account the intragrain diffusion. Additionally electrochemical methods are highly dependent on the physical analysis set-up, where changes in the resistance of the equipment can vastly alter the observed values for  $\text{Li}^+$  diffusion. For this reason, the use of a local technique that is free from these influences would be an ideal tool for examining diffusion kinetics.

### 1.3.2 Muon spin relaxation as a $\text{Li}^+$ diffusion probe

Muon spin relaxation ( $\mu\text{SR}$ ) provides an opportunity as a local probe technique for characterising diffusive properties of ionic species in Li-ion battery constituents, and has been successfully employed in a number of materials.<sup>60–74</sup>  $\mu\text{SR}$  provides a non-destructive intim-

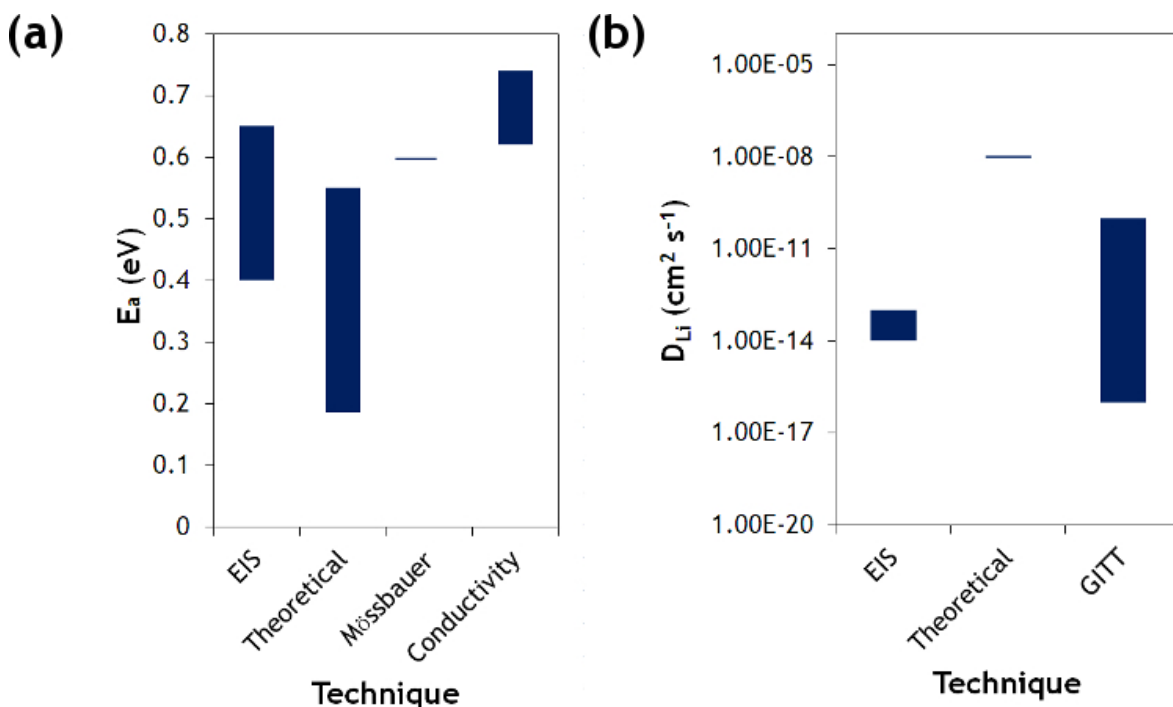


**Figure 1.12:** Distribution of (a) the lithium diffusion coefficient ( $D_{Li}$ ) and (b) the activation energy ( $E_a$ ) of this process for  $\alpha$ -LiFePO<sub>4</sub>. It can be seen that there is large difference in reported values between the techniques.<sup>21,28,49–58</sup>

ate probe for Li<sup>+</sup> diffusion that does not consider any influences from bulk effects allowing calculation of  $D_{Li}$  and  $E_a$  of Li<sup>+</sup> diffusion on a local scale. To date, cathode materials have been the most widely studied battery component to date using  $\mu$ SR.

Muon spin relaxation is a local-probe technique not unlike Li<sup>+</sup> NMR. However, it works on a faster timescale, so the characterisation of dynamic diffusion processes of positive ionic species, such as Li<sup>+</sup>, is possible. It was first realised by Kaiser *et al.* [ 75] that ionic species diffusing through materials could perturb the muon decay and thus, the rate at which this process occurred could be quantified, with Li<sub>x</sub>(Mn<sub>1.96</sub>Li<sub>0.04</sub>)O<sub>4</sub> seeing the onset of Li<sup>+</sup> mobility at 230 K and 300 K for  $x = 1$  and 0.2 respectively.<sup>75</sup> There are several factors to consider prior to  $\mu$ SR experiments. Firstly, Li<sup>+</sup> diffusion is a thermally activated process and the rate at which lithium diffuses increases with increasing temperature. Therefore, the measurement temperature range should be carefully selected with any possible phase transitions or decomposition temperatures taken into account.<sup>49</sup> Furthermore, where the muon implants into a given sample is crucial. The number of muon sites and the location of

these sites can alter the results observed. Predictions of these sites can be calculated by electrostatic potential calculations and usually reside in electron clouds of negative elements such as  $O^{2-}$  forming a stable  $O^{2-}-\mu^+$  bond.<sup>64,65,68</sup>

### 1.3.3 Muon spin relaxation of Li-ion intercalation electrodes

Layered transition metal oxides have been of interest for battery materials since they are simple structures which generally adopt a layered arrangement (Figure 1.11 b) and have shown to reversibly intercalate  $Li^+$ .  $\mu$ SR studies of  $Li_{0.6}TiO_2$  have shown that the timescale on which  $Li^+$  diffuses is less than a microsecond.<sup>62</sup> Similar studies on  $LiCoO_2$  reinforce the theory that  $Li^+$  diffusion is a rapid process.<sup>67</sup> Metal doping of  $LiCoO_2$  to  $Li_xCo_{1/3}Ni_{1/3}Mn_{1/3}O_2$  can cause a reduction of the  $D_{Li}$  by an order of magnitude.<sup>65,76</sup>  $\mu$ SR of the related compound  $LiNiO_2$  exhibited a  $D_{Li}$  of  $10^{-11} \text{ cm}^2 \text{ s}^{-1}$ , while  $LiCrO_2$  showed no  $Li^+$  diffusion at all which explains its electrochemical inactivity.<sup>63</sup>

Layered  $Li_2MnO_3$  has shown that  $Li^+$  diffuses mainly along the  $c$ -axis with a  $D_{Li}$  and  $E_a$  of  $10^{-11} \text{ cm}^2 \text{ s}^{-1}$  and 0.156 eV respectively at 300 K.<sup>64</sup> The spinel structured oxides  $LiMn_2O_4$  and  $Li_{1.33}Mn_{1.67}O_4$  have also been successfully studied by  $\mu$ SR, showing a decrease in the activation temperature of  $Li^+$  diffusion with increasing lithiation.<sup>66,69</sup> Furthermore, these studies have suggested that the temperature dependence of  $Li^+$  diffusion is highly linked to the dimensionality of diffusion pathways, when compared to layered structures. While the aforementioned oxides have been used as cathode materials,  $Li^+$  mobility was also observed by  $\mu$ SR in  $Li_2O$ , a candidate as a solid-state electrolyte.<sup>72</sup> It was found that doping  $Li_2O$  with hydroxide and fluoride groups did not affect the diffusion rate of the  $Li^+$ .<sup>73</sup>

Doped lithium nitride materials,  $Li_{3-x}M_xN$ , have recently been reported as candidates as possible anode materials due to  $Li_3N$  (Figure 1.11 a) exhibiting the highest  $Li^+$  conductivity for a crystalline material.<sup>77</sup> Attempts to study the  $Li^+$  diffusion mechanics of these materials using  $Li^+$  NMR proved unsuccessful due to interference from metal paramagnetic moments, but these have been made possible using  $\mu$ SR. Studies have successfully found that at increased temperatures there is intralayer diffusion in  $Li_3N$ , and doping  $Li_3N$  with Ni has shown to lower the temperature at which this is observed.<sup>60</sup> Furthermore,  $\mu$ SR has also shown doping  $Li_2N$  with Co also lowers the  $E_a$  of intralayer  $Li^+$  diffusion.<sup>61</sup>

Studies on  $\alpha$ -LiFePO<sub>4</sub> have found that, regardless of the dynamic function chosen, the resulting  $D_{\text{Li}}$  and  $E_a$  are reproducible. Sugiyama *et al* employed the Keren function and observed  $D_{\text{Li}}$  in the order of  $10^{-9}$  to  $10^{-10}$  cm<sup>2</sup>s<sup>-1</sup> whereas Baker *et al* employed the Kubo-Toyabe function and also calculated  $D_{\text{Li}}$  in the order of  $10^{-10}$  cm<sup>2</sup>s<sup>-1</sup> to  $10^{-9}$  cm<sup>2</sup> s<sup>-1</sup>.<sup>68,71</sup> Both studies calculated values of  $E_a$  in the order of 100 meV, which is in good agreement with first principle calculations and highlights the robustness of the technique.<sup>28</sup> Furthermore, these studies prepared  $\alpha$ -LiFePO<sub>4</sub> by separate synthetic routes and observed similar diffusion mechanics. However, neither paper investigated nanostructured particles, which may enhance the diffusion mechanics for several reasons, and have yet to be studied with  $\mu$ SR.

## 1.4 Nanostructured insertion electrodes

Nanomaterials have become attractive materials for Li-ion electrode applications with many review articles published, highlighting their electrochemical benefits.<sup>1,78–82</sup> The appeals of nanomaterials can be divided into five main categories: (a) improved accommodation of strain, (b) new reactions that are not possible in bulk materials, (c) greater electrode-electrolyte contact, (d) shorter electronic transport pathlengths, (e) shorter Li<sup>+</sup> diffusion pathlengths.

Increased accommodation of strain in nanomaterials (a) has led to increased cyclability in insertion electrodes.<sup>83</sup> This effect has also shown that the nanostructures exhibit a larger solid-solution range, enabling a material to intercalate more Li<sup>+</sup> before undergoing a structural, or phase change. An increase in the solid-solution range is usually manifested in electrochemical cycling as a diminishing miscibility gap. It has also been proposed that there is a critical particle size where a solid-solution is achievable at all lithium concentrations.

New reactions in nanoparticles (b) have also been observed, that cannot be sustained in bulk materials, such as the conversion of cubic Li<sub>x>1</sub>Mn<sub>2</sub>O<sub>4</sub> to tetragonal Li<sub>x<1</sub>Mn<sub>2</sub>O<sub>4</sub>.<sup>84</sup> In the bulk, this reaction leads to poor reversible intercalation of Li<sup>+</sup> due to fracturing of the material from Jahn-Teller induced strain, causing the evolution of inactive and electronically isolated nanodomains of tetragonal Li<sub>x<1</sub>Mn<sub>2</sub>O<sub>4</sub> in the Li<sub>x>1</sub>Mn<sub>2</sub>O<sub>4</sub> host. However, when nanoparticles of Li<sub>x>1</sub>Mn<sub>2</sub>O<sub>4</sub> were prepared, no electronic isolation or fracturing was ob-

served due to the accommodation of strain, and a 13 % increase in particle volume upon lithiation.<sup>85,86</sup> These effects led to an improved electrochemical performance in the nanoparticles versus the bulk material.<sup>87</sup> Mesoporous  $\text{LiMn}_2\text{O}_4$  has also shown a similar improvement in performance.<sup>88</sup> Electronic isolation has also been observed in bulk  $\alpha\text{-LiFePO}_4$ , showing that the theoretical capacity cannot be achieved.<sup>89</sup> Nanoparticles of  $\alpha\text{-LiFePO}_4$  have been shown to limit this effect, coupled with carbon coating or doping with a conductive metal to improve both the  $\text{Li}^+$  diffusion and the electronic conductivity, respectively.<sup>90,91</sup> Nanosizing has been shown to enhance the reversibility in conversion anodes as well, such as  $\text{SnO}_2$ , where particles below a critical size of 3 nm avoid detrimental effects from particle expansion upon lithiation.<sup>92</sup>

Although no specific research has been undertaken for increased electrolyte-electrode contact with decreasing particle size ( $c$ ), classical mathematics dictates that as the scale of a 3D object decreases, there is an exponential increase in the surface area to volume ratio. This property allows nanoparticles to possess more surface area available for interaction with electrolyte than bulk materials, aiding the movement of lithium from the particles to the electrolyte. Additionally, studies of  $\text{V}_2\text{O}_5$  nanoparticles have shown that tuning the morphology, surface texture or mesoporosity to enhance the surface area of the particles leads to an increase in capacity.<sup>93,94</sup> However, increased surface area in nanoparticles has also been linked to detrimental effects, such as increased formation of a solid electrolyte interphase (SEI) that can hinder  $\text{Li}^+$  deinsertion. This has been observed in  $\text{LiCoO}_2$  where 100 nm nanoparticles showed a SEI layer of 30 nm to 40 nm compared to 300 nm particles that exhibited a SEI layer < 10 nm.<sup>95</sup> The increase in SEI thickness is also accompanied by a decrease in the rate capability from  $90 \text{ mAh g}^{-1}$  in the 300 nm particles to  $30 \text{ mAh g}^{-1}$  in the 100 nm particles, at 7C.

Finally, both the electronic conduction pathlengths ( $d$ ) and the  $\text{Li}^+$  diffusion pathlengths ( $e$ ) have been investigated in nanomaterials, and are dependent on each other. Intercalation processes modeled by computational methods have found that if defects are present in the material, the amount of  $\text{Li}^+$  able to deintercalate decreases with increasing diffusion pathlength.<sup>96</sup> This effect will lower the overall capacity observed in larger particles. Further computational studies have suggested ionic and electronic conductivity are responsible for

higher capacities at higher rates, with decreasing particle radius.<sup>97</sup>

## 1.5 Synthetic routes to nanostructured insertion electrodes

### 1.5.1 Solid state synthesis

Although nanomaterials have proven to be highly attractive for Li-ion electrode applications, synthetic routes must first be discovered to obtain them. In solid-state synthesis simple reactants containing the constituent elements are placed into a heat-resistant crucible and heated for ca. 12 hours at high temperatures (300 °C to 700 °C).<sup>98</sup> This method relies on the diffusion of solid starting materials, hence the high temperatures and long times employed. Also, solid state syntheses are unable to produce nanoparticles of material since there is no dilution of the reactants, typically yielding particles many tens to hundreds of  $\mu\text{m}$  in size. To limit particle size a chemical flowing agent (flux) can be employed, as in molten salt preparations.<sup>99,100</sup> Another option is sol-gel synthesis.

Sol-gel synthesis can be thought of as a hybrid solid state and hydrothermal syntheses. Firstly a sol is created by mixing soluble precursors and a gelling agent (to create a host matrix) into a solvent (typically water) and stirred while heating to create a homogenous distribution of starting materials. The heating continues until all the solvent has been evaporated and an intimate mixture of the starting materials and the matrix is obtained, limiting the amount of diffusion required for the reactants. The mixture is then placed into a furnace or oven and calcined at high temperatures. The host matrix allows the reactants to diffuse and react, but also limits the diffusion in so much that particle growth is limited. Particles of  $\alpha\text{-LiFePO}_4$  obtained by this method exhibit particle sizes between 20 nm and 500 nm.<sup>101,102</sup> However, both the particle size and products formed can be altered by improving the diffusion of reactants further by employing a liquid reaction media and access materials at lower temperatures and shorter times.

### 1.5.2 Hydrothermal and solvothermal synthesis

In hydrothermal synthesis, reactants containing the constituent elements are placed into a closed system reaction vessel along with a given solvent. The reaction vessel is usually a

solid steel construction with a poly(tetrafluoroethylene) (PTFE) lining able to withstand high pressure when heated. The synthesis of  $\alpha$ -LiFePO<sub>4</sub>, for example, is typically carried out for 48 hours at temperatures between 180 °C and 250 °C.<sup>103</sup> Particles obtained from hydrothermal synthesis are typically smaller than solid state synthesis, ranging from tens to hundreds of nm big. Furthermore, several morphologies of  $\alpha$ -LiFePO<sub>4</sub> have been obtained from hydrothermal synthesis including rods, platelets and hollow spheres. These have corresponded to capacities of 168 mAh g<sup>-1</sup> (C/10), 145 mAh g<sup>-1</sup> (C/10) and 160 mAh g<sup>-1</sup> (C/10), with a decrease in dimensionality in the [0 1 0] (*b*-axis) being linked to improved electrochemical performance.<sup>104–106</sup>

Solid-state, hydrothermal and sol-gel reactions rely on conductive heating from an external heat source, meaning a large heat gradient can be present within the sample. Not only is this an energy inefficient way of heating, since much energy is lost to the surrounding environment, but can also lead to unwanted side reactions and a lack of uniformity of the resulting particles. For example, impurity phases of FeP and Fe<sub>2</sub>P can arise in high temperature solid-state synthesis of  $\alpha$ -LiFePO<sub>4</sub> due to Li<sup>+</sup> evaporation.<sup>107</sup> Thus, continued efforts have been focused on finding an energy efficient, rapid heating process that minimises the energy gradient. Microwave-assisted solvothermal synthesis is an emerging synthetic route that allows rapid heating of reactants in a solvent, at significantly lower temperatures than solid-state routes.

### 1.5.3 Microwave synthesis

Microwaves are a form of electromagnetic radiation between 0.3 GHz and 300 GHz in wavelength, and can be used to heat materials by two main mechanisms: dipole polarisation and ionic conduction, depending on the material irradiated. Microwave heating has been used to drive chemical reactions in both the solid state and solvent based applications and been employed to synthesise many inorganic materials including oxides, carbides, nitrides, silicates, zeolites and apatite.<sup>108</sup> This list is not exhaustive, and microwave-assisted heating initially accrued interest for organic reactions.<sup>109–111</sup> Effective microwave-assisted heating requires a medium or reagents that can heavily absorb the irradiation. In solid-state methods, a susceptor can be mixed with the reagents, such as a metal, silicon carbide, or

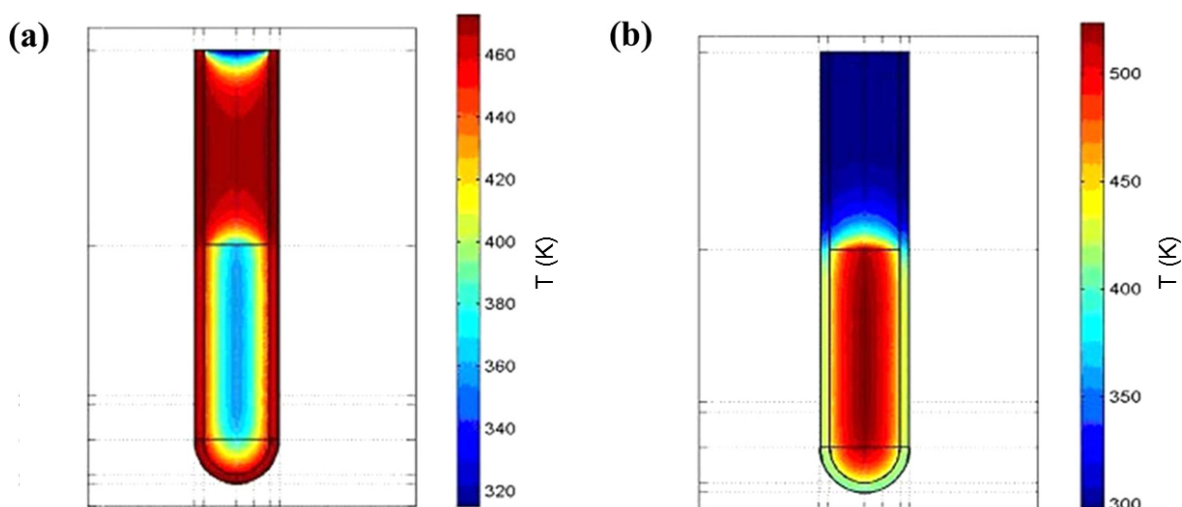


**Figure 1.13:** Conventional heating in an oil-bath (a) versus microwave-assisted heating (b) shows rapid heating, unhindered by the vessel walls after just 60 s of irradiation. Reproduced from Reference 113 with permission from Elsevier publishing.

graphite to absorb irradiation in place of the reagents and heat the reaction.<sup>112</sup> However, this may instigate a heating gradient across the sample. In solution based microwave-assisted synthesis it is commonly the solvent that absorbs the irradiation to heat and drive the reaction. Thermal imaging has shown that solution based microwave-heating in a Discover SP microwave synthesiser (Figure 1.13 b) can avoid heating gradients caused by conventional conduction heating in a water bath (Figure 1.13 a) and rapidly heat the system.<sup>113</sup> The zone containing the reactants (lower tube) show a large difference in temperature after just 60 s of heating, where microwave heating heats the whole reaction simultaneously. Furthermore, as microwaves can pass in to and/or through a solution, energy can be transferred to many local sites simultaneously. This will mean that, compared to conventional hydro-thermal methods, the uniformity of the heat distribution within the sample will be greater in microwave methods. Rapid access to uniform heat distribution means that impurities formed at lower temperatures and longer times can be reduced or avoided.

Mainly, two types of solvents have been employed in solution based synthesis: polar solvents and ionic liquids. Both of these media undergo different heating mechanisms, affecting their efficiency at heating reactions.<sup>114</sup> Polar substances undergo dipolar polarisation which occurs due to coupling of the dipole moment of a molecule to the electric component

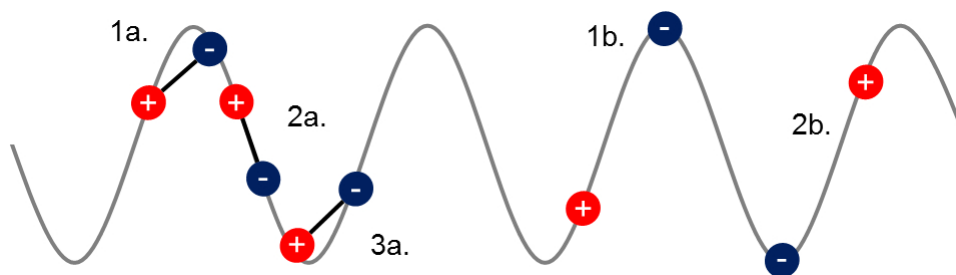


**Figure 1.14:** Schematic showing the difference behaviour of ionic and polar substances irradiated with microwaves. Dipolar molecules (1a, 1b, 1c) undergo a polarisation mechanism, whereas ionic molecules (2a, 2b) experience a much stronger conduction mechanism.

of the microwave irradiation (Figure 1.14).

As the microwave oscillates, the dipoles of the molecules attempt to align with the electric component of the wave. This causes the molecules to wobble, transferring energy to their surrounding environment in the forms of dielectric loss and molecular friction, and ultimately producing heat. The effectiveness of dipole polarisation has been shown to be dependent on the frequency of the microwave employed for each solvent. If the frequency is too high or too low, the molecules will either not oscillate at all or oscillate too slowly to have any considerable heating effect respectively. This is because higher frequencies will not give the dipoles long enough to reorient themselves, whereas lower frequencies will not promote enough interaction between neighbouring molecules. However, since most commercial microwave sources operate at a frequency of 2.45 GHz it is necessary to retroactively couple a complementary solvent to the wavelength. The loss tangent ( $\tan\delta$ ) is used to evaluate the heating properties of a solvent at a particular wavelength, described by the following Equation:

$$\tan\delta = \frac{\epsilon'}{\epsilon''} \quad (1.10)$$

where  $\epsilon'$  is the dielectric constant (which is directly proportional to the solvents ability to absorb microwaves), and  $\epsilon''$  is the loss factor (the efficiency of the solvent to convert absorbed microwave energy to heat). Examples of different solvents and their their ability to couple to microwaves during synthesis can be seen in Table 1.1. From Equation 3.1 and the supplied values it is apparent that solvents with increasing dielectric constants ( $\epsilon'$ ) require

Solvent	b.p. (°C)	$\epsilon'$	$\epsilon''$	$\tan \delta$	Microwave absorbance
Ethylene glycol	197	37	49.9	1.35	Very high
Ethanol	78	24.3	22.89	0.94	High
Methanol	63	32.6	21.48	0.66	High
Water	100	80.4	9.889	0.12	Medium
Toluene	110	2.4	0.096	0.04	Very low

**Table 1.1:** A comparison of common solvents and their physical properties as candidates for solvents for microwave syntheses.

increasing loss factors ( $\epsilon''$ ) to efficiently heat a system.

Ionic solvents (or ions in solution) undergo a heating mechanism called ionic conduction. When an ionic solution is irradiated with microwaves it couples with the electric component of the microwave. Rather than pivoting round the dipole moment like a polar substance, the ion attempts to trace the electric component of the wave, culminating in conduction of the ions. Since the ion is effectively being pulled through the solution, it collides with other molecules and generates heat through molecular friction. Ionic conduction interacts more strongly with microwave radiation since the ions are always in contact with the wave, whereas during dipole polarisation this is not the case. The most basic example of this can be seen by heating tap water and deionised water with microwaves.<sup>115</sup> If both are irradiated with microwaves for the same amount of time, the final temperature of the tap water will be greater. This is because the tap water contains ions which create stronger interactions with the microwave radiation than just the dipolar water molecules alone in deionised water. The effect of ionic conduction is even further emphasised in salt water, which contains a high concentration of  $\text{Na}^+$  ions.

Microwave heating has been shown to produce pure products at shorter reaction times (as little as 5 to 15 minutes) than conventional methods while retaining controlled size and morphology. The provision of small particles in a short time frame makes microwave synthesis an extremely attractive route to functional materials. Microwave-assisted routes have been employed to access several different families of materials. Most simply, nanostructured Cu and Ni metal have been prepared by a microwave-assisted ionothermal route, yielding

particles 100 nm in diameter in just 10 min ( $P = 900$  W,  $\nu = 2.45$  GHz).<sup>116</sup> Metal sulphides have also been prepared by an ionothermal microwave-assisted approach for Li-ion insertion electrode applications. Synthesis of SnS<sub>2</sub>/reduced graphene oxide (RGO) composites showed the construction of SnS<sub>2</sub> particles embedded in the RGO framework, prepared after 20 min at of microwave irradiation ( $\nu = 2.45$  GHz) 180 °C.<sup>117</sup> Their electrochemical analyses showed improved performance versus materials prepared by hydrothermal routes with longer heating times, attributed to the increased electrical conductivity (from the RGO), and the smaller particle size (due to the rapid synthesis), of the SnS<sub>2</sub>.<sup>118</sup>

#### 1.5.4 Preparation of metal oxides by microwave-assisted synthesis

An area of large research of microwave prepared materials is metal oxides. One typical anode material that has been studied is SnO<sub>2</sub>. SnO<sub>2</sub> prepared by various routes has shown 1-3 nm particles from microwave-assisted hydrothermal routes (30 min 85 C), 6 nm from a microwave oven route (2450 MHz, 700 W, 60 s), and 9 nm from a water bath method(85 C for 3 h).<sup>119</sup> All samples show an initial capacity of 450 mAh g<sup>-1</sup>, however both microwave assisted approaches gave a capacity retention of 90 % after 40 cycles, whereas the water bath method shows a lower retention of 75 % after 40 cycles (at a current rate of 0.4 mA cm<sup>-2</sup>). Microwave-assisted sol-gel approaches have also been employed to synthesise SnO<sub>2</sub> in 6 min ( $P = 1.24$  kW,  $\nu = 2.45$  GHz), producing 30 nm particles with superior electrochemical behaviour to bulk SnO<sub>2</sub>.<sup>120</sup> Furthermore, graphene has been successfully decorated with SnO<sub>2</sub> particles, < 100 nm in diameter, in as little as 20 min of microwave irradiation at 120 °C by microwave-assisted hydrothermal routes.<sup>23,121,122</sup>

Another well studied metal oxide, prepared by microwave assisted approaches, is Co<sub>3</sub>O<sub>4</sub>. Nanoparticles of Co<sub>3</sub>O<sub>4</sub> were successfully prepared after 1 min to 4 min of microwave irradiation ( $\nu = 2.45$  GHz) at 90 °C.<sup>123</sup> Macroporous structures, several hundreds of nm in size were obtained and showed the best rate capability of Co<sub>3</sub>O<sub>4</sub> as an anode to date (746 mAh g<sup>-1</sup> at 4450 mA g<sup>-1</sup>). A microwave-assisted hydrothermal reflux method has also been employed yielding hierarchical, flower-like macro structures ("petals" 5 nm thick) of Co<sub>3</sub>O<sub>4</sub> after 15 min of microwave irradiation ( $\nu = 2.45$  GHz) at 85 °C.<sup>124</sup> Graphene has also successfully been decorated with Co<sub>3</sub>O<sub>4</sub> nanoparticles by a microwave-assisted hydrothermal route.<sup>125</sup>

Several  $\text{FeO}_x$ /carbon composites have also been prepared by microwave-assisted routes.  $\text{Fe}_3\text{O}_4$ /C nanowires, approximately 20 nm in thickness with a uniform 5 nm thick carbon coating, were successfully obtained from a 150 °C microwave irradiation ( $\nu = 2.45$  GHz) for 15 min.<sup>126</sup>  $\text{Fe}_3\text{O}_4$ /graphene was prepared by a microwave-assisted hydrothermal reflux for 1 h, yielding particles < 20 nm in diameter.<sup>127</sup> An  $\text{Fe}_2\text{O}_3$ /graphene composite was obtained by irradiating for 20 min at 200 °C, yielding metal oxide particles around 100 nm in diameter.<sup>128</sup> A beautiful example of the morphological complexity that can be achieved by microwave-assisted routes can be seen for  $\alpha\text{-Fe}_2\text{O}_3$ .<sup>129</sup> Snowflake-like dendrites and star-shaped particles, tens of microns in diameter, were obtained changing the length and temperature of the irradiation (180 °C to 250 °C, 30 s to 10 min) to control the morphology. The growth of carbon nanotubes from graphene sheets, catalysed by  $\text{FeO}_x$  nanoparticles grown in parallel, has also been demonstrated by microwave-assisted routes.<sup>130</sup>

Manganese oxides have also been prepared, such as  $\text{Mn}_3\text{O}_4$ ,  $\beta$ - and  $\gamma\text{-MnO}_2$  and MnO.  $\text{Mn}_3\text{O}_4$  nanoparticles were prepared by microwave-assisted hydrothermal route (150 °C for 30 min), 20 nm in diameter, and show an outstanding capacity retention close to 100 %.<sup>6</sup>  $\beta$ - and  $\gamma\text{-MnO}_2$  polymorphs prepared by microwave-assisted hydrothermal synthesis show that reaction temperature can be altered to obtain different phases with different electrochemical performance (150 mAh g<sup>-1</sup> and 170 mAh g<sup>-1</sup>, respectively). MnO/C macroporous structures prepared by microwave-assisted routes in as little as 10 min at 195 °C ( $\nu = 2.45$  GHz).<sup>131,132</sup> The MnO nanoparticles observed are below 20 nm in diameter and show Coulombic efficiencies and capacity retentions close to 100 % after 140 cycles.

Other metal oxides that have been investigated include CuO/graphene composites,  $\text{MoO}_3$  and  $\text{CoMoO}_4$  as well as lithiated metal oxides for Li<sup>+</sup> insertion electrode applications.<sup>133–135</sup>  $\text{Li}_4\text{Ti}_5\text{O}_{12}$  nanoparticles < 50 nm in diameter were prepared by a solid-state microwave-assisted method in a conventional microwave oven after 10 min ( $P = 500$  W).<sup>136</sup> These nanoparticles show a capacity retention of 90 % after 20 cycles. In addition,  $\text{Li}_4\text{Ti}_5\text{O}_{12}$  hierarchical microspheres (nanoflake subunits 40 nm in thickness) were obtained from a microwave-assisted hydrothermal method (150 °C for 15 min), showing a capacity retention of around 95 % and a Coulombic efficiency close to 100 %.<sup>137</sup> Similar observations have also been observed in microwave prepared  $\text{Li}_4\text{Ti}_5\text{O}_{12}$ /RGO composite.<sup>138</sup>

$\text{LiMn}_2\text{O}_4$  is another well studied  $\text{Li}^+$  battery electrode material prepared by microwave-assisted routes. Like many other materials detailed here,  $\text{LiMn}_2\text{O}_4/\text{RGO}$  composited materials have been prepared by microwave-assisted routes.<sup>139</sup>  $\text{LiMn}_2\text{O}_4$  has also been successfully doped with electronegative (fluorine) and electropositive (neodymium) elements using microwave-assisted routes.<sup>140,141</sup>

### 1.5.5 Preparation of vanadium oxide materials by microwave-assisted approaches

The first reports of vanadate phases being obtained by microwave-assisted routes were prepared by a solid-state method in a conventional microwave oven, with intermittent grinding.<sup>108</sup> The studies showed it was possible to obtain irregular shaped particles of  $\text{Li}_x\text{V}_2\text{O}_5$  and  $\text{Cu}_x\text{V}_2\text{O}_5$  tens of  $\mu\text{m}$  in diameter, and rods of  $\text{K}_x\text{V}_2\text{O}_5$  tens of  $\mu\text{m}$  in length. Multiple electron transfer (MET) capable  $\text{LiV}_3\text{O}_8$  was also prepared by a similar solid-state route, giving rise to nanosheets several  $\mu\text{m}$  in diameter and 3 nm thick after just 30 min of microwave-irradiation.<sup>142</sup> These particles exhibited a high discharge capacity of  $335 \text{ mAh g}^{-1}$ .

More recently, hollow  $\text{VO}_2(\text{B})$  spheres 100 nm to 600 nm in diameter were prepared by a microwave-assisted route, in a microwave oven ( $200^\circ\text{C}$  for 30 min).<sup>143</sup> The spheres were subsequently converted to  $\text{V}_2\text{O}_5$  by annealing in an oven, and exhibit discharge capacities up to  $378 \text{ mAh g}^{-1}$  at  $50 \text{ mA g}^{-1}$ .  $\text{V}_2\text{O}_5$  nanorods 100 nm in diameter and several  $\mu\text{m}$  in length were also obtained by microwave-assisted hydrothermal routes, showing an initial discharge capacity of  $330 \text{ mAh g}^{-1}$  at  $50 \text{ mA g}^{-1}$ .<sup>144</sup>

Microwave-assisted solid-state preparation of silver vanadium oxides  $\text{Ag}_2\text{V}_4\text{O}_{11}$  and  $\text{Ag}_3\text{VO}_4$  has also been investigated for high power applications in implantable cardioverter defibrillators.<sup>145,146</sup> It was found that phase pure materials could be obtained after as little as 5 min to 30 min of microwave irradiation ( $P = 600 \text{ W}$ ) in a domestic microwave oven. The  $\text{Ag}_2\text{V}_4\text{O}_{11}$  particles exhibited a large discharge capacity of  $272 \text{ mAh g}^{-1}$  at  $31.5 \text{ mA g}^{-1}$ .

These studies have shown that it is possible to obtain vanadate phases with large discharge capacities through microwave-assisted routes. However, there are many other vanadate phases that have yet to be accessed by microwave routes.

### 1.5.6 Preparation of olivine phosphate materials by microwave-assisted approaches

Although examples of the microwave-assisted preparation of other polyanionic materials exist, such as  $\text{Li}_2\text{FeSiO}_4$  and  $\text{Li}_2\text{MnSiO}_4$ , olivine phosphates have accrued the most interest.<sup>35</sup> Initial studies on microwave-assisted preparation of  $\alpha\text{-LiFePO}_4$  were investigated using solid-state routes. The first investigation employed a conventional microwave oven as the heating source.<sup>147</sup> Pellets of the precursor materials were placed into an alumina crucible, and heated under an Ar atmosphere for 5 min to 20 min ( $P = 500 \text{ W}$ ,  $\nu = 2.45 \text{ GHz}$ ). At 10 min of irradiation, phase pure micron-sized particles of  $\alpha\text{-LiFePO}_4$  were obtained. These particles exhibited a stable capacity of around  $120 \text{ mAh g}^{-1}$  at a C/11 rate.

Other methods have also been employed, such as mixing the precursors with microwave susceptors (graphite, activated carbon etc.) allowing better microwave absorption and faster heating.<sup>148</sup> Materials prepared in this way showed phase pure  $\alpha\text{-LiFePO}_4$  could be obtained without an inert atmosphere, most likely from carbothermal reduction maintaining a  $\text{Fe}^{2+}$  state and preventing oxidation. The resulting particles showed an average size of  $1 \mu\text{m}$  in diameter after 4 min of irradiation, with an initial discharge capacity of  $151 \text{ mAh g}^{-1}$  at C/10. The use of microwave susceptors has also led to the preparation of  $\alpha\text{-LiFePO}_4$  nanoparticles through a solid-state coordination technique.<sup>149</sup> Powders prepared by this method led to particles  $< 100 \text{ nm}$  in diameter after several min of microwave irradiation ( $P = 850$ ,  $\nu = 3.0 \text{ GHz}$ ) and capacities up to  $125 \text{ mAh g}^{-1}$  at a C/2 rate. Moreover, the use of susceptors has also provided a route to carbon coated  $\alpha\text{-LiFePO}_4$  with stable capacities up to  $160 \text{ mAh g}^{-1}$  after 50 cycles at a C/10 rate.<sup>150</sup>

To investigate the use of microwaves and their ability to produce interesting particle architectures further, solution based hydrothermal and solvothermal approaches have also been explored. Two major advantages of solution based approaches are that (a) the reactants can be diluted in an attempt to form smaller particles and (b) diffusion of reactants is easier to overcome than in solid-state syntheses, allowing quicker reaction times.  $\alpha\text{-LiFePO}_4$  obtained by a microwave solvothermal route in benzyl alcohol was shown to produce phase pure mesocrystals in as little as 3 min of microwave irradiation ( $180^\circ\text{C}$ ,  $\nu = 2.45 \text{ GHz}$ ).<sup>151</sup> The mesocrystals were  $1.5 \mu\text{m}$  in diameter and constructed of smaller crystallites around

50 nm to 100 nm in diameter. Electrochemical investigations showed that the mesocrystals delivered a capacity of 150 mAh g<sup>-1</sup> at a 2C rate and stable over 150 cycles. Nanocrystals of LiMnPO<sub>4</sub> were also prepared by a similar method but showed a lower capacity of 125 mAh g<sup>-1</sup>. Other metal olivine phosphates prepared by microwave-assisted solvothermal synthesis in tetraethylene glycol have showed more promise such as LiCoPO<sub>4</sub> (120 mAh g<sup>-1</sup>), but still underperform compared to α-LiFePO<sub>4</sub> particles prepared in a similar manner (145 mAh g<sup>-1</sup>) at a rate of C/10 due to less structural stability.<sup>152</sup>

Doped α-LiFePO<sub>4</sub> has also been successfully prepared by a microwave-assisted solvothermal approach in benzyl alcohol after 3 min of irradiation (180 °C, ν2.45 GHz), producing mesocrystals.<sup>153</sup> XRD studies showed that doping of Ni, Zn, Al, Mn and Ti had all been successful (at 2 %, 5 % and 7 % atomic ratios versus Fe). At 2 atomic %, all dopants improved the electrochemical capacity of α-LiFePO<sub>4</sub>.

Synthesis of carbon coated α-LiFePO<sub>4</sub> nanorods (200 nm in width) has also been possible by microwave-assisted a hydrothermal route using glucose or an amorphous, conductive carbon (such as superP) as the carbon source after 5-20 min of microwave irradiation (300 °C, ν = 2.45 GHz).<sup>154,155</sup> The nanorods showed improved electrochemical properties versus α-LiFePO<sub>4</sub> prepared by a microwave hydrothermal route, but carbon coated *ex situ*. Similar methods have also been employed for LiMnPO<sub>4</sub> and LiCoPO<sub>4</sub> showing lower capacities (< 50 mAh g<sup>-1</sup>, C/10 rate) versus uncoated material.<sup>155</sup> The obtained particles exhibited various sizes, from 200 nm thick rods (Fe), 100 nm thick rods (Mn) and micron-sized cuboids (Co).

α-LiFePO<sub>4</sub> has also been coated with various other materials during microwave-assisted hydrothermal/solvothermal synthesis to improve electrochemical properties. These include carbon nanotubes, graphene and conducting polymers. Syntheses with carbon nanotubes were conducted in tetraethylene glycol, yielding phase pure α-LiFePO<sub>4</sub> nanorods (25 nm width, 100 nm length) after 5 min of irradiation (300 °C, 2.45 GHz). The coated materials showed improved electronic conductivity attributed to the carbon nanotubes. Graphene coated α-LiFePO<sub>4</sub> crystallites (150 nm diameter) prepared hydrothermally after 15 min (200 °C, ν= 2.45 GHz) showed a similar improvement in electronic conductivity.<sup>156</sup> Lastly, poly(3,4-ethylenedioxythiophene) (PEDOT) coated α-LiFePO<sub>4</sub> particles have also been syn-

thesised by a microwave-assisted solvothermal approach in tetraethylene glycol, after 5 min of microwave irradiation (300 °C,  $\nu = 2.45$  GHz). The resulting nanorods were 30 nm in width, with a discharge capacity of 166 mAh g<sup>-1</sup> at C/15 rate.

These experimental studies highlight the wide range of methodologies already explored for microwave-assisted approaches. Varying the reaction conditions can alter both the size and morphology of the resulting particles and, ultimately, the electrochemical performance. Although there have been many investigations, there still remains a wealth of knowledge to be gained from altering synthesis parameters, such as the solvent employed, reaction temperature and microwave irradiation time.

## 1.6 Summary of aims and objectives

The main aims of this work are to investigate microwave-assisted solvothermal synthesis routes to nanostructured insertion electrodes. The synthesis conditions will be modified in an attempt to access phase pure materials and new phases by altering the temperature, time and reaction media. This research will hope to provide materials with improved electrochemical performance compared to conventional synthesis routes, for more efficient insertion electrodes. The effect of different reaction media on  $\alpha$ -LiFePO<sub>4</sub> will be investigated in initial studies, as it is a well understood material. In an attempt to access materials with large discharge capacities, routes to vanadium based MET capable phases, oxides and oxyhydroxides, will be investigated. Additionally, investigation of the local behaviour of insertion cathodes is a significant area of interest which will be investigated using state-of-the-art synchrotron based techniques.  $\mu$ SR will be employed to study the Li<sup>+</sup> ion diffusion dynamics and *in situ* X-ray absorption spectroscopy will be used to investigate the evolution of the structure and oxidation state in nanostructured Li-ion insertion cathodes. This further knowledge of Li-ion insertion cathodes will help in the development of future materials, and aid in the generation of efficient energy storage.

## Chapter 2: Experimental methods

### 2.1 Microwave synthesis

All microwave synthesis was conducted in a CEM Discover SP microwave synthesiser emitting 2.45 GHz irradiation. The power is varied between 0-300 W to achieve and maintain the temperatures required for synthesis. For safety reasons a pressure limit of 300 PSI is used.

#### 2.1.1 Preparation of $\text{LiFePO}_4$ polymorphs in polyol media

$\text{FeC}_2\text{O}_4 \cdot 2\text{H}_2\text{O}$  (0.180 g; 1 mmol; Sigma-Aldrich 99.0 %) and  $\text{LiH}_2\text{PO}_4$  (0.104 g; 1 mmol; Sigma-Aldrich 99.0 %) was placed into a 10 ml microwave reaction vessel. To this, 4 ml of either ethylene glycol (Sigma-Aldrich, 99.0 %), DEG (Sigma-Aldrich, 99.0 %) or TEG (Sigma-Aldrich, 99.0 %) was added. The mixtures were magnetically stirred for 5 min and then sealed with a Teflon<sup>TM</sup> cap. The mixtures were then irradiated with microwaves in a CEM Discover SP microwave synthesiser ( $\nu = 2.45$  GHz) between 200 °C and 250 °C for 15 min to 5 h. The resulting precipitates were washed under centrifugation at 4000 RPM with deionised water, ethanol and acetone until the supernatant was clear. The precipitates were dried in a vacuum oven at 80 °C overnight yielding fine off-white and pale green powders.

For the sample of  $\alpha/\beta\text{-LiFePO}_4$  prepared for  $\mu\text{SR}$  analysis,  $\text{FeC}_2\text{O}_4 \cdot 2\text{H}_2\text{O}$  (0.456 g; 2.54 mmol; Sigma-Aldrich 99.0 %) and  $\text{LiH}_2\text{PO}_4$  (0.263 g; 2.54 mmol; Sigma-Aldrich 99 %) were placed into a 35 ml microwave reaction vessel. 10 ml of EG was added and the mixture was then irradiated with microwaves in a CEM Discover SP microwave synthesiser ( $\nu = 2.45$  GHz) at 250 °C for 3 h. The resulting precipitate was washed under centrifugation at 4000 RPM with deionised water, ethanol and acetone until the supernatant was clear. The precipitate was dried in a vacuum oven at 80 °C overnight yielding a pale green powder.

#### 2.1.2 Preparation of $\text{LiFePO}_4$ polymorphs in ionic liquids

$\text{FeC}_2\text{O}_4 \cdot 2\text{H}_2\text{O}$  (0.180 g; 1 mmol; Sigma-Aldrich 99.0 %) and  $\text{LiH}_2\text{PO}_4$  (0.104 g; 1 mmol; Sigma-Aldrich 99.0 %) was placed into a 10 ml microwave reaction vessel. To this, 4 ml of either 1-ethyl-3-methyl imidazolium trifluoromethanesulfonate (EMIM-TFMS; Solvionic 99.5 %) or 1-ethyl-3-methylimidazolium bis(trifluorosulfonyl)imide (EMIM-TFSI; Solvionic 99.9 %)

was added. Ionic liquids were introduced to the microwave vessel in an Ar filled glovebox to avoid oxidation of the solvent. The mixtures were sealed with a Teflon<sup>TM</sup> cap and magnetically stirred for 5 min. The mixtures were then irradiated with microwaves in a CEM Discover SP microwave synthesiser ( $\nu = 2.45$  GHz) at 250 °C for 3 to 5 h. The resulting precipitates were washed under centrifugation at 4000 RPM with deionised water, ethanol and acetone until the supernatant was clear. The precipitates were dried in a vacuum oven at 80 °C overnight yielding fine off-white and pale green powders.

For the sample of  $\alpha$ -LiFePO<sub>4</sub> prepared for  $\mu$ SR analysis, FeC<sub>2</sub>O<sub>4</sub> · 2 H<sub>2</sub>O (0.456 g; 2.54 mmol; Sigma-Aldrich 99.0 %) and LiH<sub>2</sub>PO<sub>4</sub> (0.263 g; 2.54 mmol; Sigma-Aldrich 99 %) were placed into a 35 ml microwave reaction vessel. 10 ml of EMIM-TFMS was added and the mixture was then irradiated with microwaves in a CEM Discover SP microwave synthesiser ( $\nu = 2.45$  GHz) at 250 °C for 3 h. The resulting precipitate was washed under centrifugation at 4000 RPM with deionised water, ethanol and acetone until the supernatant was clear. The precipitate was dried in a vacuum oven at 80 °C overnight yielding an off-white powder.

### 2.1.3 Preparation of LiFePO<sub>4</sub> polymorphs in deep eutectic solvents

All deep eutectic solvents (DES) were prepared by adding molar ratios of an ammonium salt (choline chloride, ChCl or tetramethylammonium chloride, TMAC) to a hydrogen bond donor. A summary of these mixtures are given in Table 4.1. The mixtures were placed into a 35 ml microwave vessel and sealed with a Teflon<sup>TM</sup> cap. The mixtures were then irradiated for 5 min at 100 °C under magnetic stirring. After cooling, clear solutions were produced in all cases with no additional steps employed before use in synthesis of nanoparticles.

For the preparation of  $\alpha$ -LiFePO<sub>4</sub>, FeC<sub>2</sub>O<sub>4</sub> · 2 H<sub>2</sub>O (0.180 g; 1 mmol; Sigma-Aldrich 99.0 %) and LiH<sub>2</sub>PO<sub>4</sub> (0.104 g; 1 mmol; Sigma-Aldrich 99.0 %) was placed into a 10 ml microwave reaction vessel. To this, 4 ml of a DES solvent was added. The mixtures were magnetically stirred for 5 min and then sealed with a Teflon<sup>TM</sup> cap. The mixtures were then irradiated with microwaves in a CEM Discover SP microwave synthesiser ( $\nu = 2.45$  GHz) between 200 °C and 250 °C for 1 min to 5 h. The resulting precipitates were washed under centrifugation at 4000 RPM with deionised water, ethanol and acetone until the supernatant was clear. The precipitates were dried in a vacuum oven at 80 °C overnight yielding fine

Salt	HBD	Salt:HBD (mol)
Choline chloride	Ethylene glycol	1:2
Choline chloride	Ethylene glycol	1:3
Choline chloride	Ethylene glycol	2:3
Choline chloride	Diethylene glycol	1:2
Choline chloride	Tetraethylene glycol	1:2
Choline chloride	Glycerol	1:2
Choline chloride	Glucose	1:2
Choline chloride	Sucrose	1:2
Tetramethyl ammonium chloride	Ethylene glycol	1:2

**Table 2.1:** Investigated salts and hydrogen bond donors (HBD) for deep eutectic mixtures.

off-white powders.

#### 2.1.4 Preparation of VO<sub>2</sub> (B) and V<sub>3</sub>O<sub>7</sub>

##### Microwave-assisted reduction of V<sub>2</sub>O<sub>5</sub> in formaldehyde

V<sub>2</sub>O<sub>5</sub> (0.1 g; 0.55 mmol; Sigma-Aldrich ≥ 98.0 %) was dissolved into formaldehyde solution (37%, Sigma-Aldrich) in a 10 ml glass reaction vessel. The mixtures were irradiated with microwaves ( $\nu = 2.45$  GHz) to 50 °C for 5 min after which the temperature was increased to 180 °C for 1 h to 6 h. The reactions yielded a blue-black precipitate which was washed with ethanol and acetone until the supernatant was clear and dried in a vacuum oven at 80 °C overnight. All reactions yielded fine blue-black powders. Reactions were also repeated in a similar fashion for 3 h of microwave irradiation adding 1 mg, 2.5 mg, 5 mg and 10 mg of polyvinylpyrrolidone (PVP; Sigma-Aldrich, 10,000 mwt.) also yielding fine blue-black powders.

##### Microwave-assisted reduction of V<sub>2</sub>O<sub>5</sub> in formaldehyde and ethylene glycol (EG)

V<sub>2</sub>O<sub>5</sub> (0.1 g; 0.55 mmol; Sigma-Aldrich ≥ 98.0 %) was dissolved into mixtures of formaldehyde solution (Sigma-Aldrich 37%) and EG (Alfa Aesar 99.8%) in a 10 ml glass reaction vessel. The mixtures were irradiated with microwaves ( $\nu = 2.45$  GHz) to 50 °C for 5 min

after which the temperature was increased to 180 °C for 3 hours. The reactions yielded a blue-black precipitate which was washed with ethanol and acetone until the supernatant was clear and dried in a vacuum oven at 80 °C overnight. All reactions yielded fine blue-black powders.

#### **Microwave-assisted reduction of $V_2O_5$ in formaldehyde and diethylene glycol (DEG)**

$V_2O_5$  (0.1 g; 0.55 mmol; Sigma-Aldrich  $\geq$  98.0 %) was dissolved into mixtures of formaldehyde solution (Sigma-Aldrich 37%) and diethylene glycol (Alfa Aesar 99.8%) in a 10 ml glass reaction vessel. The mixtures were irradiated with microwaves ( $\nu= 2.45$  GHz) to 50 °C for 5 min after which the temperature was increased to 180 °C for 3 hours. The reactions yielded a blue-black precipitate which was washed with ethanol and acetone until the supernatant was clear and dried in a vacuum oven at 80 °C overnight. All reactions yielded fine blue-black powders.

#### **2.1.5 Microwave-assisted reduction of $V_2O_5$ in isopropanol (IPA)**

$V_3O_7$  was obtained by the following synthesis.  $V_2O_5$  (0.1 g; 0.55 mmol; Sigma-Aldrich  $\geq$  98.0 %) was dissolved into 4 ml of IPA in a 10 ml glass reaction vessel. The mixture was irradiated with microwaves ( $\nu= 2.45$  GHz) to 50 °C for 5 min after which the temperature was increased to 180 °C for 3 hours. The reaction yielded a blue-black precipitate which was washed with water, instantaneously forming an orange gel. The gel was transferred to a petri dish and the solvent was evaporated at 100 °C forming a lustrous and brittle blue black deposit. The sample was also ground in a pestle and mortar and annealed at 400 °C for 1 h in a tube furnace under Ar yielding a blue-black powder.

#### **2.1.6 Microwave-assisted preparation of $H_2V_3O_8$**

$V_2O_5$  (0.1 g; 0.55 mmol; Sigma-Aldrich  $\geq$  98.0 %) was dissolved into mixtures of deionised water and isopropanol (IPA) in ratios of 1 ml:3 ml, 2 ml:2 ml and 3 ml:1 ml in a 10 ml glass reaction vessel. The mixture was irradiated with microwaves ( $\nu= 2.45$  GHz) to 50 °C for 5 min after which the temperature was increased to 180 °C for 3 hours. The reactions carried out in 2 ml:2 ml and 3 ml:1 ml, water:IPA yielded orange solutions which were washed with

ethanol and acetone until the supernatant was clear and dried in a vacuum oven at 80 °C overnight resulting in fine orange powders. The reaction in 1 ml:3 ml, water:IPA yielded a green solution which was washed with ethanol and acetone until the supernatant was clear and dried in a vacuum oven at 80 °C overnight resulting in a green fibrous mass.

### 2.1.7 Microwave-assisted preparation of $V_4O_6O(OH)_4$

$V_2O_5$  (0.1 g; 0.55 mmol; Sigma-Aldrich  $\geq 98.0\%$ ) was dissolved into 5 ml DEG (Alfa Aesar, 99.8%) in a 10 ml glass reaction vessel. The mixture was irradiated with microwaves ( $\nu = 2.45$  GHz) to 50 °C for 5 min after which the temperature was increased to 180 °C for 3 hours. The reaction yielded a blue-black precipitate which was washed with ethanol and acetone until the supernatant was clear and dried under vacuum at room temperature overnight resulting in a coarse black powder.

## 2.2 Solvothermal preparation of $VO_2$ (B)

Solvothermal  $VO_2$ (B) was prepared using a similar method to Reference 157.  $V_2O_5$  (1.81 g; 1 mmol; Sigma-Aldrich  $\geq 98.0\%$ ) was placed into a 45 ml Teflon<sup>TM</sup> lined steel autoclave, adding 30 ml of 37 % formaldehyde solution (Sigma-Aldrich). The resulting orange suspension mixed under magnetic stirring for 30 min before the autoclave was sealed and heated in a convection oven at 180 °C (at 10 °C/min) for 48 h. The resulting blue-black precipitate was washed with water, ethanol and acetone under centrifugation at 4000 RPM until the supernatant became clear and dried in a vacuum oven at 80 °C overnight. A fine-blue black powder was obtained.

## 2.3 Chemical lithiation of $H_2V_3O_8$

Chemical lithiation was performed similar to previous literature methods. 100 mg of microwave prepared  $H_2V_3O_8$  was dispersed in 15 ml of deionised water and stirred for 10 min. To this LiOH (89 mg; 3.7 mmol; Sigma-Aldrich 98 %) was added and stirred for a further 15 min changing the solution from green to blue. Finally, ascorbic acid (187 mg; 1.05 mmol; Sigma-Aldrich  $\geq 99\%$ ) was added as an antioxidant to prevent any oxidation of the  $V^{4+}$

to  $V^{5+}$  and stirred for 15 min. The resulting blue mixture separated using vacuum filtration through a 0.2  $\mu\text{m}$  nylon membrane filter, washing with deionised water and dried at room temperature.

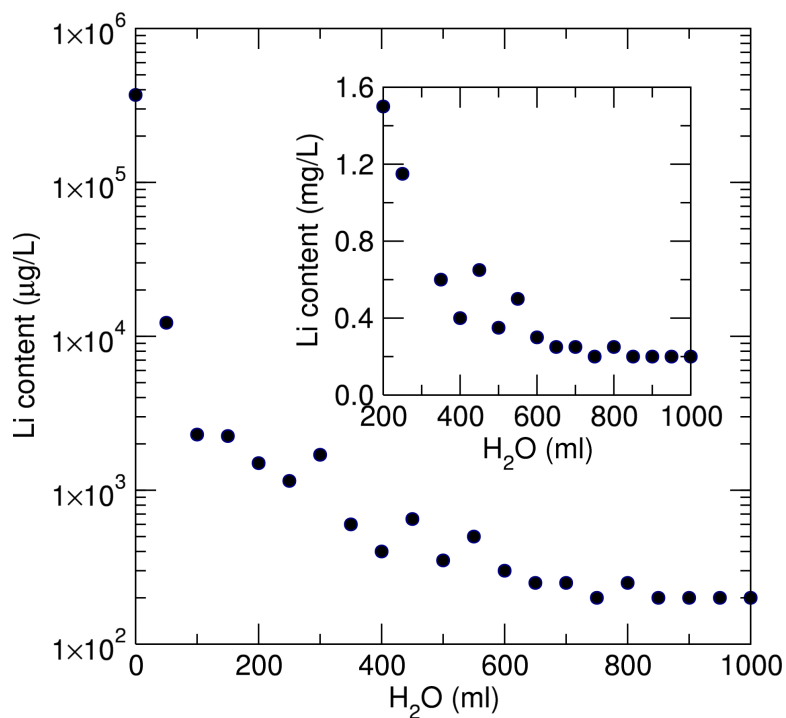


**Figure 2.1:** Concentration of lithium in washings from the chemical lithiation of  $\text{H}_2\text{V}_3\text{O}_8$  taken every 50 mL. A rapid decrease is observed in Li concentration up until 750 mL where the concentration becomes constant.

Flame photometry results for  $\text{Li}^+$  concentration in the washings every 50 ml of deionised water can be seen in Figure 2.1, showing a minimum concentration is reached after 750 mL of deionised water with a constant 0.2 mg/L present. The constant nature of the  $\text{Li}^+$  concentration in the washings after 750 mL suggests the  $\text{Li}^+$  may be coming from the migration of  $\text{Li}_x\text{H}_2\text{V}_3\text{O}_8$  nanowires through the filter. Flame photometry of the  $\text{Li}_x\text{H}_2\text{V}_3\text{O}_8$  nanowires suggested a stoichiometry of  $\text{Li}_{0.4}\text{H}_2\text{V}_3\text{O}_8$ . The concentration of  $\text{Li}^+$  in the washings after 1 L accounted for only 0.3 % of  $\text{Li}^+$  in the nanowires indicating that the presence of any possible  $\text{LiOH}$  contamination was minimal.

## 2.4 Flame photometry

Flame photometry is a quantitative analytical method for group I and group II metals. A solution containing metal atoms is passed through a nebuliser into a flame. When the metal atoms are heated in the flame they enter an unstable excited state, and then quickly relax to the ground state by emission of radiation in the visible region of the electromagnetic spectrum. The wavelength of the released radiation is element specific, and the intensity of the emitted radiation is proportional to the concentration of metal atoms. These signals are picked up by a photodetector specific to the wavelength of interest.

Flame photometry experiments were carried out by dissolving  $\text{Li}_{0.4}\text{H}_2\text{V}_3\text{O}_8$  in nitric acid and heated on a hotplate for several hours at 50 °C. A calibration curve was constructed using standard solutions containing lithium mixed with nitric acid to avoid a matrix effect ( $R^2$  of 0.9998). A Sherwood Model 410 Single Channel flame photometer was used to measure the concentration of lithium in the samples, with a detector set at 670 nm (emission wavelength of Li).

## 2.5 Carbon coating of $\text{LiFePO}_4$

All samples of  $\alpha\text{-LiFePO}_4$  were carbon coated before electrochemical investigations.  $\alpha\text{-LiFePO}_4$  (15.0 mg; 0.095 mmol) was added to 2 ml of deionised water and 2 ml of ethanol in a glass sample jar. To this, a suitable amount of sucrose was added to give 15 % carbon by weight (5.35 mg; 0.015 mmol) with respect to  $\alpha\text{-LiFePO}_4$ . This was determined by considering the thermal decomposition pathway for sucrose which occurs as a dehydration:



The deionised water and ethanol were slowly evaporated while mixing at 80 °C on a hot plate. The off-white dried sucrose/ $\alpha\text{-LiFePO}_4$  mixture was recovered and placed into an alumina crucible and heated in a tube furnace at 700 °C for 2 h in an Ar atmosphere to decompose the sucrose (ramp rate 10 °C/min). The black powder was cooled to room temperature and transferred to an Ar filled glovebox for battery cell preparation. All samples prepared in this way were subjected to CHN analysis to confirm the final mass % of carbon

in the sample.

## 2.6 Fourier transform infrared spectroscopy

Fourier transform infrared (FTIR) is a vibrational spectroscopic method used to analyse the presence of functional groups. Certain functional groups such as O-H, C=O and C-C absorb specific wavelengths of infrared radiation depending on the difference between their ground and excited vibrational states. A spectrum can be collected of % absorbance or % transmittance against the wave-number of infrared radiation ( $\text{cm}^{-1}$ ). In a transmittance spectrum, minima express an absorption event of a functional group, indicating its presence in the sample. This allows for qualitative assessment of the substance by assigning the wave-numbers of the minima to the value from a library or reference pattern. FTIR was performed using a Shimadzu FTIR-8400S in transmittance mode using an ATR stage. Samples were analysed with no additional preparation.

## 2.7 Powder X-ray diffraction

Powder X-ray diffraction (PXRD) is a technique used for characterisation of crystalline materials using X-ray radiation. A sample is irradiated with X-rays of a fixed wavelength and at a fixed angle. The intensity of diffracted radiation is recorded using a goniometer. Crystalline materials have repeating units of atoms and when these atoms diffract X-rays, constructive interference can occur at specific angles depending on the distance between the atoms. This is manifested as a peak in intensity and indicates a plane of atoms. The constructive interference is also proportional to the number of reflections. As the wavelength of the radiation and the angles at which it is employed and reflected are known, the interatomic spacings ( $d_{hkl}$ ) between atoms can be calculated using the Bragg equation:

$$\sin\theta = \frac{n\lambda}{2d} \quad (2.2)$$

where  $\theta$  is half of the diffraction angle,  $d$  is the net plane spacing,  $n$  is the number of reflections and  $\lambda$  is the wavelength of incident X-rays. For particles  $> 100$  nm (and crystalline domains in larger polycrystalline particles), the peak widths are inversely proportional to the

particle size. This is due to a phenomenon known as Scherrer broadening. The Scherrer equation can be used to calculate the crystalline domain size of a material:

$$D = \frac{K\lambda}{B\cos\theta} \quad (2.3)$$

where  $D$  is the domain size,  $K$  is the shape factor, and  $B$  is the line broadening at full width half maximum (FWHM). The shape factor takes into account the crystallite domain shape, and has been shown to affect the broadening observed.<sup>158</sup> Typically a spherical crystallite domain shape ( $K = 0.9$ ) is assumed for convenience, as determination of the precise domain shape in a material is complicated. The FWHM can be obtained from Rietveld refinement, a least squares analysis method used mainly for phase analysis. Rietveld refinement can be employed to compare experimental data to standard data from the literature to analyse the closeness of fit. Equation 2.4 defines the minimisation function of Rietveld refinement.

$$\phi = \sum_{i=1}^n w_i (y_i^{\text{obs}} - y_i^{\text{calc}})^2 \quad (2.4)$$

$$y_i^{\text{calc}} = b_i + K \sum_{j=1}^m I_j y_j(x_j) \quad (2.5)$$

$W_i$  is the weighting of peak  $i$ ,  $y_i^{\text{obs}}$  is the observed intensity at angle  $2\theta_i$ , and  $y_i^{\text{calc}}$ .  $y_i^{\text{calc}}$  can be defined by Equation 2.5, where  $b_i$  is the background at  $2\theta_i$ ,  $K$  is the scale factor of the fit,  $m$  is the number of Bragg reflections contributing to the intensity,  $I_j$  is the area under the peak (integral) at reflection  $j$  and  $y_j(x_j)$  is the peak shape function. For refinements carried out in this Thesis, a pseudo-Voigt (PV( $x$ )) peak shape was employed. A pseudo-Voigt is a combination of a Gaussian and Lorentzian peak shape. Within the pseudo-Voigt function  $U$ ,  $V$  and  $W$  are peak shape parameters which are refined during the Rietveld process.

To comment on the goodness of fit, three main parameters are scrutinised.  $R_{\text{wp}}$  is the weighted R-factor which is a statistical measure of how close the observed data points are to the theoretical model  $R_{\text{exp}}$  is the calculated, best possible  $R_{\text{wp}}$  obtainable with the observed data.<sup>159</sup>  $R$  values are reported as a percentage, with the smallest value implying a better fit.  $\chi^2$  is a goodness of fit parameter that takes both  $R_{\text{exp}}$  and  $R_{\text{wp}}$  into account and can be calculated by Equation 2.6. The value of  $\chi^2$  indicates a better fit when closer to a value of 1.

$$\chi^2 = (R_{wp}/R_{exp})^2 \quad (2.6)$$

It must be stated, however, that the purpose of Rietveld refinement is not to achieve the smallest statistical parameters, but to get good agreement between the structural model and the collected experimental data. To this end, the fit should also be inspected visually to and with awareness of the calculated crystal parameters. In this Thesis, PXRD patterns were collected using a PANalytical X'Pert powder diffractometer using  $\text{CuK}\alpha$  radiation ( $\lambda = 1.540 \text{ \AA}$ ). The samples were prepared in aluminium sample holders used in conjunction with a flat plate PW3064 Reflection-transmission Spinner. Rietveld refinement was performed using the Fullprof Suite software.

## 2.8 Scanning electron microscopy

Scanning electron microscopy (SEM) is a technique for the analysis of particle size and morphology. An electron beam is used to scan a sample and interacts with atoms on the surface, causing secondary electrons to be ejected from the atom's K-shell by inelastic scattering. The electron signals are detected using a detector and quantified as electrical intensity. A colour gradient is then used to visually display the differences in electrical intensity at different sites on a sample and used to construct an image. This is the most common method of SEM analysis using electron beam energies of less than 50 eV although others may be employed, such as analysis of back-scattered electrons from the electron beam itself which uses much higher energy electrons.

All SEM samples were prepared by gold coating using a plasma sputter coater with a 99:1, Au:Pt target to reduce glow-discharge from the lithium. They were then analysed at several magnifications using a Carl Zeiss Sigma field-emission SEM at 10 kV.

## 2.9 Galvanostatic cycling with potential limitation

Galvanostatic cycling with potential limitation (GCPL) is the technique of cycling an electrochemical cell between two defined voltages at a constant current. This allows the investigation of how the potential of the cell is changing with respect to voltage. Lithium insertion

electrodes are most commonly tested versus Li/Li<sup>+</sup> as a counter electrode. Two main pieces of information can be obtained from GCPL in this way; the operational potential of the working electrode ( $E_{we}$ , V) and the specific capacity of the material ( $Q$ , Ah kg<sup>-1</sup>). The capacity can be calculated by using Faraday's laws of electrolysis:

$$Q = \frac{It}{W} \quad (2.7)$$

where  $W$  is the mass of active material in the working electrode (in g) and  $t$  is the time taken to travel between the upper and lower voltage limits (in h). The value of  $Q$  can then be used to calculate the number of Li<sup>+</sup> inserted into the working electrode by the following equation:

$$n = \frac{QM}{F} \quad (2.8)$$

where  $n$  is the number of Li<sup>+</sup> inserted,  $F$  is the Faraday constant (96485 C mol<sup>-1</sup>, the electric charge per mol of electrons) and  $M$  is the molecular mass of the electrode material (g mol<sup>-1</sup>).<sup>160</sup>

## 2.10 Cyclic voltammetry

Cyclic voltammetry (CV) is a technique that allows for the identification of redox events by cycling a battery between two defined voltage limits at a constant voltage, and measuring the change in current ( $I$ ). The technique is useful for identifying the potential at which reduction and oxidation occur, how many redox steps take place upon intercalation, and any changes in behaviour over multiple cycles.

## 2.11 Preparation of electrochemical half cells

20 mg electrodes were prepared by forming composite pellets containing 60 % active material, 30 % carbon black (Ketjen) and 10 % PTFE binder. The mixtures were ground and pressed in a 13 mm die at 1.2 T for 5 min before being weighed. All preparation of battery cells was conducted in an Ar filled glovebox to prevent oxidation of any materials

used. Firstly, the main stainless steel housing of the Swagelok™ cell was lined a non-conductive mylar layer. The first current collector plunger (positive) was placed into the housing and tightened. Next, the working electrode pellet was placed inside the housing onto the positive current collector. A glass fibre separator (Whatman) was then placed on top of the pellet and soaked with 12 drops of electrolyte (1 M LiPF<sub>6</sub> in 1:1, ethylene carbonate:dimethylcarbonate). Lastly, a disc of lithium metal foil was placed on top of the separator and a spring loaded current collector was used to compress the entire stack and tightened. All GCPL and CV experiments were conducted versus Li/Li<sup>+</sup> on a Biologic VSP potentiostat. Rates and voltage windows are specified in the relevant Chapters.

## 2.12 X-ray absorption spectroscopy

When a sample is irradiated with X-rays it can undergo several processes where the electric component of the radiation interacts with the sample, such as scattering, fluorescence, the emission of photoelectrons and transmission. These rely on two key processes, either scattering of X-rays or absorption of X-rays. The absorption of X-rays, or more precisely the quantity absorbed, at a specific wavelength can provide a great deal of information about the atoms electronic structure. The absorbance can be measured by the difference between the incident radiation ( $I_0$ ) and the transmitted radiation ( $I$ ). The magnitude of transmitted X-rays is dependent on the linear absorption coefficient ( $\mu$ ) of the material (Beer-Lambert law), such that:

$$\mu x = \ln\left(\frac{I_0}{I}\right) \quad (2.9)$$

where  $x$  is the thickness of the material and  $\mu$  is affected by the density of the material. At certain energies of X-ray radiation an atom may absorb a large amount of incident radiation, known as absorption edges. Physically, an absorption edge occurs when an atom absorbs sufficient energy from irradiation to excite an electron in to the continuum (Figure 2.2 a) producing a photoelectron. It is noted that the absorption edge is not a simple energy step, but an incline, due to the ability of an electron to rest in an infinite number of  $p$ -states in the continuum and relax back to the ground state. The excitations of an electron from different ground states are labeled K, L and M respective to the shell they are excited from in the

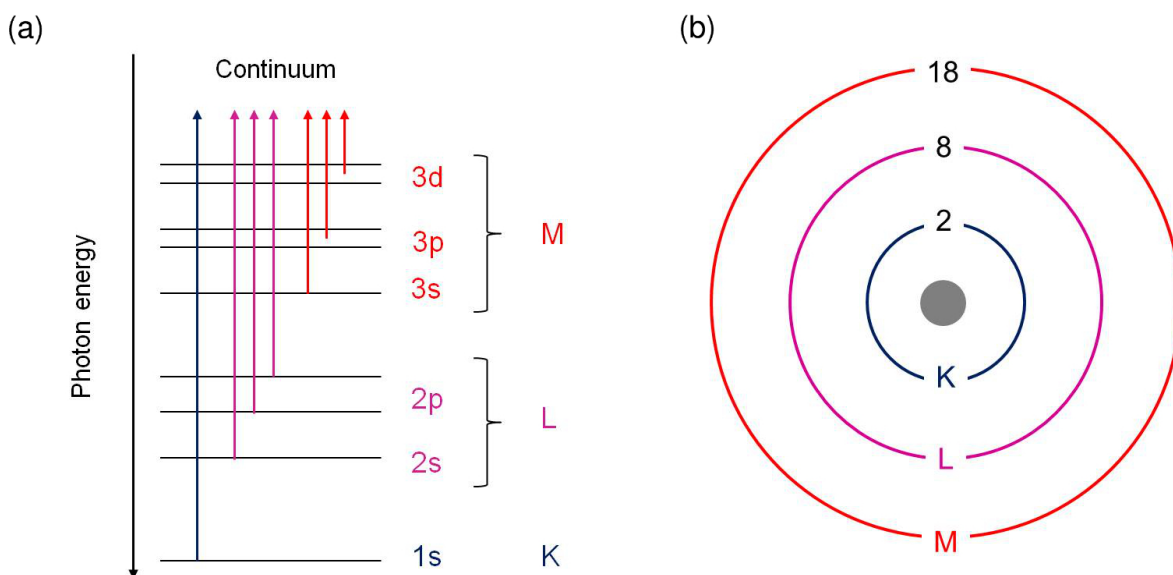


**Figure 2.2:** (a) Core electron excitations in XAS are named by the electronic level from which they originate (K, L, M). (b) The Bohr atomic model showing the various electronic levels. The binding energy of the electrons is greater, closer to the nucleus.

Bohr atomic model (Figure 2.2 b). As an example, K-edge XAS of transition metals will be considered to satisfy the scope of this Thesis.

In an X-ray absorption spectrum, the absorption edge can be seen as a steep incline in absorption (Figure 2.3, B). However, the absorption edge is not the only feature that is observed. Lower energy X-rays than those able to excite an electron into the continuum may excite an electron into an unoccupied state, such as the 3d orbital in transition metals, if it does not violate the Laporte rule by promoting the electron to a symmetrical electronic state. However, the normally dipole forbidden transition of 1s to 3d may become allowed if the metal is not in a perfectly octahedral environment (i.e. distorted  $MO_6$  or tetrahedral) due to quadrupole allowed transitions from  $d/p$  orbital mixing. This process is manifested as a pre-edge peak (Figure 2.3 A), and its intensity is proportional to the asymmetry of the atom's environment.

Features A and B, and indeed the entire spectrum, may shift in energy depending on the oxidation state of the transition metal under investigation.<sup>161</sup> This occurs due to deshielding of the nucleus as electrons are removed from the valence shell, meaning more energy is required to remove the inner electrons and promote them to the 3d state as the oxidation

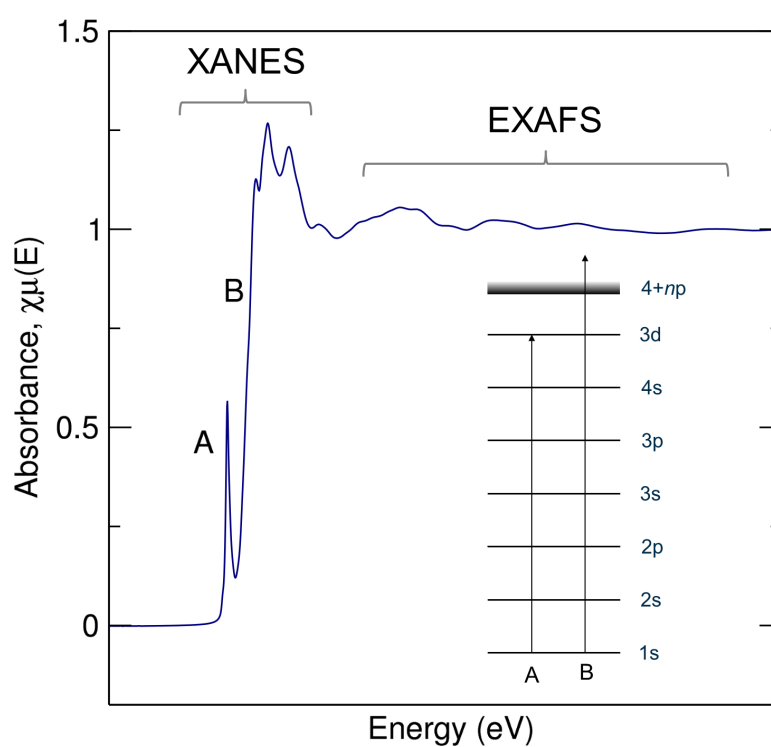


**Figure 2.3:** K-edge XAS spectrum collected for  $V_2O_5$ . The feature labelled A is the pre-edge and B the rising edge. Inset is a diagram showing the electronic transitions that give rise to features A and B.

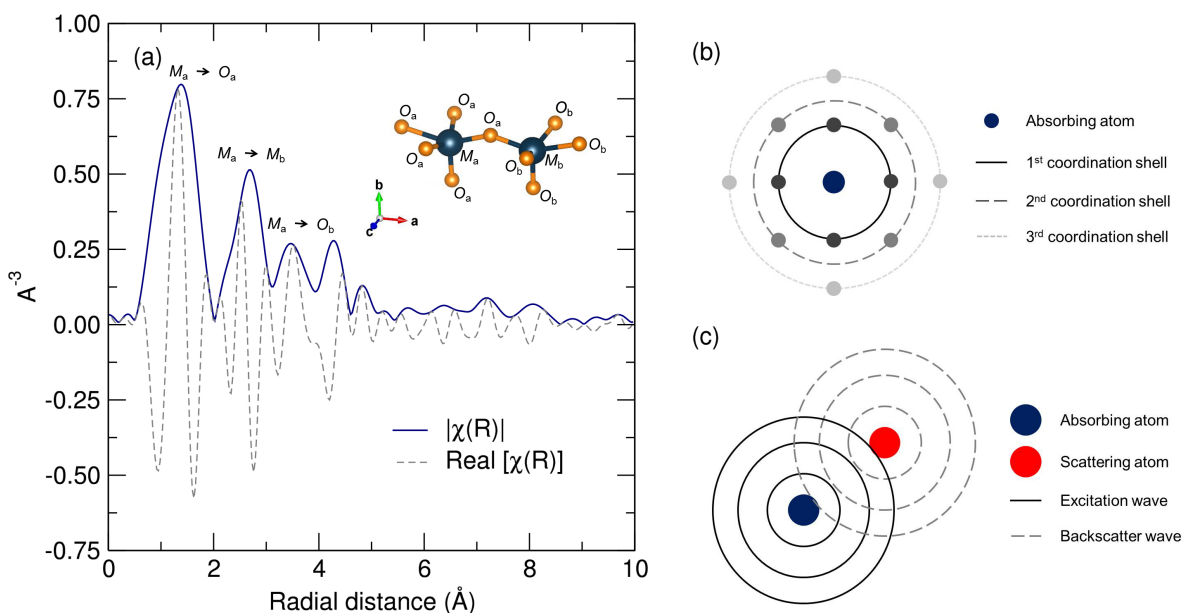


**Figure 2.4:** (a) Real space plot of EXAFS data, peaks in  $|\chi(R)|$  can be attributed to separate contributions from interatomic distances (inset). (b) Schematic describing coordination shells in a material. (c) Schematic describing the wave behaviour of the scattering and absorbing atoms. Constructive and destructive interference can occur when the outgoing and incoming waves interact.

state increases. Features A and B are typically considered as their own set of observations, known as X-ray absorption near-edge structure (XANES) and deal primarily with electronic information.

There is also another set of observations available, at higher energies than the absorption edge, that provide information about the local structure of a material, extended X-ray absorption fine structure (EXAFS). EXAFS (Figure 2.4 a) occur when an atom has absorbed sufficient energy to eject a photoelectron into the continuum. The photoelectron can then be backscattered by neighbouring atoms and these atoms are split into ordered "shells" numbered 1<sup>st</sup>, 2<sup>nd</sup> 3<sup>rd</sup> etc., according to their distance from the absorbing atom (Figure 2.4 b).

As the vector of an ejected electron from the atom is random they can be thought of as a wave of concentric rings extending from the central atom, and similarly with the scattering atom (Figure 2.4 c). Constructive and destructive interference between the ejection and backscattering waves cause maxima and minima in the spectra to occur. These oscillations

can be interpreted by using the EXAFS equation (Equation 2.10), in conjunction with a known molecular model for the sample, to give an understanding of the scattering distances and thus evaluate interatomic distance.<sup>162</sup>

$$\chi(k) = \sum_j \frac{N_j f_j(k) e^{-2k^2 \sigma_j^2}}{k R_j^2} \sin[2k R_j + \delta(k)] \quad (2.10)$$

$f(k)$  and  $\delta(k)$  are scattering properties of the backscattering atom,  $N$  is the number of backscattering atoms,  $R$  is the distance between the excited atom and the backscattering atom, and  $\sigma^2$  is the disorder of the distance between the excited atom and the backscattering atom. The  $f(k)$  and  $\delta(k)$  parameters can be calculated using the FEFF program (the mathematics of these calculations are beyond the scope of this Thesis).<sup>163,164</sup> By fitting collected EXAFS data to the EXAFS equation, the distance from the absorber to the scatterer can be calculated and allow the assessment of the structure on a local level. The Fourier transform of the EXAFS region (Figure 2.4 a) can also be plotted to visualise the absorber-scatterer distances in real space ( $|\chi(R)|$ ).

XAS analyses were performed on the B18 Core EXAFS beamline at STFC Diamond Light Source in Didcot, United Kingdom and on the BM28 beamline at ESRF in Grenoble, France. The data were interpreted using Athena (XANES and normalisation) and Artemis (EXAFS).<sup>165</sup>

### 2.12.1 Preparation of *ex situ* samples

*Ex situ* samples and standards were prepared by mixing the materials with a cellulose binder and pressing into pellets 1.3 cm diameter, with varying thicknesses depending on the concentration of material. The concentration of each material was calculated using the Beer-Lambert law to ensure enough X-ray radiation could be transmitted through the sample for a sufficient resolution to be obtained.

### 2.12.2 Preparation of *in situ* AMPIX cells

A 150 mg mixture was prepared of 20 % VO<sub>2</sub> (B)\_ST or VO<sub>2</sub> (B)\_μλ\_3h (30 mg), 20 % PTFE binder (30 mg), 30 % graphite powder (45 mg) and 30 % Vulcan XC72 carbon black (Cabot). The mixture was then ground in a pestle and mortar thoroughly before pressing

into 25 mg pellets. The pellets were transferred to a plastic housing with X-ray transparent glassy carbon window/current collector supplied by Argonne National Laboratory.<sup>166</sup> The electrochemical cells were constructed by adding consecutive layers of Celgard™, Kapton™ sponge soaked with electrolyte (LiPF<sub>6</sub> in a 1:1, v:v, ratio of ethylene carbonate and dimethyl carbonate), a second Celgard™ separator and a Li<sup>+</sup> metal disc as the anode (Figure 2.5). The cells were discharged using a Biologic VSP multi-channel potentiostat and *in situ* XAS was performed at the ESRF BM23 beamline in Grenoble, France.

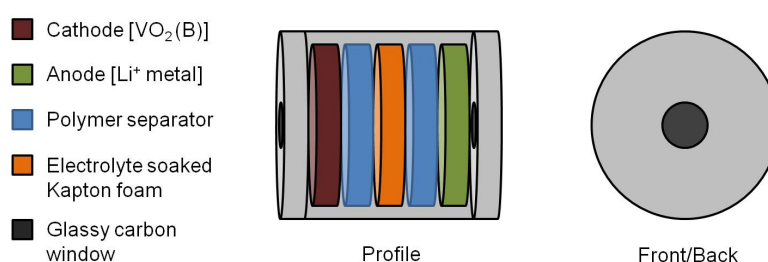


**Figure 2.5:** Schematic showing the construction of electrochemical cells for *in situ* X-ray absorption spectroscopy (XAS).

## 2.13 Muon spin relaxation

Muons are subatomic particles with  $S = \frac{1}{2}$  with an average lifetime of 2.2  $\mu\text{s}$  and a large gyromagnetic ratio ( $\gamma/2\pi = 135.5 \text{ MHz T}^{-1}$ ).<sup>167,168</sup> In muon spin relaxation positive muons are selectively filtered, polarised and directed towards a sample using focusing quadrupole magnets ensuring a muon's spin is always anti-parallel to its momentum upon implantation. Upon implantation  $\mu^+$  rest in the electron cloud of  $\text{O}^{2-}$  and form a stable bond.<sup>169</sup> The  $\mu^+$  then attempts to align with, and precess around any local magnetic moments (depolarisation) at a rate proportional to the field strength ( $B$ ) and projects a beam of positron emission in the direction of spin. A good analogy for this is a lighthouse emitting a beam of light as it rotates.<sup>170</sup> The stronger the local contribution, the faster the muon will become depolarised.

When a muon decays it releases a positron preferentially in the direction of its spin, and this decay positron is detected by a front or back bay of detectors (depending on the orientation of the muon upon decay). In a sample where there are no electronic or nuclear contributions, the muon decay will occur preferentially towards the back detector. However,

if the muon experiences local nuclear fields, depolarisation occurs and positrons can decay towards the back detector.

This process can be assessed by looking at the asymmetry of positron detection, i.e. the difference in the muons detected in the front and back detectors, showing that as time increases a relaxation occurs in the asymmetry due to increasing depolarisation of the muon. When a muon is implanted into a material that exhibits Li<sup>+</sup> diffusion, the nuclear interaction of a Li<sup>+</sup> ion moving past a muon is sufficient to produce perturbations in the muon decay. At a given temperature, diffusion should occur at a constant rate, and motivate a proportional fluctuation rate ( $\nu$ ) in the muon decay. The diffusion process can be modelled by applying a dynamic function to the observed relaxation data. One example of these is shown in equation 2.11 where by  $A_F \exp(-\lambda_F t)$  describes the contribution from nuclear magnetic spins on the muon relaxation,  $A_{KT} \exp(-\lambda_{KT} t) \times G^{DGKT}(\delta, \nu, t, H_{LF})$  is the modified Kubo-Toyabe function used to describe the dynamic diffusion processes and  $A_{BG}$  is a constant background component.<sup>171</sup>

$$A_0 P_{LF}(t) = A_F \exp(-\lambda_F t) + A_{KT} \exp(-\lambda_{KT} t) \times G^{DGKT}(\Delta, \nu, t, H_{LF}) + A_{BG} \quad (2.11)$$

An alternative equation to the Kubo-Toyabe to describe this behaviour is the Keren function, a modified analytical version of the Abragam function (equation 2.12).<sup>172</sup>

$$P_z(t) = \exp[-\Gamma(\Delta, \nu, \omega_L, t)] \times \exp(-\lambda t) \quad (2.12)$$

Both of the described functions allow the retrieval of two important parameters; the fluctuation rate ( $\nu$ ) is a measure of the perturbation frequency of the muon precession and thus the rate of diffusion. The field distribution width at the muon stopping site ( $\Delta$ ) allows us to confirm that it is not a change in the magnetic environment with temperature which is affecting the behaviour of the fluctuation rate and so should be a relative constant, although experimentally it has been found that a slight decrease is observed. This decrease can be assigned to a motional narrowing effect where the muons themselves become mobile at higher temperatures.<sup>71</sup> Since the fluctuation rate is proportional to the rate of Li<sup>+</sup> diffusion, it can then be linked to the diffusion pathlength in a material to calculate the Li<sup>+</sup> diffusion coefficient of a given material ( $D_{Li}$ ). Furthermore, as Li<sup>+</sup> diffusion is a thermally activated

process,  $D_{\text{Li}}$  will increase with temperature, given that no detrimental structural changes occur upon heating. The values of  $D_{\text{Li}}$  can then be used in an Arrhenius equation to calculate the  $E_a$  of a  $\text{Li}^+$  atom hopping from one interstitial site to the next.

To accurately determine the nuclear contribution from  $\text{Li}^+$  on the muon decay, however, the nuclear contributions from magnetic atoms in the sample must be eliminated or dampened. This can be achieved by applying a longitudinal field ( $B_{\text{LF}}$ ) in the direction of the muons implantation, anti-parallel to the spin direction. If  $B_{\text{LF}}$  is larger than the nuclear magnetic moment of the magnetic atoms, the muons spin will only be altered by the diffusion of  $\text{Li}^+$  (decoupling).

### **2.13.1 Preparation of $\mu\text{SR}$ samples**

Samples were packed into titanium sample holders with a 30 mm diameter circular recess, 3 mm deep. This was covered by a titanium foil secured with a titanium bezel. The sample holder was placed into the spectrometer which was sealed and placed under a vacuum. Experiments were conducted between 100 K and 400 K in 20 K increments, decreasing the steps to 10 K over the thermally activated region of  $\text{Li}^+$  diffusion. All experiments were conducted on the EMU beamline at the STFC ISIS Muon and Neutron Facility, Didcot, UK.

## Chapter 3: Microwave-assisted polyol and ionothermal synthesis of $\text{LiFePO}_4$ polymorphs

### 3.1 Introduction

$\alpha\text{-LiFePO}_4$  is one of the most promising developments in positive insertion electrodes for Li-ion batteries to date. Broadly speaking  $\alpha\text{-LiFePO}_4$  is industrially attractive since it is environmentally benign and capitalises on the most abundant redox metal in the Earth's crust, iron, making it cost-effective. Additionally  $\alpha\text{-LiFePO}_4$  also possesses a stable operating voltage (versus  $\text{Li/Li}^+$ ) of 3.45 V and a modest theoretical capacity of  $170 \text{ mAh g}^{-1}$  suitable for commercial applications.<sup>19</sup>

As with many other insertion electrodes, the theoretical capacity is rarely achieved especially at high charge and discharge rates required for commercial applications.<sup>173</sup> For  $\alpha\text{-LiFePO}_4$ , this is especially an issue due to the 1D diffusion pathways, and poor electronic conductivity.<sup>20,21</sup> However, improving and maximising the observed capacity in Li-ion battery materials is the focus of much scientific interest. One way of improving the electrochemical behaviour is nanostructuring of the  $\alpha\text{-LiFePO}_4$  particles. Previous reports have shown that an improvement in electrochemical properties can be directly linked to smaller particle size due to shorter  $\text{Li}^+$  diffusion pathways.<sup>174</sup>

To obtain nanostructured  $\alpha\text{-LiFePO}_4$  new routes must be developed as conventional solid-state techniques yield bulk materials with large particles. Solvothermal synthesis has previously been employed to obtain nanostructured materials however these methods typically require extended heating times between 10 h and 48 h.<sup>175,176</sup> An alternative methodology is microwave-assisted synthesis which has been successfully employed as a rapid route to nanostructured materials in as little as 3 h to 3 min.<sup>148,151,155</sup>

In this Chapter, microwave heating properties of polyol and ionic media for their use in microwave-assisted synthesis are evaluated. Synthetic routes have been developed to obtain nanostructured phase pure  $\alpha\text{-LiFePO}_4$  in both polyol and ionic media and products have been investigated with PXRD and SEM. Effects of polymorphism on the  $\text{Li}^+$  diffusion in nanostructured  $\beta\text{-LiFePO}_4$  on a local level have also been investigated by  $\mu\text{SR}$ . Finally, the

electronic and structural changes which occur in  $\alpha\text{-LiFePO}_4$  as it undergoes a charge cycle have been probed by *in situ* XANES and EXAFS analyses.

### 3.2 Microwave spectroscopy of polar and ionic liquids

The ability of a solvent to absorb microwave irradiation and convert it heat is highly dependent on the frequency ( $\nu$ ) of microwave irradiation employed. Typical commercial microwave appliances and synthesisers (such as the CEM Discover SP) operate at  $\nu$  of 2.45 GHz, a frequency that efficiently heats water. However water cannot be used in microwave-assisted approaches to obtain  $\alpha\text{-LiFePO}_4$  as it leads to the formation of iron oxides. Therefore alternative media that can efficiently absorb microwaves at 2.45 GHz have been sought. The two types of media investigated here are polyols and ionic liquids. Furthermore their potential as reducing media is important to retain a  $\text{Fe}^{2+}$  oxidation state necessary in  $\alpha\text{-LiFePO}_4$ .

To get a better understanding of their potential to absorb microwave irradiation microwave spectroscopy studies of the polyol EG and ionic liquid 1-ethyl-3-methylimidazolium trifluoromethanesulfonate (EMIM-TFMS) were conducted. Measurements were taken in a frequency range of 0.01 GHz to 10 GHz using a broadband coaxial probe connected to a microwave network analyser (N5232A PNA-L, Agilent Technologies). All measurements were taken at a constant temperature of 27.5 °C. Figure 3.1 (a) shows the real permittivity ( $\epsilon'$ ), also known as the dielectric constant, of the EG and EMIM-TFMS as a function of frequency. The value of  $\epsilon'$  describes how efficiently the molecules in either solvent are polarised by the electric field of the microwave irradiation. It is observed that as the microwave frequency increases, there is a decrease in  $\epsilon'$  for both solvents. This is expected as an increase in frequency means the molecules have less time to re-orientate in the electric field of the incoming microwave irradiation. It is also observed that EG is much more easily polarised by the microwave irradiation ( $\epsilon' = 16.0 \pm 0.2$ ) than the ionic liquid ( $\epsilon' = 11.6 \pm 0.1$ ) at the proposed synthetic frequency of 2.45 GHz (see dotted line in plot).

Figure 3.1 (b) shows calculated values for the imaginary permittivity  $\epsilon''$ . The value of  $\epsilon''$  is a measure of how efficient the solvent is at converting the absorbed microwave radiation into heat. It is observed that EG exhibits an initial increase in  $\epsilon''$  up to a frequency of 1.5 GHz, after which it slowly declines. In contrast, a continual decrease in  $\epsilon''$  is observed for EMIM-

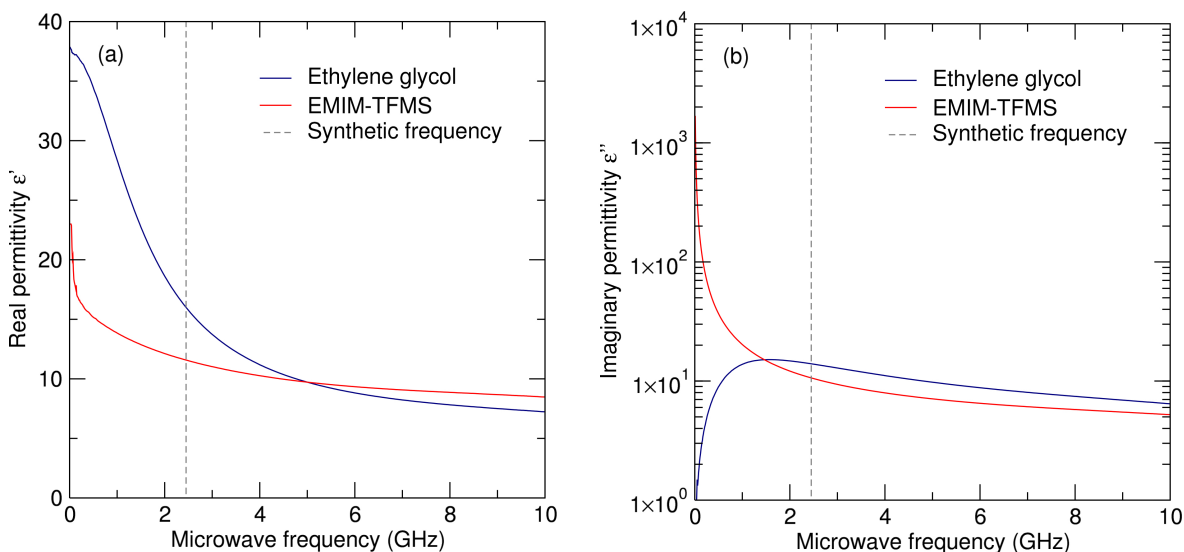


**Figure 3.1:** Microwave spectroscopy of polyol (ethylene glycol) and ionic (EMIM-TFMS) media. The real (a) and imaginary (b) permittivities describe the microwave absorbance and the incoming radiation to heat energy conversion respectively. The dashed line indicates the synthetic frequency of 2.45 GHz.

TFMS. At the proposed synthetic frequency of 2.45 GHz, EG exhibits a modestly higher  $\epsilon''$  ( $14.0 \pm 0.1$ ) than EMIM-TFMS ( $10.6 \pm 0.1$ ).

The values of  $\epsilon'$  and  $\epsilon''$  at 2.45 GHz can be used to assess the overall efficiency of microwave-to-heat conversion in the solvents by calculating the loss tangent ( $\tan\delta$ ) using Equation 3.1 where a larger value indicates higher efficiency.

$$\tan\delta = \frac{\epsilon''}{\epsilon'} \quad (3.1)$$

The value  $\tan\delta$  is calculated as 0.725 for EG and 0.757 for EMIM-TFMS indicating that EMIM-TFMS is slightly more efficient. Furthermore the calculated values of  $\tan\delta$  for EG and EMIM-TFMS are much higher than those previously observed for water (0.123). The large values of  $\tan\delta$  present EG and EMIM-TFMS as good candidates to drive the reaction temperatures required for synthesis of  $\alpha\text{-LiFePO}_4$ .

### 3.3 Microwave-assisted preparation of $\text{LiFePO}_4$ in polyol media

To determine the best polyol candidate for synthesis of *Pnma*  $\alpha$ -structured  $\text{LiFePO}_4$ , three polyol solvents ethylene glycol (EG), diethylene glycol (DEG) and tetraethylene glycol (TEG) were examined. Their polar nature and relatively high boiling points (197 °C, 244 °C and 314 °C, respectively) make them ideal candidates as synthesis media.

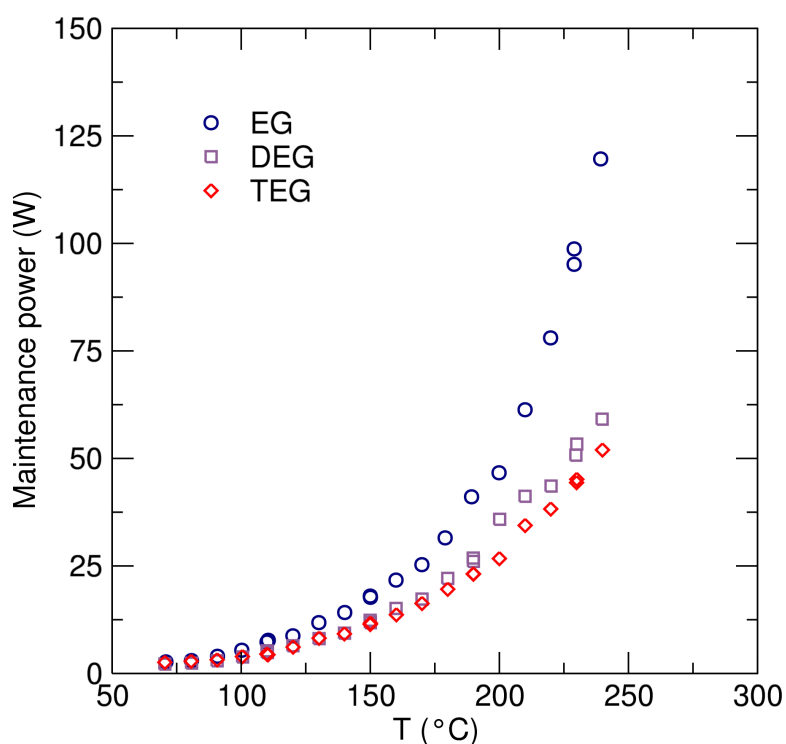


**Figure 3.2:** Average power consumption of EG, DEG and TEG heated by microwave irradiation. Exponential relationships are observed in all cases with lower maintenance power observed as polyol chain length increases.

For an efficient microwave-assisted synthetic process it is paramount that the power required to heat the reaction is as low as possible. The previous Section has demonstrated that the microwave heating properties are highly sensitive to the choice of solvent and  $\nu$  of microwave radiation supplied. To further this investigation, experiments were conducted to investigate the microwave heating properties of the polyol solvents in the synthetic environment using a Discover SP microwave synthesizer ( $\nu = 2.45$  GHz). 4 ml of either EG, DEG or TEG was placed into a 10 ml microwave vessel and irradiated with microwaves until a

temperature of 70 °C was reached. Once the solvent had reached 70 °C the power of microwave irradiation was allowed to vary to maintain a temperature of 70 °C. The temperature was held for 2 min and the average power applied by the microwave was calculated. This was repeated in 10 °C steps up to 250 °C in 10 °C increments. The recorded averages for power consumption of the solvents as a function of temperature are given in Figure 3.2.

All three solvents exhibit an exponential relationship between the temperature and the power required to maintain the temperature. The data for EG, DEG and TEG were fit with simple exponential equations ( $y = ae^{bx}$ ) and the values are presented Table 3.1. It has previously been observed that the  $\tan\delta$  value of polyols decrease as temperature increases.<sup>177</sup> This leads to a loss of microwave-to-heat conversion efficiency with increasing temperature which explains the increase in energy required to heat the solvent with increasing temperature. The fundamental reason for this behaviour has previously been reported as an increase in the rotation correlation time of the Debye relaxation of the solvent with increasing temperature.<sup>114,178</sup> This means that the time taken for a molecule to reorient itself to align with incoming microwave irradiation becomes less complementary to the frequency of microwave irradiation, causing a lag between molecular polarisation.

It is also observed that as the molecular weight of the polyol increases, the power of 2.45 GHz microwave irradiation required decreases. This relationship is consistent at all temperatures. It is observed that the higher the molecular weight of the material the lower the exponent, or lower gradient of the increase in power observed. This indicates that as the chain lengths of the polyol increases it becomes more efficient at converting microwave irradiation into heat.

Solvent	Exponent	Pre-exponential	R <sup>2</sup>
Ethylene glycol	0.0244	0.5824	0.997
Diethylene glycol	0.0201	0.5498	0.993
Tetraethylene glycol	0.0185	0.6596	0.994

**Table 3.1:** Values of the exponential fits to maintenance power studies in Figure 3.2.

The consistent relationship between longer chain length in the polyols and decreased power required to heat the solvent could be explained by the extensive hydrogen bonding

observed in polyols.<sup>179</sup> A microwave irradiation study of EG shows that when hydrogen bonding is disrupted by addition of DMSO, the molecules are able to couple and orientate more strongly with microwave irradiation, and show an increased ability to convert radiation to heat.<sup>180</sup> There is less hydrogen bonding in DEG, and even less in TEG due to less hydroxyl groups per unit volume. This allows longer chained polyols to orientate more freely in the electric field and heat the system more efficiently.

### 3.3.1 Synthesis and characterisation of $\alpha\text{-LiFePO}_4$ in polyol media

Syntheses were performed in each of the three polyol media using 4 ml of either EG, DEG or TEG in a 10 ml microwave vessel and a stoichiometric mixture of 1 mmol  $\text{FeC}_2\text{O}_4 \cdot 2\text{H}_2\text{O}$  and 1 mmol  $\text{LiH}_2\text{PO}_4$  irradiated with microwave-irradiation ( $\nu = 2.45\text{ GHz}$ ) for 3 hours at  $220\text{ }^\circ\text{C}$ . All three reactions yielded fine light green powders which were characterised using PXRD (Figure 3.3).

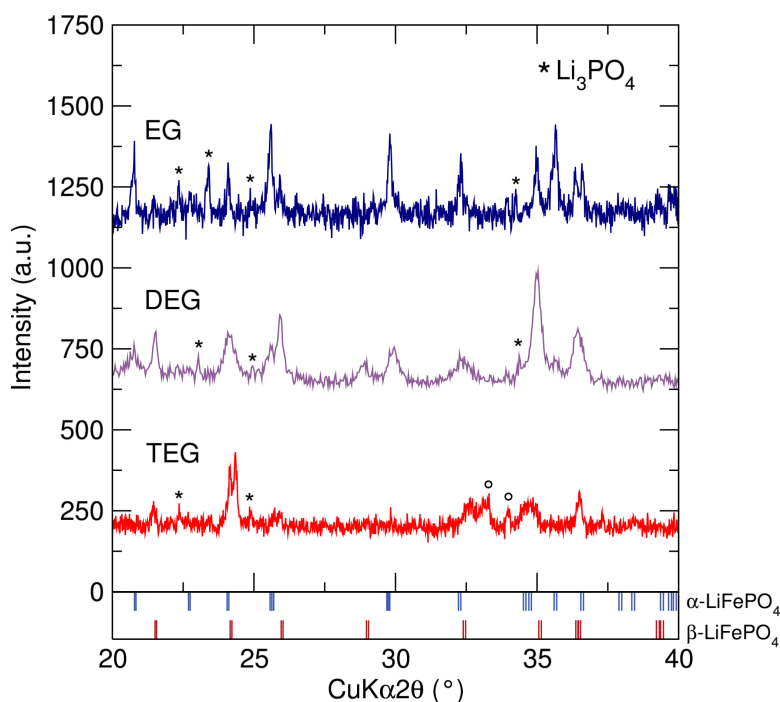


**Figure 3.3:** PXRD patterns of syntheses conducted in EG, DEG and TEG at  $220\text{ }^\circ\text{C}$  for 3 hours. Mixed phases of  $Pnma$  ( $\alpha$ , Reference 31) and  $Cmcm$  ( $\beta$ , Reference 181) structured  $\text{LiFePO}_4$  are observed with impurities of  $\text{Li}_3\text{PO}_4$  (\*) and an unidentified impurity phase (°).

The reaction carried out in EG produced a mixed phase of  $\alpha\text{-LiFePO}_4$ ,  $\beta\text{-LiFePO}_4$  and

$\text{Li}_3\text{PO}_4$  (\*). It has recently been brought to light that the  $\beta$ -phase can appear in reactions at low temperatures and pressures by liquid phase and microwave-assisted solvothermal routes and is thought to be near electrochemically inert<sup>182,183</sup>. The DEG reaction produced similar results, but with more intense peaks from  $\beta$ - $\text{LiFePO}_4$ . The reaction carried out in TEG appears to be a mixture of  $\beta$ - $\text{LiFePO}_4$ ,  $\text{Li}_3\text{PO}_4$  (\*) and an unidentified phase ( $^\circ$ ). Although no single phase product was obtained from these syntheses, they highlight EG as the best potential candidate for further synthetic investigation.

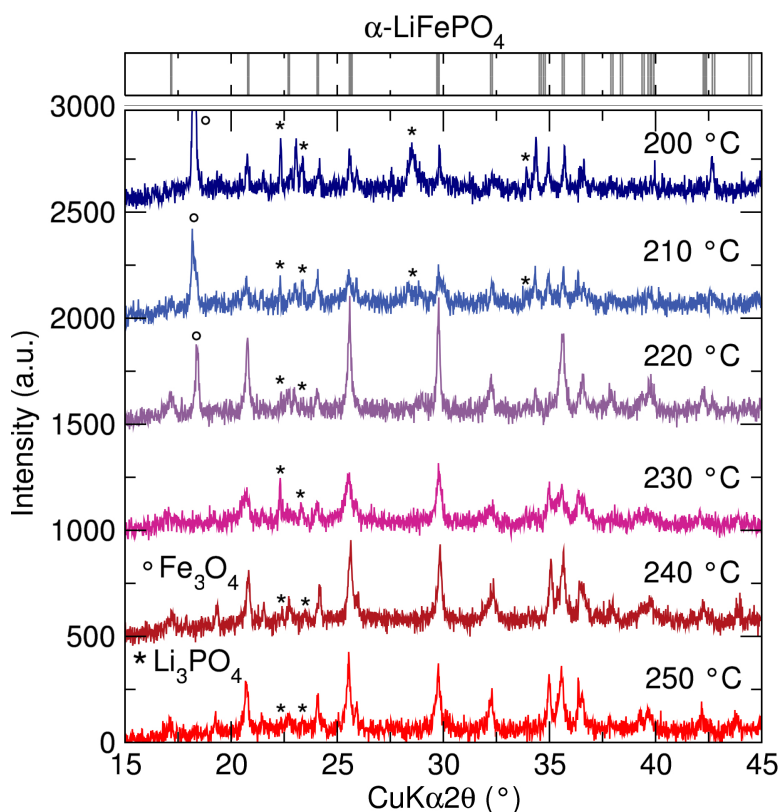


**Figure 3.4:** XRD of products prepared by a microwave-assisted route in ethylene glycol for 1 h. Peak positions for  $Pnma$  structured  $\alpha$ - $\text{LiFePO}_4$  are shown at the top of the data taken from Reference 31.

### 3.3.2 Synthesis and characterisation of $\alpha$ - $\text{LiFePO}_4$ in ethylene glycol

To further probe the use of EG as a potential solvent candidate for the synthesis of  $\alpha$ - $\text{LiFePO}_4$ , a systematic study from 200 °C to 250 °C in 10 °C increments was performed with 1 h of microwave irradiation ( $\nu = 2.45$  GHz). Syntheses at all temperatures yielded a

fine light green powder after drying which were interrogated using PXRD (Figure 3.4).

It is observed that phase pure  $\alpha\text{-LiFePO}_4$  was not obtained at any temperature after 1 h of irradiation. Impurity phases of  $\beta\text{-LiFePO}_4$  and  $\text{Li}_3\text{PO}_4$  (\*) were present. Previous studies have also found  $\text{Li}_3\text{PO}_4$  as an impurity phase when attempting to synthesise  $\alpha\text{-LiFePO}_4$  by solvothermal methods.<sup>184</sup> It is essential to obtain  $\alpha\text{-LiFePO}_4$  free of  $\text{Li}_3\text{PO}_4$  as the impurity acts as inert mass in electrochemical cells, lowering the electrochemical capacity.<sup>185,186</sup> Below 230 °C, an impurity of  $\text{Fe}_3\text{O}_4$  (°) was also present.

Syntheses were then conducted under 3 h of microwave irradiation. Syntheses again yielded pale green powders which were analysed by PXRD (Figure 3.5).

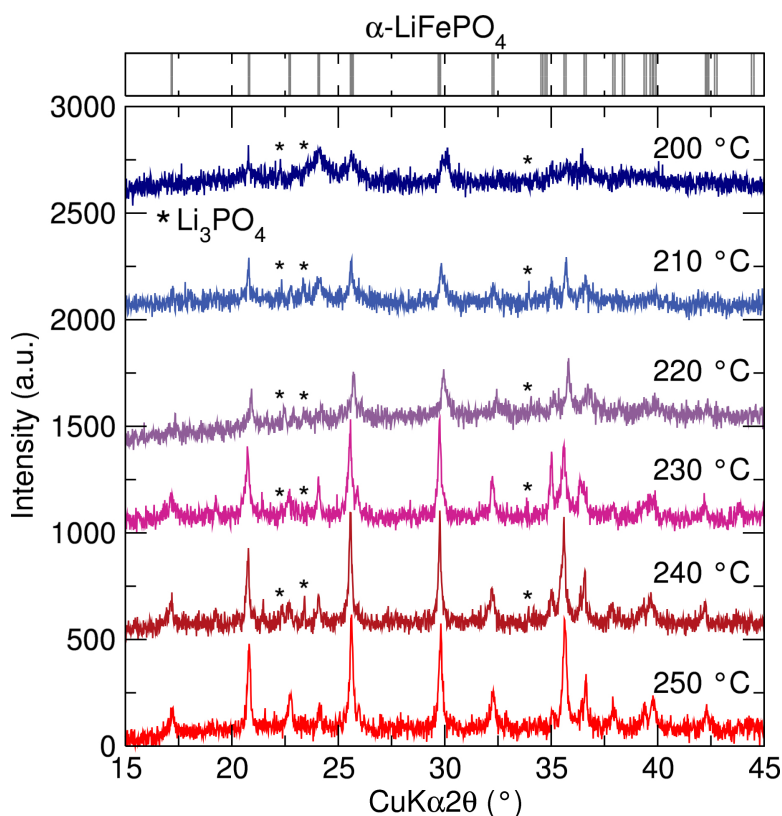


**Figure 3.5:** PXRD of products prepared by a microwave-assisted route in ethylene glycol for 3 h. Peak positions for  $Pnma$  structured  $\alpha\text{-LiFePO}_4$  are shown at the top of the data taken from Reference 31.

It is observed that phase pure  $\alpha\text{-LiFePO}_4$  is not achievable at 3 h of microwave irradiation with both  $\beta\text{-LiFePO}_4$  and  $\text{Li}_3\text{PO}_4$  (\*) present at all temperatures. At 250 °C, the PXRD pattern reveals a small peak at approximately 35 ° $2\theta$  attributable to  $\beta\text{-LiFePO}_4$ .<sup>181</sup> At these

extended times there is no indication of an  $\text{Fe}_3\text{O}_4$  impurity at lower temperatures as with the 1 h irradiation. Increasing the temperature during the 3 h irradiation promotes narrowing of the diffraction peaks implying a higher degree of crystallinity. Overall the peaks observed after 3 h are more intense than those observed after 1 h of irradiation.

PXRD of the products after 5 h of microwave irradiation (Figure 3.6) reveals that phase pure  $\alpha\text{-LiFePO}_4$  is only obtained at 250 °C. The intensity peaks from  $\text{Li}_3\text{PO}_4$  impurities are less intense than in the 3 h suggesting an advance towards phase purity of  $\alpha\text{-LiFePO}_4$  with increasing time.

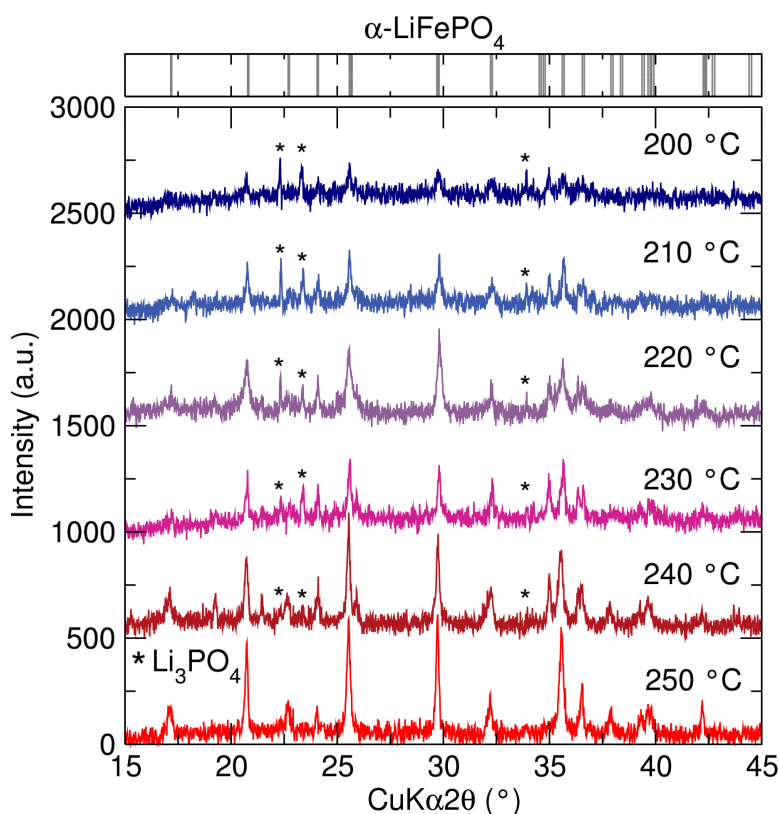


**Figure 3.6:** PXRD of products prepared by a microwave-assisted route in ethylene glycol for 5 h. Peak positions for  $Pnma$  structured  $\alpha\text{-LiFePO}_4$  are shown at the top of the data taken from Reference 31.

The overall trend that the presence of  $\text{Li}_3\text{PO}_4$  is reduced at longer times and higher temperatures. Rietveld refinement of the sample prepared at 250 °C over 5 h of microwave irradiation (EG\_LFP\_250) shows a good match to phase pure  $Pnma$  structured  $\alpha\text{-LiFePO}_4$  taken from the literature with no impurities (Figure 3.7).<sup>31</sup> Calculated parameters from the

Rietveld refinement are given in Table 3.2. SEM shows the particles have a large distribution of sizes, typically between 200 nm and 300 nm in diameter.

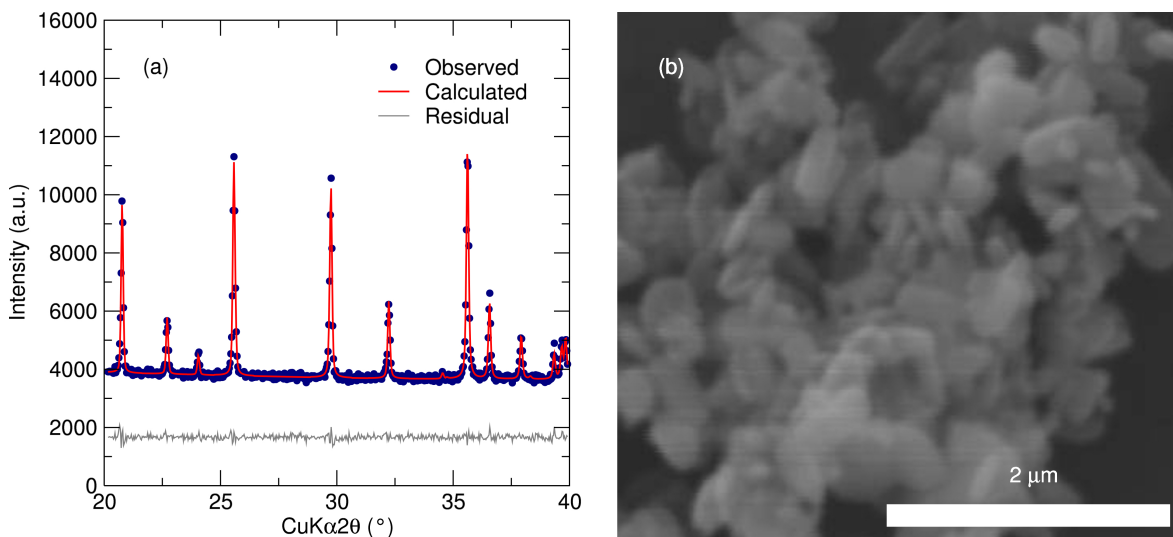


**Figure 3.7:** (a) Rietveld refinement of EG\_LFP\_250  $Pnma$  structured  $\alpha$ -LiFePO<sub>4</sub> (Reference pattern taken from Reference 31). Calculated Rietveld parameters for EG\_LFP\_250 are shown in Table 3.2. (b) SEM of  $\alpha$ -LiFePO<sub>4</sub> exhibiting a large size distribution with particles typically between 200 nm and 300 nm in diameter.

<b>Space group</b>	<i>Pnma</i>				
<b>a (Å)</b>	10.321(4)	<b>U</b>	0.10(8)	<b>Atom</b>	<b>x</b>
<b>b (Å)</b>	6.001(2)	<b>V</b>	-0.03(4)	<b>Li</b>	0
<b>c (Å)</b>	4.694(2)	<b>W</b>	0.014(1)	<b>Fe</b>	0.283(1)
<b>Zero</b>	0.067170	<b>R<sub>p</sub></b>	20.9 %	<b>P</b>	0.097(1)
<b>Displacement</b>	-0.000020	<b>R<sub>wp</sub></b>	11.7 %	<b>O1</b>	0.101(3)
<b>Scale</b>	0.001994	<b>R<sub>exp</sub></b>	8.95 %	<b>O2</b>	0.451(4)
		<b>χ<sup>2</sup></b>	1.70	<b>O3</b>	0.167(4)
					<b>y</b>
					0
					<b>z</b>
					0
					0.972(2)
					0.424(4)
					0.746(6)
					0.212(3)
					0.272(3)

**Table 3.2:** Calculated Rietveld refinement parameters from the PXRD patterns of α-LiFePO<sub>4</sub> prepared in EG at 250 °C for 5 h.

### 3.4 Heat treatment of $\beta\text{-LiFePO}_4$ to produce phase pure $\alpha\text{-LiFePO}_4$

Heat treatment of mixed phase  $\alpha/\beta\text{-LiFePO}_4$  was investigated as a route to obtaining phase pure  $\alpha\text{-LiFePO}_4$ . Niederberger and co-workers have previously established that  $\beta\text{-LiFePO}_4$  undergoes a phase transition to  $\alpha\text{-LiFePO}_4$  at 475 °C under  $\text{N}_2$  but also observed an impurity phase of  $\text{Fe}_2\text{P}_2\text{O}_7$ .<sup>183</sup> Figure 3.8 shows the mixed phase  $\alpha/\beta\text{-LiFePO}_4$  sample (prepared after 3 h of irradiation at 220 °C) after heating at 600 °C in Ar for 2 hours. It is observed that the material converts from a mixed phase  $\alpha/\beta$  to  $\alpha\text{-LiFePO}_4$  with a small unidentified impurity (\*).

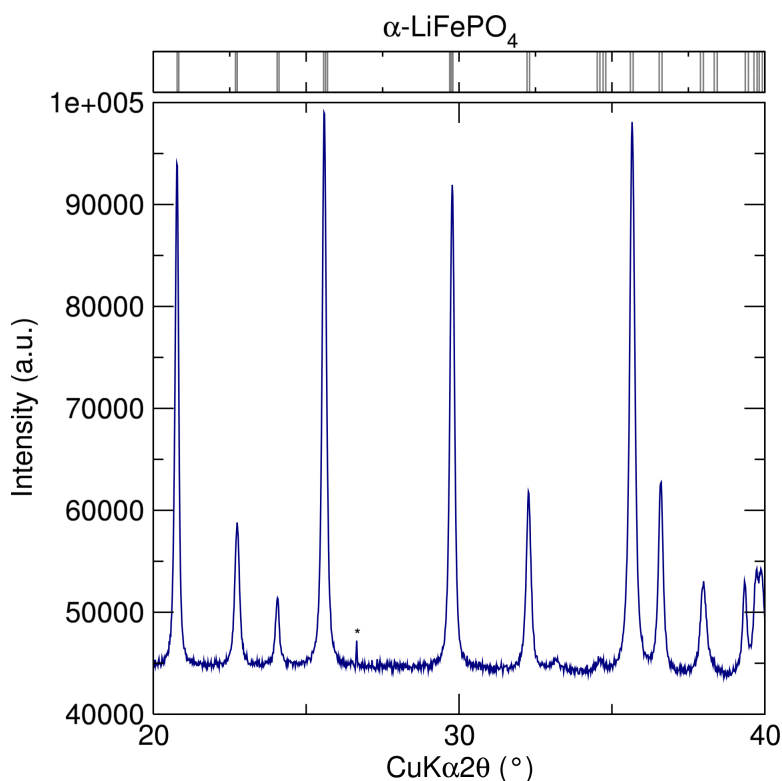


**Figure 3.8:** PXRD pattern of a mixed  $\alpha/\beta\text{-LiFePO}_4$  sample heat treated in a tube furnace under an Ar atmosphere at 600 °C for 2 hours showing conversion of the  $\beta$ - to  $\alpha\text{-LiFePO}_4$  with a small unidentified impurity noted (\*).

To examine an alternative approach to solid-state heating, a second microwave treatment step was applied to the  $\alpha/\beta\text{-LiFePO}_4$  mixed phase sample. After heating the mixture for 15 min and 45 min, the sample was washed and dried then returned to the microwave for a further 15 min or 45 min. The PXRD patterns for these samples can be seen in Figure 3.9

(a) showing the presence of  $\alpha\text{-LiFePO}_4$ ,  $\beta\text{-LiFePO}_4$  and  $\text{Li}_3\text{PO}_4$  (\*) for both the 15 min and 45 min samples. After the second irradiation, (Figure 3.9 b) both samples show phase pure  $\alpha\text{-LiFePO}_4$ .

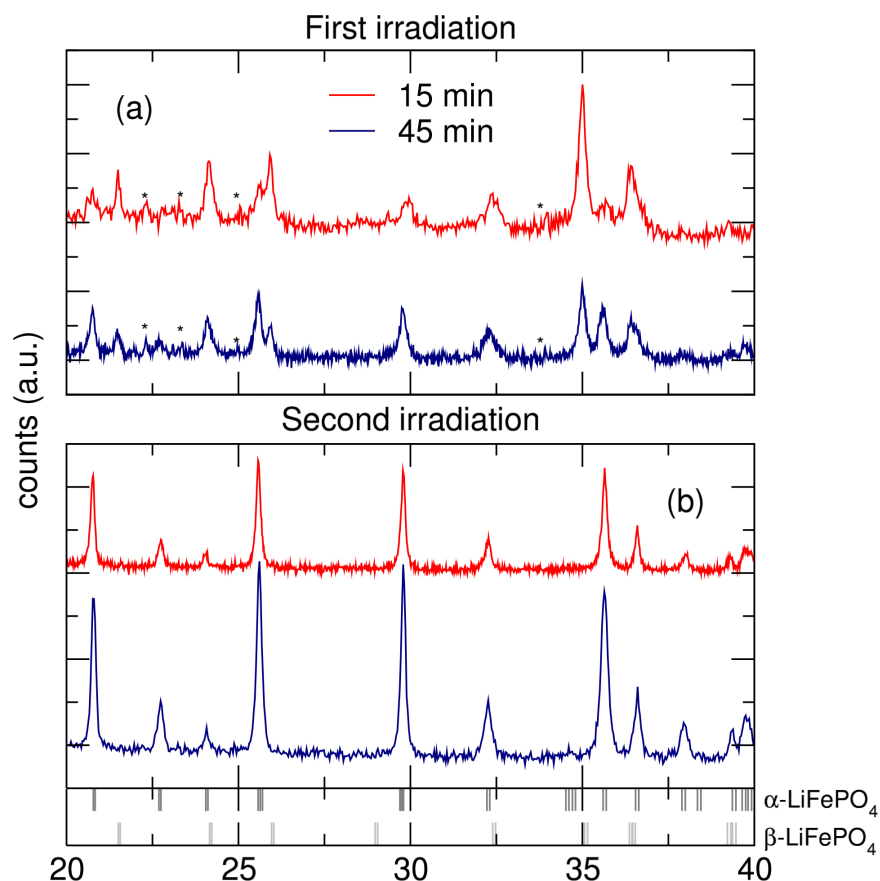


**Figure 3.9:** (a) XRD after 15 min and 45 min of microwave irradiation. (b) 15 min and 45 min samples were dried, resuspended in EG and irradiated for 15 min and 45 min further respectively yielding phase pure  $\alpha\text{-LiFePO}_4$ .

Figure 3.10 shows SEM images taken for the 15 min synthesis (a) and after a the second microwave-irradiation for 15 min (b). It is observed that the platelet morphology of the mixed  $\alpha/\beta\text{-LiFePO}_4$  sample is preserved after it is converted to pure  $\alpha\text{-LiFePO}_4$  with a thickness of 20 nm and typical diameter of 700 nm in both cases. These observations present the opportunity to use morphologies only accessible during the growth of  $\beta\text{-LiFePO}_4$  as a template for  $\alpha\text{-LiFePO}_4$  particles.

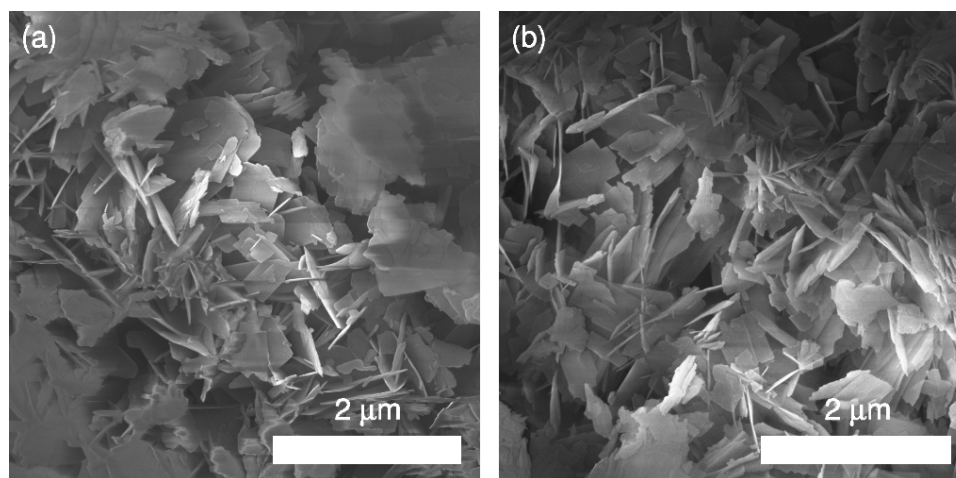


**Figure 3.10:** (a) SEM image of mixed phase  $\alpha/\beta\text{-LiFePO}_4$  prepared after 15 min of microwave irradiation of stoichiometric ratios of  $\text{FeC}_2\text{O}_4 \cdot 2\text{H}_2\text{O}$  and  $\text{LiH}_2\text{PO}_4$  in EG at  $220\text{ }^\circ\text{C}$ . (b) SEM image of the same sample after 15 min of further irradiation in EG showing that morphology is preserved after conversion to pure  $\alpha\text{-LiFePO}_4$ .

### 3.5 Microwave-assisted preparation of $\alpha\text{-LiFePO}_4$ in ionic liquid

Similarly to the polyols, two ionic liquids (ILs) 1-ethyl-3-methylimidazolium trifluoromethanesulfonate (EMIM-TFMS) and 1-ethyl-3-methylimidazolium bis(trifluorosulfonyl)imide (EMIM-TFSI) were investigated (Figure 3.11) as both are also excellent mediators of microwave heating. Furthermore, EMIM-TFSI has previously shown promise as a reaction medium for the synthesis of  $\alpha\text{-LiFePO}_4$  in conventional solvothermal routes at  $250\text{ }^\circ\text{C}$  for 24 h.<sup>187</sup> At shorter times however, impurity phases of  $\text{Fe}_3\text{O}_4$  and  $\text{Li}_3\text{PO}_4$  were observed.

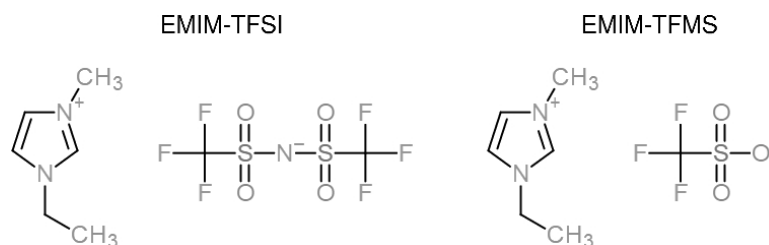


**Figure 3.11:** Chemical structure of the two ionic liquids investigated for microwave-assisted ionothermal synthesis of  $\alpha\text{-LiFePO}_4$ .

The microwave heating properties were characterised by irradiating 4 ml of each solvent

with microwave irradiation ( $\nu = 2.45$  GHz) in the CEM Discover SP synthesiser until temperatures between  $70$  °C and  $250$  °C were achieved in  $10$  °C increments. The power required to maintain a given temperature was recorded and averaged over 2 min (Figure 3.12 a). An exponential relationship is observed between the maintenance power and temperature similar to that of the polyol investigations. However, the values of the maintenance power for both IL's are an order of magnitude lower (12 W) than EG (121 W) at the highest temperature of  $250$  °C, and significantly lower than those for DEG (60 W) and TEG (52 W). This behaviour can be explained by ionic conduction heating mechanism exhibited by IL's being a much more effective than the dipole-polarisation in polyols. It is noted that there is no discernible difference in the power consumption of the two IL's.

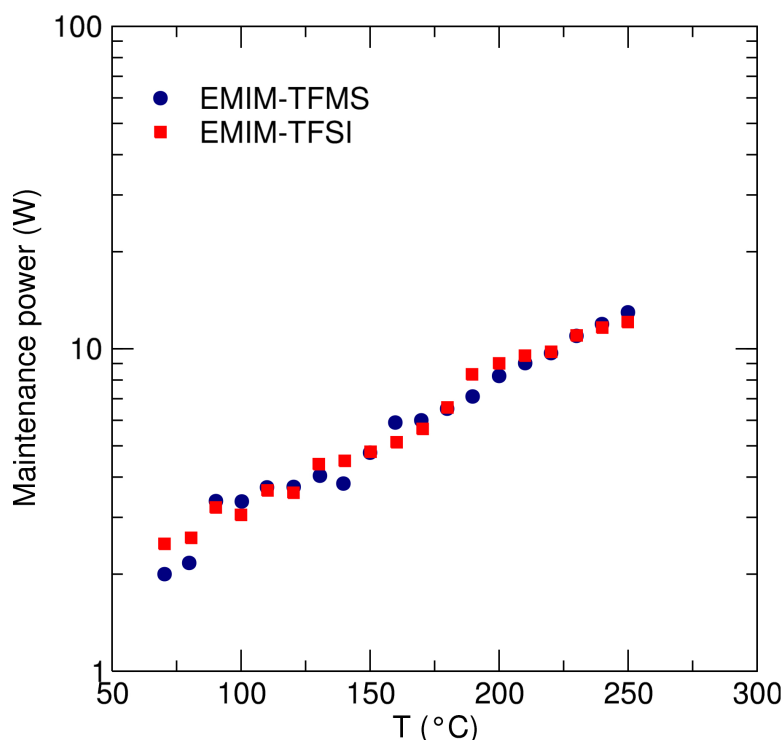


**Figure 3.12:** Power consumption of two ionic liquids, EMIM-TFMS (blue) and EMIM-TFSI (red). The exponential relationship between temperature, and power consumption is almost identical in both cases.

$\alpha$ - $\text{LiFePO}_4$  was prepared using 4 ml of either EMIM-TFMS or EMIM-TFSI in a 10 ml microwave reaction vessel and a stoichiometric amount of  $\text{FeC}_2\text{O}_4 \cdot 2\text{H}_2\text{O}$  (1 mmol) and  $\text{LiH}_2\text{PO}_4$  (1 mmol). The mixtures were irradiated with microwaves ( $\nu = 2.45$  GHz) for 3 h

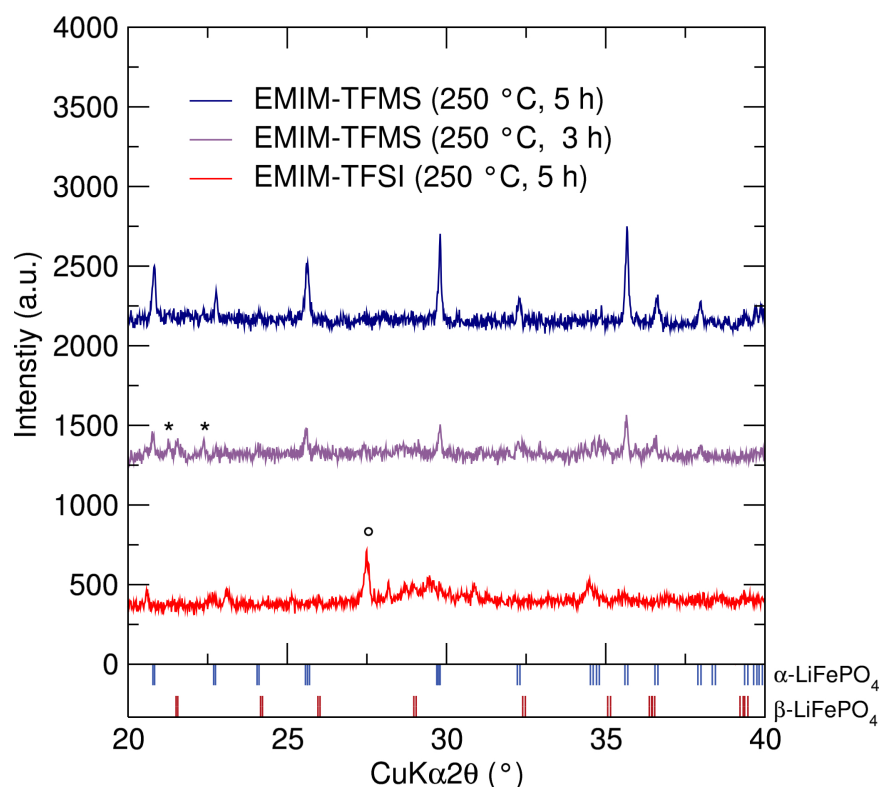


**Figure 3.13:** PXRD patterns for irradiation of a stoichiometric mixture of  $\text{FeC}_2\text{O}_4 \cdot 2\text{H}_2\text{O}$  and  $\text{LiH}_2\text{PO}_4$  in either EMIM-TFMS or EMIM-TFSI, including impurity phases of  $\text{Li}_3\text{PO}_4$  and  $\text{Fe}_2\text{PO}_5$ . Reference patterns are taken from Reference 31 and 181 for  $\alpha$ - and  $\beta$ - $\text{LiFePO}_4$  respectively.

and 5 h at 250 °C. PXRD patterns collected for the samples are presented in Figure 3.13.

It is observed that phase pure  $\alpha$ - $\text{LiFePO}_4$  can be obtained after irradiation at 250 °C for 5 h in EMIM-TFMS. Lowering the time to 3 h in EMIM-TFMS leads to the presence of a  $\text{Li}_3\text{PO}_4$  impurity (\*). Employing EMIM-TFSI at 250 °C for 5 h leads to no identifiable phase pure product with the most intense peak indexed to  $\text{P}_2\text{O}_5$  (°). This observation is contrary to previous reports on a by conventional heating methods in an autoclave employing EMIM-TFSI for 24 h at 250 °C where phase pure  $\alpha$ - $\text{LiFePO}_4$  was obtained.<sup>188</sup> It was also noted that the EMIM-TFSI had changed from colourless to dark brown after the irradiation, whereas the EMIM-TFMS remained clear, which may arise from decomposition of EMIM-TFSI under microwave heating conditions. For this reason, EMIM-TFSI was abandoned as a microwave heating solvent.

## 3.6 Preparation of $\text{LiFePO}_4$ polymorphs for local studies

### 3.6.1 Larger scale synthesis of $\text{LiFePO}_4$ polymorphs

The rate of  $\text{Li}^+$  diffusion in active electrodes underpins their electrochemical performance. To analyse the diffusion properties across a range of  $\text{LiFePO}_4$  polymorphs,  $\alpha$ - $\text{LiFePO}_4$ ,  $\beta$ - $\text{LiFePO}_4$  and mixed  $\alpha$ - $\beta$ - $\text{LiFePO}_4$  were prepared by microwave-assisted approaches. Pure  $\alpha$ - $\text{LiFePO}_4$  was prepared in a larger volume (2.45 mmol, 10 ml solvent) using the previous method with ionic liquid (EMIM-TFMS, 3 h, 250 °C). The PXRD pattern is shown in Figure 3.14.

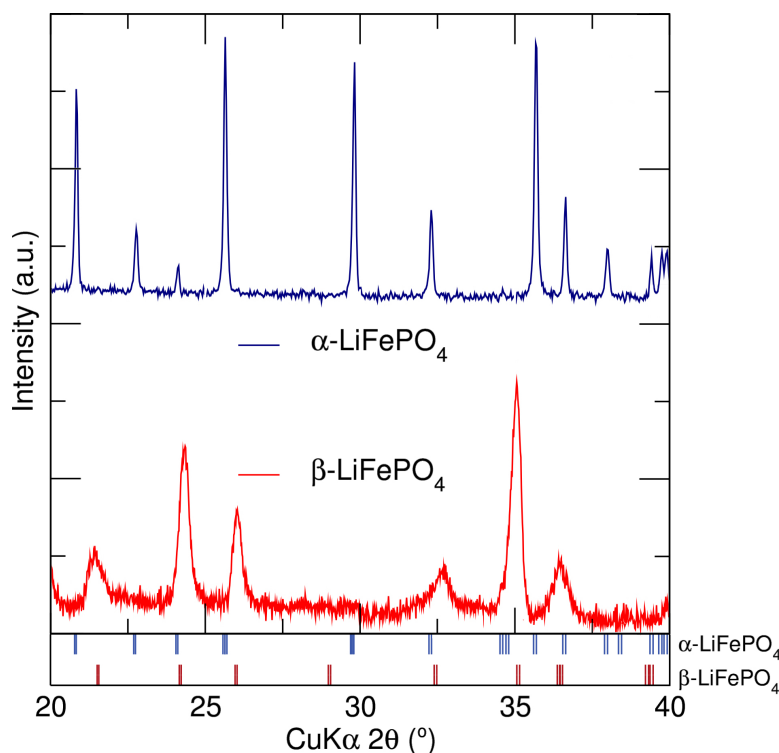


**Figure 3.14:** X-ray diffraction patterns of pure  $\alpha$ - $\text{LiFePO}_4$  and  $\beta$ - $\text{LiFePO}_4$  with Reference patterns taken from Reference 31 ( $\alpha$ ) and 181 ( $\beta$ ).

Phase pure  $\beta$ - $\text{LiFePO}_4$  was obtained by a previously reported synthesis by Niederberger and co-workers and carried out in a Ar glovebox.<sup>183</sup> PXRD of the  $\beta$ - $\text{LiFePO}_4$  can be seen in Figure 3.14 showing the material was obtained with no additional phases present.

Mixed phase  $\alpha/\beta$ - $\text{LiFePO}_4$  was prepared by a similar method to  $\alpha$ - $\text{LiFePO}_4$ , in EG (250 °C, 3 h, 10 ml of solvent, 2.45 mmol). It is observed that the larger volume synthesis gives

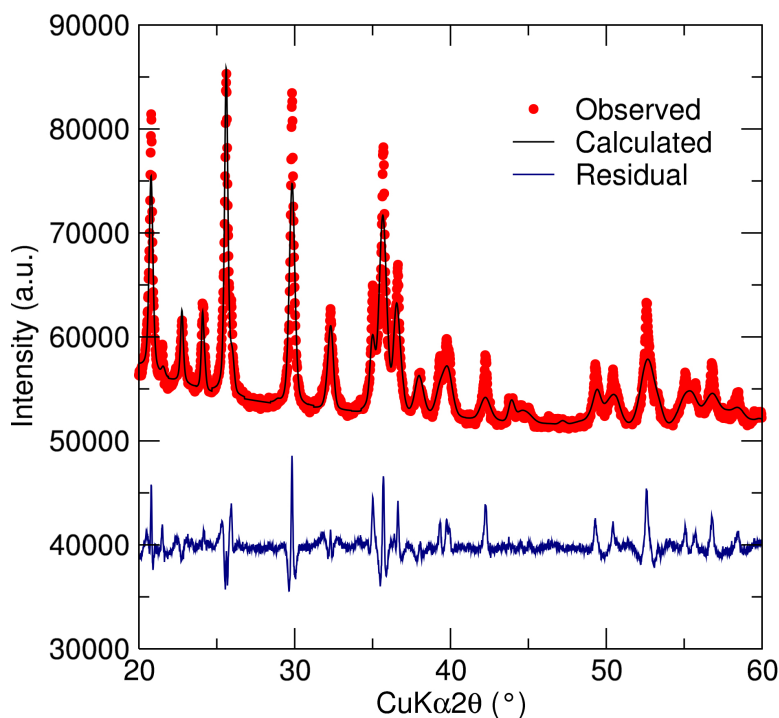


**Figure 3.15:** Dual phase Rietveld refinement of the mixed  $\alpha$ -/ $\beta$ - $\text{LiFePO}_4$ . Reference patterns are taken from Reference 31 and 181 for  $\alpha$ - $\text{LiFePO}_4$  and  $\beta$ - $\text{LiFePO}_4$  respectively.

rise to a significant amount of  $\beta$ - $\text{LiFePO}_4$ , compared to the lower volume synthesis under the same conditions in Figure 3.5. The relative amounts of  $\alpha$ - $\text{LiFePO}_4$  and  $\beta$ - $\text{LiFePO}_4$  were quantified using Rietveld refinement (Figure 3.15). The calculated values for the two phases can be seen in Table 8.1, indicating 84 %  $\alpha$ - $\text{LiFePO}_4$  and 16 %  $\beta$ - $\text{LiFePO}_4$  are present in the sample.

### 3.6.2 Electron microscopy of $\text{LiFePO}_4$ polymorphs

Figure 3.16 shows SEM images of  $\text{LiFePO}_4$  polymorphs synthesised by a microwave-assisted solvothermal route. The samples exhibited different morphologies. The particles of pure  $\alpha$ - $\text{LiFePO}_4$  prepared in EMIM-TFMS (3 h, 250 °C) seen in Figure 3.16 (a) exhibit defined crystallites typically 500 nm in diameter. The particles of the mixed phase  $\alpha$ -/ $\beta$ - $\text{LiFePO}_4$  (3 h, 250 °C) in EG exhibit sheets between 200 nm to 600 nm in width and length and 20 nm in thickness. The particles of  $\beta$ - $\text{LiFePO}_4$  prepared in a mixture of benzyl alcohol and 2-pyrrolidinone (3 min, 195 °C) exhibit a similar hierarchical bow shaped morphology reported previously with particles between 700 nm and 2  $\mu\text{m}$  in diameter.<sup>183</sup>

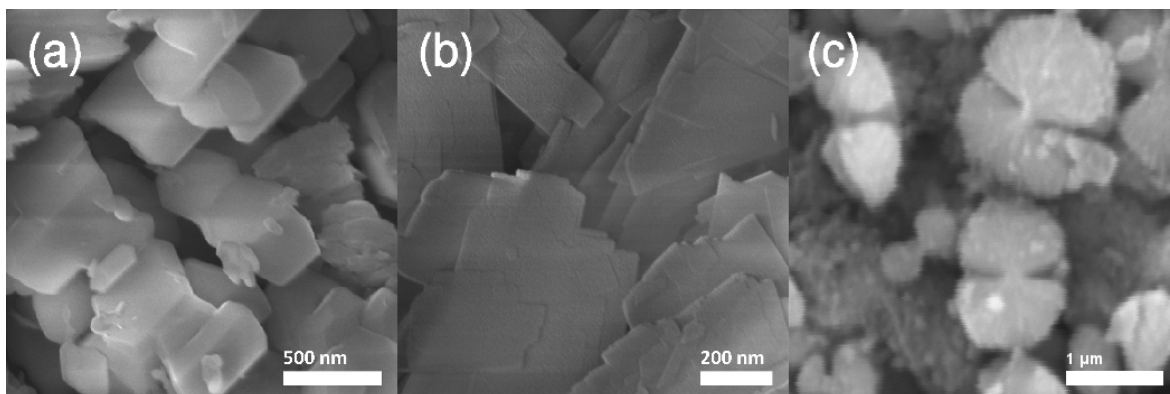


**Figure 3.16:** Scanning electron microscopy images taken of (a)  $\alpha\text{-LiFePO}_4$ , (b)  $\alpha\text{-}\beta\text{-LiFePO}_4$  and (c)  $\beta\text{-LiFePO}_4$  synthesised by a microwave assisted solvothermal route exhibiting different morphologies depending on the synthetic route employed.

### 3.6.3 Electrochemical characterisation of $\text{LiFePO}_4$ polymorphs

The electrochemical performance of  $\alpha\text{-LiFePO}_4$ ,  $\beta\text{-LiFePO}_4$  and mixed  $\alpha\text{-}\beta\text{-LiFePO}_4$  were investigated using galvanostatic cycling with potential limitation (GCPL) between 2.2 V and 4 V at a rate of C/10. All samples were first carbon coated as described in the Experimental section. Figure 3.17 (a) shows the first charge/discharge cycle of each of the three samples. It is observed that the  $\alpha\text{-LiFePO}_4$  is able to intercalate the most  $\text{Li}^+$  on the first cycle, 0.6  $\text{Li}^+$ , corresponding to a discharge capacity of  $102 \text{ mAh g}^{-1}$ .

The mixed  $\alpha\text{-}\beta\text{-LiFePO}_4$  sample showed intercalation of 0.35  $\text{Li}^+$ , corresponding to a discharge capacity of  $59 \text{ mAh g}^{-1}$ . This indicates that the presence of  $\beta\text{-LiFePO}_4$  is having a negative effect on the intercalation of  $\text{Li}^+$  into  $\alpha\text{-LiFePO}_4$ , as the loss in discharge capacity is not proportional to the amount of  $\beta\text{-LiFePO}_4$  (16 %) in the mixed sample. The pure  $\beta\text{-LiFePO}_4$  sample exhibited the intercalation of 0.02  $\text{Li}^+$ , corresponding to a discharge capacity of  $3 \text{ mAh g}^{-1}$ . This is in good agreement with literature reports on  $\beta\text{-LiFePO}_4$  which show it is near electrochemically inert.<sup>183</sup> Figure 3.17 (b) shows the discharge capacities after 20 cycles. All three samples show a good capacity retention  $> 95 \%$ , but the discharge capacities are much lower than the theoretical capacity of  $170 \text{ mAh g}^{-1}$  and best reports from the literature for microwave prepared  $\alpha\text{-LiFePO}_4$ ,  $160 \text{ mAh g}^{-1}$  at C/10.<sup>19,150</sup>

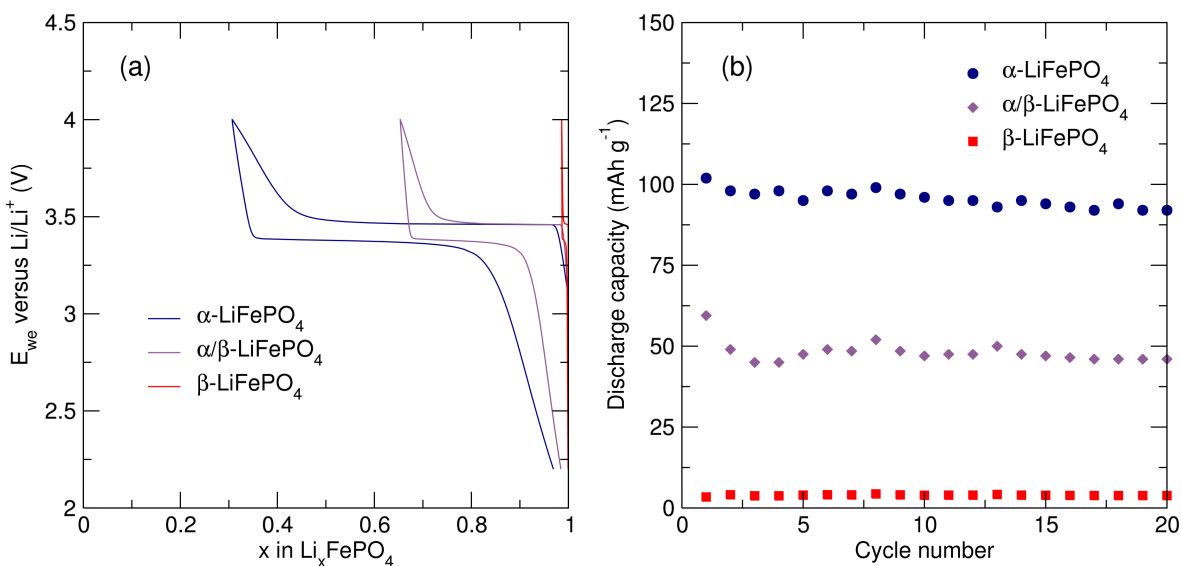


**Figure 3.17:** (a) First galvanostatic cycle with potential limitation between 2.2 V and 4 V of  $\text{LiFePO}_4$  polymorphs at C/10. (b) Discharge capacity of  $\text{LiFePO}_4$  polymorphs over 20 cycles at C/10.

### 3.7 Muon spin relaxation of $\text{LiFePO}_4$ polymorphs

By varying the reaction conditions, the microwave-assisted routes have shown to produce two polymorphs of  $\text{LiFePO}_4$  with different crystal structures, both of which have been previously demonstrated significantly different electrochemical performances.<sup>183</sup> Electrochemical performance is strongly influenced by the diffusion of  $\text{Li}^+$  within the structure. To probe this on a local level, muon spin relaxation ( $\mu\text{SR}$ ) was employed to investigate the impact any structural changes have on the  $\text{Li}^+$  diffusion, and thus explain the electrochemical behaviour, in both polymorphs. Since the spin polarised muons are embedded within the crystal lattice during measurement, this is a truly local probe as muon spin is perturbed by nearby  $\text{Li}^+$  diffusion. For this study, samples of pure  $\alpha$ - $\text{LiFePO}_4$ , pure  $\beta$ - $\text{LiFePO}_4$  and a mixed phase of  $\alpha/\beta$ - $\text{LiFePO}_4$  were investigated and the spin polarised muons implanted into the samples over the temperature range of 100 K to 400 K at three fields (0 G, 5 G and 10 G) using the EMU beamline at ISIS.

Figure 3.18 shows raw data collected at longitudinal fields of 0, 5 and 10 Gauss at 200 K for  $\alpha$ - $\text{LiFePO}_4$ .  $\alpha$ - $\text{LiFePO}_4$  exhibits a fast relaxation at short times, which indicates a

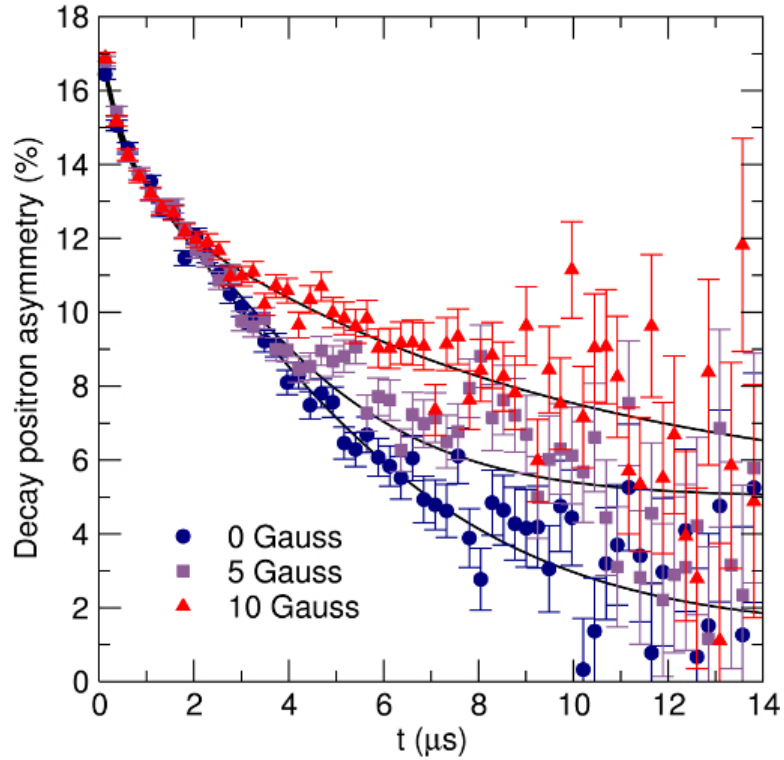


**Figure 3.18:** Raw muon spin relaxation data collected at three fields (0 G, 5 G and 10 G) for  $\alpha\text{-LiFePO}_4$  at 200 K fit with a dynamic Kubo-Toyabe model.

contribution from paramagnetic moments in the sample, in this case  $\text{Fe}^{2+}$ . At longer times, the slower relaxation can be attributed to muon interactions with nuclear magnetic fields of other atoms in the sample, here  $^7\text{Li}$ ,  $^6\text{Li}$  and  $^{31}\text{P}$ . Applying a longitudinal field decouples the muons decay behaviour from the nuclear contributions which is observed as a dampening in the relaxation. The data collected for  $\alpha\text{-LiFePO}_4$  were fit using Equation 3.2.

$$A_0 P_{\text{LF}}(t) = A_{\text{F}} \exp(-\lambda_{\text{F}} t) + A_{\text{KT}} \exp(-\lambda_{\text{KT}} t) \times G^{\text{DGKT}}(\Delta, \nu, t, H_{\text{LF}}) + A_{\text{BG}} \quad (3.2)$$

$A_{\text{F}} \exp(-\lambda_{\text{F}} t)$  is an exponentially relaxing component which describes the contribution from nuclear magnetic spins on the muon relaxation,  $A_{\text{KT}} \exp(-\lambda_{\text{KT}} t) \times G^{\text{DGKT}}(\Delta, \nu, t, H_{\text{LF}})$  is the modified Kubo-Toyabe function used to describe the dynamic diffusion processes and  $A_{\text{BG}}$  is a constant background component.<sup>171</sup> Within the Kubo-Toyabe equation, the  $\Delta$  function is the quasielastic local field distribution of the muon implantation site,  $\nu$  is the fluctuation rate of the muon's Larmor precession,  $t$  is the lifetime of the muon and  $H_{\text{LF}}$  is the longitudinal field strength. Using this model provides an excellent fit to the raw  $\mu\text{SR}$  data collected for

pure phase  $\alpha\text{-LiFePO}_4$ , as seen in Figure 3.18. The fluctuation rate,  $\nu$ , is found to be 0.425 MHz at 200 K, indicating the diffusion of  $\text{Li}^+$  ions occurs even at this low temperature.

The raw  $\mu\text{SR}$  data collected for  $\beta\text{-LiFePO}_4$  was fit using a series of combinations of parameters and functions, but none gave a reliable fit to the data. Figure 3.19 (a) shows the fit used for  $\alpha\text{-LiFePO}_4$  applied for  $\beta\text{-LiFePO}_4$ , at 200 K which describes the data very poorly indicating a lack of  $\text{Li}^+$  diffusion in the material. However, at the highest temperature measured (400 K) the model is in good agreement indicating that there may be the onset of  $\text{Li}^+$  diffusion at high temperatures in  $\beta\text{-LiFePO}_4$ . Thermally activated behaviour for  $\text{Li}^+$  diffusion in  $\alpha\text{-LiFePO}_4$  has previously been observed in range of 160 K to 240 K.<sup>71</sup> At 400 K a  $\nu$  of 0.09 MHz is calculated from the dynamic fittings, much lower than the  $\alpha\text{-LiFePO}_4$  sample at 200 K (0.425 MHz). This indicates that the  $\text{Li}^+$  diffusion process is slower in  $\beta\text{-LiFePO}_4$  than in  $\alpha\text{-LiFePO}_4$ , and is only observable at elevated temperatures.

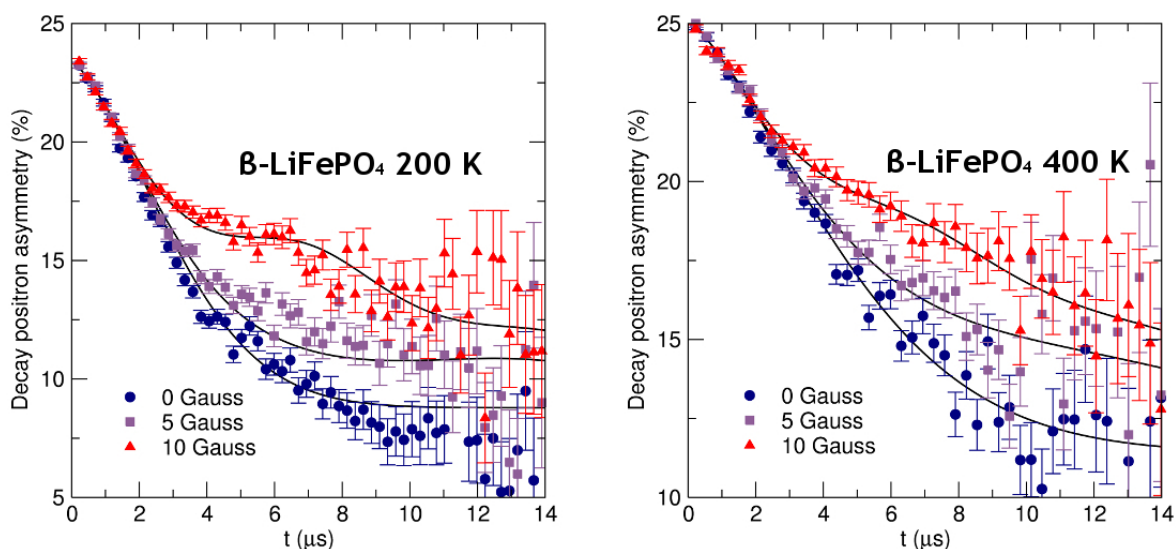


**Figure 3.19:** Raw muon spin relaxation data for (a)  $\beta\text{-LiFePO}_4$  at 200 K and (b)  $\beta\text{-LiFePO}_4$  at 400 K fit with a dynamic Kubo-Toyabe model. It is observed that a good fit can only be obtained at higher temperatures.

Figure 3.20 shows calculated values for  $\nu$  (a) and  $\Delta$  (b) in  $\alpha\text{-LiFePO}_4$  with increasing temperature. The onset of thermal activation for  $\alpha\text{-LiFePO}_4$  begins at 160 K, indicated by an increase in  $\nu$ . This continues up until 230 K after which a steep decline in  $\nu$  is observed. This is due to  $\text{Li}^+$  diffusion becoming too fast to observe in the muon's lifetime, prior to decay.<sup>71</sup> The values of  $\Delta$  for  $\alpha\text{-LiFePO}_4$  do not show a significant change indicating that the

observed values of  $\nu$  can be wholly attributed to the diffusion  $\text{Li}^+$  and are independent of any magnetic influences in the material. A weak decline in  $\Delta$  is observed and attributed to muons becoming mobile and diffusing as temperature increases, in good agreement with previous reports.<sup>68</sup>

Since it was not possible to fit the entire temperature range of data obtained for pure  $\beta$ - $\text{LiFePO}_4$ , the mixed phase  $\alpha/\beta$ - $\text{LiFePO}_4$  was studied in order to more completely probe the effect of  $\beta$ - $\text{LiFePO}_4$  on the  $\text{Li}^+$  diffusion dynamics. Figure 3.20 shows calculated values for  $\nu$  (c) and  $\Delta$  (d) in  $\alpha/\beta$ - $\text{LiFePO}_4$  with increasing temperature.  $\alpha/\beta$ - $\text{LiFePO}_4$  exhibits thermal activation of  $\nu$  around 180 K and an increase in  $\nu$  up to temperatures of 400 K. The observed  $\text{Li}^+$  diffusion at higher temperatures in the mixed phase  $\text{LiFePO}_4$  compared to the  $\alpha$ - $\text{LiFePO}_4$  is attributed to the onset for thermal activation in the  $\beta$ - $\text{LiFePO}_4$ , in agreement with the data collected for pure  $\beta$ - $\text{LiFePO}_4$ . As with the pure  $\alpha$ - $\text{LiFePO}_4$ , there is little change in the value of  $\Delta$  with increasing temperature, with the weak decline being similarly attributed to muon diffusion.

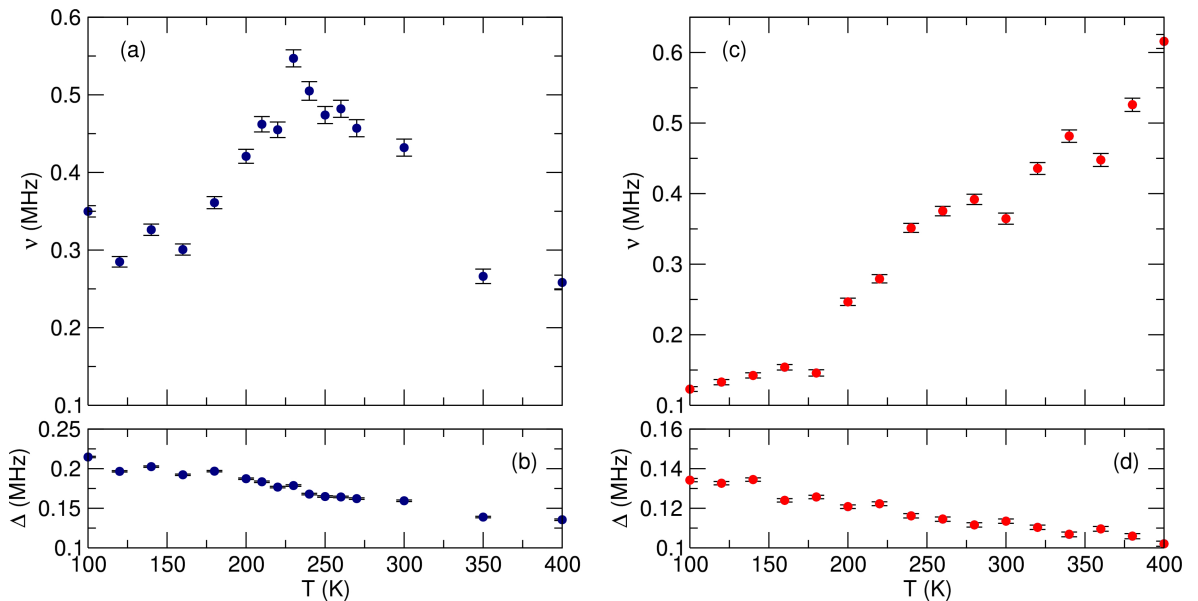


**Figure 3.20:** Temperature dependence of fluctuation rate ( $\nu$ ) for  $\alpha$ - $\text{LiFePO}_4$  (a) and  $\alpha/\beta$ - $\text{LiFePO}_4$  (c) and field distribution width ( $\Delta$ ) for  $\alpha$ - $\text{LiFePO}_4$  (b) and  $\beta$ - $\text{LiFePO}_4$  (d).

The fluctuation rate ( $\nu$ ) is directly influenced by the rate at which  $\text{Li}^+$  is diffusing past an implanted muon at a given rate. This rate is known as the  $\text{Li}^+$  diffusion rate ( $D_{\text{Li}}$ ). The  $D_{\text{Li}}$  in these samples can be calculated by using the values of  $\nu$  extracted from the fits and the

distance between two interstitial sites between which Li<sup>+</sup> hop. Equation 3.3 can be used to calculate the  $D_{\text{Li}}$  where  $b$  is the distance between two interstitial Li<sup>+</sup> taken from Reference 31. It has previously been identified from computational and experimental work that the  $b$ -axis is the primary route of diffusion in  $\alpha$ -LiFePO<sub>4</sub>.<sup>20,21</sup>

$$D_{\text{Li}} = b^2\nu/4 \quad (3.3)$$

Employing equation 3.3 for  $\alpha$ -LiFePO<sub>4</sub> gives a value of  $D_{\text{Li}} = 5.4 \times 10^{-10} \text{cm}^2\text{s}^{-1}$  at 300 K, in good agreement with  $\mu\text{SR}$  measurements on bulk  $\alpha$ -LiFePO<sub>4</sub> samples reported in the literature.<sup>68,71</sup> This shows that the mechanics of Li<sup>+</sup> diffusion remain consistent regardless of the preparation method. In comparison,  $\alpha/\beta$ -LiFePO<sub>4</sub> gives a value of  $D_{\text{Li}} = 4.0 \times 10^{-10} \text{cm}^2\text{s}^{-1}$  at 300 K, and for  $\beta$ -LiFePO<sub>4</sub>  $D_{\text{Li}} = 7.4 \times 10^{-11} \text{cm}^2\text{s}^{-1}$  at 400 K. It is observed that as the presence of  $\beta$ -LiFePO<sub>4</sub> increases, the diffusion of Li<sup>+</sup> becomes slower. The reason for observing such a low  $D_{\text{Li}}$  at high temperatures in  $\beta$ -LiFePO<sub>4</sub> could be due to the lack of clear pathways for Li<sup>+</sup> diffusion to occur.  $\alpha$ -LiFePO<sub>4</sub> (Figure 3.21 a) exhibits clear channels for Li<sup>+</sup> diffusion compared to the structure of  $\beta$ -LiFePO<sub>4</sub> (Figure 3.21 b) where distortions of the FeO<sub>6</sub> octahedra lead to interference from the PO<sub>4</sub> tetrahedra in the Li<sup>+</sup> diffusion pathways. Furthermore, these distortions lead to an increased Li-Li distance in  $\beta$ -LiFePO<sub>4</sub> which is expected to increase the  $E_a$  of the lithium hopping mechanism. These findings conclude that the Li<sup>+</sup> diffusion properties of  $\beta$ -LiFePO<sub>4</sub> are poor, concurrent with electrochemical impedance spectroscopy studies performed previously and explain the poor electrochemical performance observed for samples containing the  $\beta$  polymorph.<sup>183</sup>

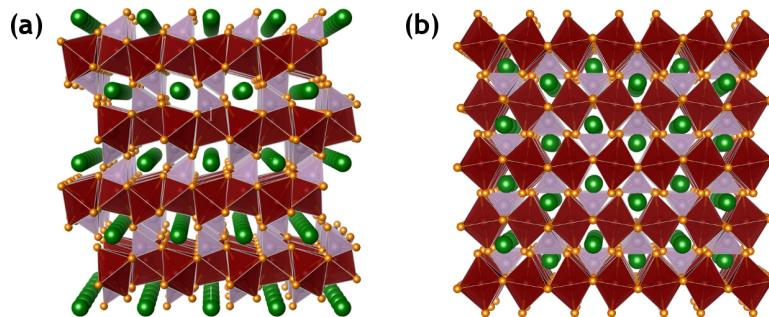


**Figure 3.21:** Crystal structures of (a)  $\alpha$ -LiFePO<sub>4</sub>, space group  $Pnma$ , and (b)  $\beta$ -LiFePO<sub>4</sub>, space group  $Cmcm$ .

The calculated values of  $D_{\text{Li}}$  were used to construct Arrhenius plots for the  $\alpha\text{-LiFePO}_4$  and  $\alpha/\beta\text{-LiFePO}_4$  samples (Figure 3.22) in order to obtain values for the activation energy ( $E_a$ ) of the  $\text{Li}^+$  hopping mechanism. For  $\alpha\text{-LiFePO}_4$  the value of  $E_a$  19 meV, while for the mixed  $\alpha/\beta\text{-LiFePO}_4$  a value of 38 meV is obtained. Referring to Figure 1.12, the values of  $E_a$  agree more closely with theoretical calculations than any other technique. Furthermore, the values of  $E_a$  and  $D_{\text{Li}}$  remain on the same order of magnitude as previous studies on  $\alpha\text{-LiFePO}_4$  highlighting the reproducibility of results using  $\mu\text{SR}$ .<sup>68,71</sup> The results indicate that the lower electrochemical performance of  $\beta\text{-LiFePO}_4$  or  $\beta$ -containing  $\text{LiFePO}_4$  is due to deleterious changes of  $\text{Li}^+$  diffusion.

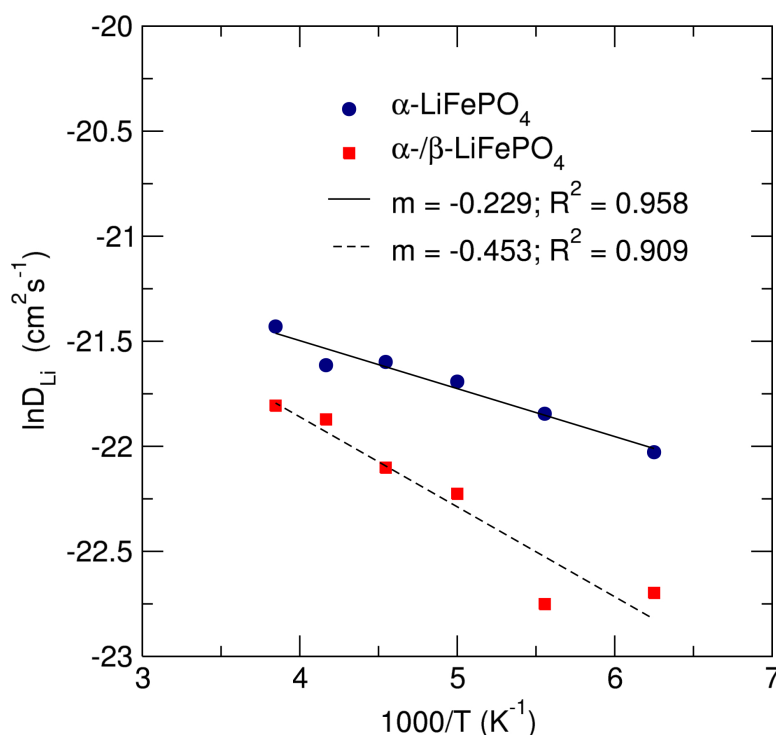


**Figure 3.22:** Arrhenius plot of the lithium diffusion coefficient of  $\alpha\text{-LiFePO}_4$  and  $\alpha/\beta\text{-LiFePO}_4$  calculated from Equation 3.3.

### 3.8 *In situ* XANES of $\text{LiFePO}_4$ polymorphs

To investigate the effects of  $\text{Li}^+$  extraction on the local structure of  $\alpha\text{-LiFePO}_4$ , Fe K-edge X-ray absorption spectra (XAS) were collected for samples of pure  $\alpha\text{-LiFePO}_4$  and  $\alpha/\beta\text{-LiFePO}_4$ . XAS allows a simultaneous study of changes in the oxidation state and nearest

neighbour coordination environments of materials. This is of particular interest for insertion electrodes, where these changes can be monitored as a function of  $\text{Li}^+$  extraction during cell operation.

Firstly, *ex situ* XAS of the Fe K-edge in pure  $\alpha\text{-LiFePO}_4$  and  $\alpha/\beta\text{-LiFePO}_4$  were performed in order to examine the spectra prior to  $\text{Li}^+$  extraction. The normalised absorption spectra (Figure 3.23 a) reveal that both  $\text{LiFePO}_4$  samples exhibit similar profiles in both the pre-edge (A) and rising edge (B). Two standards corresponding to  $\text{Fe}^{2+}$  and  $\text{Fe}^{3+}$  were also measured for comparison,  $\text{FeO}$  and  $\text{Fe}(\text{NO}_3)_3$ , respectively.

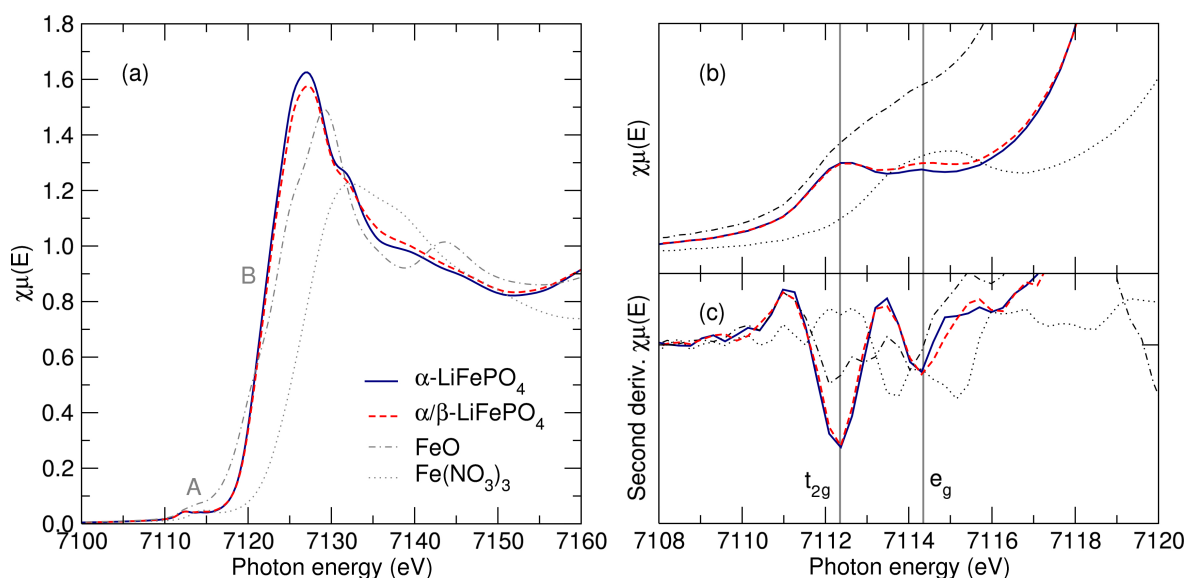


**Figure 3.23:** (a) Normalised *ex situ* Fe K-edge X-ray absorption near edge spectra (XANES) of  $\alpha\text{-LiFePO}_4$ , mixed  $\alpha/\beta\text{-LiFePO}_4$  prepared by a microwave-assisted route and standards containing  $\text{Fe}^{2+}$  ( $\text{FeO}$ ) and  $\text{Fe}^{3+}$  ( $\text{Fe}(\text{NO}_3)_3$ ). The pre-edge (A) and rising edge (B) show a shift to lower energy with decreasing oxidation state. (b) Second derivative of the normalised XANES spectra over the pre-edge region shows minima corresponding to contributions from  $\text{Fe}^{2+}$   $t_{2g}$  and  $e_g$  orbitals.

The rising edge (B) can be assigned to the quadrupole allowed excitation of an electron in a core  $1s$  orbital to the  $4+np$  (where  $n$  is an integer) during the absorption of X-ray radiation of a specific wavelength, and is sensitive to the oxidation state of the interrogated target atom. The rising edge of the  $\text{LiFePO}_4$  samples lie close to the  $\text{FeO}$  standard suggesting an initial oxidation state of  $\text{Fe}^{2+}$  which is the expected state in order to maintain charge balance

of the stoichiometric material.

The pre-edge feature is present when the normally dipole forbidden transition of a core  $1s$  electron to the outer  $3d$  orbitals is allowed by  $p$ -orbital to  $d$ -orbital mixing. This effect can occur when the coordination environment surrounding an atomic species is not centrosymmetric. A greater departure from centrosymmetry leads to a higher peak intensity. The pre-edge feature (Figure 3.23 b and c) shows two separate peaks arising from the splitting of the  $e_g$  and  $t_{2g}$   $d$ -orbitals of the  $\text{Fe}^{2+}$  due to the octahedral symmetry of the  $\text{FeO}_6$  polyhedra in  $\alpha\text{-LiFePO}_4$ . The difference in energy between the  $e_g$  and  $t_{2g}$  of 2 eV is a direct measurement of the octahedral crystal field splitting energy (CFSE),  $\Delta_o$ . The value of  $\Delta_o$  observed is in good agreement with previous XANES studies of  $\alpha\text{-LiFePO}_4$ .<sup>189</sup>

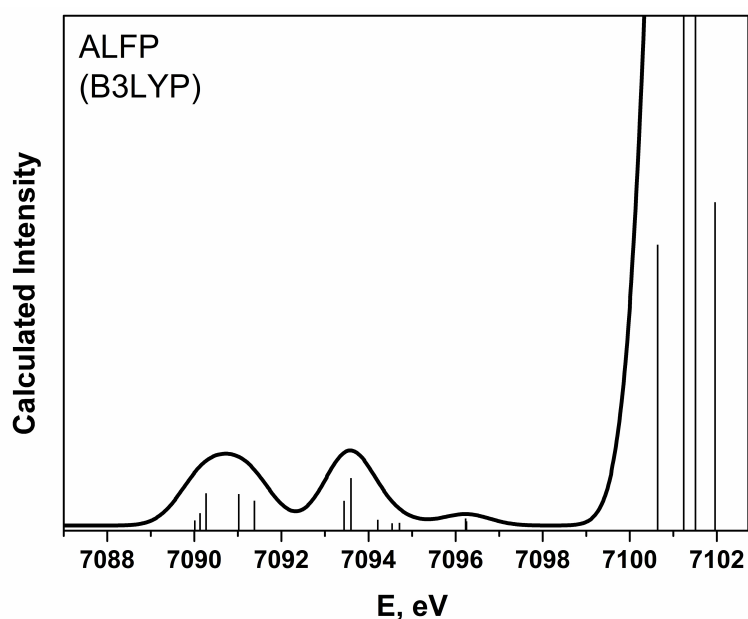


**Figure 3.24:** B3LYP DFT simulation of the Fe K-edge spectrum expected for  $\alpha\text{-LiFePO}_4$ . The two low energy features arise from the core  $1s$  to  $3d$  ( $t_{2g}$  and  $e_g$ ) orbitals and a high energy incline from  $1s$  to  $4+n_p$  excitations.

Density functional theory calculations (DFT) were performed using a B3LYP method to compare the data collected for the  $\text{LiFePO}_4$  samples to what is expected computationally using the asymmetric unit of  $\alpha\text{-LiFePO}_4$  (Figure 3.24). Due to the use of the asymmetric unit, the energy scale is shifted, but the relative positions of the features can be compared between computational and experimental observations. The DFT calculation confirms the

$d$ -orbital splitting in  $\alpha\text{-LiFePO}_4$ ,  $t_{2g}$  orbitals at 7090.8 eV and  $e_g$  orbitals at 7093.5 eV. The calculated energy gap is approximately 2.7 eV close to the experimentally observed energy gap. The large incline at higher energy is the rising edge ( $1s$  to  $4+n p$ ) transitions that are separated from the  $t_{2g}$  feature by approximately 10 eV in good agreement with the experimental data.

Figure 3.25 (a) shows the *in situ* normalised XANES spectra of the  $\alpha\text{-LiFePO}_4$  sample during electrochemical charging (delithiation) down to a  $\text{Li}^+$  concentration of  $\text{Li}_{0.77}\text{FePO}_4$ .

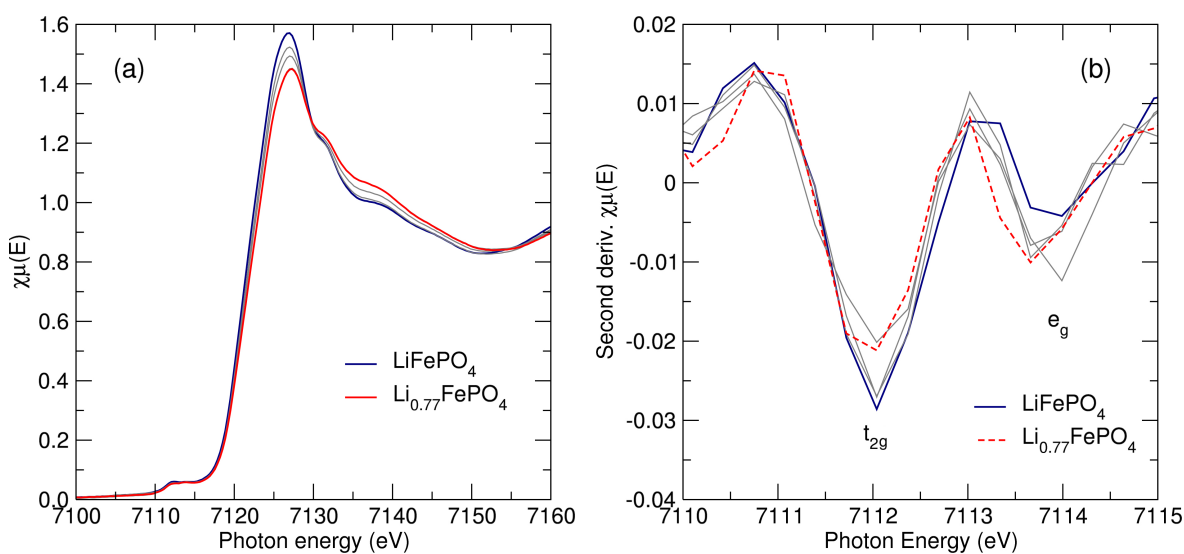


**Figure 3.25:** (a) Normalised *in situ* Fe K-edge XAS of  $\alpha\text{-LiFePO}_4$  prepared by a microwave-assisted route during electrochemical charging ( $\text{Li}^+$  deintercalation). The pre-edge (A) and rising edge (B) shift to lower energy as  $\text{Li}^+$  is removed from the structure. (b) The second derivative of the pre-edge shows an increase in  $\text{Fe}^{3+}$  and a decrease in  $\text{Fe}^{2+}$  as  $\text{Li}^+$  is deintercalated.

As  $\text{Li}^+$  is removed from  $\text{LiFePO}_4$ , the rising edge shifts to higher energy through the loss of  $d$ -electrons and the oxidation of  $\text{Fe}^{2+}$  to  $\text{Fe}^{3+}$ . This is due to the stabilisation of the core  $1s$  electrons in Fe relative to the  $4+n p$  orbitals which leads to an increase the  $1s$  binding energy, manifested here as the photon energy. Figure 3.25 (b) shows the second derivative of the normalised XANES for  $\alpha\text{-LiFePO}_4$  over the pre-edge region. It is observed that upon  $\text{Li}^+$  deinsertion the  $t_{2g}$  feature decreases in intensity while the  $e_g$  feature increases. This is due to the overlap in energy of the  $\text{Fe}^{2+}$   $e_g$  and the  $\text{Fe}^{3+}$   $t_{2g}$  orbital sets. As  $\text{Li}^+$  is inserted, the abundance of  $\text{Fe}^{3+}$  grows relative to  $\text{Fe}^{2+}$ , increasing the intensity of the  $\text{Fe}^{3+}$   $d$ -orbital

peaks. This is manifested as a diminishing of the  $\text{Fe}^{2+} t_{2g}$  orbital contribution and a shifting of the  $\text{Fe}^{2+} e_g/\text{Fe}^{3+} t_{2g}$  peaks.

It is observed that as  $\text{Li}^+$  is extracted from  $\alpha\text{-LiFePO}_4$ , the  $\Delta_o$  does not change. This indicates that the  $\text{FeO}_6$  polyhedra remain in octahedral symmetry during the  $\text{Li}^+$  extraction process. Departure from octahedral symmetry would lead to increased interaction of the O  $2p$  and Fe  $3d$  orbitals causing further splitting of the  $e_g$  and  $t_{2g}$ . This is due to an decrease in metal-to-ligand orbital overlap between Fe and O as electrons are removed from Fe, increasing the energy of the bonding interactions and decreasing the energy of the antibonding interactions. Since  $\Delta_o$  is defined as the gap between non-bonding  $t_{2g}$  and antibonding  $e_g$  orbitals, an increase in  $\Delta_o$  would be expected if the  $\text{FeO}_6$  polyhedra departed from octahedral symmetry.

The normalised XANES spectra for  $\alpha\text{-}/\beta\text{-LiFePO}_4$  (Figure 3.26 a) exhibit similar behaviour to those observed in  $\alpha\text{-LiFePO}_4$  where a shift to higher energy occurs upon  $\text{Li}^+$  extraction. The second derivative of the normalised pre-edge (Figure 3.26 b) also shows reduction of the  $\text{Fe}^{2+}$  and growth of the  $\text{Fe}^{3+}$  peaks due to the oxidation process when removing  $\text{Li}^+$ .

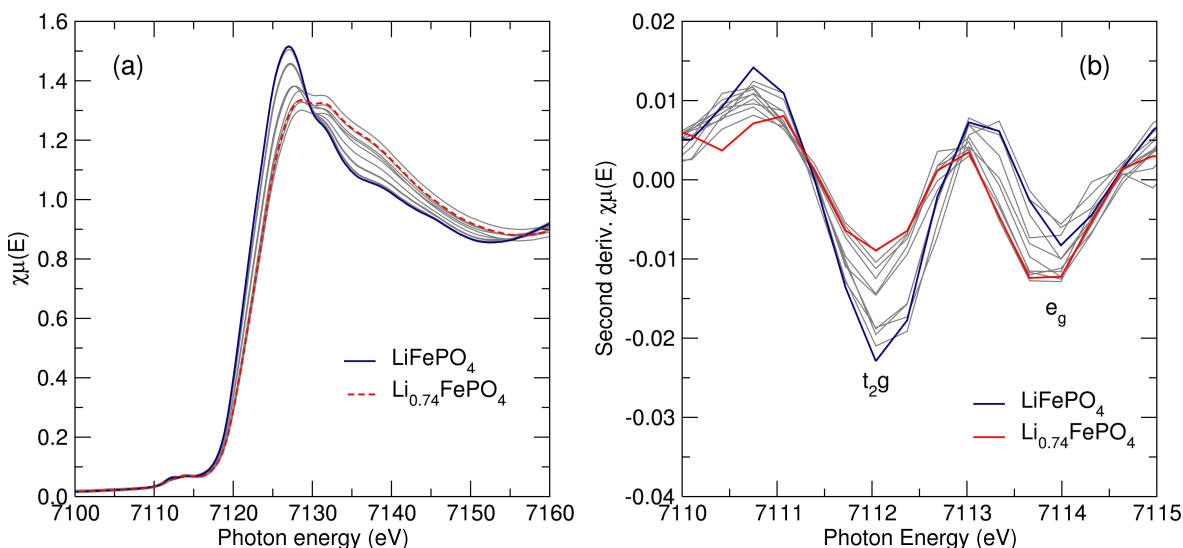


**Figure 3.26:** (a) Normalised *in situ* Fe K-edge XAS of  $\alpha/\beta\text{-LiFePO}_4$  prepared by a microwave-assisted route during electrochemical charging ( $\text{Li}^+$  deintercalation). The pre-edge (A) and rising edge (B) shift to lower energy as  $\text{Li}^+$  is removed from the structure. (b) The second derivative of the pre-edge shows an increase in  $\text{Fe}^{3+}$  and a decrease in  $\text{Fe}^{2+}$  as  $\text{Li}^+$  is deintercalated.

### 3.9 *In situ* EXAFS of $\alpha\text{-LiFePO}_4$

Changes in the local coordination environment of  $\alpha\text{-LiFePO}_4$  were further investigated by examining the EXAFS region of the XAS data collected. Although XANES is able to give a general evaluation of the coordination environment, it can give no appreciation of local distances between atoms. The normalised and background subtracted XAS data collected for nanostructured  $\alpha\text{-Li}_1\text{FePO}_4$  prepared by a microwave assisted ionothermal route were fit using the Artemis software package. Scattering paths for photons originating at the Fe atom were calculated using the Feff and Atoms software from an ICSD bulk  $\alpha\text{-LiFePO}_4$  sample taken from Reference 31. The first coordination shell Fe-O paths and second coordination shell Fe-P paths were used to fit the data  $k_1$ ,  $k_2$  and  $k_3$  k-weighting between 1.5 Å and 3.5 Å using a Hanning window.

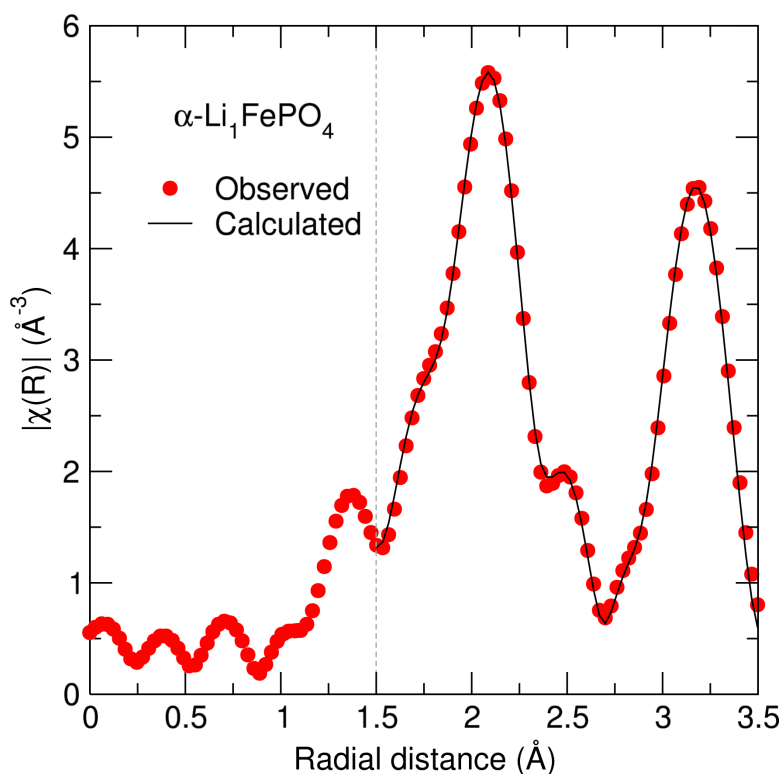


**Figure 3.27:** Raw data and EXAFS fit of  $\alpha\text{-LiFePO}_4$  to  $Pnma$  structured  $\text{LiFePO}_4$ . 31 Two features are observed for the Fe-O radial distances (2.0 Å) and Fe-P (3.2 Å).

Figure 3.27 shows a fit to the raw data collected for  $\alpha\text{-Li}_1\text{FePO}_4$  to  $Pnma$  structured  $\alpha\text{-LiFePO}_4$ . The raw data exhibits two main features above 1.5 Å corresponding to the Fe-O

scattering paths centered around 2.0 Å, and the Fe-P scattering paths centered around 3.2 Å. The calculated values for these scattering paths are presented in Table 3.3.  $\sigma^2$  is the standard deviation of the model, R is the absorber-scatterer pathlength from the literature values,  $R_{\text{eff}}$  is the absorber-scatterer pathlength calculated and  $\Delta R$  is the difference between the model and the literature values and the calculated model.

Path	Degen.	$\sigma^2$	R	$\Delta R$	$R_{\text{eff}}$
O1	3	0.00605	2.0914	-0.06255	2.02885
O2	1	0.00047	2.2208	-0.10161	2.11919
O3	2	0.00485	2.268	-0.03506	2.23294
P1	1	0.00827	2.847	-0.02398	2.82302
P2	1	0.00993	3.2355	0.33871	3.57421
P3	3	0.00492	3.2709	-0.01022	3.26068

**Table 3.3:** Calculated EXAFS parameters for nanostructured  $\alpha\text{-Li}_1\text{FePO}_4$  fit to data from a bulk sample of  $\alpha\text{-LiFePO}_4$  taken from Reference 31.

A decrease in Fe-O distance is observed in nanostructured  $\alpha\text{-LiFePO}_4$  compared to the bulk reference. A significant difference is observed in the distance of the atom P2 of 0.34 Å. The real distance between the atoms derived from phase correction is given by the value  $R_{\text{eff}}$ . It is observed that the average  $R_{\text{eff}}$  for the Fe-O distances in nanostructured  $\alpha\text{-LiFePO}_4$  is 2.12 Å. The average  $R_{\text{eff}}$  for the Fe-P distance is calculated as 3.21 Å.

The data collected for the sample after Li<sup>+</sup> extraction ( $\text{Li}_{0.77}\text{FePO}_4$ ) could not be fit to the  $\alpha\text{-LiFePO}_4$  model from the literature. However, a fit was successfully achieved by employing calculated Fe-O and Fe-P scattering paths from *Pnma* structured FePO<sub>4</sub> taken from Reference 31. This observation confirms, in agreement with previous reports, that after extraction of 0.23 Li<sup>+</sup> from  $\alpha\text{-LiFePO}_5$  the *Pnma* structure is preserved but changes in interatomic distance occur.<sup>189</sup> Figure 3.28 shows a fit to the raw data collected for  $\alpha\text{-Li}_{0.77}\text{FePO}_4$  to *Pnma* structured FePO<sub>4</sub>.

The raw EXAFS data for  $\alpha\text{-Li}_{0.77}\text{FePO}_4$  exhibits different features to  $\alpha\text{-LiFePO}_4$  due to a change in scattering distance and thus interatomic distances. The first two features above 1.5 Å, at 1.8 Å and 2.2 Å, correspond to the Fe-O scattering lengths. The features at 2.5

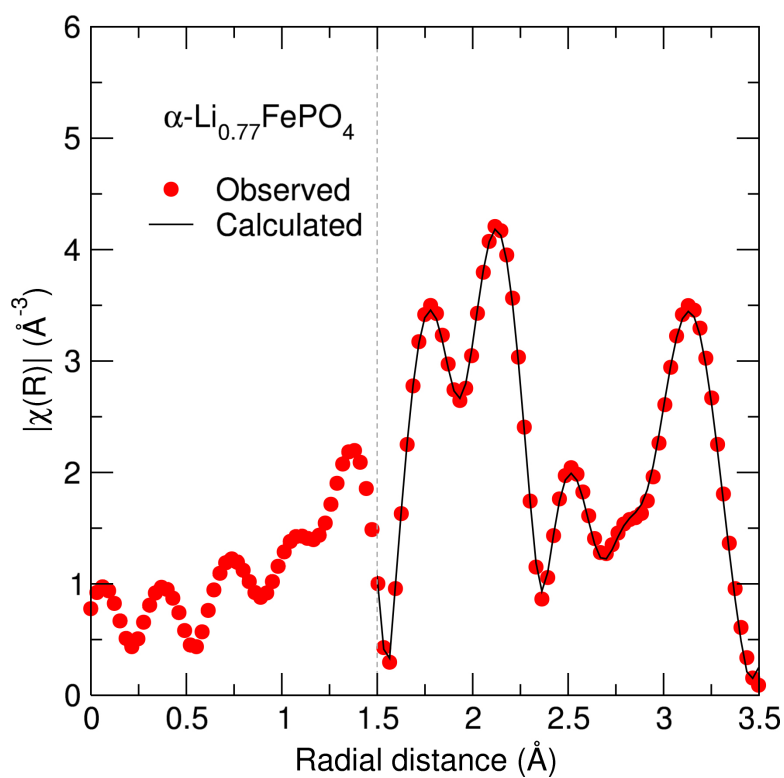


**Figure 3.28:** Raw data and EXAFS fit of  $\alpha\text{-Li}_{0.77}\text{FePO}_4$  to Pnma structured  $\text{FePO}_4$  taken from Reference 31. Two features are observed for the Fe-O radial distances at 1.8  $\text{\AA}$  and 2.2  $\text{\AA}$  and two for Fe-P radial distances at 2.5  $\text{\AA}$  and 3.1  $\text{\AA}$ .

Å and 3.1 Å correspond to the Fe-P distances. The calculated values for these scattering paths are presented in Table 3.4.

**Table 3.4:** Calculated EXAFS parameters for nanostructured  $\alpha\text{-Li}_{0.77}\text{FePO}_4$  fit to data from a bulk sample of  $\text{FePO}_4$  taken from Reference 31.

Path	Degen.	$\sigma^2$	$\Delta R$	R	$R_{\text{eff}}$
O1	2	0.00977	0.07312	1.9332	2.00632
O2	2	0.00903	-0.18325	2.0472	1.86395
O3	2	0.00989	0.1692	2.1545	2.3237
P1	1	0.009	-0.10127	2.793	2.69173
P2	4	0.01157	0.21372	3.1866	3.40032

The values of  $\Delta R$  suggest that there is a significant difference between the distances observed for the nanostructured  $\alpha\text{-Li}_{0.77}\text{FePO}_4$  and the bulk *Pnma*  $\text{FePO}_4$  since only partial delithiation has been achieved. The average value of  $R_{\text{eff}}$  calculated for Fe-O in  $\alpha\text{-Li}_{0.77}\text{FePO}_4$  is found to be 2.06 Å and for the Fe-P distance 3.05 Å. This shows that both the average Fe-O and Fe-P interatomic distances become shorter upon delithiation from  $\alpha\text{-LiFePO}_4$  to  $\alpha\text{-Li}_{0.77}\text{FePO}_4$ .

To explore this relationship between  $\text{Li}^+$  concentration and interatomic distance further, fits were conducted in a similar manner for the other EXAFS spectra collected during delithiation using a *Pnma*  $\text{FePO}_4$  standard.<sup>31</sup> Figure 3.29 shows the average Fe-O and Fe-P distances calculated from EXAFS fits with decreasing  $\text{Li}^+$  concentration. It is observed that as  $\text{Li}^+$  concentration decreases in  $\alpha\text{-LiFePO}_4$ , there is a small decrease in the average Fe-O and Fe-P distances. This observation is in good agreement with the well known volumetric contraction in  $\alpha\text{-LiFePO}_4$  (7 %) upon delithiation to  $\text{FePO}_4$ .<sup>31</sup> The reason for this contraction is due to the Fe-O bonds becoming more covalent. This is due to the removal of  $\text{Li}^+$  causing the oxidation of  $\text{Fe}^{2+}$  to  $\text{Fe}^{3+}$  (witnessed in the XANES) making the Fe atoms more electro-positive. The relatively small contraction observed from EXAFS and retention of symmetry confirmed from XANES for nanostructured  $\alpha\text{-LiFePO}_4$  obtained from microwave-assisted ionothermal synthesis indicates that good structural stability is maintained during electrochemical lithium extraction.

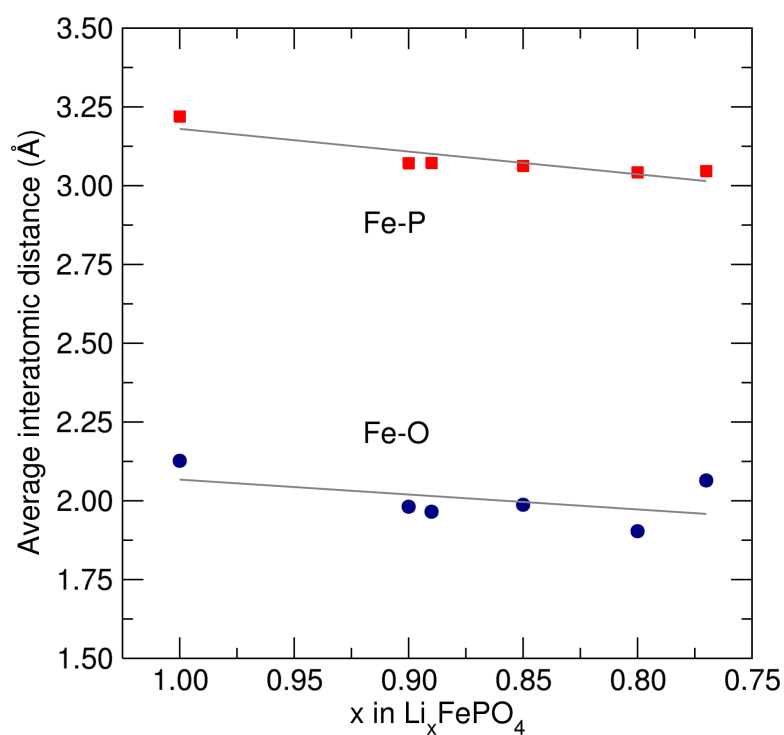


**Figure 3.29:** The average interatomic distance of Fe-O and Fe-P calculated from EXAFS data collected for  $\alpha\text{-Li}_x\text{FePO}_4$  shows a small decrease with decreasing  $\text{Li}^+$  concentration.  $\alpha\text{-Li}_1\text{FePO}_4$  was fit with a *Pnma* structured  $\alpha\text{-LiFePO}_4$  standard while all other concentrations were fit with a *Pnma*  $\text{FePO}_4$  standard taken from Reference 31.

### 3.10 Conclusions

These findings show that the  $\beta$ -LiFePO<sub>4</sub> appears as a side product during the synthesis of  $\alpha$ -LiFePO<sub>4</sub> from oxalate based materials in polyol media. This has also recently been corroborated by the synthesis of *Cmcm* structured LiMPO<sub>4</sub> (M = Fe, Mn, Co and Ni) from metal oxalate starting materials in TEG.<sup>190</sup> Increasing the temperature and/or time of the reaction appears to promote the conversion of  $\alpha$ -LiFePO<sub>4</sub> to  $\beta$ -LiFePO<sub>4</sub>.

It has also been shown that this conversion can also be induced by two routes. Dry, solid-state methods can be applied to convert from the *Cmcm* structure to the *Pnma* structure, however this can give rise to impurities even under an inert atmosphere. More conveniently  $\alpha$ -LiFePO<sub>4</sub> can be converted to  $\beta$ -LiFePO<sub>4</sub> using a microwave-assisted solvothermal treatment allowing us to access phase pure  $\alpha$ -LiFePO<sub>4</sub> at significantly lower synthetic times. This method could provide an interesting pathway to access new morphologies as the particles shape is preserved after heat treatment.

Furthermore ILs have proven a superior medium for heating microwave-assisted reactions requiring significantly less microwave power to achieve elevated temperatures required for microwave synthesis of  $\alpha$ -LiFePO<sub>4</sub> (EMIM-TFMS = 12 W and EG = 121 W at 250 °C). However the choice of solvent is important as phase pure  $\alpha$ -LiFePO<sub>4</sub> was only obtained in EMIM-TFSI.

Although a capacity of only 105 mAh g<sup>-1</sup> has been achieved by the microwave synthesised  $\alpha$ -LiFePO<sub>4</sub>, studies of  $\beta$ -LiFePO<sub>4</sub> and the mixed polymorph sample have provided insight into the detrimental effect of the  $\beta$ -polymorph. Muon investigations have supported the electrochemical data, showing that structural changes can affect the Li<sup>+</sup> diffusion characteristics intercalation materials significantly with the onset of lithium diffusion only observable at 400 K in  $\beta$ -LiFePO<sub>4</sub>. It was also observed that the presence of 16 %  $\beta$ -LiFePO<sub>4</sub> in the  $\alpha$ -LiFePO<sub>4</sub> doubled the calculated Li<sup>+</sup> hopping E<sub>a</sub> underlining the importance of eradicating detrimental polymorphism from  $\alpha$ -LiFePO<sub>4</sub> to ensure the Li<sup>+</sup> diffusion dynamics and electrochemical performance are not perturbed.

Lastly *in situ* XANES analysis shows that as Li<sup>+</sup> is removed from the structure of both pure  $\alpha$ -LiFePO<sub>4</sub> and  $\alpha$ -/ $\beta$ -LiFePO<sub>4</sub> a shift in the oxidation state from Fe<sup>2+</sup> to Fe<sup>3+</sup> is observed

as expected, with no significant differences occurring in the  $\alpha/\beta$ - $\text{LiFePO}_4$ . This indicates that although the  $\text{Li}^+$  hopping energy is affected by the presence of the  $\beta$ -polymorph does not cease  $\text{Li}^+$  deintercalation in the  $\alpha$ -phase. Finally it has been observed from the XANES analysis that the octahedral symmetry is retained. EXAFS analysis shows a small reduction in the average Fe-O interatomic distances. This highlights that the *Pnma* structure is well preserved in nanostructured  $\alpha$ - $\text{LiFePO}_4$  prepared by a microwave-assisted approach upon electrochemical delithiation, ideal for battery applications.

## Chapter 4: Deep eutectic solvents as media for microwave-assisted synthesis

Ionic media are superior at converting microwave irradiation to heat than polar media, such as polyols, due to strong interaction of ILs with the electric field of microwave irradiation through ionic conduction. It has also been shown in Chapter 3 and previous reports that ILs represent a viable and efficient synthesis media for nanostructured  $\alpha$ -LiFePO<sub>4</sub>.<sup>187</sup> However, large scale implementation of ILs in microwave synthetic applications is hindered by their air and/or moisture sensitivity, toxicity and in particular, high cost. Therefore, further investigations are required to find ionic media that keep the benefits and avert the disadvantages of ILs. One such promising family are the deep eutectic solvents (DES).

Simply DESs are comprised of a salt and a hydrogen bond donor or metal halide, at concentrations close to the eutectic point. This combination gives rise to a mixture with a relatively high boiling point and low vapour pressure.<sup>191</sup> One common DES, reline, is a 1:2 mixture of urea and the ammonium salt choline chloride (ChCl) shown in Figure 4.1.<sup>192</sup> The role of the hydrogen bond donor is to aid the dissociation of the salt by lowering the lattice energy, and therefore the melting temperature, of the salt through favourable intermolecular interactions.<sup>193</sup> More interestingly, however, this also promotes the dissociation of the salt to create free ions in solution, ideal for designing a candidate medium for microwave-assisted synthesis.

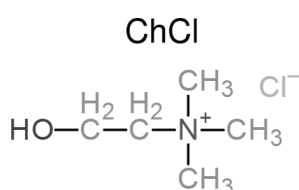


**Figure 4.1:** Chemical structure of choline chloride (ChCl).

The preparation of DESs can be performed with either a mixture of solids, liquids or a solid and a liquid. DESs can also be split into four sub-categories summarised in Table 4.1.<sup>193</sup> The group of immediate interest for microwave-assisted preparation of  $\alpha$ -LiFePO<sub>4</sub> are type III DESs since they do not contain metal salts which may react with the reagents used in the synthesis of  $\alpha$ -LiFePO<sub>4</sub>. Reline is a type III DES but there are issues with its use

Type	Salt	Metal salt/hydrogen bond donor
Type I	Imidazolium/Ammonium/Phosphonium	Metal halide
Type II	Imidazolium/Ammonium/Phosphonium	Hydrated metal halide
Type III	Imidazolium/Ammonium/Phosphonium	R-CONH, R-COOH or R-OH
Type IV	Metal halide	R-CONH or R-OH

**Table 4.1:** Composition of DES mixtures Type I, II, II and IV reproduced from Reference 193. All contain metals except which may contaminate synthesis of  $\alpha$ -LiFePO<sub>4</sub> except type III.

in the synthesis of  $\alpha$ -LiFePO<sub>4</sub> as the hydrogen bond donor (urea) begins decomposing at 133 °C to give ammonia gas.<sup>194</sup> An alternative is to employ hydrogen bond donors that have higher boiling points and better thermal stability in conjunction with ChCl. Polyols present themselves as prime hydrogen bond donor candidates due to their low or absent toxicity, low cost and ability to hydrogen bond through O-H functional groups.

The main aims of this Chapter are to provide alternative ionic media for the synthesis of  $\alpha$ -LiFePO<sub>4</sub>. Furthermore substitution of the hydrogen bond donor, ammonium salt and composition of the DES mixtures will be altered to provide a solvent with competitive heating capabilities to ILs. The morphology, crystallinity and cycling behaviour of the materials obtained will also be investigated.

## 4.1 Preparation of $\alpha$ -LiFePO<sub>4</sub> in diethylene glycol, tetraethylene glycol and glycerol based eutectics

Diethylene glycol (DEG), tetraethylene glycol (TEG), glycerol (Gly), glucose and sucrose were chosen as initial candidates as hydrogen bond donors for DES. When combined with ChCl in a 1:2 ChCl:hydrogen bond donor ratio all forming a clear liquid. 4 ml of each mixture was placed into a 10 ml reaction vessel and irradiated with microwaves until a temperature of 70 °C was reached. Once the solvent had reached 70 °C the power of microwave irradiation was allowed to vary to maintain a temperature of 70 °C. The temperature was held for 2 min, and the average power applied by the microwave was calculated. This was repeated in 10

°C steps up to 250 °C in 10 °C increments. The mixtures containing glucose and sucrose exceeded the safe pressure limit of the CEM Discover SP microwave synthesiser after 20 s of irradiation heating to 200 °C and were not investigated further. The recorded averages for power consumption of the DEG:ChCl and TEG:ChCl [(di)ethaline and (tetra)ethaline] as a function of temperature are given in Figure 4.2 (a).

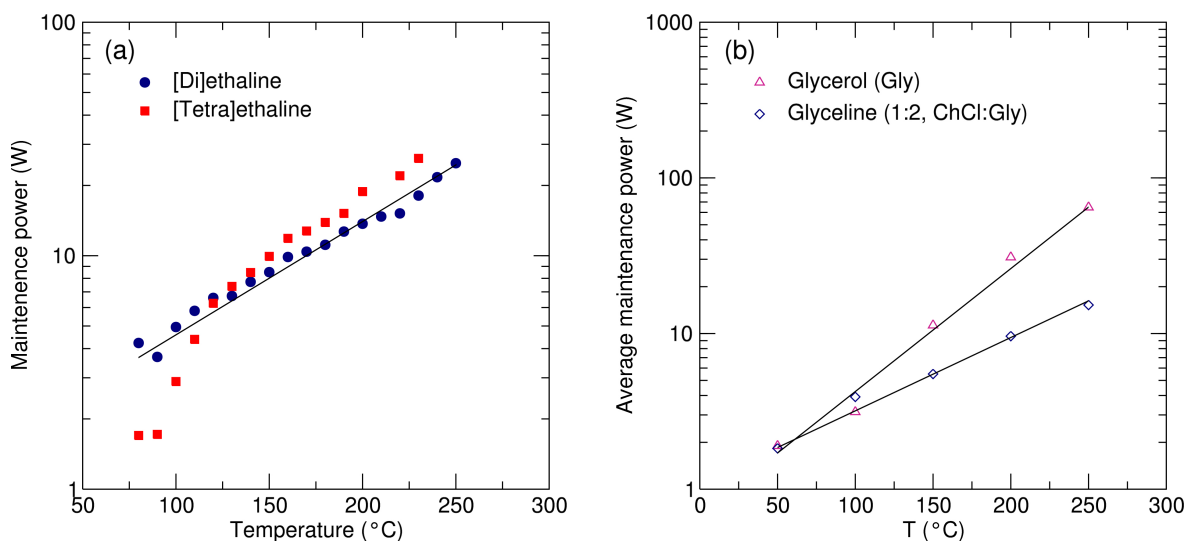


**Figure 4.2:** (a) Average power required to maintain a given temperature for 4 ml of (di)ethaline and (tetra)ethaline irradiated with microwaves ( $\nu = 2.45$  GHz). (b) Average power required to maintain a given temperature for 4 ml of glyceline or Gly irradiated with microwaves ( $\nu = 2.45$  GHz).

It is observed that as temperature increases the power required to heat the solvents also increases. It is also observed that the addition of the ammonium salt to diethylene glycol lowers power of microwave irradiation required from 60 W to 25 W (58 % reduction) at 250 °C. A similar relationship is also observed with tetra(ethaline), but the experiments conducted above 230 °C exceeded the safe pressure limit of the microwave synthesiser. The addition of ChCl to TEG provided a reduction in required power from 43 W to 27 W (37 % reduction).

Figure 4.2 (b) shows the average power of microwave irradiation (2.45 GHz) required to heat 4 ml of glyceline (2:1, Gly:ChCl) to temperatures between 70 °C and 250 °C, and a 4 ml Gly standard. The addition of ChCl to Gly lowers the power required to maintain all temperatures, similar to the EG and TEG syntheses. At the highest temperature of 250 °C

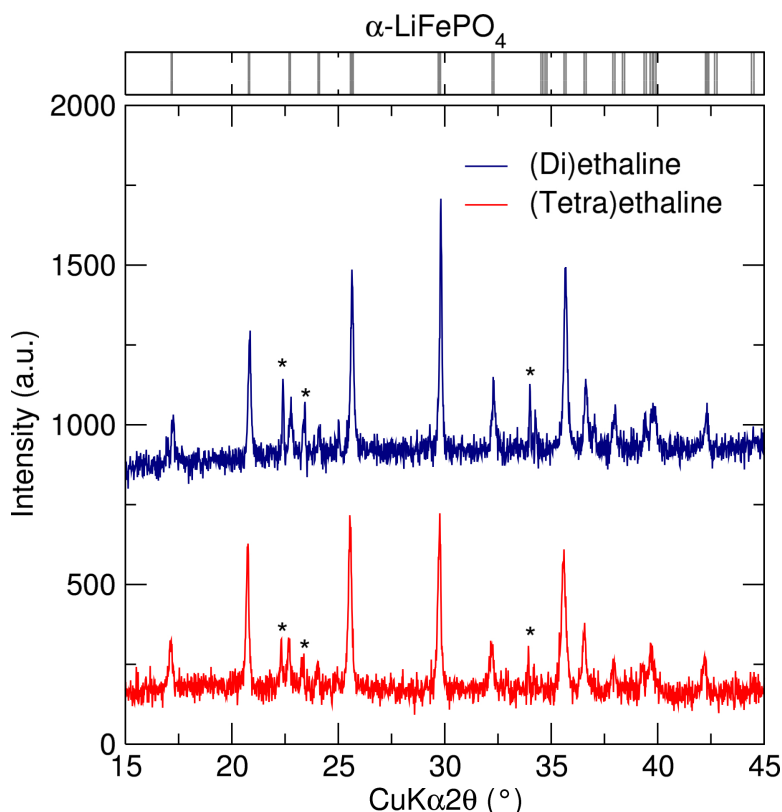


**Figure 4.3:** PXRD patterns collected for  $\alpha$ -LiFePO<sub>4</sub> syntheses conducted in a 1:2 molar ratio of ChCl and either DEG [(di)ethaline] or TEG [(tetra)ethaline] for 3 h at 220 °C.  $\alpha$ -LiFePO<sub>4</sub> and an impurity of Li<sub>3</sub>PO<sub>4</sub> (\*) is obtained in both cases.

the power is reduced from 65 W to 16 W (75 % reduction).

#### 4.1.1 Synthesis and characterisation of $\alpha$ -LiFePO<sub>4</sub> prepared in (di)ethaline, (tetra)ethaline and glyceline

Synthesis of  $\alpha$ -LiFePO<sub>4</sub> was attempted by adding a stoichiometric mixture of FeC<sub>2</sub>O<sub>4</sub> · 2 H<sub>2</sub>O (1 mmol) and LiH<sub>2</sub>PO<sub>4</sub> (1 mmol) in 4 ml of (di)ethaline or (tetra)ethaline in a 10 ml microwave vessel. The mixtures were irradiated with microwaves ( $\nu = 2.45$  GHz) for 3 h at 220 °C. In both cases  $\alpha$ -LiFePO<sub>4</sub> and an impurity of Li<sub>3</sub>PO<sub>4</sub> (\*) was obtained. An interesting observation in these synthesis is that there is no presence of  $\beta$ -LiFePO<sub>4</sub>, in contrast to the pure DEG and TEG syntheses.

PXRD of the glyceline syntheses after 3 h of microwave irradiation at 200 °C, 210 °C and 220 °C can be seen in Figure 4.4. Both  $\alpha$ -LiFePO<sub>4</sub> and an impurity phase of Li<sub>3</sub>PO<sub>4</sub> are

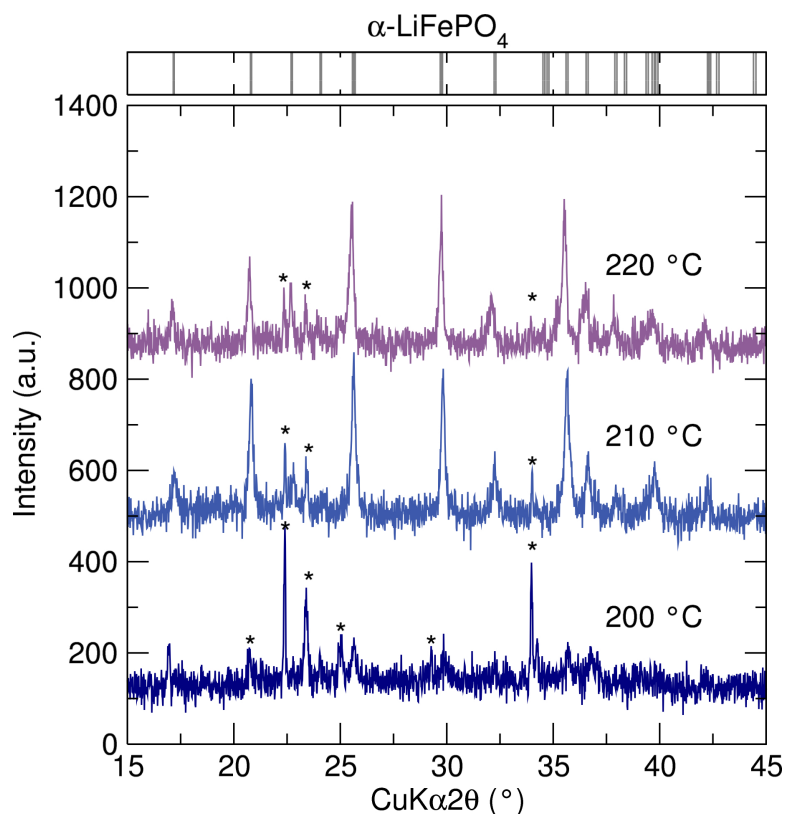


**Figure 4.4:** PXRD of products obtained from the microwave-assisted synthesis of  $\alpha$ -LiFePO<sub>4</sub> in a 1:2 ChCl:Gly after 3 h of irradiation.  $\alpha$ -LiFePO<sub>4</sub> and an impurity of Li<sub>3</sub>PO<sub>4</sub> (\*) is obtained at all temperatures.

obtained at all temperatures. As the synthesis temperature is decreased, the intensity of the diffraction peaks for Li<sub>3</sub>PO<sub>4</sub> increase relative to those for  $\alpha$ -LiFePO<sub>4</sub>, with Li<sub>3</sub>PO<sub>4</sub> present as the apparent majority phase at 200 °C. At temperatures above 220 °C the reactions surpassed the safe pressure limit CEM Discover SP microwave synthesiser.

Although pure  $\alpha$ -LiFePO<sub>4</sub> cannot be obtained with these solvents it provides a promising foundation to improve upon by adapting the synthetic methodology.

## 4.2 Microwave heating of ethaline

To find an alternative hydrogen bond donor capable of mediating the synthesis of pure  $\alpha$ -LiFePO<sub>4</sub> ethylene glycol was investigated (EG). A 1:2 molar mixture of ChCl and EG (ethaline) was irradiated with microwaves ( $\nu = 2.45$  GHz) until a set temperature between 50 °C and 250 °C was achieved, in 50 °C increments, and held for 2 minutes. The same procedure was adopted for a pure sample of EG as a standard. The average power required to maintain the temperature was calculated for each solvent over the 2 min period and is plotted as a function of temperature in Figure 4.5. The addition of ChCl to EG leads to a dramatic reduction in the power required to maintain the temperature of the solvent. A decrease in the power required from 131 W to 19 W (85.5%) is observed at 250 °C. These values are competitive to those observed for the ILs (12 W at 250 °C).

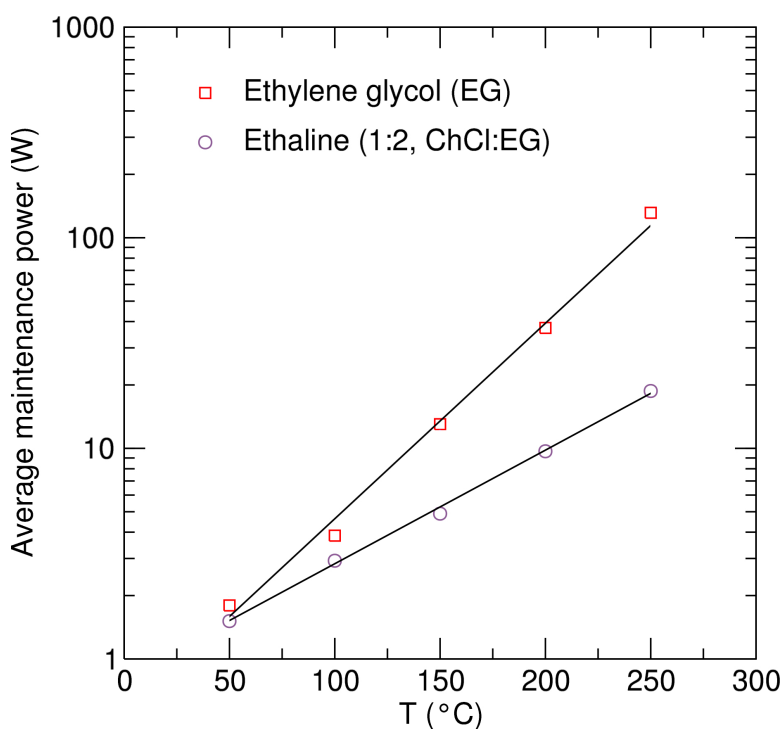


**Figure 4.5:** Power consumption versus temperature of pure ethylene glycol and ethaline in the CEM Discover SP microwave synthesiser ( $\nu = 2.45$  GHz).

The decomposition of ethaline upon microwave irradiation and heating was investigated using FTIR (Figure 4.6). Characteristic features for EG were observed at 3400  $\text{cm}^{-1}$  (O-H), 2800  $\text{cm}^{-1}$  (C-H) and 1040  $\text{cm}^{-1}$  (primary alcohol C-O). For ChCl characteristic peaks

were observed at  $3000\text{ cm}^{-1}$  (N-H ammonium),  $3300\text{ cm}^{-1}$  (C-H) and O-H stretch between  $3500\text{ cm}^{-1}$  and  $3000\text{ cm}^{-1}$ . When the two chemicals are combined the FTIR resembles a combination of the two separate components. The FTIR spectrum after heating to heating to  $250\text{ }^{\circ}\text{C}$  shows no significant change in the DES components up to this temperature, suggesting they can withstand the temperatures required for microwave-assisted synthesis of  $\alpha\text{-LiFePO}_4$ . A FTIR spectrum was also taken after attempting the synthesis of  $\alpha\text{-LiFePO}_4$  using stoichiometric quantities of  $\text{FeC}_2\text{O}_4 \cdot 2\text{H}_2\text{O}$  (1 mmol) and  $\text{LiH}_2\text{PO}_4$  (1 mmol) in 4 ml ethaline, reacted at  $250\text{ }^{\circ}\text{C}$  for 3 h. The mixture was irradiated with microwaves ( $\nu = 2.45\text{ GHz}$ ) for 3 hours at  $250\text{ }^{\circ}\text{C}$ . The solvent was filtered to separate the solvent from the solid material. FTIR of the ethaline post-synthesis shows the growth of a peak at  $1150\text{ cm}^{-1}$  characteristic of a C-O bond from a carboxylic acid. This feature appears due to the presence of oxalic acid from the  $\text{FeC}_2\text{O}_4 \cdot 2\text{H}_2\text{O}$  reagent.

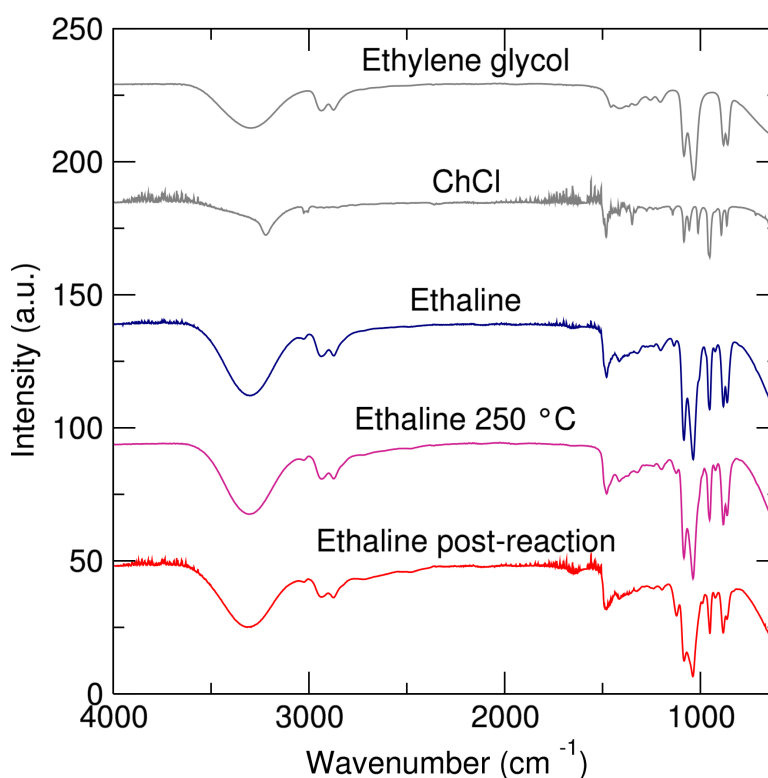


**Figure 4.6:** FTIR spectra of choline chloride and ethylene glycol and the mixture of the two (ethaline). The solvent shows good chemical stability upon heating to temperatures required for microwave-assisted synthesis of  $\alpha\text{-LiFePO}_4$  nanoparticles.

### 4.3 Ethaline mediated microwave-assisted synthesis of $\alpha$ -LiFePO<sub>4</sub>

#### 4.3.1 Structural characterisation of ethaline mediated $\alpha$ -LiFePO<sub>4</sub>

Microwave-assisted synthesis of  $\alpha$ -LiFePO<sub>4</sub> was performed using stoichiometric quantities of FeC<sub>2</sub>O<sub>4</sub> · 2H<sub>2</sub>O (1 mmol) and LiH<sub>2</sub>PO<sub>4</sub> (1 mmol) in ethaline. The mixtures were irradiated with microwaves ( $\nu = 2.45$  GHz) for 1 hour at temperatures between 200 °C and 250 °C. After washing and drying all syntheses yielded fine off-white powders and were interrogated using PXRD (Figure 4.7). It is observed that after 1 h of irradiation phase pure LiFePO<sub>4</sub> is only obtained at 250 °C. At temperatures lower than 250 °C an impurity of Li<sub>3</sub>PO<sub>4</sub> is observed (\*). It is also observed that as temperature increases the peaks attributable to  $\alpha$ -LiFePO<sub>4</sub> become narrower.

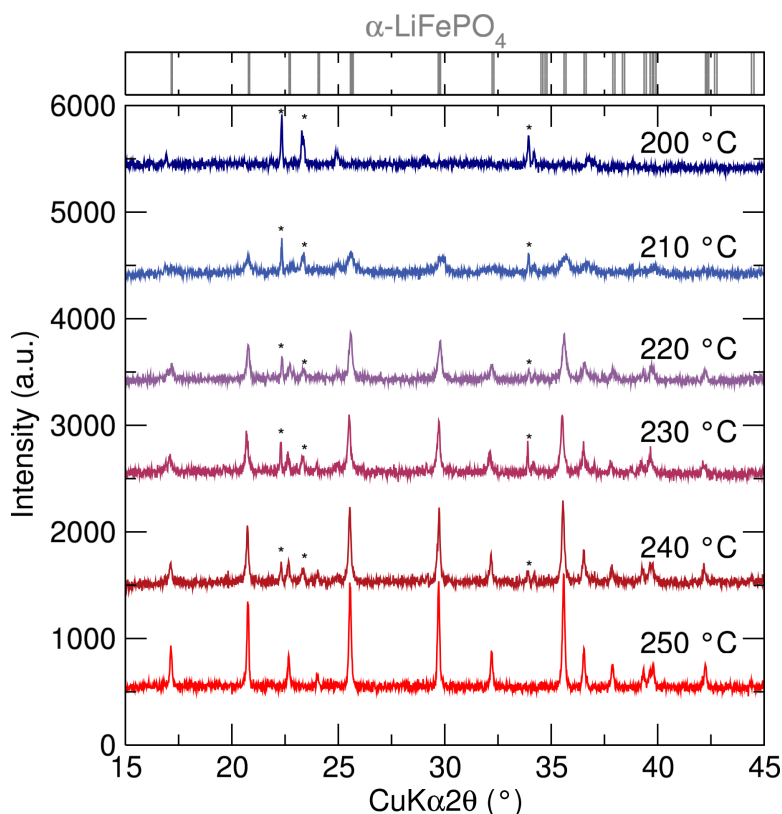


**Figure 4.7:** PXRD patterns for products obtained after 1 h microwave-assisted solvo-thermal preparation in ethaline and expected reflections for  $\alpha$ -LiFePO<sub>4</sub>.<sup>31</sup> Impurity peaks from Li<sub>3</sub>PO<sub>4</sub> are observed below 250 °C.

$\alpha$ -LiFePO<sub>4</sub> was also prepared by increasing the irradiation time to 3 h between 200 °C and 250 °C and the products were characterised using PXRD (Figure 4.7). It is observed that  $\alpha$ -LiFePO<sub>4</sub> can be obtained at 250 °C and 240 °C. Below 240 °C, an impurity of Li<sub>3</sub>PO<sub>4</sub> is present (\*). Similarly to the 1 h synthesis, peak broadening is observed at lower temperatures.

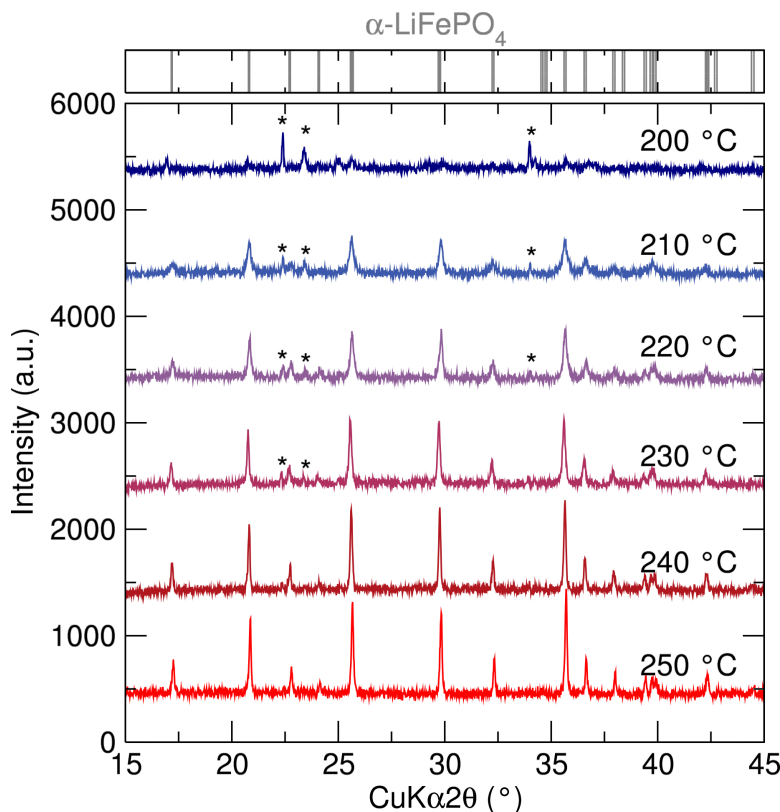


**Figure 4.8:** PXRD patterns for products obtained after 3 h microwave-assisted solvothermal preparation in ethaline and expected reflections for  $\alpha$ -LiFePO<sub>4</sub>.<sup>31</sup> Impurity peaks from Li<sub>3</sub>PO<sub>4</sub> are observed below 240 °C.

$\alpha$ -LiFePO<sub>4</sub> was prepared by further increasing the irradiation time to 5 h between 200 °C and 250 °C. It was found that the syntheses conducted at 240 °C and 250 °C exceeded the safe pressure limit of the CEM Discover SP microwave synthesiser after 3.5 h of irradiation and were stopped. Fine off-white powders were obtained at all temperatures consistent with the previous observations and characterised with PXRD (Figure 4.9). It is observed from the PXRD that pure  $\alpha$ -LiFePO<sub>4</sub> can be obtained at 220 °C and 230 °C.  $\alpha$ -LiFePO<sub>4</sub> can also be obtained at 240 °C and 250 °C regardless of exceeding the pressure limit, however these

materials were not investigated further due to lack of control over the synthetic procedure. Below 220 °C an impurity of  $\text{Li}_3\text{PO}_4$  is observed (\*). Peak sharpening is observed with increasing irradiation time from 200 °C to 230 °C. This relationship is interrupted at 240 °C where the peaks become broader due to the lower reaction time. The sharpening then continues again at 250 °C.

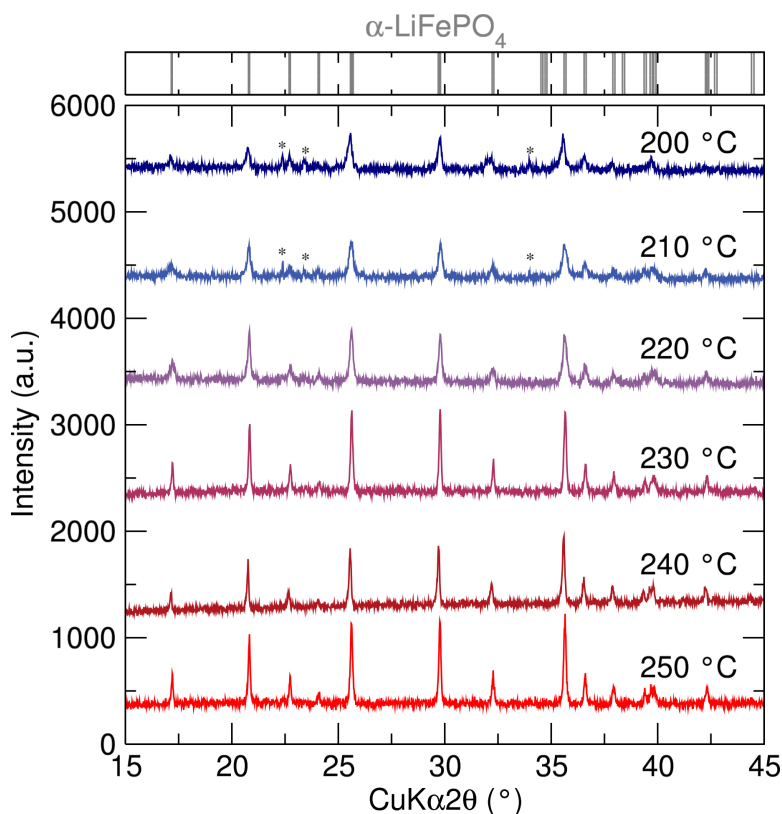


**Figure 4.9:** PXRD patterns for products obtained after 5 h microwave-assisted solvo-thermal preparation in ethaline and expected reflections for  $\alpha\text{-LiFePO}_4$ .<sup>31</sup> Impurity peaks from  $\text{Li}_3\text{PO}_4$  are observed below 220 °C.

The observations from the PXRD confirm that increasing the irradiation time allows  $\alpha\text{-LiFePO}_4$  to be obtained at lower temperatures. Furthermore increasing irradiation temperature or irradiation time can lead to sharpening of diffraction peaks. Another important observation is that  $\beta\text{-LiFePO}_4$  is not present at any temperature or time in 2:1 ethaline media. This suggests an alternate reaction pathway is present, promoting  $\alpha\text{-LiFePO}_4$  as the kinetic product in ethaline.

SEM was employed to investigate the morphology of materials prepared at the lowest

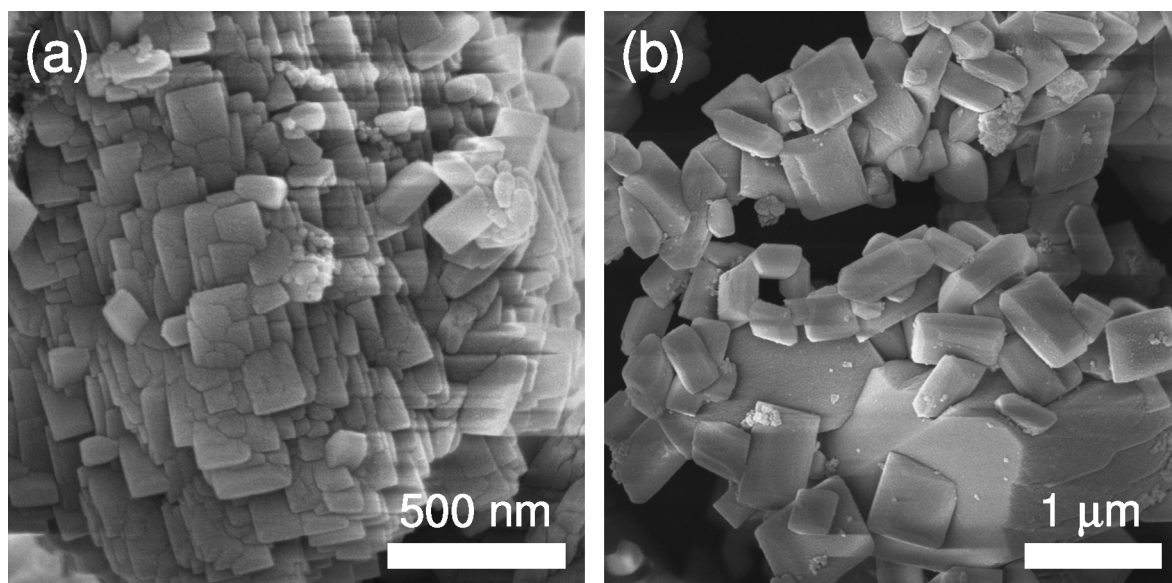


**Figure 4.10:** SEM images of  $\alpha$ -LiFePO<sub>4</sub> prepared in 1:2 ethaline after 5h of  $\mu\lambda$  irradiation at (a) 220 °C and (b) 230 °C.

temperatures after the full 5 h of microwave irradiation (Figure 4.10).  $\alpha$ -LiFePO<sub>4</sub> obtained after 220 °C of microwave irradiation for 5 h (a) exhibits platelets typically 100 nm to 300 nm in diameter and 70 nm in thickness.  $\alpha$ -LiFePO<sub>4</sub> obtained at 230 °C exhibits a mixture of much smoother, faceted particles than the 220 °C sample (typically 500 nm to 800 nm in length, 250 nm to 500 nm in width and typically 250 nm in thickness) and larger poorly-defined micron-sized particles.

## 4.4 Effect of choline chloride concentration on ethaline mediated microwave-assisted synthesis of $\alpha$ -LiFePO<sub>4</sub>

### 4.4.1 Effect of salt concentration on microwave heating properties in 1:3 ethaline and 2:3 ethaline

Due to the success of synthesising  $\alpha$ -LiFePO<sub>4</sub> in 1:2 ethaline more investigations were conducted in an attempt to obtain phase pure material at lower times and temperatures. The first of these studies was to change the ratio of ChCl to EG in the solvent to monitor its effect on phase purity. Molar mixtures of 1:3 and 2:3 ChCl:EG (1:3 ethaline and 2:3 ethaline, respectively) were prepared to study the effect of salt concentration on the microwave properties. At higher ChCl concentrations than 2:3 the solution became saturated and ChCl precipitated out. These mixtures were not investigated further.

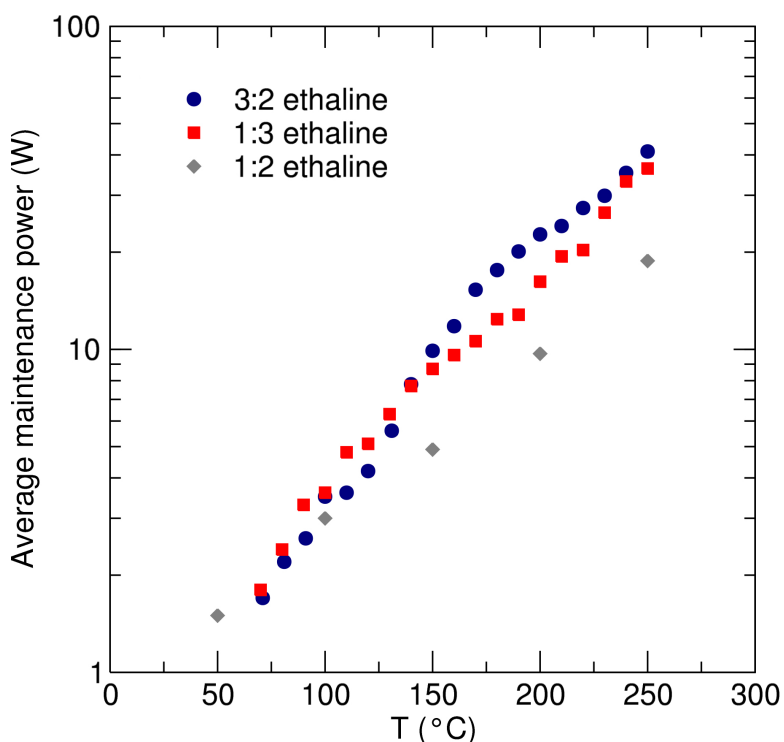


**Figure 4.11:** Average power required to maintain a temperature of 4 ml of 1:3 ethaline or 2:3 ethaline with microwave irradiation ( $\nu = 2.45$  GHz) showing an increase in both cases versus the results for 1:2 ethaline.

Figure 4.11 (a) shows the average microwave power required to maintain temperatures

between 70 °C and 250 °C of 4 ml 2:3 ethaline and 1:3 ethaline. The values obtained for 1:2 ethaline are also included for comparison. Above 150 °C 2:3 ethaline and 1:3 ethaline require significantly more power to maintain the temperatures (41 W and 36 W at 250 °C respectively) than compared with 1:2 ethaline (19 W at 250 °C).

#### 4.4.2 Synthesis and characterisation of $\alpha$ -LiFePO<sub>4</sub> 1:3 ethaline

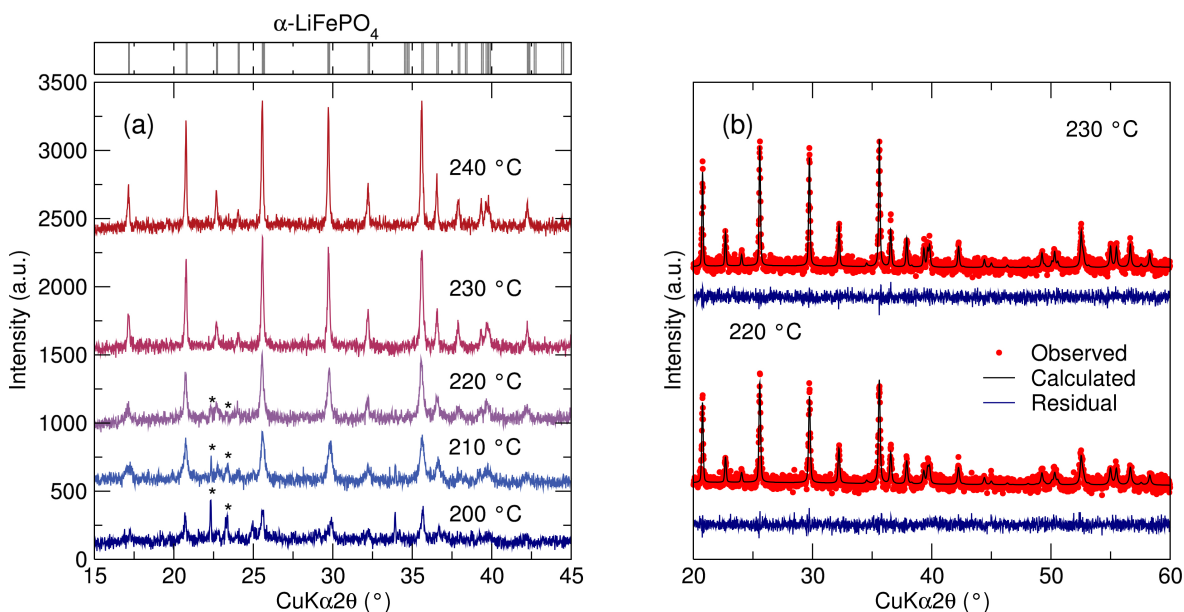


**Figure 4.12:** (a) PXRD  $\alpha$ -LiFePO<sub>4</sub> synthesised in a 1:3, ChCl:EG molar mixture. Below 230 °C an impurity of Li<sub>3</sub>PO<sub>4</sub> is observed (\*). (b) Rietveld refinement of PXRD data collected for  $\alpha$ -LiFePO<sub>4</sub> prepared in 1:3 ethaline at 230 °C and 240 °C after 3 h of microwave irradiation ( $\nu = 2.45$  GHz). A good fit to the ICSD literature pattern is observed in both cases.<sup>31</sup>

1:3 ethaline was employed as the solvent in the microwave-assisted preparation of  $\alpha$ -LiFePO<sub>4</sub>. Stoichiometric quantities of FeC<sub>2</sub>O<sub>4</sub> · 2 H<sub>2</sub>O (1 mmol) and LiH<sub>2</sub>PO<sub>4</sub> (1 mmol) were mixed in 4 ml of 1:3 ethaline in a 10 ml microwave vessel and irradiated with microwaves for 3 h at temperatures between 200 °C and 250 °C. Figure 4.12 (a) shows the powder XRD patterns collected for the syntheses carried out in 1:3 ethaline for 3 h. It is observed that  $\alpha$ -LiFePO<sub>4</sub> is obtained at all temperatures, however below 230 °C an impurity of Li<sub>3</sub>PO<sub>4</sub> is present. Furthermore, as temperature decreases the diffraction peaks for  $\alpha$ -LiFePO<sub>4</sub> become sharper. This is indicative of an increase in crystallinity which may be due to particle size or morphology.

Rietveld refinement was conducted on the pure  $\alpha$ -LiFePO<sub>4</sub> to investigate the structural similarities to a literature standard. A good fit to the ICSD reference pattern is observed.<sup>31</sup> The parameters calculated from Rietveld refinement can be seen in Table 4.2.

SEM was employed to investigate the morphological differences of pure  $\alpha$ -LiFePO<sub>4</sub> prepared in 1:3 ethaline at 230 °C (Figure 4.13 a) and 240 °C (Figure 4.13 b). It is observed that both samples exhibit particles smaller than 1  $\mu$ m, although at this resolution no indication of particle shape is available.

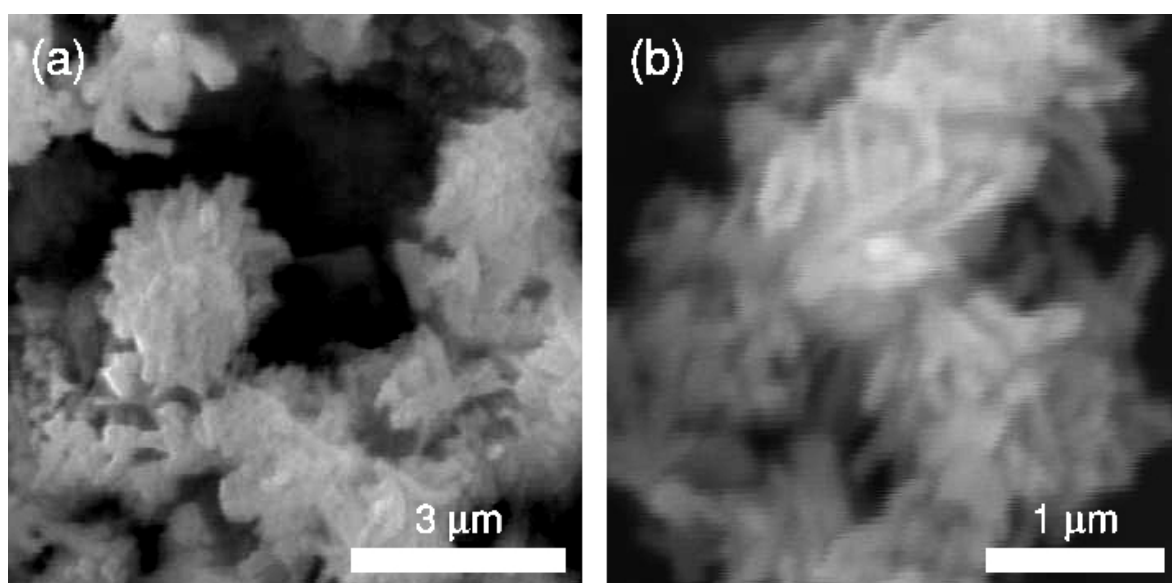


**Figure 4.13:** SEM images of  $\alpha$ -LiFePO<sub>4</sub> prepared in 1:3 ethaline at (a) 230 °C and (b) 240 °C after 3 h of microwave irradiation ( $\nu = 2.45$  GHz).

#### 4.4.3 Electrochemical analysis $\alpha$ -LiFePO<sub>4</sub> of 1:3 ethaline

The electrochemical performance of  $\alpha$ -LiFePO<sub>4</sub> prepared in 1:3 ethaline after 3 h of microwave irradiation ( $\nu = 2.45$  GHz) was investigated using GCPL. All electrochemical tests were conducted by first carbon coating  $\alpha$ -LiFePO<sub>4</sub> with sucrose (15 % C by weight) in an Ar atmosphere at 700 °C. The carbon coated  $\alpha$ -LiFePO<sub>4</sub> samples were mixed with carbon black and PTFE binder in the ratios 30:60:10. 10 mg pellets of the resulting mixtures were pressed under 1.2 T of pressure and used as the cathode in a Swagelok cell employing Li metal as the counter electrode, a glass fibre separator and LiPF<sub>6</sub> in EC:DMC as the electrolyte.

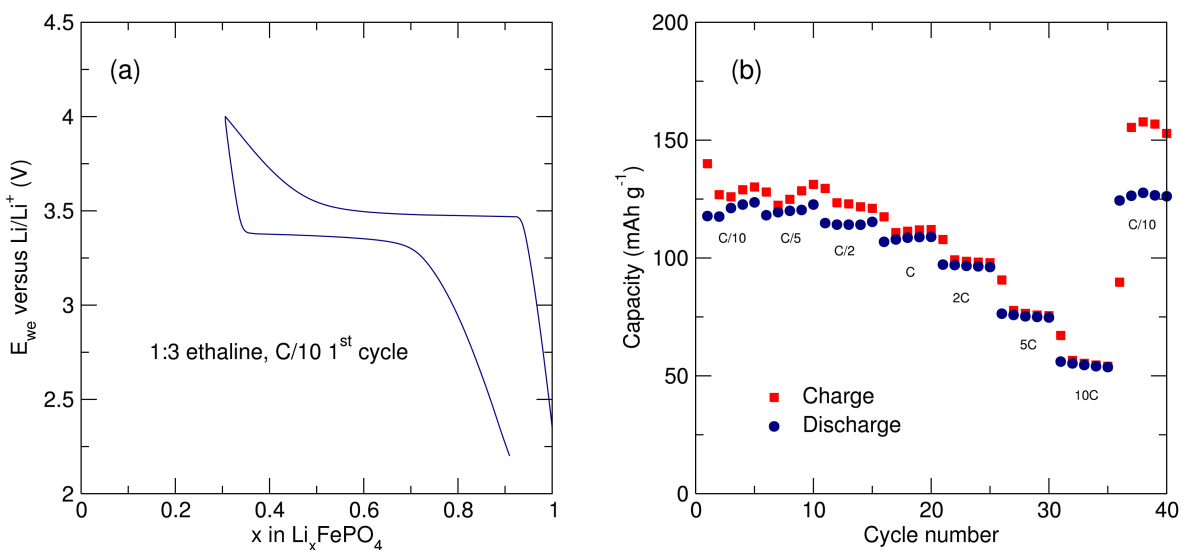


**Figure 4.14:** (a) First charge and discharge cycle from GCPL of carbon coated  $\alpha$ -LiFePO<sub>4</sub> synthesised in 1:3 ethaline at 240 °C. Cycling was carried out at a C/10 rate between 2.2 V and 4 V. (b) GCPL of  $\alpha$ -LiFePO<sub>4</sub> synthesised in 1:3 ethaline for 3 h at 240 °C at increasing rates.

Figure 4.14 (a) shows the first charge and discharge cycle for  $\alpha$ -LiFePO<sub>4</sub> prepared in 1:3 ethaline at 240 °C for 3 h at a C/10 rate between 2.2 V and 4 V. It is observed that the profile exhibits a stable plateau around 3.45 V characteristic of the Fe<sup>2+</sup>/Fe<sup>3+</sup> redox couple in  $\alpha$ -LiFePO<sub>4</sub>.<sup>19</sup> During electrochemical charging 0.7 Li<sup>+</sup> is extracted from  $\alpha$ -LiFePO<sub>4</sub>. However only 0.6 Li<sup>+</sup> is reversibly inserted back into the structure during electrochemical discharge leading to a Coloumbic efficiency of only 85 %. To investigate the rate capability of carbon coated  $\alpha$ -LiFePO<sub>4</sub> prepared in 1:3 ethaline experiments were conducted at increasing rates (Figure 4.14 b).

As the rate increases, the discharge and charge capacities both decrease. The material exhibits an average charge and discharge capacity of 130 mAh g<sup>-1</sup> and 121 mAh g<sup>-1</sup> respectively at the slowest rate (C/10). These capacities diminish significantly at the highest rate (10C) to a charge and discharge capacity of 58 mAh g<sup>-1</sup> and 53 mAh g<sup>-1</sup>, well below the theoretical capacity of  $\alpha$ -LiFePO<sub>4</sub> (170 mAh g<sup>-1</sup>). This has previously been attributed to slow intercalation kinetics of Li<sup>+</sup> into  $\alpha$ -LiFePO<sub>4</sub> through 1D channels at high rates, compared to layered materials.<sup>195,196</sup> These electrochemical results are not competitive to previous reports of microwave prepared  $\alpha$ -LiFePO<sub>4</sub> in the literature (160 mAh g<sup>-1</sup> at C/10), but are an

improvement on the results obtained for the IL synthesis ( $105 \text{ mAh g}^{-1}$ ).<sup>150</sup>

#### 4.4.4 Synthesis and characterisation of $\alpha\text{-LiFePO}_4$ 2:3 ethaline

Synthesis of  $\alpha\text{-LiFePO}_4$  was conducted in 2:3 ethaline by microwave-assisted in a similar manner. PXRD patterns for the syntheses carried out in 2:3 ethaline for 1 h at increasing temperatures are shown in Figure 4.15 (a).  $\alpha\text{-LiFePO}_4$  was obtained in all cases with an impurity of  $\text{Li}_3\text{PO}_4$  present at temperatures below  $230^\circ\text{C}$ . As the temperature is increased, the diffraction peaks become sharper indicating an increase in crystallinity.

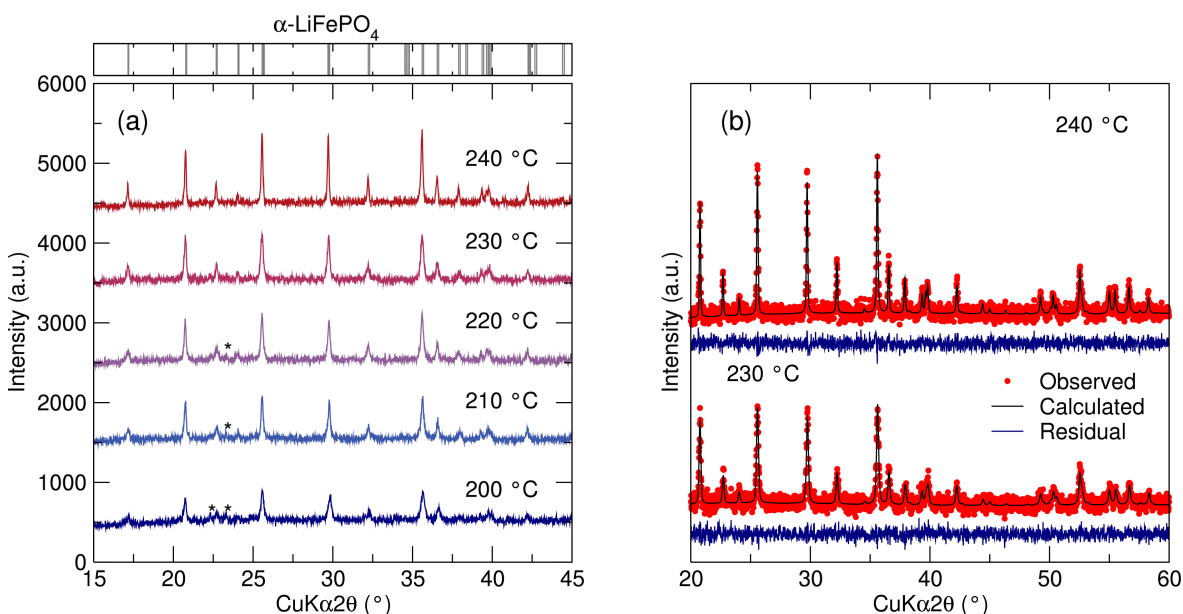


**Figure 4.15:** (a) PXRD of  $\alpha\text{-LiFePO}_4$  prepared in 2:3 ethaline after 1 h of microwave irradiation ( $\nu = 2.45 \text{ GHz}$ ). Peaks from an impurity of  $\text{Li}_3\text{PO}_4$  are denoted by \*. (b) Rietveld refinement of PXRD data collected for  $\alpha\text{-LiFePO}_4$  prepared in 2:3 ethaline at  $230^\circ\text{C}$  and  $240^\circ\text{C}$  after 1 h of microwave irradiation ( $\nu = 2.45 \text{ GHz}$ ). A good fit to the ICSD literature pattern is observed in both cases.

31

Figure 4.15 (b) shows Rietveld refinement conducted on the pure  $\alpha\text{-LiFePO}_4$  prepared in 2:3 ethaline at  $230^\circ\text{C}$  and  $240^\circ\text{C}$  after 1 h of microwave irradiation ( $\nu = 2.45 \text{ GHz}$ ). A good fit to the ICSD reference pattern is observed with the parameters calculated from Rietveld refinement given in Table 4.3.

In an attempt to obtain phase pure  $\alpha\text{-LiFePO}_4$  at lower temperatures, and to investigate

the effect of temperature on the morphology obtained, syntheses were conducted for 3 h of microwave irradiation. PXRD patterns for  $\alpha$ -LiFePO<sub>4</sub> prepared in 2:3 ethaline after 3 h of microwave irradiation can be seen in Figure 4.16 (a). Initial observations reveal a stark contrast to the pure EG synthesis with no presence of Li<sub>3</sub>PO<sub>4</sub> or  $\beta$ -LiFePO<sub>4</sub>, even at 200 °C. The reaction at 250 °C exceeded the safe pressure limit of 300 psi after 45 min and therefore did not reach completion. It is observed that as the synthesis temperature increases the peaks become sharper similar to the 1 h synthesis.

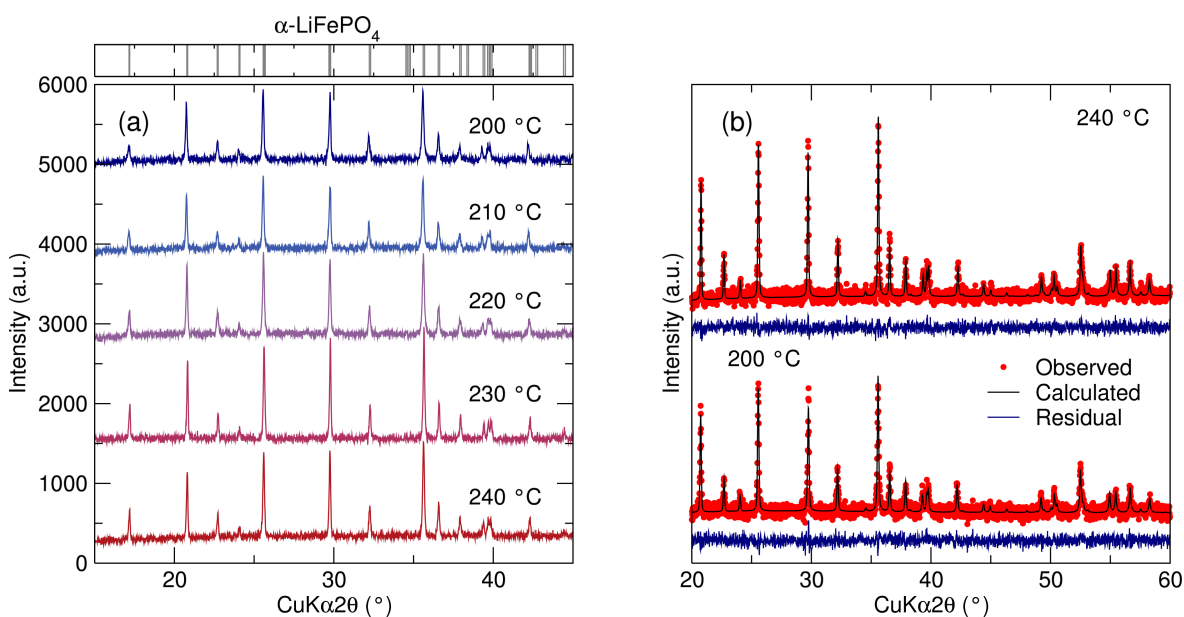


**Figure 4.16:** (a) PXRD patterns collected for the synthesis of  $\alpha$ -LiFePO<sub>4</sub> in 2:3 ethaline after 3 h of microwave irradiation ( $\nu = 2.45$  GHz). Phase pure  $\alpha$ -LiFePO<sub>4</sub> is obtained at all temperatures with peak broadening observed with decreasing temperature. (b) Rietveld refinement of PXRD data collected for  $\alpha$ -LiFePO<sub>4</sub> prepared in 2:3 ethaline at 200 °C and 240 °C after 3 h of microwave irradiation ( $\nu = 2.45$  GHz). A good fit to the ICSD literature pattern is observed in both cases.<sup>31</sup>

Figure 4.16 (b) shows Rietveld refinement conducted on the pure  $\alpha$ -LiFePO<sub>4</sub> prepared in 2:3 ethaline at 200 °C and 240 °C after 3 h of microwave irradiation ( $\nu = 2.45$  GHz). A good fit to the ICSD reference pattern is observed.<sup>31</sup> The parameters calculated from Rietveld refinement can be seen in Table 4.4.

SEM images were collected for the 2:3, 3 h ethaline  $\alpha$ -LiFePO<sub>4</sub> to investigate the morphology of the particles obtained. The 200 °C  $\alpha$ -LiFePO<sub>4</sub> (Figure 4.17 a) exhibited platelets

with a typical length of 1  $\mu\text{m}$ , width of 700 nm, and thickness of 50 nm. The 210  $^{\circ}\text{C}$  sample (Figure 4.17 b) also exhibits platelets that are much more regular in size and shape than the 200  $^{\circ}\text{C}$  with similar dimensions. The 220  $^{\circ}\text{C}$  sample (Figure 4.17 c) exhibited inhomogenous particles ranging from approximately 200 nm diameter crystallites to 1.5  $\mu\text{m}$  length particles. At 230  $^{\circ}\text{C}$  (Figure 4.17 d) more globular particles are observed with one or all dimensions above 1  $\mu\text{m}$ . This increase in particles size is also seen at 240  $^{\circ}\text{C}$  (Figure 4.17 e).

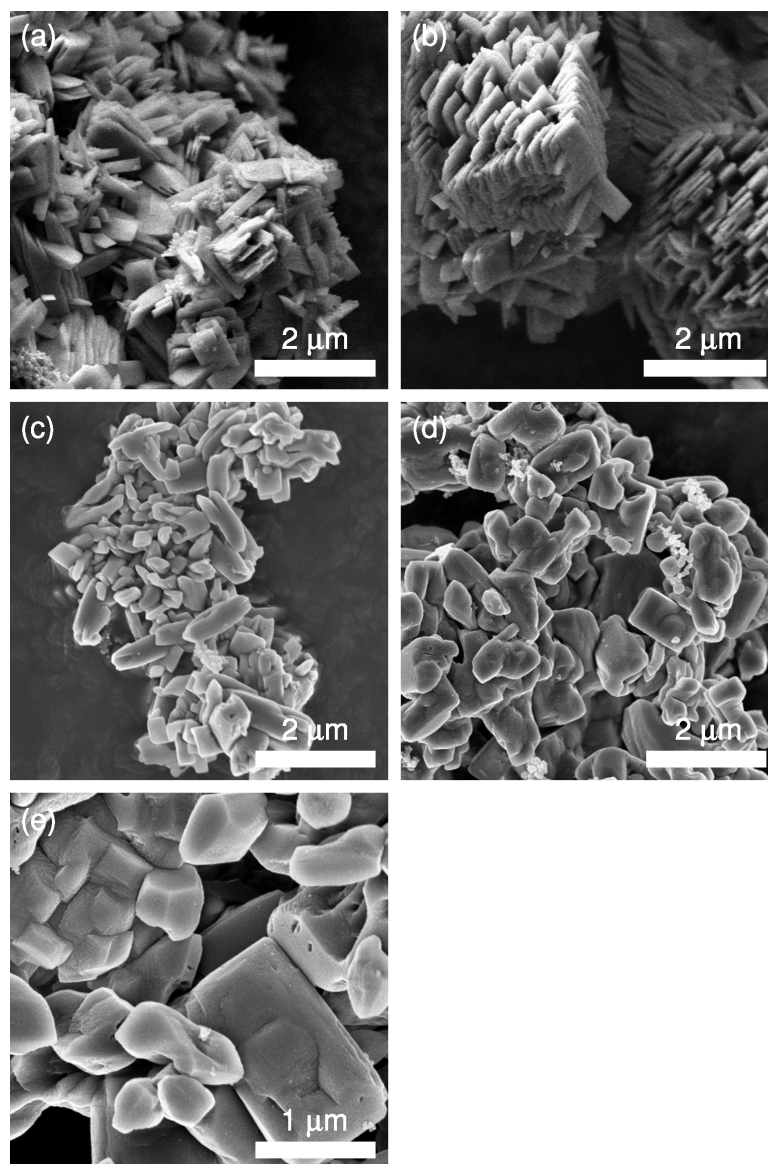


**Figure 4.17:** SEM images of  $\alpha$ -LiFePO<sub>4</sub> prepared in 2:3 ethaline after 3 h of irradiation at (a) 200 °C, (b) 210 °C, (c) 220 °C, (d) 230 °C and (e) 240 °C.

Reactions were also performed at 5 hours of microwave irradiation to further examine the effect of reaction time on the resulting particle morphology. Figure 4.18 (a) shows the PXRD patterns collected for the syntheses conducted in 2:3 ethaline at after 5 h of microwave irradiation ( $\nu = 2.45$  GHz). Phase pure  $\alpha$ -LiFePO<sub>4</sub> is obtained at all temperatures, however at temperatures above 230 °C the synthesis exceeded the pressure limit of the microwave synthesiser and did not reach completion. A large difference in peak broadening is observed at 200 °C compared with the higher temperatures indicating a distinct difference in crystallinity.

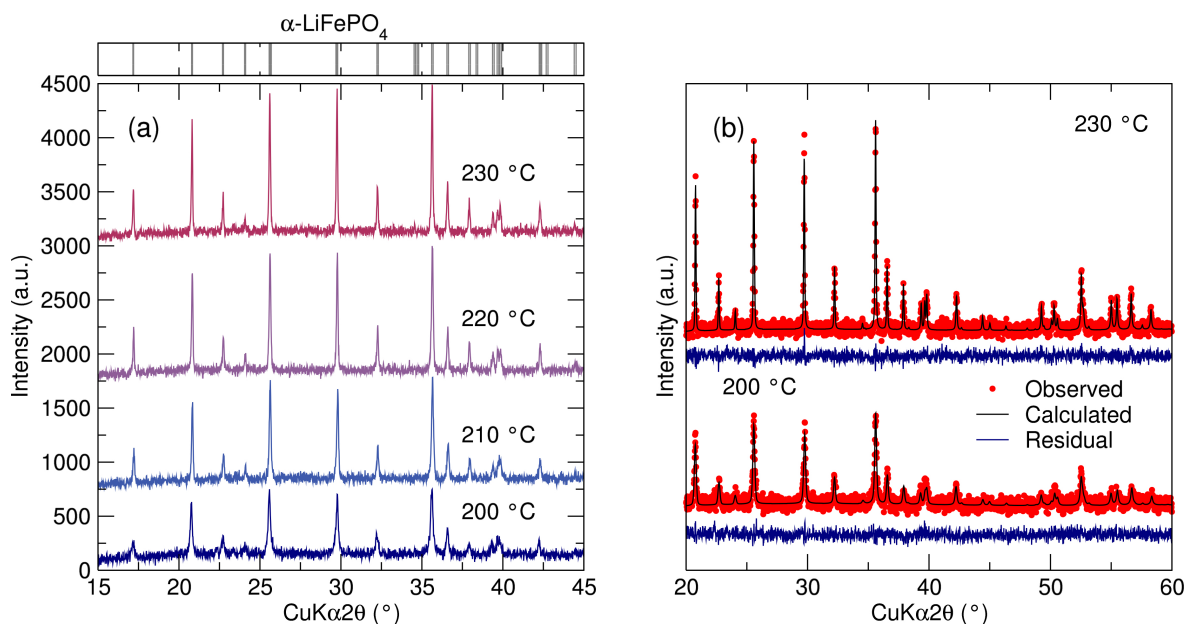


**Figure 4.18:** (a) PXR D patterns collected for the synthesis of  $\alpha$ -LiFePO<sub>4</sub> in 2:3 ethaline after 5 h of microwave irradiation ( $\nu = 2.45$  GHz). Phase pure  $\alpha$ -LiFePO<sub>4</sub> is obtained at all temperatures with peak broadening observed with decreasing synthesis temperature. (b) Rietveld refinement of PXR D data collected for  $\alpha$ -LiFePO<sub>4</sub> prepared in 2:3 ethaline at 200 °C and 230 °C after 5 h of microwave irradiation ( $\nu = 2.45$  GHz). A good fit to the ICSD literature pattern is observed in both cases.<sup>31</sup>

Figure 4.18 (b) shows Rietveld refinement conducted on the pure  $\alpha$ -LiFePO<sub>4</sub> prepared in 2:3 ethaline at 200 °C and 230 °C after 5 h of microwave irradiation ( $\nu = 2.45$  GHz). A good fit to the ICSD reference pattern is observed.<sup>31</sup> The parameters calculated from Rietveld refinement can be seen in Table 4.5.

SEM images collected for  $\alpha$ -LiFePO<sub>4</sub> prepared in 2:3 ethaline after 5 h of microwave irradiation and can be seen in Figure 4.19. The 200 °C 5 h 2:3 ethaline  $\alpha$ -LiFePO<sub>4</sub> (Figure 4.19 a) exhibited cubic particles with all dimensions typically below 200 nm. At 210 °C (Figure 4.19 b) the particles lose their definition which could be due particle agglomeration. At 220 °C (Figure 4.19 c) there are presence of additional small particles is reduced however the morphology is still irregular with many particles exhibiting at least one dimension over 1  $\mu$ m. The 230 °C 5 h 2:3 ethaline  $\alpha$ -LiFePO<sub>4</sub> (Figure 4.19 d) exhibited highly faceted particles similar in shape to the 230 °C 1:2 ethaline  $\alpha$ -LiFePO<sub>4</sub>, with a large size dispersion.

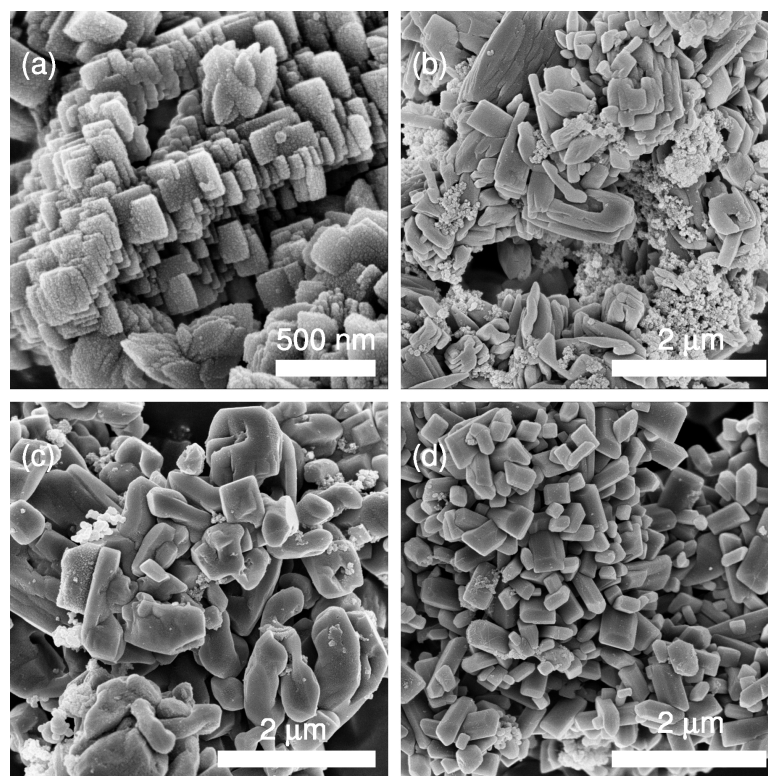


**Figure 4.19:** SEM images of  $\alpha$ -LiFePO<sub>4</sub> prepared in 2:3 ethaline at (a) 200 °C, (b) 210 °C, (c) 220 °C and (d) 230 °C.

The particles range from 150 nm to 1 μm in length, 100 nm to 600 nm in width and 50 nm to 250 nm in thickness. These particles have a larger variation in size in the sample than those prepared at 230 °C 5 h 1:2 ethaline, but with no evidence for multimicron sized particles.

The electrochemical performance of  $\alpha$ -LiFePO<sub>4</sub> prepared in 2:3 ethaline after 3 h of irradiation was investigated using GCPL similar to previous tests (Section 4.4.3). Samples prepared at 200 °C, 220 °C and 240 °C showed the most morphological variation, and were studied to provide insight into the effect of morphology on electrochemical performance. Figure 4.20 shows the 2:3 ethaline 3 h samples at 200 °C, 220 °C and 240 °C after carbon coating. It is observed that the *Pnma* structure of the  $\alpha$ -LiFePO<sub>4</sub> is preserved after the heat treatment with no impurities present for all samples.

Figure 4.21 (a) shows the first charge and discharge cycle for carbon coated  $\alpha$ -LiFePO<sub>4</sub> prepared in 2:3 ethaline after 3 h of irradiation. It is observed that all samples exhibit a stable plateau around 3.45 V typical of the Fe<sup>2+</sup>/Fe<sup>3+</sup> redox couple in  $\alpha$ -LiFePO<sub>4</sub>.<sup>19</sup> The sample prepared at 200 °C shows the highest Li<sup>+</sup> deintercalation of the three samples (0.9 Li<sup>+</sup> per

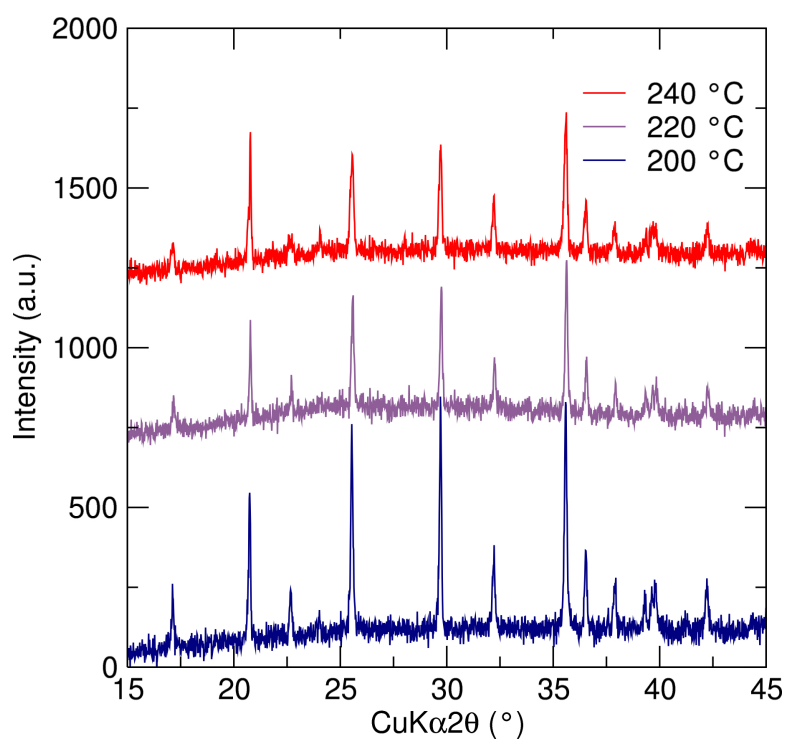


**Figure 4.20:** PXRD of  $\alpha$ -LiFePO<sub>4</sub> prepared in 2:3 ethaline at 200 °C, 220 °C and 240 °C after carbon coating with sucrose and annealing at 700 °C. Phase purity of the *Pnma* structured  $\alpha$ -LiFePO<sub>4</sub> is retained in all samples.

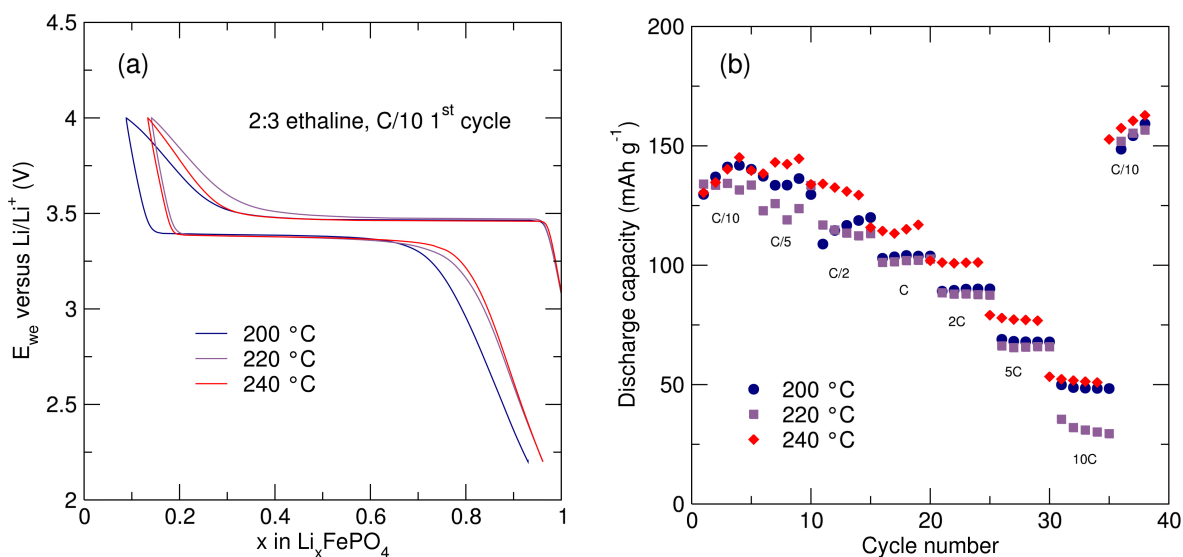


**Figure 4.21:** (a) First charge and discharge cycle from GCPL of carbon coated  $\alpha$ -LiFePO<sub>4</sub> synthesised in 2:3 ethaline after 3 h of microwave irradiation at 200 °C, 220 °C and 240 °C. Cycling was carried out at a C/10 rate between 2.2 V and 4 V. (b) GCPL of carbon coated  $\alpha$ -LiFePO<sub>4</sub> synthesised in 2:3 ethaline for 3 h between 2.2 V and 4 V. The rate capability shows that the 240 °C has a superior discharge capacity at all rates compared to 200 °C.

formula unit, 153 mAh g<sup>-1</sup>). However, all three temperatures exhibit similar behaviour upon the intercalation step with the reinsertion of 0.8 Li<sup>+</sup> per formula unit, due to irreversible Li<sup>+</sup> extraction. The rate behaviour of the samples prepared in 2:3 ethaline was also investigated (Figure 4.21 b).

The sample prepared at 240 °C exhibits consistently higher capacities at all rates above C/5, with a capacity retention of 142 mAh g<sup>-1</sup> at the initial C/10 and 53 mAh g<sup>-1</sup> at the highest rate of 10C. The 220 °C sample exhibits the lowest capacity at all rates with an average capacity of 130 mAh g<sup>-1</sup> for the initial C/10 and 32 mAh g<sup>-1</sup> at 10 C. The 200 °C sample exhibits a similar average capacity to the sample prepared at 240 °C (141 mAh g<sup>-1</sup>) and a similar capacity at 10C of 54 mAh g<sup>-1</sup>. This highlights that materials with similar electrochemical performance at the highest rate studied can be obtained at the lower synthesis temperature of 200 °C. Again, the discharge capacities observed are still lower than the best literature reports (160 mAh g<sup>-1</sup> at C/10), but improve upon the materials synthesised in 1:3 ChCl:EG.<sup>150</sup>

PXRD patterns of the samples post-cycling (Figure 4.22) reveal the retention of the *Pnma*

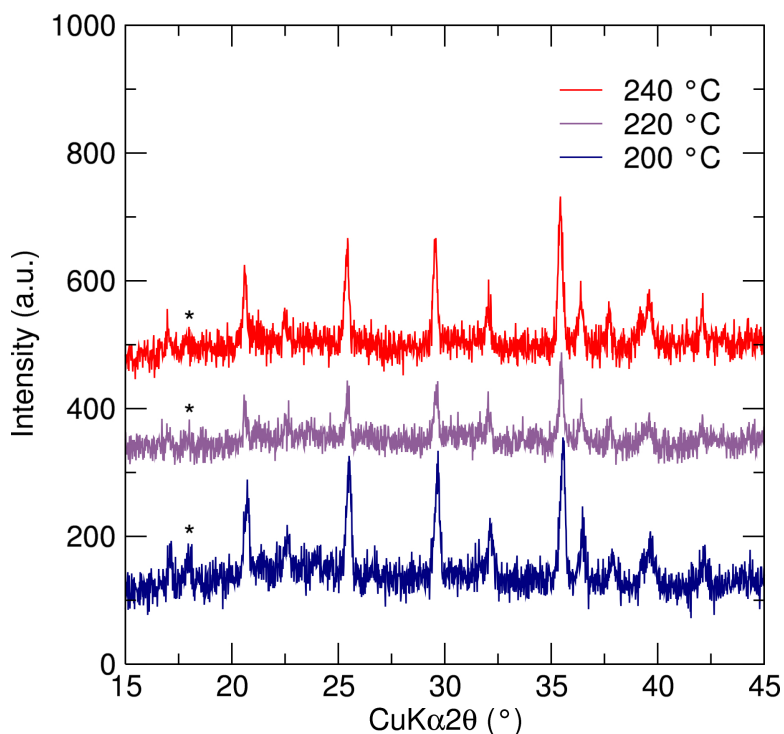


**Figure 4.22:** PXRD of  $\alpha$ -LiFePO<sub>4</sub> prepared in 2:3 ethaline at 200 °C, 220 °C and 240 °C post-cycling. The *Pnma* structure of  $\alpha$ -LiFePO<sub>4</sub> is retained in all samples with the evolution of FePO<sub>4</sub> (\*) due to irreversible Li<sup>+</sup> deintercalation.

$\alpha$ -LiFePO<sub>4</sub> structure however one extra peak (\*) is present from FePO<sub>4</sub>. This occurs as the lithium reinsertion into LiFePO<sub>4</sub> was not fully achieved during electrochemical cycling of the electrodes. The presence of diffraction peaks from FePO<sub>4</sub> is in good agreement with studies of chemical delithiation of  $\alpha$ -LiFePO<sub>4</sub> where the emergence of the FePO<sub>4</sub> peaks grow with decreasing lithium content in LiFePO<sub>4</sub>.<sup>197</sup>



2:3 $\alpha$ -LiFePO <sub>4</sub> (240 °C)		2:3 $\alpha$ -LiFePO <sub>4</sub> (230 °C)	
<b>Space group</b>	<i>Pnma</i>	<b>U</b>	0.03(3)
<b>a (Å)</b>	10.3284(8)	<b>V</b>	0.00(2)
<b>b (Å)</b>	6.0052(5)	<b>W</b>	0.013(3)
<b>c (Å)</b>	4.6929(5)	<b>R<sub>p</sub></b>	3.66
		<b>R<sub>wp</sub></b>	4.59
		<b>R<sub>exp</sub></b>	4.33
		<b>X<sup>2</sup></b>	1.12
		<b>Atom</b>	<b>x</b>
		<b>Li</b>	0
		<b>Fe</b>	0.2824(6)
		<b>P</b>	0.095(1)
		<b>O1</b>	0.087(3)
		<b>O2</b>	0.452(4)
		<b>O3</b>	0.158(2)
		<b>Atom</b>	<b>y</b>
		<b>Li</b>	0
		<b>Fe</b>	0.25
		<b>P</b>	0.25
		<b>O1</b>	0.25
		<b>O2</b>	0.25
		<b>O3</b>	0.058(3)
		<b>Atom</b>	<b>z</b>
		<b>Li</b>	0
		<b>Fe</b>	0.975(2)
		<b>P</b>	0.426(3)
		<b>O1</b>	0.754(5)
		<b>O2</b>	0.213(4)
		<b>O3</b>	0.281(3)
		<b>Atom</b>	<b>x</b>
		<b>Li</b>	0
		<b>Fe</b>	0.2815(7)
		<b>P</b>	0.095(2)
		<b>O1</b>	0.087(4)
		<b>O2</b>	0.448(4)
		<b>O3</b>	0.163(3)
		<b>Atom</b>	<b>y</b>
		<b>Li</b>	0
		<b>Fe</b>	0.25
		<b>P</b>	0.25
		<b>O1</b>	0.25
		<b>O2</b>	0.25
		<b>O3</b>	0.060(3)
		<b>Atom</b>	<b>z</b>
		<b>Li</b>	0
		<b>Fe</b>	0.972(2)
		<b>P</b>	0.419(3)
		<b>O1</b>	0.744(6)
		<b>O2</b>	0.201(4)
		<b>O3</b>	0.284(3)
<b>Space group</b>	<i>Pnma</i>	<b>U</b>	-0.15(7)
<b>a (Å)</b>	10.317(1)	<b>V</b>	0.13(5)
<b>b (Å)</b>	5.9990(7)	<b>W</b>	0.0125(8)
<b>c (Å)</b>	4.6948(7)	<b>R<sub>p</sub></b>	3.49 %
		<b>R<sub>wp</sub></b>	4.37 %
		<b>R<sub>exp</sub></b>	4.21 %
		<b>X<sup>2</sup></b>	1.08

**Table 4.3:** Calculated Rietveld refinement parameters from the PXRD patterns of  $\alpha$ -LiFePO<sub>4</sub> prepared in 2:3 ethaline after 1 h of microwave irradiation (textnu = 2.45 GHz) at 230 and 240 °C.

		<b>2:3 <math>\alpha</math>-LiFePO<sub>4</sub> (240 °C)</b>					
<b>Space group</b>	<i>Pnma</i>	<b>U</b>	0.017(3)	<b>Atom</b>	<b>x</b>	<b>y</b>	<b>z</b>
<b>a (Å)</b>	10.3301(4)	<b>V</b>	0.0005(2)	<b>Li</b>	0	0	0
<b>b (Å)</b>	6.0054(2)	<b>W</b>	0.011(4)	<b>Fe</b>	0.2823(5)	0.25	0.973(2)
<b>c (Å)</b>	4.6927(2)	<b>R<sub>p</sub></b>	3.59 %	<b>P</b>	0.096(1)	0.25	0.422(3)
		<b>R<sub>wp</sub></b>	4.48 %	<b>O1</b>	0.091(2)	0.25	0.748(4)
		<b>R<sub>exp</sub></b>	4.23 %	<b>O2</b>	0.449(3)	0.25	0.221(3)
		<b>X<sup>2</sup></b>	1.12	<b>O3</b>	0.158(2)	0.055(3)	0.278(3)
		<b>2:3 <math>\alpha</math>-LiFePO<sub>4</sub> (200 °C)</b>					
<b>Space group</b>	<i>Pnma</i>	<b>U</b>	-0.005(2)	<b>Atom</b>	<b>x</b>	<b>y</b>	<b>z</b>
<b>a (Å)</b>	10.3349(6)	<b>V</b>	0.012(4)	<b>Li</b>	0	0	0
<b>b (Å)</b>	6.0003(3)	<b>W</b>	0.013(1)	<b>Fe</b>	0.2825(6)	0.25	0.976(2)
<b>c (Å)</b>	4.7003(3)	<b>R<sub>p</sub></b>	3.54 %	<b>P</b>	0.094(3)	0.25	0.418(4)
		<b>R<sub>wp</sub></b>	4.46 %	<b>O1</b>	0.089(3)	0.25	0.748(5)
		<b>R<sub>exp</sub></b>	4.18 %	<b>O2</b>	0.452(4)	0.25	0.213(4)
		<b>X<sup>2</sup></b>	1.14	<b>O3</b>	0.158(2)	0.055(3)	0.286(3)

**Table 4.4:** Calculated Rietveld refinement parameters from the PXRD patterns of  $\alpha$ -LiFePO<sub>4</sub> prepared in 2:3 ethaline after 3 h of microwave irradiation (textnu = 2.45 GHz) at 200 °C and 240 °C.

		<b>2:3 <math>\alpha</math>-LiFePO<sub>4</sub> (230 °C)</b>					
<b>Space group</b>	<i>Pnma</i>	<b>U</b>	0.01(1)	<b>Atom</b>	<b>x</b>	<b>y</b>	<b>z</b>
<b>a (Å)</b>	10.3293(5)	<b>V</b>	0.00(2)	<b>Li</b>	0	0	0
<b>b (Å)</b>	6.0050(3)	<b>W</b>	0.007(1)	<b>Fe</b>	0.2821(4)	0.25	0.971(1)
<b>c (Å)</b>	4.6915(3)	<b>R<sub>p</sub></b>	3.60 %	<b>P</b>	0.0946(1)	0.25	0.423(3)
		<b>R<sub>wp</sub></b>	4.54 %	<b>O1</b>	0.092(2)	0.25	0.754(3)
		<b>R<sub>exp</sub></b>	4.25 %	<b>O2</b>	0.449(2)	0.25	0.213(3)
		<b>X<sup>2</sup></b>	1.14	<b>O3</b>	0.158(2)	0.053(3)	0.277(3)

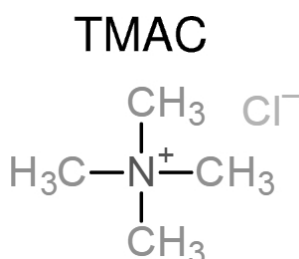
  

		<b>2:3 <math>\alpha</math>-LiFePO<sub>4</sub> (200 °C)</b>					
<b>Space group</b>	<i>Pnma</i>	<b>U</b>	0.10(8)	<b>Atom</b>	<b>x</b>	<b>y</b>	<b>z</b>
<b>a (Å)</b>	10.324(1)	<b>V</b>	-0.08(6)	<b>Li</b>	0	0	0
<b>b (Å)</b>	5.9969(8)	<b>W</b>	0.047(9)	<b>Fe</b>	0.2807(7)	0.25	0.973(2)
<b>c (Å)</b>	4.6972(8)	<b>R<sub>p</sub></b>	3.67 %	<b>P</b>	0.097(2)	0.25	0.418(4)
		<b>R<sub>wp</sub></b>	4.60 %	<b>O1</b>	0.088(4)	0.25	0.739(7)
		<b>R<sub>exp</sub></b>	4.21 %	<b>O2</b>	0.449(5)	0.25	0.202(5)
		<b>X<sup>2</sup></b>	1.19	<b>O3</b>	0.155(3)	0.057(4)	0.281(4)

**Table 4.5:** Calculated Rietveld refinement parameters from the PXRD patterns of  $\alpha$ -LiFePO<sub>4</sub> prepared in 2:3 ethaline after 5 h of microwave irradiation (textnu = 2.45 GHz) at 200 °C and 240 °C.

## 4.5 Synthesis and characterisation of $\alpha$ -LiFePO<sub>4</sub> in tetramethylammonium chloride based DES

In an attempt seek new routes to tailor morphologies using DES systems, other compositions were also attempted as proof-of-concept studies. An alternative method to substitution of the hydrogen bond donor is to replace the salt in ethaline (ChCl) with another molecule. For these investigations an ammonium salt tetramethylammonium chloride (TMAC) was chosen. The rationale for choosing TMAC is due to its structural similarities to ChCl (Figure 4.23).



**Figure 4.23:** Chemical structure of tetramethylammonium chloride (TMAC).

Samples of  $\alpha$ -LiFePO<sub>4</sub> were prepared using stoichiometric amounts of FeC<sub>2</sub>O<sub>4</sub> · H<sub>2</sub>O (1 mmol) and LiH<sub>2</sub>PO<sub>4</sub> (1 mmol) and 4 ml of 1:2 mixtures of TMAC:EG in a 10 ml microwave vessel. The mixtures were irradiated with microwaves ( $\nu = 2.45$ ) for 3 h at temperatures between 200 °C to 250 °C. Syntheses conducted at temperatures above 230 °C exceeded the safe pressure limit of the microwave synthesiser after 1 h of microwave irradiation and were not investigated further. The remaining samples were characterised using PXRD and show that  $\alpha$ -LiFePO<sub>4</sub> can be prepared at all temperatures between 200 °C and 230 °C. Peak broadening is observed with decreasing synthesis temperature, indicating a possible decrease in the crystallinity, or the emergence of nanosized particles.

Rietveld refinement was conducted for samples prepared at 200 °C and 230 °C, with a good fit in both cases to a ICSD standard of  $\alpha$ -LiFePO<sub>4</sub>.<sup>31</sup> The calculated parameters for both Rietveld refinements are given in Table 4.6.

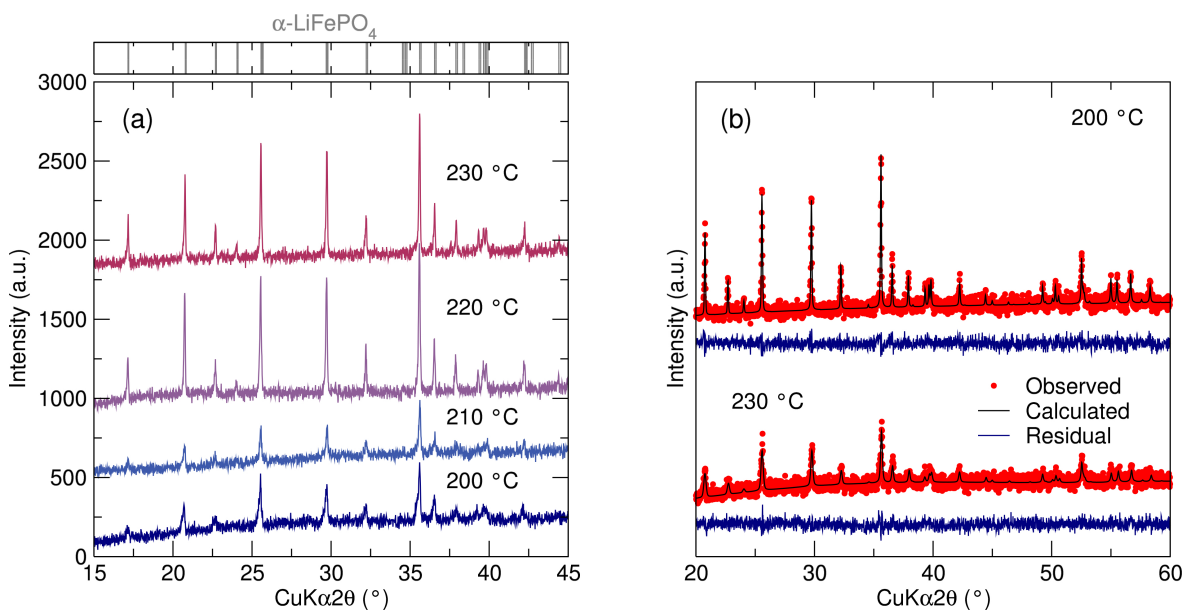


**Figure 4.24:** (a) PXR D patterns collected for samples synthesised in 1:2 EG:TMAC media after 3 h of microwave irradiation ( $\nu = 2.45$ GHz) at 200 °C, 210 °C, 220 °C and 230 °C. Phase pure  $\alpha$ -LiFePO<sub>4</sub> is obtained at all temperatures showing peak broadening with decreasing temperature. (b) Rietveld refinement of PXR D data collected for  $\alpha$ -LiFePO<sub>4</sub> prepared in 1:2 TMAC at 200 °C and 230 °C after 3 h of microwave irradiation ( $\nu = 2.45$  GHz). A good fit to the ICSD literature pattern is observed in both cases.<sup>31</sup>

SEM was performed on all samples to investigate the changes in morphology with increasing temperature. The 1:2 EG:TMAC sample at 200 °C (Figure 4.25 a) exhibits flat particles with rounded edges between 100 nm and 300 nm in diameter. These particles also appear to be stacked. At 210 °C (Figure 4.25 b), some of the rounded particles are still present but with the addition of large rectangular platelets up to 10  $\mu$ m in length, 2  $\mu$ m in width and < 50 nm in thickness. At 220 °C, the particles are irregular and large. An interesting observation is the appearance of holes in the particles, indicating some degree of porosity. At 230 °C, larger, more uniform platelets are formed with a typical length of 2  $\mu$ m, width of 1  $\mu$ m and thickness of 150 nm.

The electrochemical performance of the  $\alpha$ -LiFePO<sub>4</sub> particles prepared in 1:2 TMAC:EG were investigated by GCPL, similar to previous experiments. To investigate the rate capability of the materials GCPL was conducted at increasing rates from C/10 to 10C. Figure 4.26 shows the observed discharge capacities.

TMAC $\alpha$ -LiFePO <sub>4</sub> (230 °C)		TMAC $\alpha$ -LiFePO <sub>4</sub> (200 °C)	
<b>Space group</b>	<i>Pnma</i>	<b>U</b>	0.03(2)
<b>a (Å)</b>	10.3236(5)	<b>V</b>	-0.03(2)
<b>b (Å)</b>	6.0026(3)	<b>W</b>	0.013(3)
<b>c (Å)</b>	4.6955(3)	<b>R<sub>p</sub></b>	4.29
		<b>R<sub>wp</sub></b>	5.36
		<b>R<sub>exp</sub></b>	4.81
		<b>X<sup>2</sup></b>	1.25
		<b>Atom</b>	<b>x</b>
		<b>Li</b>	0
		<b>Fe</b>	0.2822(7)
		<b>P</b>	0.094(2)
		<b>O1</b>	0.094(4)
		<b>O2</b>	0.452(5)
		<b>O3</b>	0.163(3)
		<b>Atom</b>	<b>y</b>
		<b>Li</b>	0
		<b>Fe</b>	0.282(1)
		<b>P</b>	0.098(3)
		<b>O1</b>	0.091(7)
		<b>O2</b>	0.463(7)
		<b>O3</b>	0.160(4)
		<b>Atom</b>	<b>z</b>
		<b>Li</b>	0
		<b>Fe</b>	0.976(4)
		<b>P</b>	0.428(7)
		<b>O1</b>	0.75(1)
		<b>O2</b>	0.214(8)
		<b>O3</b>	0.266(7)
<b>Space group</b>	<i>Pnma</i>	<b>U</b>	0.3(1)
<b>a (Å)</b>	10.303(2)	<b>V</b>	-0.3(1)
<b>b (Å)</b>	5.995(1)	<b>W</b>	0.10(2)
<b>c (Å)</b>	4.699(1)	<b>R<sub>p</sub></b>	4.27 %
		<b>R<sub>wp</sub></b>	5.37 %
		<b>R<sub>exp</sub></b>	4.87 %
		<b>X<sup>2</sup></b>	1.21

**Table 4.6:** Calculated Rietveld refinement parameters from the PXRD patterns of  $\alpha$ -LiFePO<sub>4</sub> prepared in 1:2 TMAC:EG at 200 °C and 230 °C for 5 h.

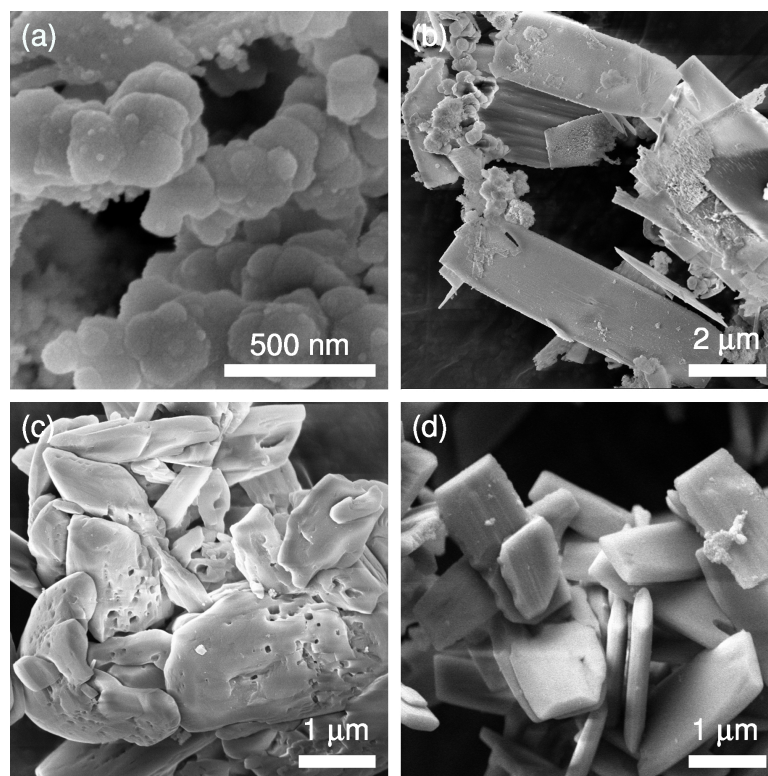


**Figure 4.25:** SEM images collected for  $\alpha$ -LiFePO<sub>4</sub> prepared in 1:2 TMAC:EG after 3 h of microwave irradiation ( $\nu = 2.45$  GHz) at (a) 200 °C, (b) 210 °C, (c) 220 °C and (d) 230 °C.

An increase in discharge capacity is observed with decreasing synthesis temperature at all rates. This is attributed to the smaller particle size and crystalline domains with decreasing synthesis temperature allowing Li<sup>+</sup> to be more easily inserted and extracted from the materials.  $\alpha$ -LiFePO<sub>4</sub> prepared at 200 °C exhibits a discharge capacity of 161 mAh g<sup>-1</sup> at C/10 and 53 mAh g<sup>-1</sup> at the highest rate of 10C, the best capacity of all the  $\alpha$ -LiFePO<sub>4</sub> samples studied, almost achieving theoretical capacity (170 mAh g<sup>-1</sup>).<sup>19</sup> These results exceed the best reports of  $\alpha$ -LiFePO<sub>4</sub> in the literature prepared by microwave-assisted routes (168 mAh g<sup>-1</sup> at C/10).<sup>150</sup> At 240 °C the capacity reduces to 122 mAh g<sup>-1</sup>. A recovery is observed after returning to C/10 in all materials, 168 mAh g<sup>-1</sup> at 200 °C and 240 °C, and 162 mAh g<sup>-1</sup> at 220 °C and 230 °C. These studies show that electrochemical performance can be enhanced by substitution of ChCl with TMAC, when compared to the 1:3 and 2:3 ChCl:EG syntheses studied in Section 4.4.3 and Section 4.4.4, respectively.

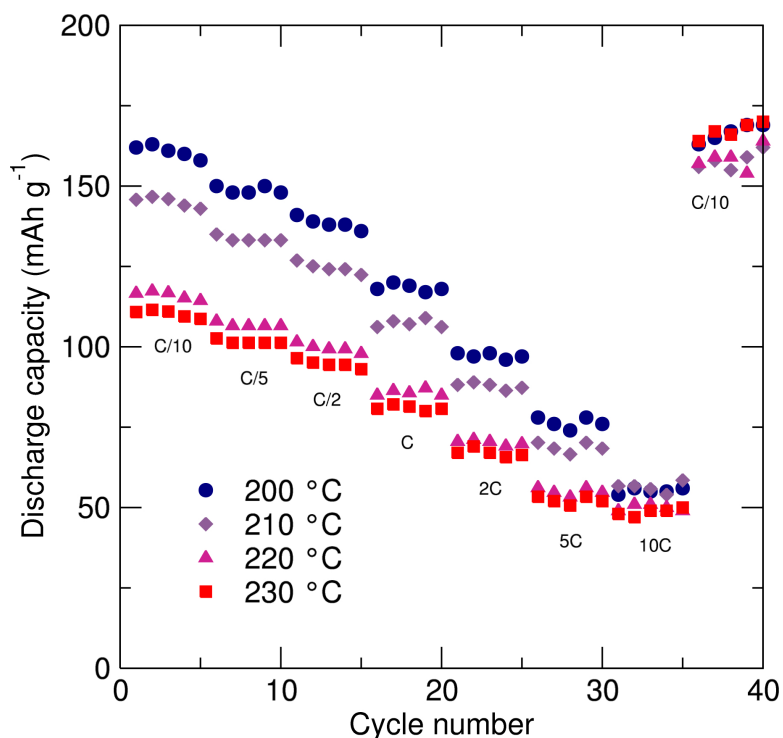


**Figure 4.26:** GCPL of carbon coated  $\alpha$ -LiFePO<sub>4</sub> synthesised in TMAC based DES at 200 °C, 210 °C, 220 °C and 230 °C showing superior discharge rates with decreasing synthesis temperature.

## 4.6 Conclusions

In this Chapter DESs have been identified as candidate ionic media for microwave-assisted applications, competitive to ILs. Phase pure  $\alpha$ -LiFePO<sub>4</sub> was obtained by all syntheses in DESs containing EG, and particle size can be decreased by lowering the synthesis temperature. The morphology of the particles is also dependent on the temperature and the solvent employed, and can be tailored to enhance the electrochemical performance of the materials. Electrochemical studies of  $\alpha$ -LiFePO<sub>4</sub> synthesised in 1:2 TMAC:EG at 200 °C for 3 h gave the best results, able to deliver an outstanding capacity at C/20 rate of 168 mAh g<sup>-1</sup> on the first cycle close to the theoretical maximum for of 170 mAh g<sup>-1</sup>, the highest current report for a microwave prepared sample of  $\alpha$ -LiFePO<sub>4</sub>.

These observations are the first reports of DESs as media for microwave-assisted synthesis and present a strong case that DESs can be employed to obtain nanostructured,

effective materials for Li-ion battery applications. The relative cost of these DESs (as of the date of this Thesis) make them extremely attractive as alternative ionic media, equating to approximately £2,750/Kg for EMI-TFMS and £35/Kg for ethaline (£45/Kg for TMAC:EG).<sup>198</sup> This underlines that  $\alpha$ -LiFePO<sub>4</sub> with excellent electrochemical performance can be obtained through microwave-assisted ionothermal routes in a solvent that costs 1.3 % of a typical IL.

## Chapter 5: Microwave-assisted synthesis of vanadium oxides for lithium ion batteries

Vanadate materials have been studied extensively due to the metal-insulator transitions many of these compounds exhibit.<sup>199,200</sup> More recently they have accumulated interest as candidate insertion electrodes, with many  $V_xO_y$  compounds investigated including  $V_2O_5$ ,  $V_6O_{13}$  and  $LiV_3O_8$ .<sup>201–204</sup> These materials exhibit open frameworks, ideal for  $Li^+$  intercalation, and the wealth of different structures available is a major draw for their investigation as electrodes. A study by Zavalij and Whittingham highlights the structural flexibility of vanadium oxides by listing 60 different  $V_xO_y$  frameworks, which are all potential candidates as battery materials.<sup>42</sup>

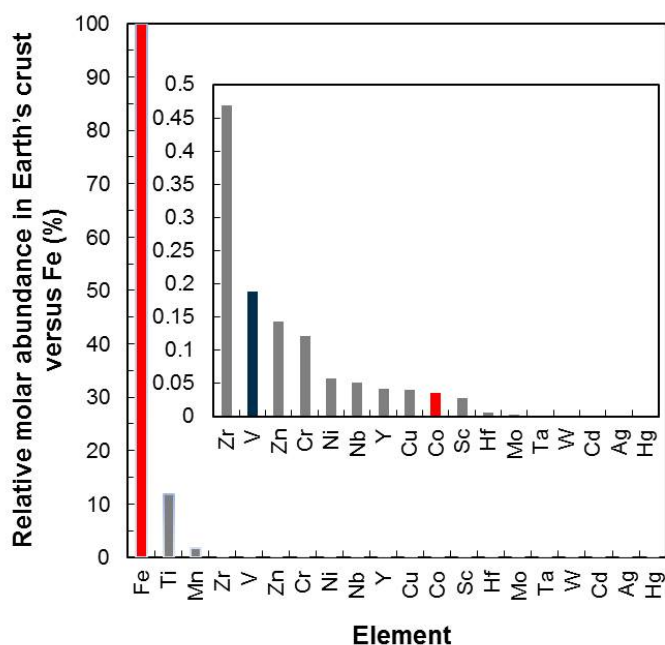


**Figure 5.1:** Relative abundance of redox metals in the Earth's crust versus iron. Inset is a zoomed view of the 3<sup>rd</sup> to 17<sup>th</sup> most abundant redox metals.

Another attractive attribute of vanadium oxide insertion electrodes is the relative availability of vanadium in the Earth's crust (Figure 5.1).<sup>11</sup> As can be seen, vanadium is the 5<sup>th</sup> most abundant redox active metal in the Earth's crust. Vanadium is also the 2<sup>nd</sup> lightest of the five most abundant redox metals, which allows a metal oxide insertion electrode con-

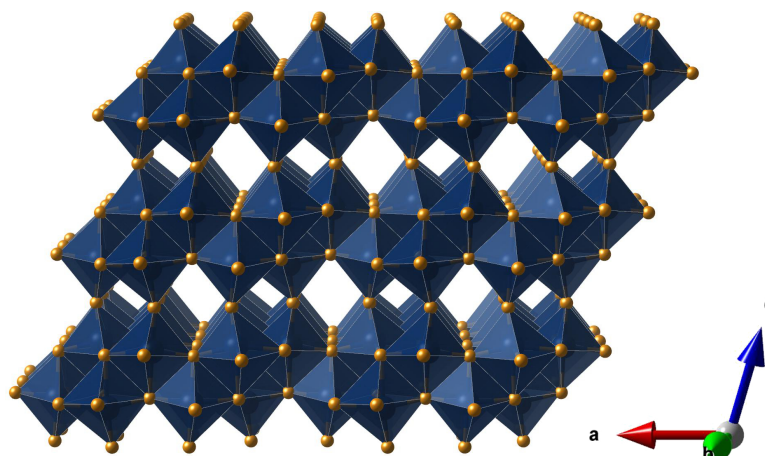


**Figure 5.2:** Crystal structure of bronze phase VO<sub>2</sub>(B) (space group *C12/m1*) showing an open framework, ideal for Li<sup>+</sup> intercalation. Vanadium atoms are shown in blue and oxygen atoms in orange. The VO<sub>6</sub> polyhedra are also in blue.

taining vanadium to exhibit a higher theoretical electrochemical capacity than one with an identical stoichiometry containing Fe, Mn or Zr. Furthermore, the modest standard reduction potentials of the V<sup>4+/3+</sup> (0.337 V) and V<sup>5+/4+</sup> (1.0 V) redox couples highlight the viability of vanadium as a redox active metal in Li<sup>+</sup> insertion electrodes.<sup>205</sup>

Bronze phase VO<sub>2</sub> (VO<sub>2</sub>(B), space group *C12/m1*), the material of focus in the current Chapter, has promising potential as a positive insertion electrode material. VO<sub>2</sub>(B) consists of corner sharing layers of edge sharing VO<sub>6</sub> octahedra. The interlayer voids provide sites for Li<sup>+</sup> intercalation suitable for electrode applications (Figure 5.2). In VO<sub>2</sub>(B), vanadium atoms exist as V<sup>4+</sup> and upon electrochemical lithiation, reduce to V<sup>3+</sup>. This redox couple produces a potential of 2.6 V versus Li/Li<sup>+</sup>, which is lower than α-LiFePO<sub>4</sub> (3.45 V). However VO<sub>2</sub>(B) exhibits a theoretical capacity of 323 mAh g<sup>-1</sup>, nearly double that of α-LiFePO<sub>4</sub> (170 mAh g<sup>-1</sup>).<sup>7</sup>

Studies on VO<sub>2</sub>(B) have led to the synthesis of many different morphologies including nanobelts, nanowires, hollow microspheres and mesoporous structures with varied electrochemical performance.<sup>13,157,206–211</sup> Correlations are observed between a decrease in dimensionality or size and higher capacities. For example, capacities of around 150 mAh g<sup>-1</sup> are observed in bulk materials, 265 mAh g<sup>-1</sup> in ultra-thin nanowires and 325 mAh g<sup>-1</sup> in nanocrystals of VO<sub>2</sub>(B) emphasising the possible influential role of nanostructured

materials for Li-ion battery applications.<sup>207,212,213</sup> Links between larger surface areas and increased availability of intercalation sites have alluded to the higher observed capacity in smaller particles.

Nanostructured VO<sub>2</sub>(B) has been successfully obtained by employing conventional solvothermal methods, where the reaction times are usually several days.<sup>157</sup> To shorten the synthesis times, while maintaining nanostructured VO<sub>2</sub>(B), alternative synthesis methods can be employed. Microwave-assisted solvothermal synthesis has been widely employed for the rapid synthesis of nanostructured Li<sup>+</sup> insertion electrode materials including LiCoO<sub>2</sub> and α-LiFePO<sub>4</sub> (also demonstrated in the previous Chapter).<sup>214,215</sup> Microwave-assisted preparation of V<sub>x</sub>O<sub>y</sub> materials have been investigated to a limited degree, mostly for use in capacitor applications.<sup>216</sup> Although there are no studies into the electrochemical characteristics of vanadium oxides prepared by microwave-assisted routes as Li<sup>+</sup> insertion electrodes, related compounds such as a vanadium oxyhydroxide H<sub>2</sub>V<sub>2</sub>O<sub>8</sub> and silver vanadium oxide Ag<sub>2</sub>V<sub>4</sub>O<sub>11</sub> have been published showing similar battery behaviour of these materials prepared using faster microwave synthesis, compared with materials prepared using conventional solvothermal methods.<sup>145,217,218</sup>

The aims of this Chapter are to investigate the possibility of synthesising phase pure VO<sub>2</sub>(B) by a microwave-assisted solvothermal route and to compare their electrochemical performance with similar materials prepared by conventional solvothermal routes. VO<sub>2</sub>(B) prepared via microwave methods has also been interrogated with *in situ* X-ray absorption spectroscopy (XAS) to investigate the evolution of the oxidation state change in VO<sub>2</sub>(B) during Li<sup>+</sup> intercalation and any differences in the intercalation behaviour between samples produce by the two routes.

Improving the electrochemical performance by enhancing the capacities achieved has also been explored by changing the synthetic methodology in two main ways (i) the use of binary solvent systems and (ii) addition of a surfactant. The purity and morphology of VO<sub>2</sub>(B) prepared by employing these synthetic modifications have been assessed and the compounds have been analysed electrochemically. The stability of the products have also been investigated over multiple cycles.

## 5.1 Attempted reduction of $V_2O_5$ in isopropanol

The reduction of  $V_2O_5$  was attempted by a microwave-assisted route employing isopropanol as both the solvent and reducing agent, similar to a conventional solvothermal approach employed by Corr *et al* [ 157] to achieve phase pure  $VO_2(B)$ .<sup>157</sup> Microwave-assisted solvothermal reduction of  $V_2O_5$  in isopropanol produced a blue/black precipitate which formed an orange gel upon washing with deionised water, in contrast to the traditional solvothermal route. After evaporation of the solvent, a brittle and lustrous blue-black deposit was obtained which was analysed using PXRD (Figure 5.3 a). The PXRD pattern exhibited a high background with very broad peaks. The powder was then annealed at 400 °C under Ar for 1 h and the resulting powder could be indexed to  $V_3O_7$ , space group  $C12/c1$  (Figure 5.3 b). This implies that isopropanol is not a strong enough reducing agent under these conditions to reduce  $V_2O_5$  ( $V^{5+}$ ) to  $VO_2(B)$  ( $V^{4+}$ ), giving rise to the mixed oxidation state compound  $V_3O_7$ . However, the crystal structure of  $V_3O_7$  exhibits an open framework and has previously proven suitable for lithium intercalation and was investigated further.<sup>219</sup>

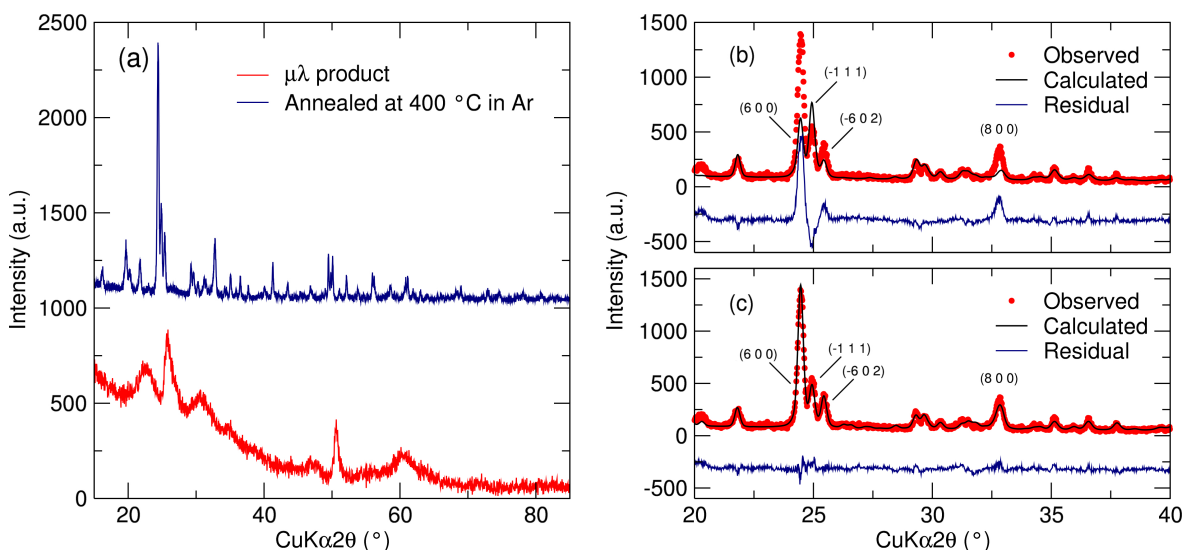


**Figure 5.3:** (a) PXRD of the sample prepared in isopropanol. A transformation to phase pure  $V_3O_7$ , space group  $C12/c1$ , is observed after heating. (b) Rietveld refinement after annealing at 400 °C in Ar with no preferred orientation showing a poor fit to  $V_3O_7$  taken from Reference 220. (c) Rietveld refinement after applying preferred orientation along the  $[n\ 0\ 0]$  direction showing an excellent fit.

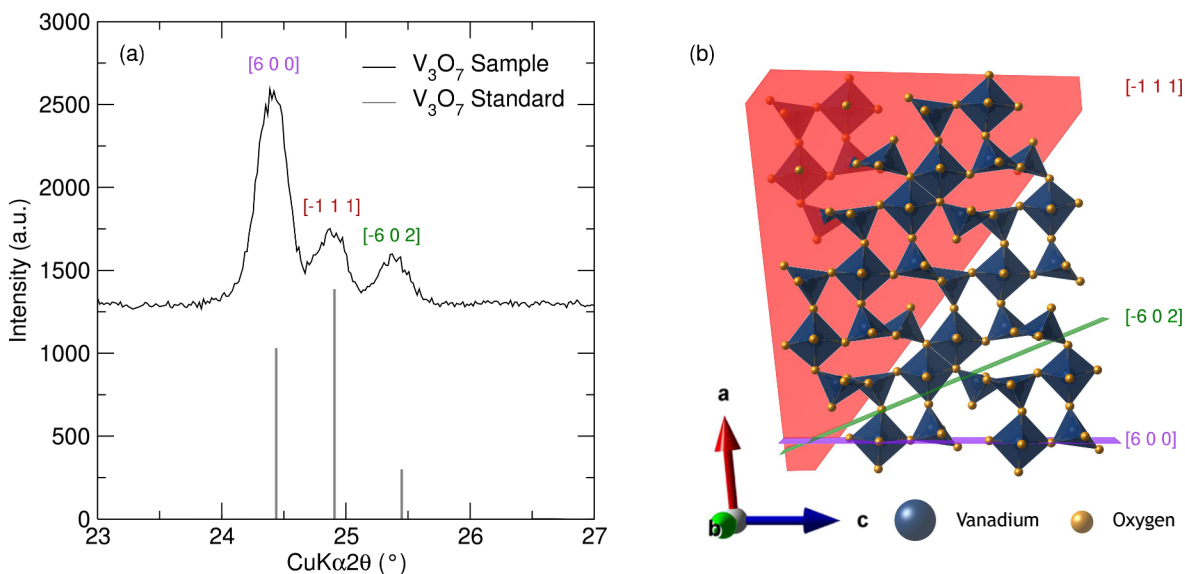


**Figure 5.4:** (a) PXRD data of  $\text{V}_3\text{O}_7$  prepared by a microwave-assisted route emphasizing the difference in peak intensity compared to an ICSD standard diffraction pattern for bulk  $\text{V}_3\text{O}_7$  taken from Reference 220. (b) Crystal structure of  $\text{V}_3\text{O}_7$  showing planes corresponding to the (-1 1 1) (red), (-6 0 2) (green) and (6 0 0) (violet) planes.

Rietveld refinement conducted on the PXRD data for  $\text{V}_3\text{O}_7$  initially provided a very poor fit (Figure 5.3 b) with a large discrepancy identified in the  $[n 0 0]$  peaks between the observed and calculated values. Depending on the direction of growth of the sheets, the electrochemical properties can be influenced due to either shortening or lengthening the  $\text{Li}^+$  diffusion pathways. Therefore, understanding the resulting morphology of these structures could allow for greater control over the resulting battery performance. Figure 5.4 (a) shows a region of the PXRD taken from the  $\text{V}_3\text{O}_7$  sample and a pattern from bulk  $\text{V}_3\text{O}_7$  from the ICSD database.

It is observed that there is a large disparity of the (-1 1 1) peak intensity relative to that of the (6 0 0) and (-6 0 2). Looking at these planes with respect to the crystal structure of  $\text{V}_3\text{O}_7$  (Figure 5.4 b) only (-1 1 1) lies predominantly in the  $ac$  plane while (6 0 0) and (-6 0 2) lay in the  $bc$  plane. Thus the relative intensity difference can be ascribed to a lack of growth in the  $b$  direction, or [-1 1 1]. Since the  $b$ -direction exhibits the most open side of the framework providing easy access to voids for  $\text{Li}^+$  to intercalate, it may be that limited growth in this direction would aid  $\text{Li}^+$  intercalation by shortening the diffusion pathways. When preferred

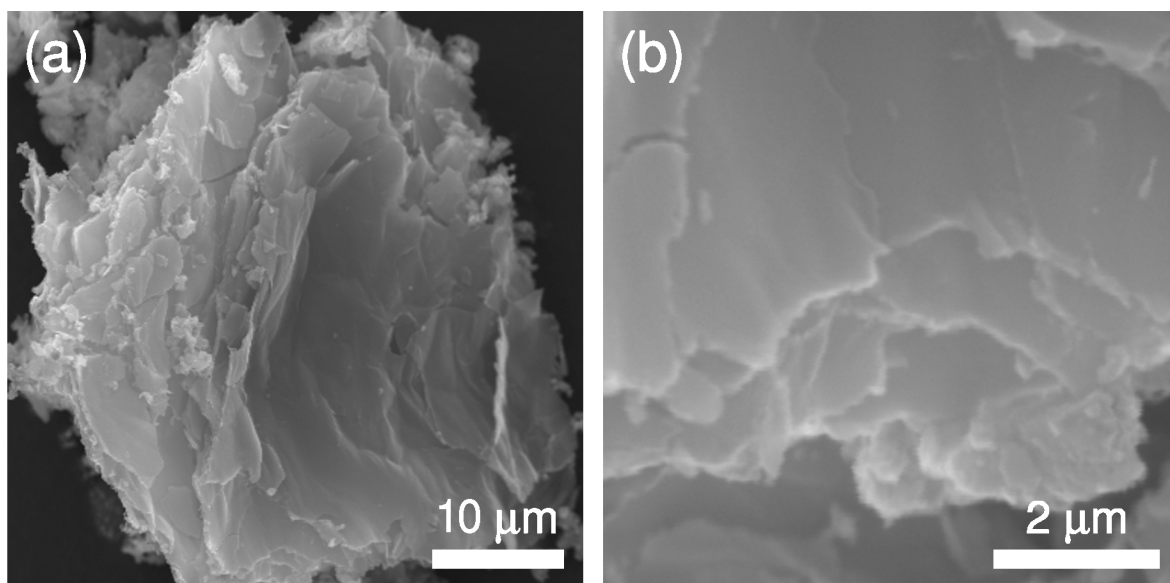


**Figure 5.5:** SEM of  $V_3O_7$  after annealing at 400 °C for 1 h at low (a) and high (b) magnification showing a sheets tens of  $\mu\text{m}$  in diameter approximately 100 nm in thickness.

orientation is included the fit improves dramatically (Figure 5.3 c) suggesting preferential growth in the  $V_3O_7$  particles. Calculated parameters for the Rietveld refinement in Figure 5.3 (c) are displayed in Table 5.1.

SEM images of the  $V_3O_7$  sample at low and high magnification (Figure 5.5 a and b respectively) reveal a sheet morphology several tens of  $\mu\text{m}$  in diameter and 40 nm in thickness. Interestingly, there are no reports in the literature of this morphology being obtained for  $V_3O_7$ , with only nanowires and bulk materials reported.<sup>219,220</sup>

Space group	C12/c1	U	0.798504	Atom	x	y	z	Atom	x	y	z
<b>a</b> (Å)	21.9216(9)	<b>V</b>	-0.750777	<b>V1</b>	0.00000	0.81087	0.75000	<b>O4</b>	0.32613	0.74560	0.76740
<b>b</b> (Å)	3.6779(3)	<b>W</b>	0.202859	<b>V2</b>	0.19549	0.82011	0.94140	<b>O5</b>	0.31591	0.24630	0.84644
<b>c</b> (Å)	18.357(1)	<b>R<sub>p</sub></b>	12.7	<b>V3</b>	0.03054	0.74814	0.94466	<b>O6</b>	0.20443	0.74730	0.83572
		<b>R<sub>wp</sub></b>	16.5	<b>V4</b>	0.16289	0.74506	0.75467	<b>O7</b>	-0.00324	0.75160	0.85923
		<b>R<sub>exp</sub></b>	10.1	<b>V5</b>	0.32839	0.74538	0.87378	<b>O8</b>	0.39756	0.74360	0.90628
		<b>X<sup>2</sup></b>	2.69	<b>O1</b>	0.19225	0.25880	0.93942	<b>O9</b>	0.8991	0.74910	0.76677
		-	-	<b>O2</b>	0.00000	0.25070	0.75000	<b>O10</b>	0.10538	0.75570	0.93727
		-	-	<b>O3</b>	0.02324	0.25020	0.97363	<b>O11</b>	0.28669	0.75220	0.95186

**Table 5.1:** Calculated Rietveld refinement parameters from PXRD data collected for  $V_3O_7$  annealed at 400 °C for 1 h with preferred orientation along [n 0 0] compared to the reference to the pattern taken from Reference 220.

### 5.1.1 Electrochemical characterisation of $V_3O_7$

A pellet consisting of 60 %  $V_3O_7$ , 30 % carbon black and 10 % PTFE was used as the active electrode in a half-cell containing  $Li^+$  as the counter electrode. The half-cell was cycled galvanostatically between 1.5 V and 3.75 V at a rate of  $100 \text{ mA g}^{-1}$ . The first discharge profile can be seen in Figure 5.6 (a). The microwave prepared  $V_3O_7$  discharge profile shows voltage plateaus at 2.8 V, 2.6 V and 2.2 V corresponding to the insertion of 3.5  $Li^+$ . The insertion of 3.5  $Li^+$  per formula unit corresponds to the reduction of the two  $V^{5+}$  in  $V_3O_7$  to  $V^{4+}$  and a further partial reduction of the remaining  $V^{4+}$  to a mixture of  $V^{3+}$  and  $V^{4+}$ . This gives rise to a large initial capacity of  $356 \text{ mAh g}^{-1}$ .

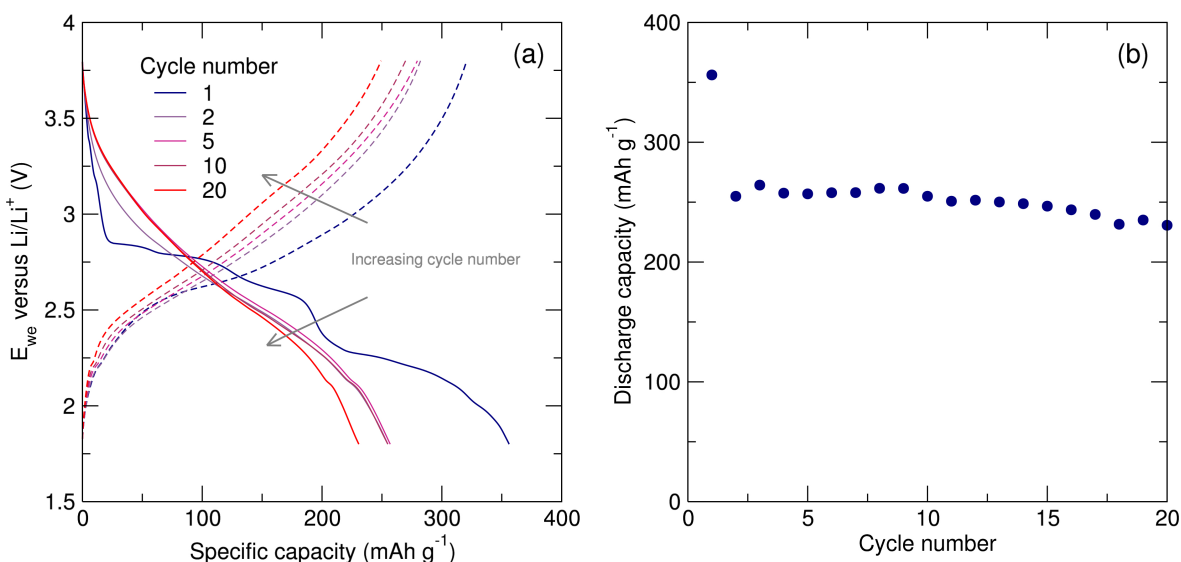


**Figure 5.6:** (a) Galvanostatic cycling of  $V_3O_7$  at  $100 \text{ mA g}^{-1}$  between 1.5 V and 3.75 V. (b) Discharge capacity of  $V_3O_7$  over 20 cycles shows a large initial loss.

On the subsequent charge/discharge cycles, no strong redox plateaus are observed and the initial capacity observed is not reversible, decreasing on the second cycle to  $253 \text{ mAh g}^{-1}$ . This behaviour has been noted in the literature to be typical of disordered layer, or single-phase electrodes which lack crystalline phase transitions.<sup>221</sup> Similar behaviour has been observed in other vanadates, such as  $V_2O_5$ .<sup>222</sup> After the second cycle, the profile remains the same with modest losses in the observed capacity. Figure 5.6 (b) shows the discharge capacity over 20 cycles for  $V_3O_7$  exhibiting a discharge capacity of  $253 \text{ mAh g}^{-1}$  on the second cycle (71 % retention) and  $236 \text{ mAh g}^{-1}$  after the 20<sup>th</sup> cycle (66 % retention).

Previous investigations of  $V_3O_7$  prepared from  $H_2V_3O_8$  nanowires as a  $Li^+$  intercalation electrode have reported a similar observations in the change of cycling profile and a lower stable capacity around  $190 \text{ mAh g}^{-1}$ .<sup>219</sup>

## 5.2 Synthesis and characterisation of $VO_2(B)$ nanostructures

As isopropanol was not a sufficiently strong enough reducing agent under the microwave heating conditions employed, formaldehyde solution (37 %) was used as an alternative to reduce  $V_2O_5$  to  $VO_2(B)$ , and has previously proven successful in conventional solvothermal synthesis.<sup>157</sup> Synthesis of  $VO_2(B)$  was attempted by mixing  $V_2O_5$  and formaldehyde solution (37 %) in 35 ml microwave vessels for 1 h ( $VO_2(B)$ \_MW\_1h), 3 h ( $VO_2(B)$ \_MW\_3h) and 6 h ( $VO_2(B)$ \_MW\_6h) of microwave irradiation ( $\nu = 2.45 \text{ GHz}$ ) at  $180 \text{ }^\circ\text{C}$ . A sample was also similarly prepared by conventional solvothermal methods ( $180 \text{ }^\circ\text{C}$  for 48 h,  $VO_2(B)$ \_ST). Both synthetic routes yielded blue-black powders which were characterised using PXRD revealing that all four separate syntheses gave phase pure  $VO_2(B)$  (Figure 5.7). An initial observation is that the peaks in the diffraction pattern collected for  $VO_2(B)$ \_ST are sharper than the microwave samples. The microwave-assisted products showed a sharpening of peak intensity with increased time indicating an increase in particle crystallinity with increased heating times.

Method	Scherrer size (nm)
$VO_2(B)$ _ST	35.04
$VO_2(B)$ _MW_1h	12.03
$VO_2(B)$ _MW_3h	14.49
$VO_2(B)$ _MW_6h	14.59

**Table 5.2:** Calculated crystallite domain sizes from the Scherrer broadening in PXRD of  $VO_2(B)$  prepared by solvothermal and microwave-assisted methods in Figure 5.7.

To investigate this effect further, the most intense peak of the PXRD pattern was used to calculate the crystal domain size using the Scherrer equation (Table 5.2). It is observed that the  $VO_2(B)$ \_MW samples all exhibited smaller values from the Scherrer equation in-

dicating smaller crystalline domains compared to the VO<sub>2</sub>(B)\_ST sample. Furthermore, as microwave irradiation times are extended from 1 h to 3 h there is an increase in the crystalline domain size 12.03 nm to 14.49 nm. Increasing the irradiation time from 3 h to 6 h gives very little change in the domain sizes calculated.

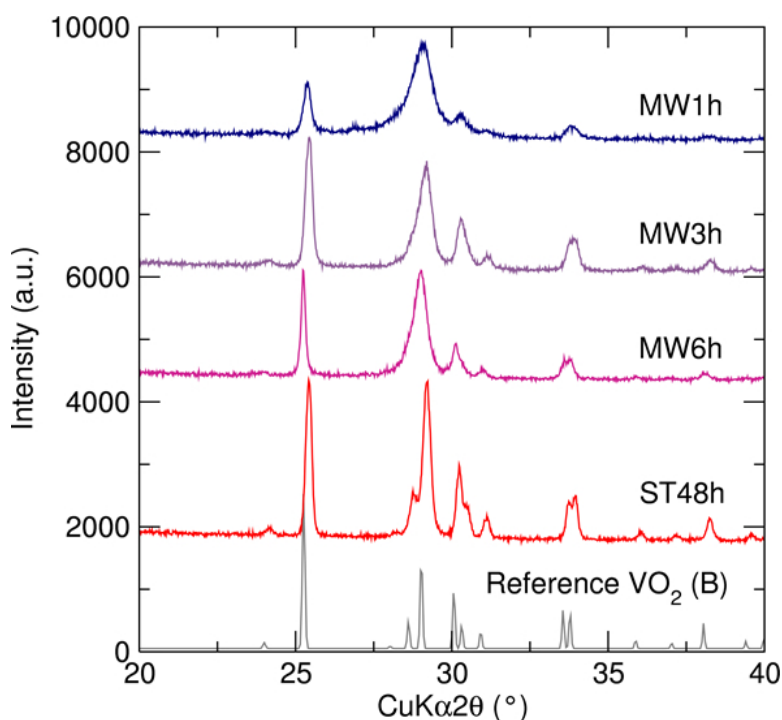


**Figure 5.7:** PXRD of products from solvothermal (48 h reaction [VO<sub>2</sub>(B)\_ST]) and microwave-assisted (1 h [VO<sub>2</sub>(B)\_MW\_1h], 3h [VO<sub>2</sub>(B)\_MW\_3h] and 6 h [VO<sub>2</sub>(B)\_MW\_1h] reactions) reduction of V<sub>2</sub>O<sub>5</sub> by 37% formaldehyde solution. All samples can be indexed to phase-pure VO<sub>2</sub>(B) (space group *C12/m1*).<sup>223</sup> Increased peak broadening is observed in VO<sub>2</sub>(B)\_MW\_*nh* samples with decreased irradiation time.

The morphology of the VO<sub>2</sub>(B) particles was investigated using SEM. All particles obtained are rod-like in morphology. Particles obtained by microwave-assisted routes after 1 h of irradiation (Figure 5.8 a) had typical lengths of 1 μm and widths of 180 nm. After 3 h of irradiation (Figure 5.8 b), lengths of 600 nm and widths of 90 nm are observed. After 6 h of irradiation (Figure 5.8 c), lengths of 700 nm and widths of 110 nm are seen. It is apparent that increasing the duration of microwave-irradiation increases both the length and the width of the particles. The solvothermal reaction (Figure 5.8 d) produced nanorods with a typical length of 1.5 μm and typical width of 160 nm, larger than any particles obtained from

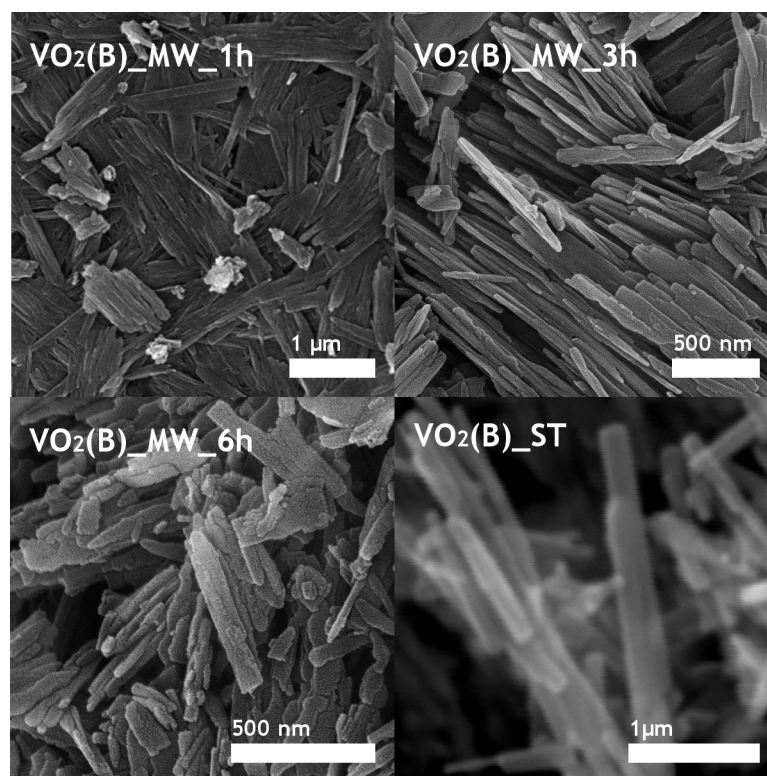


**Figure 5.8:** Scanning electron microscopy of  $\text{VO}_2(\text{B})$  prepared after 1 h [ $\text{VO}_2(\text{B})_{\text{MW}_1\text{h}}$ ] (a), 3 h [ $\text{VO}_2(\text{B})_{\text{MW}_3\text{h}}$ ] (b) and 6 h [ $\text{VO}_2(\text{B})_{\text{MW}_6\text{h}}$ ] (c) of microwave-irradiation. (d) SEM image of  $\text{VO}_2(\text{B})$  prepared by conventional solvothermal routes after 48 h of heating [ $\text{VO}_2(\text{B})_{\text{ST}}$ ]. Multimicron length rods are observed in  $\text{VO}_2(\text{B})_{\text{ST}}$  compared to sub-micron length rods from the  $\text{VO}_2(\text{B})_{\text{MW}_nh}$  samples.

microwave-assisted preparation.

### 5.2.1 Electrochemical characterisation of VO<sub>2</sub>(B) nanostructures

In order to compare the electrochemical performance of microwave prepared samples, one product [VO<sub>2</sub>(B)\_MW\_3h] was chosen to be investigated thoroughly and compared to the solvothermally derived product VO<sub>2</sub>(B)\_ST. Cyclic voltammetry of VO<sub>2</sub>(B)\_MW\_3h indicated two major peaks corresponding to the oxidation and reduction of the active material through the V<sup>4+</sup>/V<sup>3+</sup> redox couple. It is observed that although the position of the peaks move only marginally, a large difference in the intensity is observed. This indicates that an irreversible redox process is occurring in the material, and also observed in hydrothermally prepared nanorods.<sup>224</sup> The positions of the V<sup>4+</sup>/V<sup>3+</sup> redox couple peaks in the CV agree well with those observed in the literature from bulk VO<sub>2</sub>(B), implying similar redox behaviour is observed in nanostructured VO<sub>2</sub>(B), when using non-local analyses.<sup>225</sup>

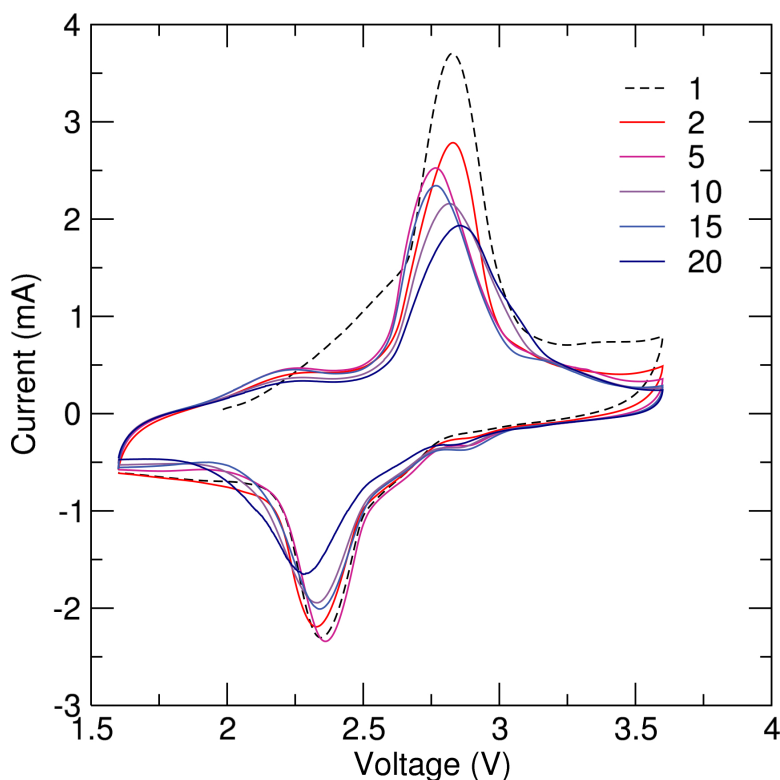


**Figure 5.9:** Cyclic voltammetry of VO<sub>2</sub>(B)\_MW\_3h between 1.6 V and 3.6 V at a rate of 0.1 mV s<sup>-1</sup> showing two peaks corresponding to the the oxidation and reduction processes arising from the V<sup>4+</sup>/V<sup>3+</sup> redox couple.

To investigate the effects of particle morphology on the electrochemical performance  $\text{VO}_2(\text{B})_{\text{MW}_3\text{h}}$  and  $\text{VO}_2(\text{B})_{\text{ST}}$  were analysed using galvanostatic cycling between 1.8 V and 3.8 V at a C/10 rate. The first cycle for both is shown in Figure 5.10. Both samples exhibit similar plateau regions indicative of a two phase reaction at 2.6 V, with the two tail regions representing a solid-solution region in agreement with the literature.<sup>226,227</sup> The solid solution phase arises from  $\text{Li}^+$  freely permeating through the  $\text{VO}_2(\text{B})$  framework giving an average  $\text{Li}_x\text{VO}_2(\text{B})$  structure, similar to observations for  $\alpha\text{-LiFePO}_4$ .<sup>24</sup> Upon reaching a critical  $\text{Li}^+$  concentration the solid-solution can no longer be sustained. This promotes the segregation of  $\text{VO}_2(\text{B})$  and  $\text{Li}_x\text{VO}_2(\text{B})$  with the emergence of a voltage plateau. It is observed that  $\text{VO}_2(\text{B})_{\text{MW}_3\text{h}}$  is able to reversibly accommodate 0.7  $\text{Li}^+$  per formula unit equating to a capacity of  $232 \text{ mAh g}^{-1}$ , higher than that observed for  $\text{VO}_2(\text{B})_{\text{ST}}$  sample (0.6  $\text{Li}^+$  per formula unit,  $197 \text{ mAh g}^{-1}$ ).

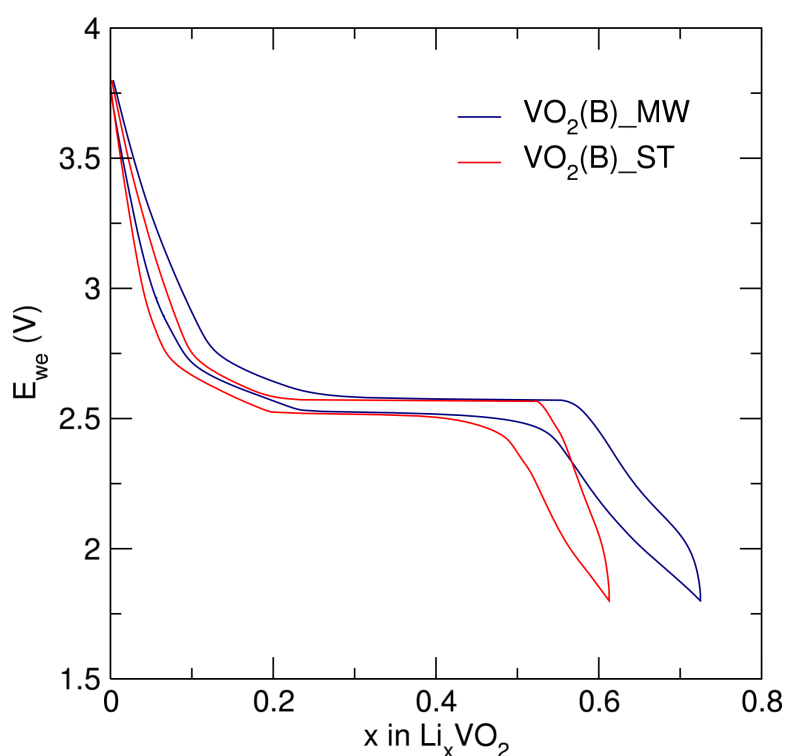


**Figure 5.10:** Galvanostatic cycling with potential limitation profile from the first discharge-charge cycle of  $\text{VO}_2(\text{B})_{\text{ST}}$  and  $\text{VO}_2(\text{B})_{\text{MW}_3\text{h}}$  from 1.8 V to 3.8 V at a C/10 rate. It is observed that  $\text{VO}_2(\text{B})_{\text{MW}_3\text{h}}$  is able to intercalate more  $\text{Li}^+$  per formula unit than the  $\text{VO}_2(\text{B})_{\text{ST}}$  sample.

GCPL was also performed at different rates to analyse the stability of the electrode during more demanding operational conditions. It is observed that the  $\text{VO}_2(\text{B})_{\text{MW}_3\text{h}}$  sample delivers consistently higher capacities than the  $\text{VO}_2(\text{B})_{\text{ST}}$ , irrespective of the rate.  $\text{VO}_2(\text{B})_{\text{MW}_3\text{h}}$  and  $\text{VO}_2(\text{B})_{\text{ST}}$  retaining capacities of 85 % and 90 % respectively when returning to the original C/10 rate. Combining these electrochemical observations with the morphological studies, it appears that as the particle size decreases, and surface area increases, there is an increase in observed capacity. This can be rationalised by more surface area being available to intercalate  $\text{Li}^+$  ions and shorter diffusion pathways. Furthermore, the smaller particles exhibit a larger solid-solution range (smaller miscibility gap) which may also attribute to the increased capacity.

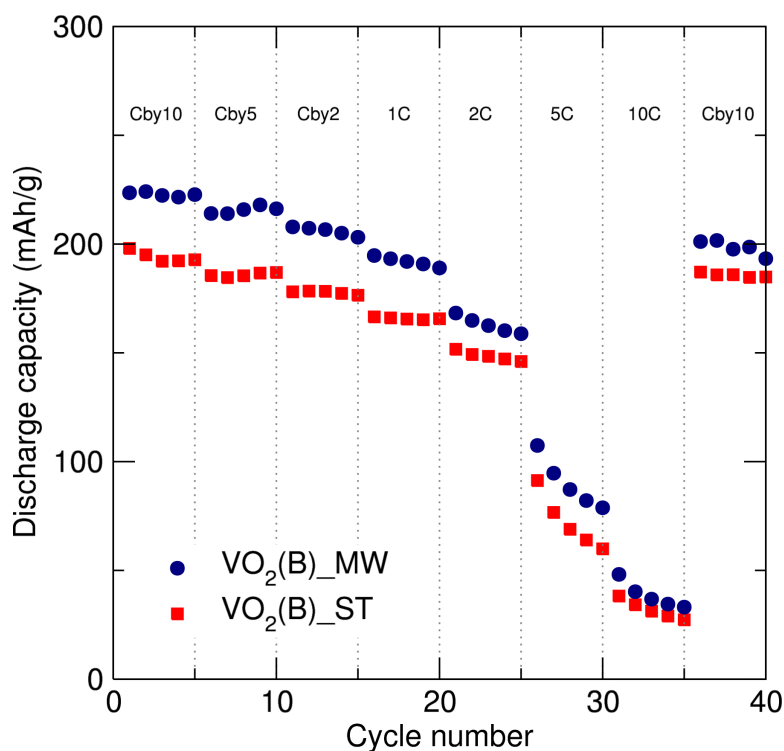


**Figure 5.11:** Discharge capacities of the  $\text{VO}_2(\text{B})_{\text{ST}}$  and  $\text{VO}_2(\text{B})_{\text{MW}_3\text{h}}$  samples at rates increasing from C/10 to 10C. The GCPL was conducted between 1.8 V and 3.8 V.

### 5.3 *In situ* X-ray absorption spectroscopy of VO<sub>2</sub>(B) nanostructures

Significant changes were observed in the battery performance of the microwave prepared sample compared to the solvothermal sample. Therefore, vanadium K-edge XAS was employed using synchrotron radiation to investigate changes in the oxidation state of vanadium during electrochemical discharge in VO<sub>2</sub>(B)\_ST and VO<sub>2</sub>(B)\_MW3h. Vanadium K-edge XAS spectra were also collected for vanadium standards (V<sup>3+</sup> (V<sub>2</sub>O<sub>3</sub>), V<sup>4+</sup> (VC) and V<sup>5+</sup> (V<sub>2</sub>O<sub>5</sub>)) to compare the initial oxidation states of VO<sub>2</sub>(B)\_ST and VO<sub>2</sub>(B)\_MW3h *ex situ* (Figure 5.12).

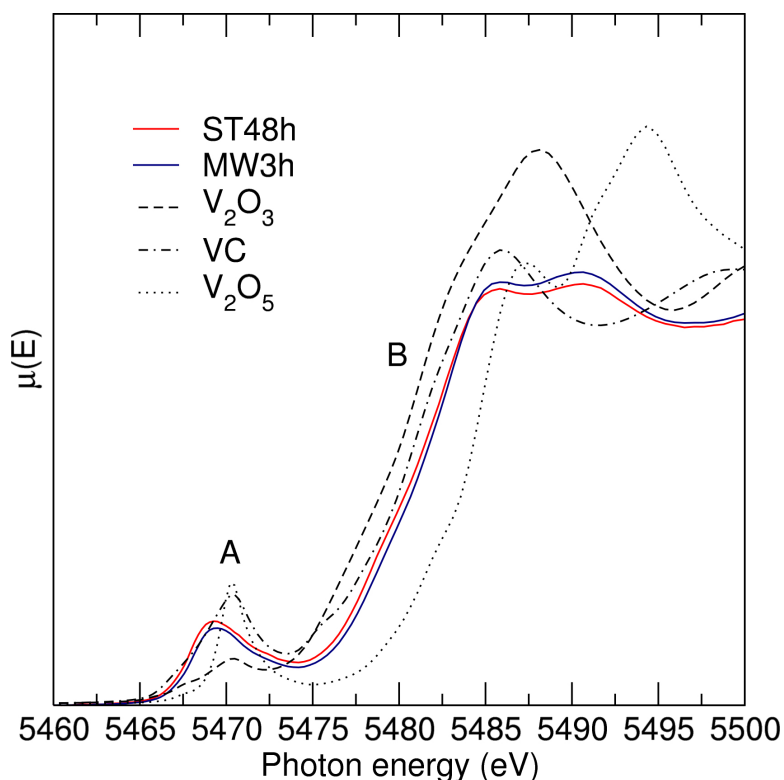


**Figure 5.12:** XAS spectra collected on the vanadium K-edge of vanadium standards V<sup>3+</sup> (V<sub>2</sub>O<sub>3</sub>), V<sup>4+</sup> (VC) and V<sup>5+</sup> (V<sub>2</sub>O<sub>5</sub>), and of VO<sub>2</sub>(B)\_ST, VO<sub>2</sub>(B)\_MW3h *ex situ*.

The standard and *ex situ* measurements over the XANES region show two main characteristic features A and B. Feature A is the pre-edge (at 5467 eV for the VO<sub>2</sub>(B) samples) which represents the contribution from the 1s to 3d quadrupole transition. Feature B is due

to 1s to empty 4p dipole transition.<sup>228</sup> As the oxidation states of the standards increase (i.e. going from  $V^{3+}$  to  $V^{5+}$ ) a shift to higher energy is observed for the rising edge and pre-edge features. This is due to the progressive loss of one electron, requiring more energy to excite the core 1s electron as the nucleus is less-shielded and carries a higher effective charge.

Feature A, the pre-edge, describes the centrosymmetry of the vanadium atom. If the  $VO_x$  polyhedra depart from centrosymmetry, becoming more tetrahedral, the pre-edge becomes more intense. This occurs in accordance with the Laporte rule where the transition of an electron to a  $d$  orbital is forbidden in complexes exhibiting centrosymmetry, such as vanadium in an octahedral arrangement. Due to this fact, the intensity of the pre-edge in octahedral complexes only arise from vibronic transitions, which are limited in crystalline materials, leading to a smaller or no pre-edge. However, as electrons are removed,  $s/p$  orbital mixing occurs. The hybridisation of the orbitals causes the  $VO_x$  polyhedra to distort, favouring a tetrahedral arrangement such as in  $V_2O_5$ . Since tetrahedral complexes have no centrosymmetry, the Laporte rule allows the excitation of the core 1s electrons into the 3d states. Hence,  $V_2O_5$  gives an intense pre-edge compared to octahedrally coordinated  $V_2O_3$ . It is observed that the rising edge of both  $VO_2(B)$  samples lies close to the  $V^{4+}$  standard, VC, confirming an initial oxidation states as  $V^{4+}$ .

*In situ* vanadium K-edge XAS experiments were performed on electrochemical AMPIX half-cells containing composite pellets of 60 %  $VO_2(B)_{ST}$  or  $VO_2(B)_{MW3h}$  as the active material mixed with 30 % carbon black and 10 % PTFE binder.<sup>166</sup> The batteries were discharged at a constant current of 20  $\mu A$  between 3.8 V and 1.8 V, recording the XAS spectra continuously. Figure 5.13 (a) and (c) show the spectra recorded for  $VO_2(B)_{ST}$  and  $VO_2(B)_{MW3h}$  respectively. It is observed that as  $Li^+$  is intercalated into both  $VO_2(B)$  samples, the rising edge (B) shifts to lower energy indicating a decrease in the oxidation state of vanadium from  $V^{4+}$  towards  $V^{3+}$ . It is also seen that the pre-edge feature (A) decreases in intensity and shifts to lower energy. The first derivatives of the normalised spectra clarify the contributions to the pre-edge features.  $VO_2(B)_{ST}$  and  $VO_2(B)_{MW3h}$  (Figure 5.13 (b) and (d), respectively) show that there are two contributions to the pre-edge feature from  $V^{3+}$  and  $V^{4+}$ . This is due to the emergence of  $V^{3+}$  upon lithiation manifested as a shoulder at lower energy on the main  $V^{4+}$  peak which confirms the coexistence of the both

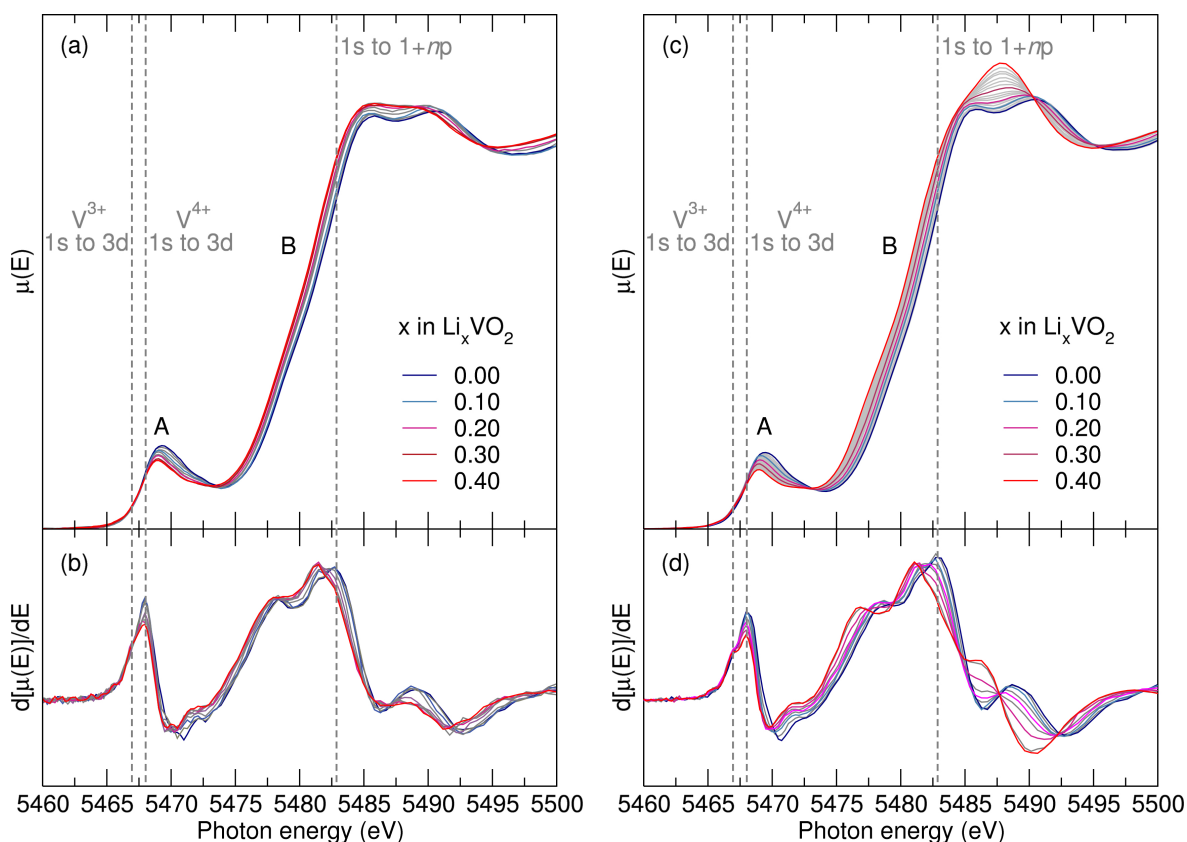


**Figure 5.13:** Normalised *in situ* XAS collected on the vanadium K-edge during electrochemical discharge of (a) VO<sub>2</sub>(B)\_MW\_3h and (c) VO<sub>2</sub>(B)\_ST. The shift in photon energy to lower eV with increasing Li<sup>+</sup> content is indicative of the V<sup>4+</sup> to V<sup>3+</sup> oxidation state change. (b) and (d) show the first derivative of (a) and (c) respectively.

oxidation states in the active material.

During electrochemical discharge of the cells, 0.4 Li<sup>+</sup> was inserted into both VO<sub>2</sub>(B)\_ST and VO<sub>2</sub>(B)\_MW3h. Previous investigations by Wong *et al.* of vanadium oxides have found that the energy of the pre-edge transition changes by 1.1 eV with unit changes in oxidation state.<sup>229</sup> Applying this observation to Li<sub>0.4</sub>VO<sub>2</sub>(B) it would be expected that the pre-edge feature would shift by -0.44 eV if a linear trend is preserved between oxidation states. The observed values for VO<sub>2</sub>(B)\_ST and VO<sub>2</sub>(B)\_MW3h are -0.35 eV and -0.55 eV, respectively. This indicates that, given the same cycling parameters, there is a greater reduction of the vanadium ions in VO<sub>2</sub>(B)\_MW3h compared to VO<sub>2</sub>(B)\_ST. This effect is also consistent with the rising edge, where a shift of -1.3 eV and -1 eV are seen in VO<sub>2</sub>(B)\_MW3h and VO<sub>2</sub>(B)\_ST respectively. These observations may that the higher capacity observed in

VO<sub>2</sub>(B)\_MW3h is due to increased reduction of the vanadium ions compared to VO<sub>2</sub>(B)\_ST. Comparing this to the morphological data bolsters the theory that more Li<sup>+</sup> is accessible at the surface of VO<sub>2</sub>(B)\_MW3h due to decreased particle size, and thus increased surface area when compared to VO<sub>2</sub>(B)\_ST.

## 5.4 Microwave-assisted synthesis of VO<sub>2</sub>(B) in binary solvent systems

Modification of synthetic conditions by changing irradiation time has been shown to promote changes in the morphology of VO<sub>2</sub>(B) and the resulting electrochemical performance. Another way to alter the synthesis is by changing the solvent media. For this reason, binary compositions of formaldehyde and the polyols, ethylene glycol (EG) and diethylene glycol (DEG), were investigated as synthetic media for VO<sub>2</sub>(B). EG and DEG were chosen due to their potential to reduce V<sup>5+</sup> in V<sub>2</sub>O<sub>5</sub> to V<sup>4+</sup> in VO<sub>2</sub>(B) and excellent microwave heating properties (studied in Chapter 3).

### 5.4.1 Microwave-assisted synthesis of VO<sub>2</sub>(B) in formaldehyde and ethylene glycol (EG)

VO<sub>2</sub>(B) samples were prepared in mixtures of formaldehyde and EG between 4 ml:1 ml and 1 ml:4 ml ratios in 1 ml increments at 180 °C for 3 h. All syntheses produced dark blue-black powders which were characterised by PXRD (Figure 5.14).

It is observed that phase pure VO<sub>2</sub>(B) cannot be obtained at lower ratios of formaldehyde:EG than 3 ml:2 ml. At higher amounts of EG, impurities are present which cannot be indexed to any vanadium oxide, hydroxide or oxyhydroxide in the literature. Increased peak broadening is observed in the PXRD pattern of VO<sub>2</sub>(B) synthesised in 3 ml:2 ml formaldehyde:EG compared to the 4 ml:1 ml sample, which may indicate smaller crystalline domains.

SEM of VO<sub>2</sub>(B) synthesised in (a) 4 ml:1 ml and (b) 3 ml:2 ml formaldehyde:EG both exhibit aggregates of rods that form hierarchical platelet structures between 1 μm and 2 μm in length (Figure 5.15). Each bundle is comprised of between 5 to 20 nanorods that are typically 120 nm in thickness and 1.8 μm in length in both the 4 ml:1 ml and 3 ml:2 ml

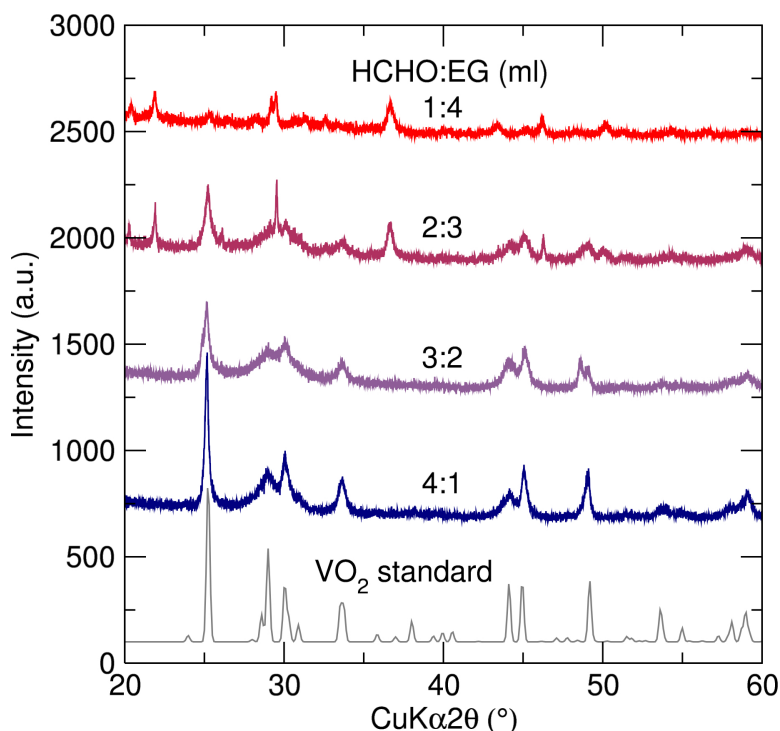


**Figure 5.14:** PXRD for the solvothermal reduction of  $V_2O_5$  by formaldehyde:EG solvent media. Phase pure  $VO_2(B)$  is obtained where the EG content of the solvent is smaller than than 3 ml.

samples.

#### 5.4.2 Electrochemical characterisation of $VO_2(B)$ synthesised in formaldehyde and ethylene glycol

To investigate the electrochemical properties of the  $VO_2(B)$  samples synthesised in formaldehyde:EG mixtures, GCPL was performed between 3.8 V and 1.8 V using Swagelok half-cells. Pellets containing 60 % active material, 30 % carbon black and 10 % PTFE binder were used as the positive electrode, Li metal as the counter electrode and a  $LiPF_6$  in EC/DMC as the electrolyte. The first galvanostatic cycles at a rate of C/10 can be seen in Figure 5.16 (a) for  $VO_2(B)$  synthesised in formaldehyde:EG ratios of 4 ml:1 ml (blue) and 3 ml:2 ml (violet). It is observed that as the volume of EG increases, the concentration of  $Li^+$  intercalated into the material on the first discharge also increases.

The 4 ml:1 ml formaldehyde:EG sample exhibits an initial capacity of  $188 \text{ mAh g}^{-1}$ , lower

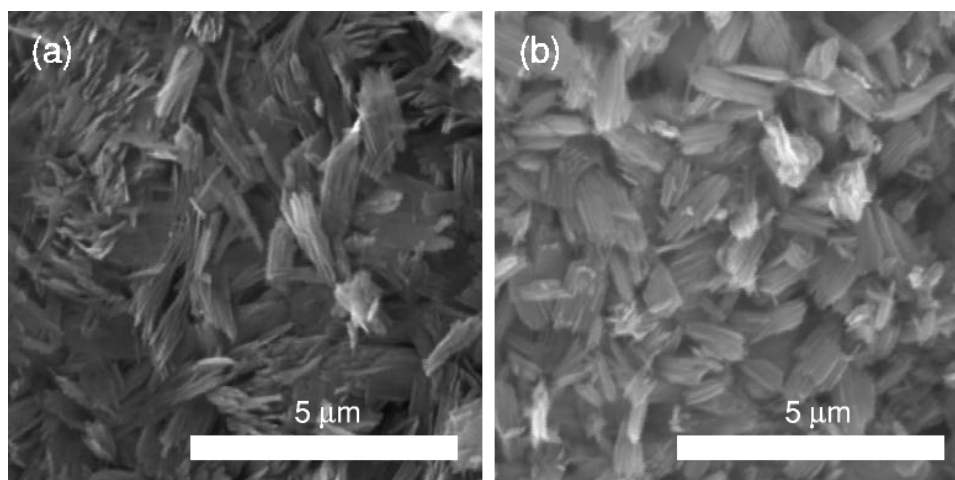


**Figure 5.15:** SEM of  $\text{VO}_2(\text{B})$  nanostructures prepared in formaldehyde:EG binary solvent mixtures of (a) 4 ml:1 ml and (b) 3 ml:2 ml.

than that in pure formaldehyde solution (37 %) under the same conditions ( $232 \text{ mAh g}^{-1}$ ).  $\text{VO}_2(\text{B})$  synthesised in 3 ml:2 ml of formaldehyde:EG shows an initial discharge capacity of  $221 \text{ mAh g}^{-1}$ , similar to the sample of  $\text{VO}_2(\text{B})$  synthesised in formaldehyde solution (37 %). Figure 5.16 (b) shows the stability of the discharge capacity over 20 cycles for  $\text{VO}_2(\text{B})$  synthesised in formaldehyde:EG ratios of 4 ml:1 ml (blue circles) and 3 ml:2 ml (violet squares). It is observed that both samples remain stable over 20 cycles with the 3 ml:2 ml sample delivering consistently higher capacity.  $\text{VO}_2(\text{B})$  synthesised in 4 ml:1 ml formaldehyde:DEG retains 95 % of the initial capacity after 20 cycles and the 3 ml: 2 ml sample retains 97 % of the initial capacity.

### 5.4.3 Microwave-assisted synthesis of $\text{VO}_2(\text{B})$ in formaldehyde and diethylene glycol

$\text{VO}_2(\text{B})$  samples were also prepared by microwave-assisted solvothermal reduction of  $\text{V}_2\text{O}_5$  in mixtures of formaldehyde and DEG between 0 ml:5 ml and 4 ml:1 ml ratios in 0.5 ml increments. The PXRD patterns for these samples can be seen in Figure 5.17. It is observed that phase pure  $\text{VO}_2(\text{B})$  can be obtained with up to 3 ml of DEG present. At 4 ml of DEG, the product contains impurity peaks and at 5 ml the material is almost amorphous.

SEM images (Figure 5.18) show that all samples exhibit rods morphologies, typically 100 nm thick, and hierarchical arrangements of the rods to form platelets or bundles at

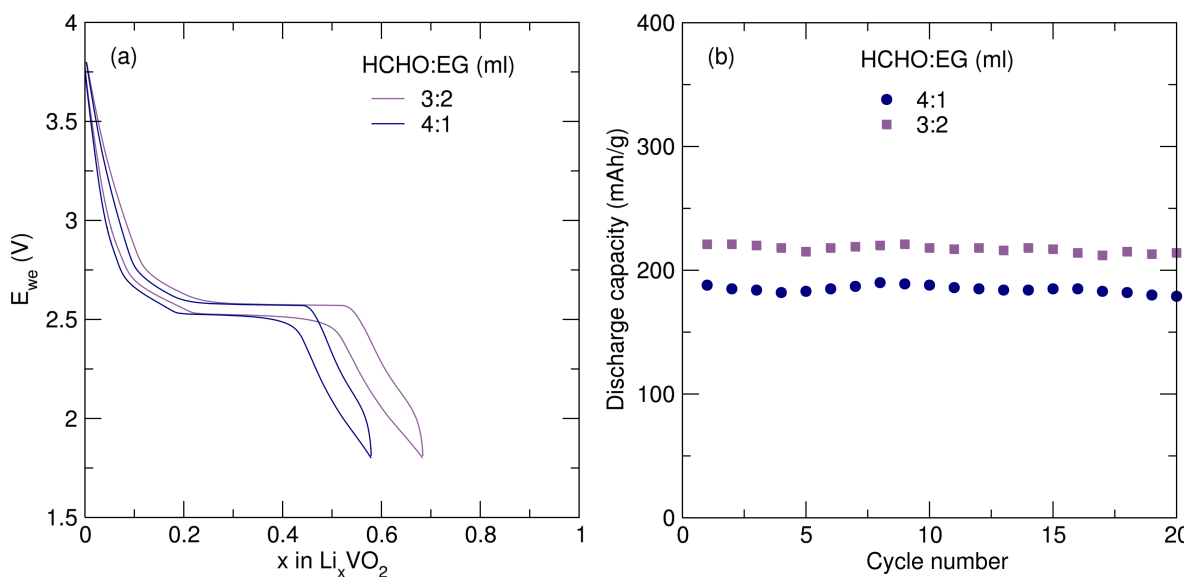


**Figure 5.16:** (a) First cycle GCPL of VO<sub>2</sub>(B) synthesised in formaldehyde:DEG ratios of 4 ml:1 ml (blue), 3 ml:2 ml (violet) and 2 ml:3 ml (red). (b) Discharge capacity over 20 cycles for VO<sub>2</sub>(B) synthesised in formaldehyde:DEG ratios of 4:1 (blue) and 3:2 (violet) showing a good capacity retention of 95 % and 96 % respectively.

DEG volumes of 1.5 ml and above. As the volume of DEG increases, the length of the particles also increase from 1.1  $\mu\text{m}$  in 4.5 ml:0.5 ml and 4.0 ml:1.0 ml, 1.6  $\mu\text{m}$  in 3.5 ml:1.5 ml and 3.0 ml:2.0 ml, 1.7  $\mu\text{m}$  in 2.5 ml to 2.5 ml and 1.9  $\mu\text{m}$  in 2 ml:3 ml formaldehyde:DEG. Furthermore as the volume of DEG increases, there are larger agglomerates formed.

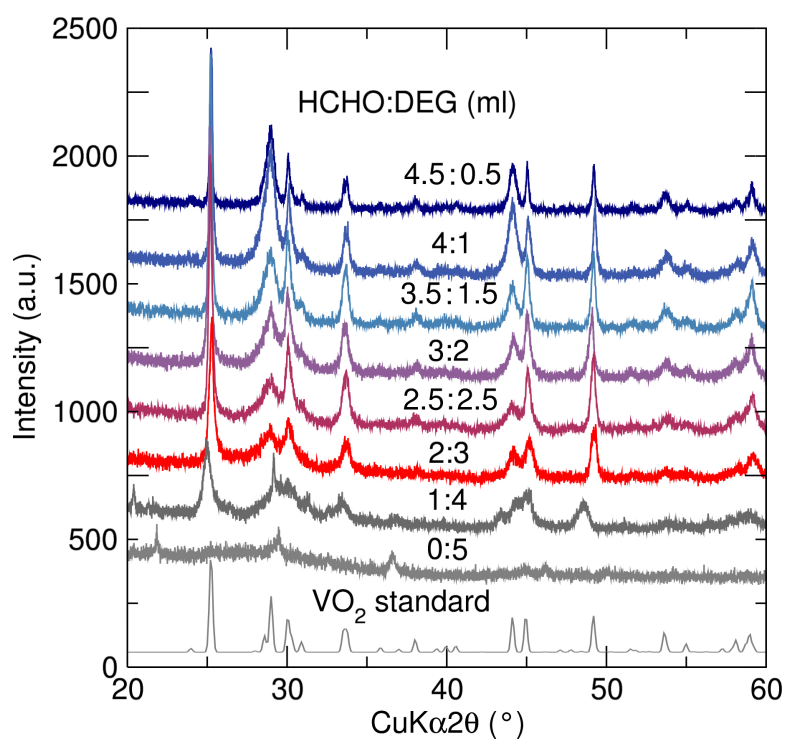


**Figure 5.17:** PXRD patterns for the solvothermal reduction of  $\text{V}_2\text{O}_5$  by formaldehyde:DEG solvent media. Increasing the volume of DEG decreases the intensity of the  $hkl$  (002) and (003) plane peaks at  $29^\circ$  and  $44^\circ 2\theta$  respectively.

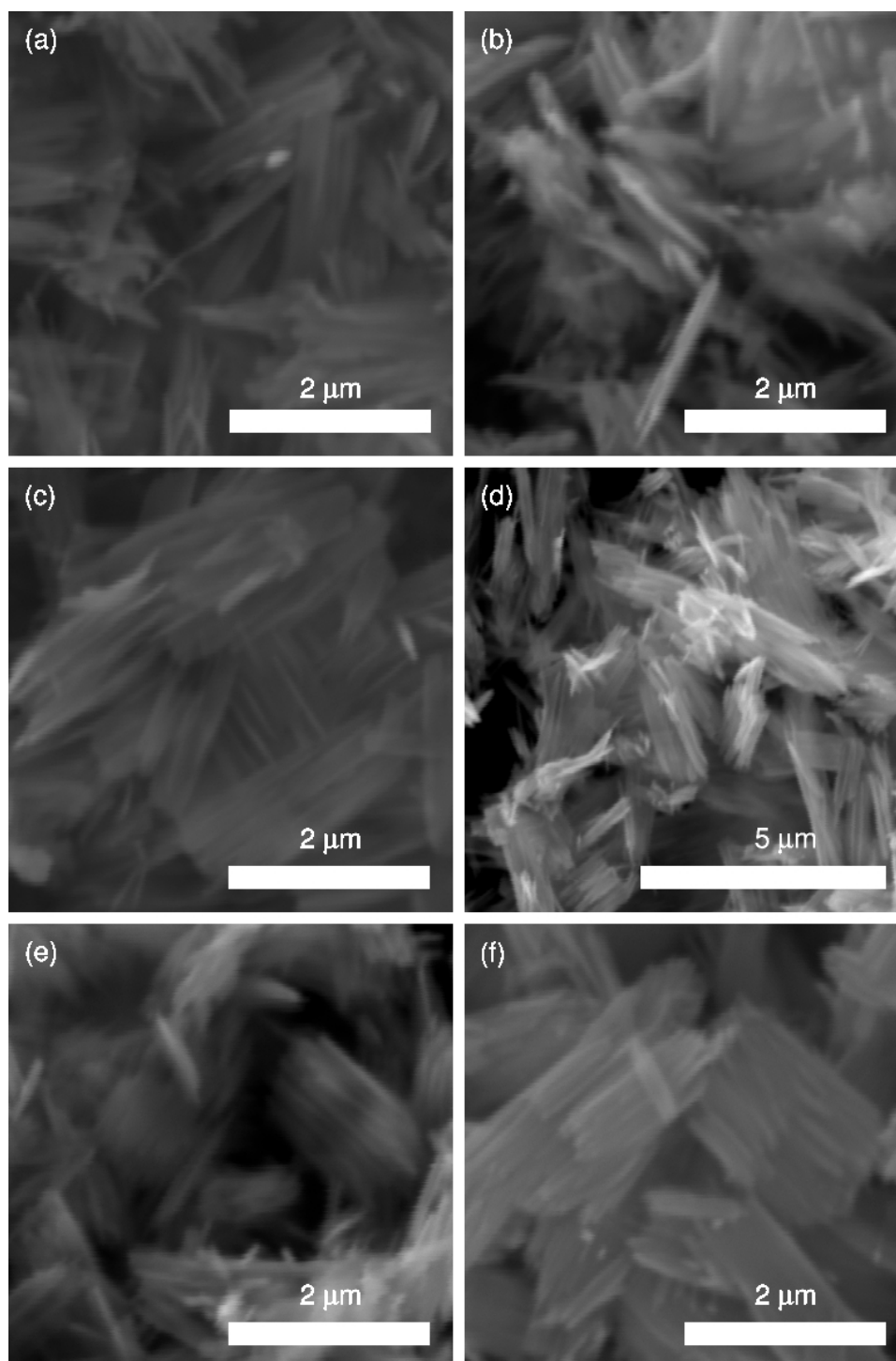


**Figure 5.18:** SEM of VO<sub>2</sub>(B) nanostructures prepared in formaldehyde:DEG binary solvent mixtures of (a) 4.5 ml:0.5 ml, (b) 4 ml:1 ml, (c) 3.5 ml:1.5 ml, (d) 3 ml:2 ml, (e) 2 ml:2 ml and (f) 2 ml:3 ml. All samples exhibit a nanorod morphology, and some exhibit hierarchical structures.

#### 5.4.4 Electrochemical characterisation of VO<sub>2</sub>(B) synthesised in formaldehyde and diethylene glycol (DEG)

To investigate the electrochemical properties of the samples of VO<sub>2</sub>(B) synthesised in formaldehyde:DEG mixtures, GCPL was performed between 3.8 V and 1.8 V using Swagelok half cells as before. The first galvanostatic cycles at a rate of C/10 can be seen in Figure 5.19 (a) for VO<sub>2</sub>(B) synthesised in formaldehyde:DEG ratios of 4 ml:1 ml (blue) and 3 ml:2 ml (violet). Similar to the EG results obtained, it is observed that as the volume of DEG increases the amount of Li<sup>+</sup> intercalated into the material per formula unit on the first discharge increases.

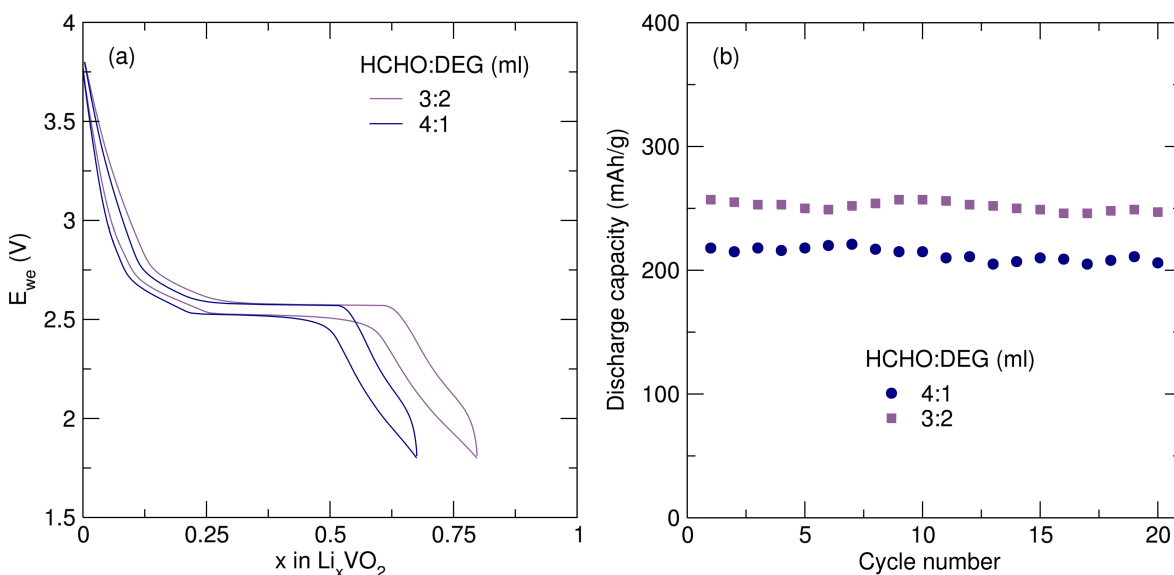


**Figure 5.19:** (a) First cycle galvanostatic cycling profiles of VO<sub>2</sub>(B) synthesised in formaldehyde:DEG ratios of 4 ml:1 ml (blue) and 3 ml:2 ml (violet). (b) Discharge capacity over 20 cycles for VO<sub>2</sub>(B) synthesised in formaldehyde:DEG ratios of 4:1 (blue) and 3:2 (violet) showing excellent capacity retentions of 95 % and 96 %, respectively.

The 4 ml:1 ml formaldehyde:DEG sample exhibits an initial capacity of 218 mAh g<sup>-1</sup>, similar to that of the sample synthesised in formaldehyde solution (37 %) alone (232 mAh g<sup>-1</sup>). VO<sub>2</sub>(B) synthesised in 3 ml:2 ml of formaldehyde:DEG shows an initial discharge capacity of 267 mAh g<sup>-1</sup>, exceeding that observed for the sample synthesised in formaldehyde solution (37 %). Figure 5.19 (b) shows the stability of the discharge capacity over 20 cycles for VO<sub>2</sub>(B) synthesised in formaldehyde:DEG ratios of 4 ml:1 ml (blue circles) and 3 ml:2

ml (violet squares). It is observed that both samples remain relatively stable over 20 cycles with the 3 ml:2 ml sample delivering consistently higher capacity. VO<sub>2</sub>(B) synthesised in 4 ml:1 ml formaldehyde:DEG retains 96 % of the initial capacity after 20 cycles and the 3 ml:2 ml sample retains 95 % of the initial capacity, similar to the results observed for VO<sub>2</sub>(B) synthesised in formaldehyde solution (37 %).

## 5.5 Microwave-assisted synthesis of VO<sub>2</sub>(B) in formaldehyde with PVP

One widely used method of size and morphology control in solution based synthesis is the use of surfactants, such as PVP. PVP has previously been shown to act as a capping agent such as in the synthesis of Ni nanoparticles, providing controlled reduction of particle size from 30 nm to 100 nm.<sup>230</sup> The use of PVP was thus implemented to investigate its ability to affect the growth of VO<sub>2</sub>(B) nanostructures, and possibly improve electrochemical performance. Samples of VO<sub>2</sub>(B) were prepared by the solvothermal reduction of V<sub>2</sub>O<sub>5</sub> in formaldehyde at 180 °C with increasing amounts of PVP (10,000 mw) added to attempt to control the morphology of the particles. All syntheses produced fine blue/black powders which were analysed with PXRD (Figure 5.20 d). It is observed that phase pure VO<sub>2</sub>(B) can be obtained with the addition of 1 mg, 2.5 mg and 5 mg of PVP. The intensity of the diffraction peaks in the VO<sub>2</sub>(B) synthesis containing 10 mg of PVP are too low to reliably assess the phase purity as only two characteristic peaks are present at 25 ° and 49 ° 2θ and much weaker features around 30 ° and 45 ° θ. The diffraction pattern collected with 1 mg of PVP added shows a large increase in intensity of the (002) and (003) peaks compared to the 2.5 mg and 5 mg syntheses. This behaviour may indicate preferential crystallographic growth of the particles.

SEM images (Figure 5.20) of the 1 mg VO<sub>2</sub>(B) sample show belt-like particles between 1 μm and 2 μm in length and typically 150 nm in width. As the amount of PVP is increased to 2.5 mg, the particles appear to increase in width, typically 200 nm to 250 nm while maintaining a similar length to the 1 mg PVP VO<sub>2</sub>(B) sample. Further increasing the amount of PVP to 5 mg introduces rough aggregates of smaller particles between 2 μm to 4 μm in length

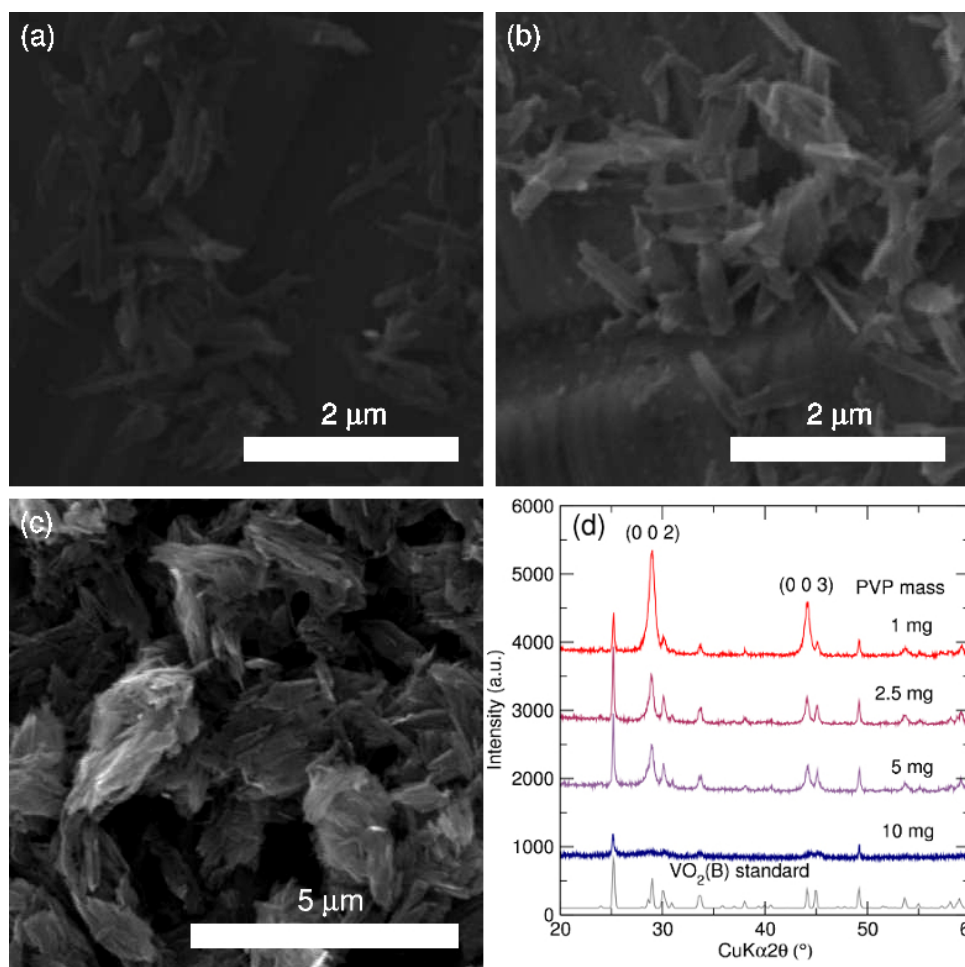


**Figure 5.20:** SEM images of VO<sub>2</sub>(B) prepared in the presence of (a) 1 mg, (b) 2.5 mg and (c) 5 mg of PVP. (d) PXRD patterns of VO<sub>2</sub>(B) synthesised by microwave-assisted reduction of V<sub>2</sub>O<sub>5</sub> in formaldehyde solution in the presence of PVP. Increasing the amount of PVP leads to a decrease in the (002) and (003) plane peak intensities.

and 1  $\mu\text{m}$  to 2  $\mu\text{m}$  in width.

### 5.5.1 Electrochemical characterisation of $\text{VO}_2(\text{B})$ synthesised in formaldehyde in the presence of PVP

As the 1 mg PVP exhibited the most dramatic effect of preferential peak growth, its electrochemical properties were investigated. Galvanostatic cycling was performed between 3.8 V and 1.8 V using Swagelok half cells, as previously described. The first galvanostatic cycle at a rate of C/10 can be seen in Figure 5.21 (a).

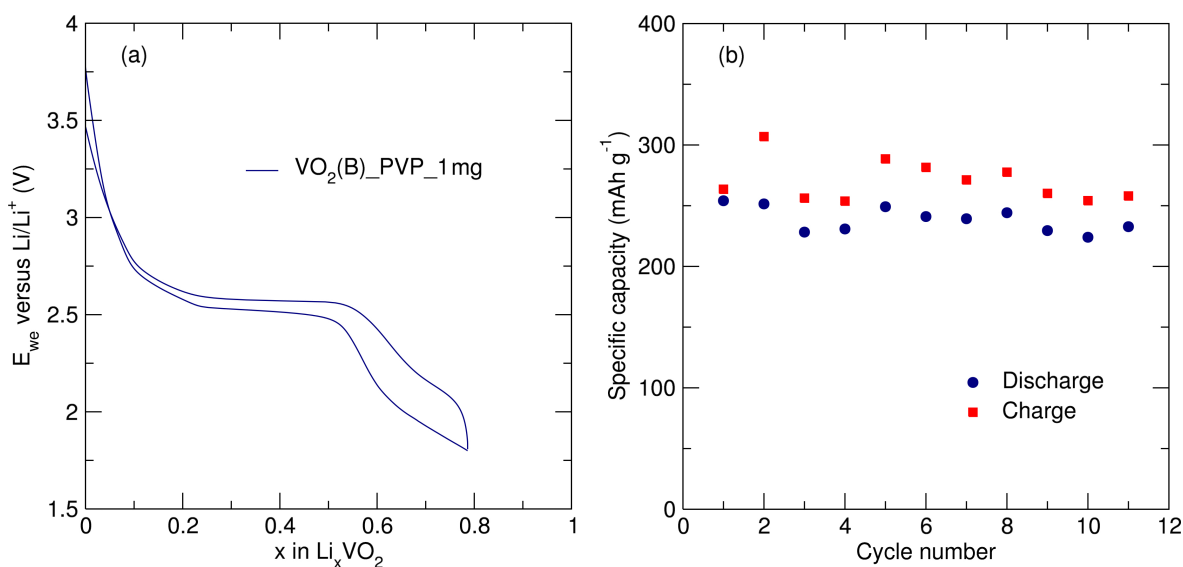


**Figure 5.21:** (a) First cycle profile for the galvanostatic cycling of  $\text{VO}_2(\text{B})$  prepared in the presence of 1 mg of PVP by microwave-assisted solvothermal reduction in formaldehyde between 3.8 V and 1.8 V at a rate of C/10. The half-cell exhibits the intercalation of 0.8  $\text{Li}^+$  per formula unit (capacity of  $258 \text{ mAh g}^{-1}$ ). The material shows excellent capacity retention over 11 cycles (b) with a capacity retention of 98 %.

It is observed that the sample is capable of intercalating 0.8  $\text{Li}^+$  per formula unit ( $259 \text{ mAh g}^{-1}$ ) on the first discharge and that the intercalation is fully reversible upon subsequent charging ( $\text{Li}^+$  extraction). The initial capacity exceeds that observed for  $\text{VO}_2(\text{B})$  synthesised in formaldehyde solution (37 %), the highest capacity of all  $\text{VO}_2(\text{B})$  samples prepared in this work. Figure 5.21 (b) shows the cycling stability at a C/10 rate over 11 cycles. It is observed that the discharge capacity remains stable with an excellent capacity retention of 98 % after

11 cycles, exceeding the stability observed for all previous samples of VO<sub>2</sub>(B) investigated in this Chapter.

## 5.6 Conclusions

Two vanadium oxides were successfully synthesised by a microwave-assisted solvothermal route, V<sub>3</sub>O<sub>7</sub> and VO<sub>2</sub>(B). The particles of V<sub>3</sub>O<sub>7</sub> exhibited a nanosheet morphology and excellent initial capacity of 356 mAh g<sup>-1</sup> which quickly decays resulting in a capacity retention of only 71 % after 20 cycles. The capacity observed in V<sub>3</sub>O<sub>7</sub> is similar to other vanadate materials investigated in the literature such as V<sub>2</sub>O<sub>5</sub> where a phase transformation occurs.<sup>221</sup> VO<sub>2</sub>(B) was successfully synthesised by both conventional solvothermal methods and microwave-assisted solvothermal methods employing formaldehyde as a solvent. The results show that an increase in microwave irradiation time leads to an increase in the crystalline domain size observed in VO<sub>2</sub>(B). Phase pure VO<sub>2</sub>(B) can be synthesised by microwave-assisted methods more rapidly than the conventional solvothermal route (1 h microwave-assisted versus 48 h solvothermal). VO<sub>2</sub>(B) synthesised by microwave-assisted routes also show improved capacity (232 mAh g<sup>-1</sup>) over solvothermally prepared VO<sub>2</sub>(B) (197 mAh g<sup>-1</sup>). *In situ* XAS analysis of VO<sub>2</sub>(B) synthesised by both microwave-assisted and conventional solvothermal routes have highlighted the influence of synthetic methodology on Li<sup>+</sup> intercalation. It has been shown that the *in situ* analyses can monitor the evolution of the oxidation state change in VO<sub>2</sub>(B) from V<sup>4+</sup> to V<sup>3+</sup> dynamically upon Li<sup>+</sup> intercalation and can provide information on how the rate of oxidation state change depends on the nanoparticle size.

The electrochemical performance of VO<sub>2</sub>(B) has also shown to be improved by employing a binary solvent media of 3:2 formaldehyde:DEG, giving the highest initial discharge capacity observed in this study of 267 mAh g<sup>-1</sup>. However, using less DEG or using a formaldehyde:EG binary mixture has a detrimental effect on the capacity observed. Furthermore impurities are found in the samples if too much EG or DEG is employed in the binary solvent. All samples of VO<sub>2</sub>(B) synthesised in binary solvents did exhibit capacity retentions of over 95 % after 20 cycles at C/10. Further improvement to the electrochemical properties of VO<sub>2</sub>(B) was made possible by introducing a PVP additive to attempt to control the morpho-

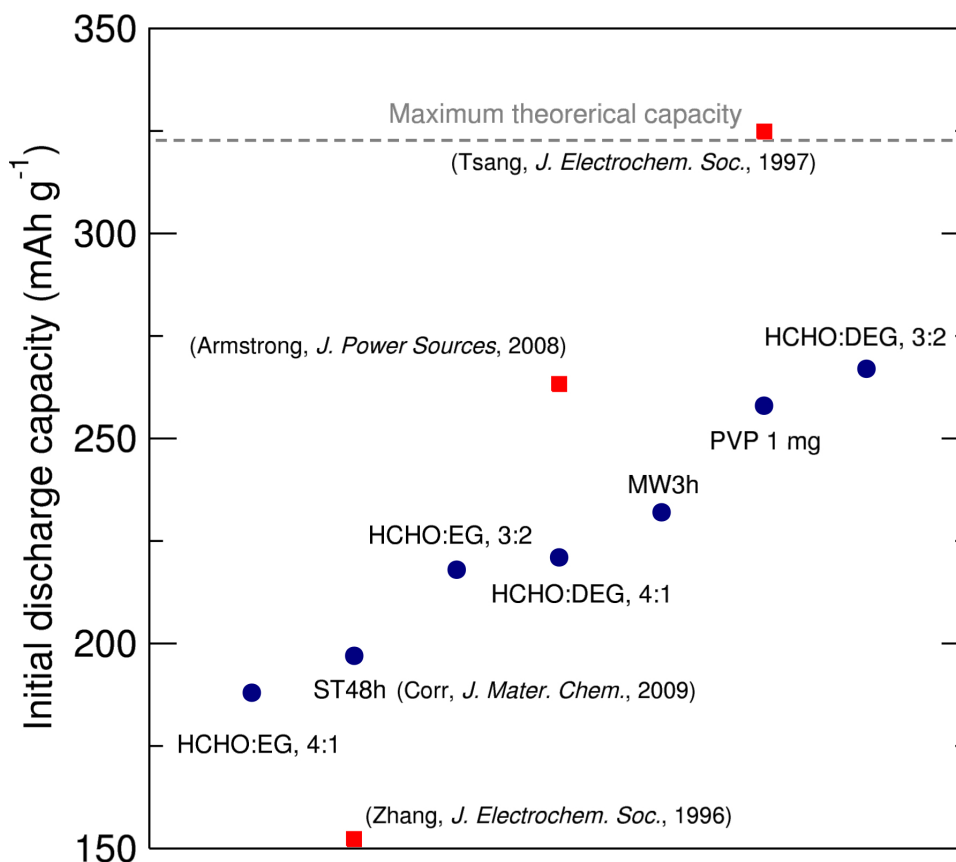


**Figure 5.22:** Electrochemical capacity of  $\text{VO}_2(\text{B})$  samples synthesised by various methods showing improvements on capacity can be made by specific modification of the solvent system or addition of a PVP additive.

logy of the  $\text{VO}_2(\text{B})$  particles with an increasing amounts of PVP leading to larger particles sizes.  $\text{VO}_2(\text{B})$  synthesised in the presence of the smallest amount of PVP (1 mg) showed a competitive capacity to the sample synthesised in 3:2 formaldehyde:DEG with a capacity of  $258 \text{ mAh g}^{-1}$  and highest capacity retention of all  $\text{VO}_2(\text{B})$  samples investigated (98 %). Figure 5.22 shows a summary of the  $\text{VO}_2(\text{B})$  samples synthesised and analysed with galvanostatic cycling in this Chapter showing that capacity can be improved by specific modification of the synthetic conditions, either by adding a surfactant (PVP) or use of a binary solvent (formaldehyde:DEG). It has also been shown that for the morphology investigated (nanorods), competitive electrochemical results to hydrothermally prepared materials (Armstrong, 2008) can be achieved by microwave synthesis, with the benefit of milder synthetic conditions.

## Chapter 6: Microwave-assisted synthesis of vanadium oxyhydroxides cathodes

### 6.1 Introduction

Metal oxyhydroxides have been extensively studied and employed as electrodes in secondary batteries, mostly in metal hydride systems.  $\text{Ni}(\text{OH})_{2.10}$  and  $\gamma\text{-CoOOH}$  show capacity retentions of up to 96 % ( $253 \text{ mAh g}^{-1}$ ) at a 5C rate after 200 cycles, making them attractive materials in rechargeable applications where high rate capability is desirable.<sup>231,232</sup> Furthermore, mixed  $\text{Ni}(\text{OH})_2/\gamma\text{-CoOOH}$  composites show a synergetic effect, limiting the expansion of the nickel hydroxide particles and stabilising capacity further.<sup>233</sup> However, layered NiAl and NiV double hydroxides have shown instability upon cycling with large losses in capacity during the first discharge.<sup>234</sup>

More recently metal oxyhydroxides have been investigated as potential electrodes in Li-ion batteries. Although FeOOH prepared by conventional hydrothermal routes has shown to deliver up to  $465 \text{ mAh g}^{-1}$  at a current density of 2C, the material suffers from rapid capacity decay due to volume change upon cycling and low electronic conductivity.<sup>235–238</sup> Although improvements have been made in increasing the electronic conductivity by mixing FeOOH with SWNTs and rGO, stabilising capacity at  $900 \text{ mAh g}^{-1}$ , this is an expensive solution.<sup>203,239</sup> Furthermore, the redox potential of FeOOH around 1 V versus Li/Li<sup>+</sup> still limits FeOOH to only tangible use in low voltage or anode applications. A composite material of FeOOH and  $\text{FeO}_2$  has also been investigated showing a discharge capacity of  $300 \text{ mAh g}^{-1}$ , however 1/3 of this capacity can be attributed to the  $\text{Fe}^{4+}/\text{Fe}^{3+}$  redox couple at 5 V, which exceeds the safe voltage window for conventional liquid electrolytes.<sup>240</sup> Further investigations have delivered  $\text{Ni}_x\text{Mn}_x\text{Co}_{1-x}(\text{OH})_2$  as a candidate oxyhydroxide Li<sup>+</sup> electrode material. However, these have relatively low discharge capacities, reaching a maximum of  $160 \text{ mAh g}^{-1}$  at  $30 \text{ mA g}^{-1}$  over all values of x between 0 and 0.5.<sup>241</sup>

Vanadium oxyhydroxides present an interesting alternative to NiOOH, FeOOH and CoOOH for two major reasons. Firstly, the  $\text{V}^{5+}/\text{V}^{4+}/\text{V}^{3+}/\text{V}^{2+}/\text{V}^0$  redox potentials all lie in a potential window complimentary to conventional electrolytes. This allows vanadium to pass through

multiple reduction and oxidation steps in a relatively small window, and capitalise on insertion of more than 1  $\text{Li}^+$  per metal atom in a single electrochemical cycle. This is generally referred to as multiple electron transfer (MET). Secondly, since vanadium can access higher oxidation states in a relatively small voltage window, it can accommodate a substitution of a  $\text{O}^{2-}$  anion for  $[\text{OH}]^-$  anion with a smaller operating voltage loss compared to Fe, Mn, Co and Ni.<sup>205</sup>

Montroseite VOOH (space group  $Pbnm$ ) exhibits an open framework ideal for  $\text{Li}^+$  intercalation (Figure 6.1 a). However, nanourchins of VOOH prepared by a conventional hydrothermal method have shown poor discharge capacity ( $80 \text{ mAh g}^{-1}$ ), poor electrochemical stability and a low operating voltage (1 V) due to no MET and limited oxidation state access (+3 to +2 only), respectively.<sup>242</sup> To improve the both the capacity and operating voltage, vanadium oxyhydroxides containing vanadium in oxidation states higher than +3 must be sought. Recent publications have brought  $\text{H}_2\text{V}_3\text{O}_8$  to light as a lead candidate for a metal oxyhydroxide  $\text{Li}^+$  insertion electrode.

$\text{H}_2\text{V}_3\text{O}_8$  (space group  $Pnma$ ) exhibits an open framework consisting of layers of  $\text{VO}_x$  polyhedra in three different environments (Figure 6.1 b).<sup>243</sup> Two  $\text{VO}_6$  octahedra and one  $\text{VO}_5$  trigonal bipyramid is present, giving rise to the mixed  $\text{V}^{4+}/\text{V}^{5+}$  oxidation state observed. The  $\text{VO}_6$  octahedra are arranged in continuous edge sharing ribbons along the  $c$ -axis. These corner share with edge sharing  $\text{VO}_5$  trigonal bipyramidal ribbons, which also form along the  $c$ -direction, to form  $\text{V}_3\text{O}_8$  layers. The  $\text{V}_3\text{O}_8$  layers stack along the  $a$ -axis to form the a layered structure. Computational approaches combined with neutron diffraction have suggested that the H atoms exist in a H-O-H, water-like moiety with H close to O(6) in the plane parallel to the  $b$ -axis between the  $\text{V}_3\text{O}_8$  layers.<sup>244</sup> However, this study also suggests that these techniques do not allow for unambiguous location of the H atoms, but that they do not exist simply as water of crystallisation. Although  $\text{H}_2\text{V}_3\text{O}_8$  is commonly also referred to as  $\text{V}_3\text{O}_7 \cdot \text{H}_2\text{O}$ , there is no structural link between  $\text{V}_3\text{O}_7$  and  $\text{H}_2\text{V}_3\text{O}_8$ .

$\text{H}_2\text{V}_3\text{O}_8$  is also a MET capable material since it possesses two  $\text{V}^{5+}$  and one  $\text{V}^{4+}$  which allows the insertion of up to 5  $\text{Li}^+$  per formula unit. This gives rise to a high theoretical capacity of  $474 \text{ mAh g}^{-1}$ . Experimental observations have shown MET capability in  $\text{H}_2\text{V}_3\text{O}_8$  nanowires, with reversible discharge capacities between  $225 \text{ mAh g}^{-1}$  and  $373 \text{ mAh g}^{-1}$  (at

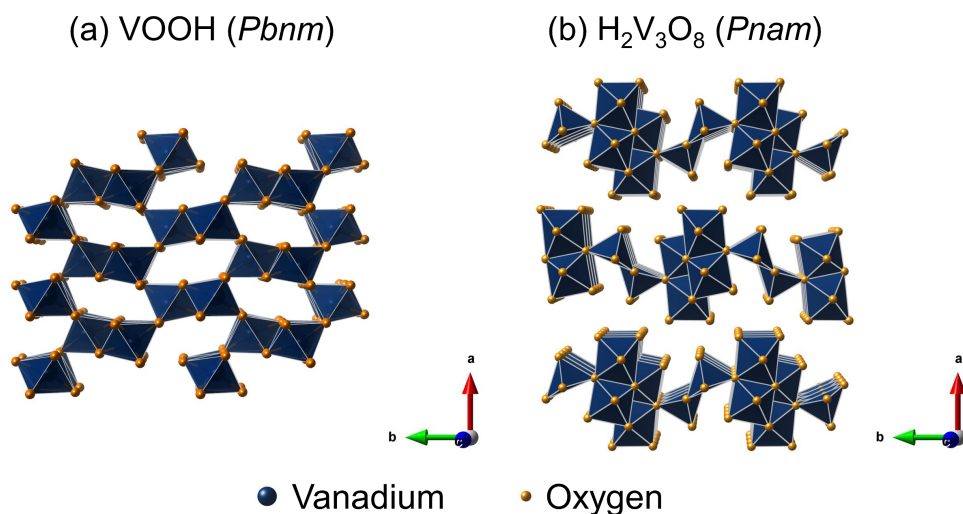


**Figure 6.1:** Crystal structures of (a) VOOH and (b)  $\text{H}_2\text{V}_3\text{O}_8$ . Both compounds exhibit open frameworks ideal for  $\text{Li}^+$  intercalation. H atoms are omitted.

discharge rates of  $100 \text{ mA g}^{-1}$ ) observed corresponding to the insertion of 2.4 and 3.7  $\text{Li}^+$  per formula unit, respectively.<sup>127,217,219,245,246</sup> Furthermore,  $\text{H}_2\text{V}_3\text{O}_8$  consistently shows capacity retentions of  $> 90 \%$  over extended cycling at  $100 \text{ mA g}^{-1}$  and promising electrochemical behaviour at rates up to  $1 \text{ A g}^{-1}$ . Both computational studies and bond enthalpy calculations have suggested that the interaction between the hydroxyl moieties and vanadium oxide layers in  $\text{H}_2\text{V}_3\text{O}_8$  contribute to the excellent electrochemical stability of the material, although the intercalation sites of  $\text{Li}^+$  are still unknown.<sup>243,244</sup> It is also suggested that the consistent nanowire/nanobelt morphology observed in  $\text{H}_2\text{V}_3\text{O}_8$  aids the electrochemical performance of  $\text{H}_2\text{V}_3\text{O}_8$  by limiting  $\text{Li}^+$  diffusion distances.  $\text{H}_2\text{V}_3\text{O}_8$  has also been investigated as a candidate electrode for Na-ion batteries with a modest discharge capacity of  $168 \text{ mAh g}^{-1}$  at  $10 \text{ mA g}^{-1}$ .<sup>247</sup> This lower capacity, compared to Li-ion applications, is mainly attributed to both the higher mass of sodium compared to lithium and the structural challenge of intercalating larger  $\text{Na}^+$  ions.<sup>225</sup>

The aims of this chapter are to attempt the synthesis of vanadium oxyhydroxides, including  $\text{H}_2\text{V}_3\text{O}_8$ , using microwave-assisted solvothermal reduction. The electrochemical performance of the materials will be assessed with galvanostatic cycling and cyclic voltammetry.  $\text{H}_2\text{V}_3\text{O}_8$  prepared by the microwave-assisted route will be investigated on a local scale, using  $\mu\text{SR}$  to report on the lithium diffusion characteristics for the first time and *in situ*

XAS to probe the oxidation state changes during electrochemical operation.

## 6.2 Preparation and investigation of $V_4O_6(OH)_4$

### 6.2.1 Synthesis and characterisation of $V_4O_6(OH)_4$

To investigate the possibility of synthesising vanadium oxyhydroxides by microwave-assisted synthesis, a solvothermal reduction of  $V_2O_5$  was attempted in DEG. The mixture was irradiated for 3 h ( $\nu = 2.45$  GHz) at  $180^\circ\text{C}$  producing a coarse black powder. The PXRD pattern collected for the material can be indexed to the mineral Häggite ( $V_4O_6(OH)_4$ ) by PXRD (Figure 6.2 a).

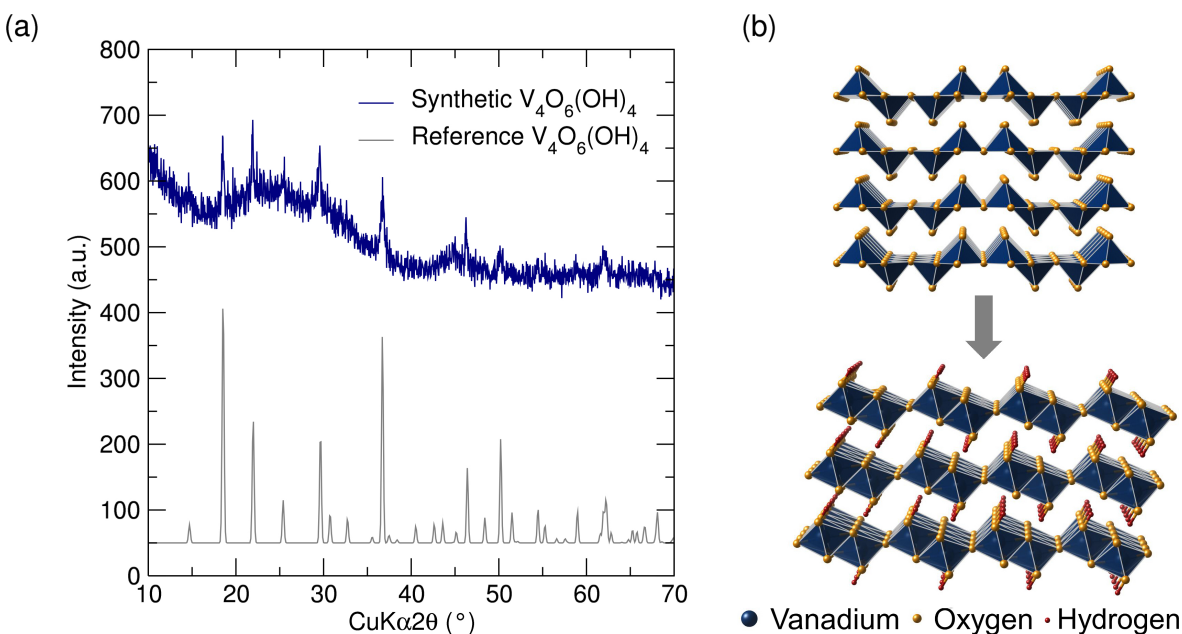


**Figure 6.2:** (a) PXRD pattern collected for synthetic  $V_4O_6(OH)_4$  and a reference pattern for the material taken from Reference 248. (b) shows the transformation during reduction from the  $V_2O_5$  structure to  $V_4O_6(OH)_4$  (Häggite) structured material.

Reports on  $V_4O_6(OH)_4$  are limited in the literature and has only been obtained twice by solid-state and solvothermal routes.<sup>248–250</sup> Figure 6.2 (b) shows the transformation in crystal structure from the  $V_2O_5$  structured material to the Häggite ( $V_4O_6(OH)_4$ ) structure. It is observed that  $V_4O_6(OH)_4$  exhibits a layered structure with terminal hydroxyl groups separating them. It is expected from bond length calculations that the location of the hydrogen atoms

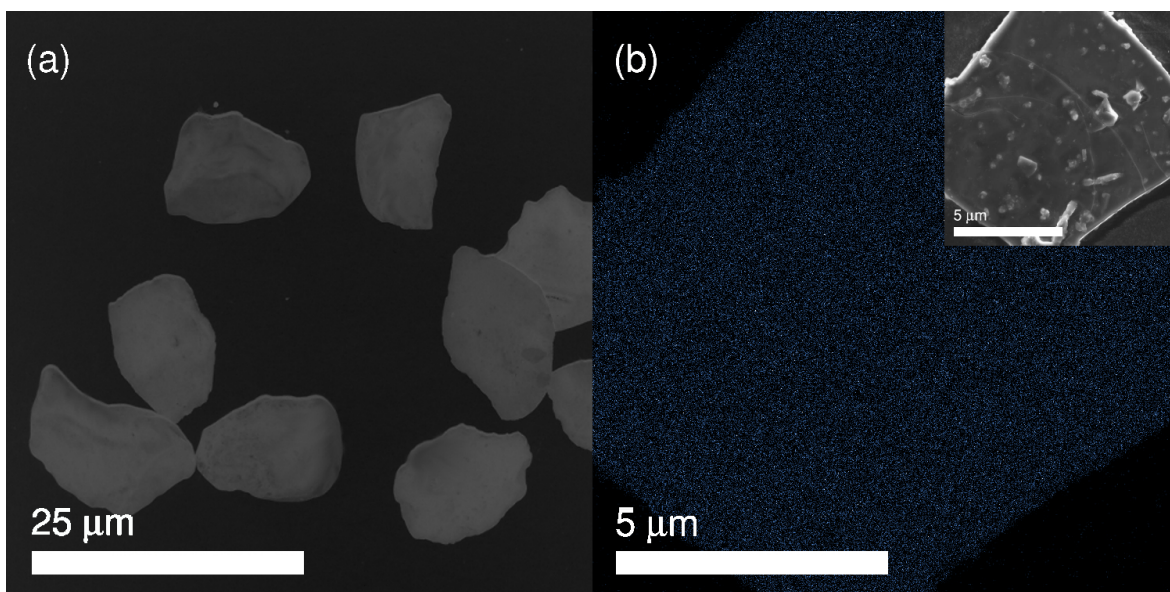


**Figure 6.3:** SEM (a) showing a typical particle of  $V_4O_6(OH)_4$  approximately 10  $\mu\text{m}$  in diameter. EDX mapping of vanadium in the sample shown in blue (b) indicates a homogenous distribution across the particle.

allows the VOx layers to hydrogen bond.<sup>250</sup> Previous reports on oxyhydroxides have suggested that this hydrogen bonding can lend stability to the structures during electrochemical  $\text{Li}^+$  insertion and extraction.<sup>217</sup>

SEM of the synthetic Häggite (Figure 6.3 a) reveals particles in the order of 10  $\mu\text{m}$  in diameter. These particles obtained are in contrast to previous solvothermal synthesis of Häggite which lead to the formation of nanobelts (100 nm width, 10 nm thickness, 100  $\mu\text{m}$  length).<sup>248</sup> EDX mapping of the material (Figure 6.3 b) confirmed a homogenous distribution of vanadium content throughout the surface of the particles.

### 6.2.2 XANES analyses of $V_4O_6(OH)_4$

Conflicting reports of Häggite have suggested the stoichiometry to be  $V_4O_4(OH)_6$ , (containing  $2 \times V^{3+}$  and  $2 \times V^{4+}$ ) and not  $V_4O_6(OH)_4$  (containing only  $V^{4+}$ ).<sup>248,251,252</sup> To investigate the oxidation environment of the vanadium atoms in  $V_4O_6(OH)_x$ , XANES were collected on the vanadium K-edge. Figure 6.4 shows that the rising edge (B) of  $V_4O_6(OH)_x$  lies close to the  $V^{4+}$  standard, with no contribution visible from other oxidation states. Furthermore, only one peak is observed in the pre-edge feature (A), corroborating that only one oxidation state

is present. These observations are in good agreement with the expected oxidation state from the  $V_4O_6(OH)_4$  stoichiometry ( $4 \times V^{4+}$ ) and reports from XPS analyses.<sup>248</sup>

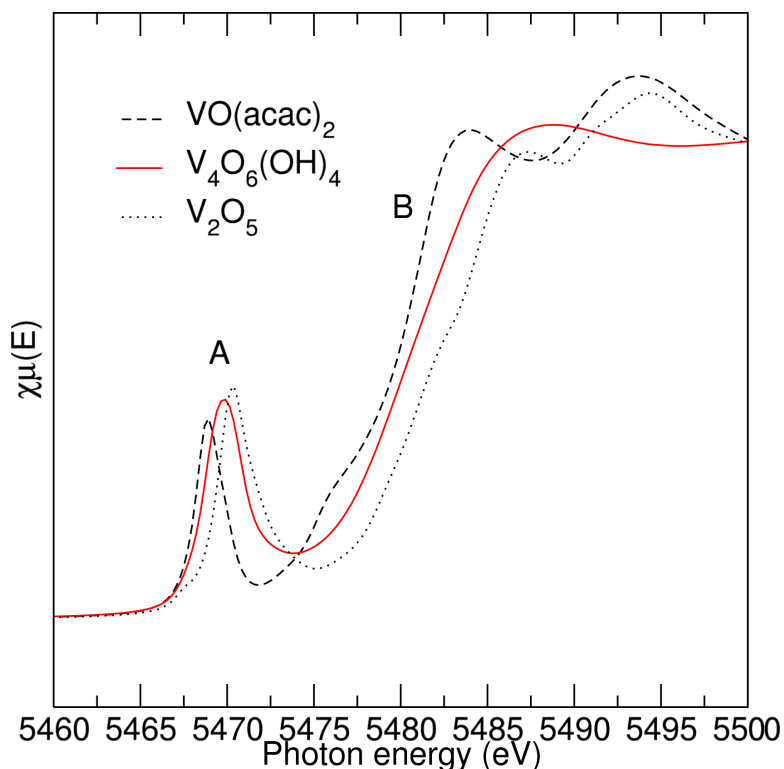


**Figure 6.4:** XANES spectra collected for  $V_4O_6(OH)_4$  prepared by a microwave assisted method, and standards of  $V^{4+}$  [ $VO(acac)_2$ ] and  $V^{5+}$  [ $V_2O_5$ ].

### 6.2.3 Electrochemical analyses of $V_4O_6(OH)_4$

To date there are no existing reports on the electrochemical performance of  $V_4O_6(OH)_4$  as a  $Li^+$  insertion electrode. To investigate this, composite pellets containing 60 % active material ( $V_4O_6(OH)_4$ ), 30 % carbon black and 10 % PTFE binder were cycled galvanostatically at a rate of  $100 \text{ mAh g}^{-1}$  between 1.8 V and 3.8 V versus  $Li/Li^+$  in Swagelok half-cells. The initial cycling profile (Figure 6.5 a) reproducibly exhibited a low charge capacity of  $23 \text{ mAh g}^{-1}$  and Coulombic efficiency of only 21 % in multiple half-cells. Subsequent increases in the charge and discharge capacities are observed with subtle changes in the cycling profile emerging. The discharge capacity reaches a maximum value at the 10th cycle of  $200 \text{ mAh g}^{-1}$  (Figure 6.5 b) which then relaxes back down to  $152 \text{ mAh g}^{-1}$  at the 20th cycle.  $V_4O_6(OH)_4$  also exhibits a reasonable Coulombic efficiency at the 20th cycle of 92.5 %.

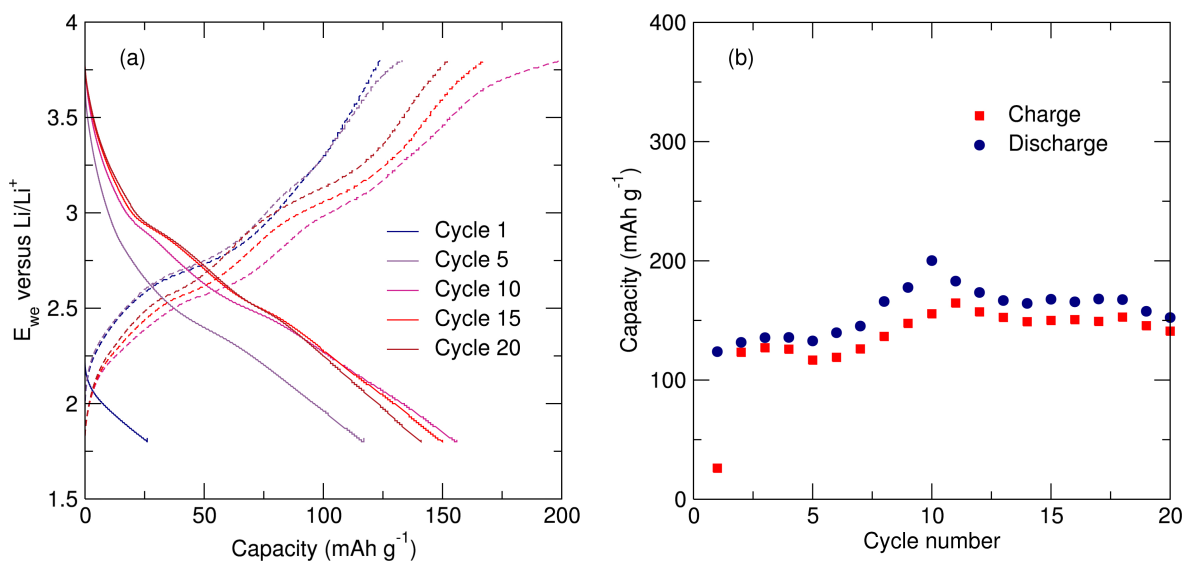


**Figure 6.5:** Galvanostatic cycling profiles (a) of  $V_4O_6(OH)_4$  at a rate of  $100 \text{ mA g}^{-1}$  and the respective charge and discharge capacities as a function of cycle number (b).

The results for  $V_4O_6(OH)_4$  show that oxyhydroxides can be successfully obtained through microwave-assisted methods and employed as insertion electrodes. However the discharge capacity observed for  $V_4O_6(OH)_4$  equates 2  $Li^+$  per formula unit, indicating that  $V_4O_6(OH)_4$  is not an MET capable material. Due to this observation,  $V_4O_6(OH)_4$  was not investigated further.

### 6.3 Preparation and investigation of $H_2V_3O_8$

#### 6.3.1 Synthesis and characterisation of $H_2V_3O_8$

To investigate alternative routes to vanadium oxyhydroxides, microwave-assisted solvothermal reduction of  $V_2O_5$  was performed in a mixture of water and isopropanol (IPA) as a reducing agent. Microwave assisted solvothermal reduction of  $V_2O_5$  carried out in 2 ml:2 ml and 3 ml:1 ml ratios of  $H_2O$ :IPA produced bright orange powders identical to the starting material. The PXRD of both samples (Figure 6.6 a) also exhibited identical peaks to those of a standard  $V_2O_5$  diffraction pattern, confirming no reduction has taken place.

Synthesis conducted in 1 ml:3 ml  $H_2O$ :IPA yielded green fibrous material which was characterised with PXRD (Figure 6.6 b and c). Rietveld refinement carried out on the sample

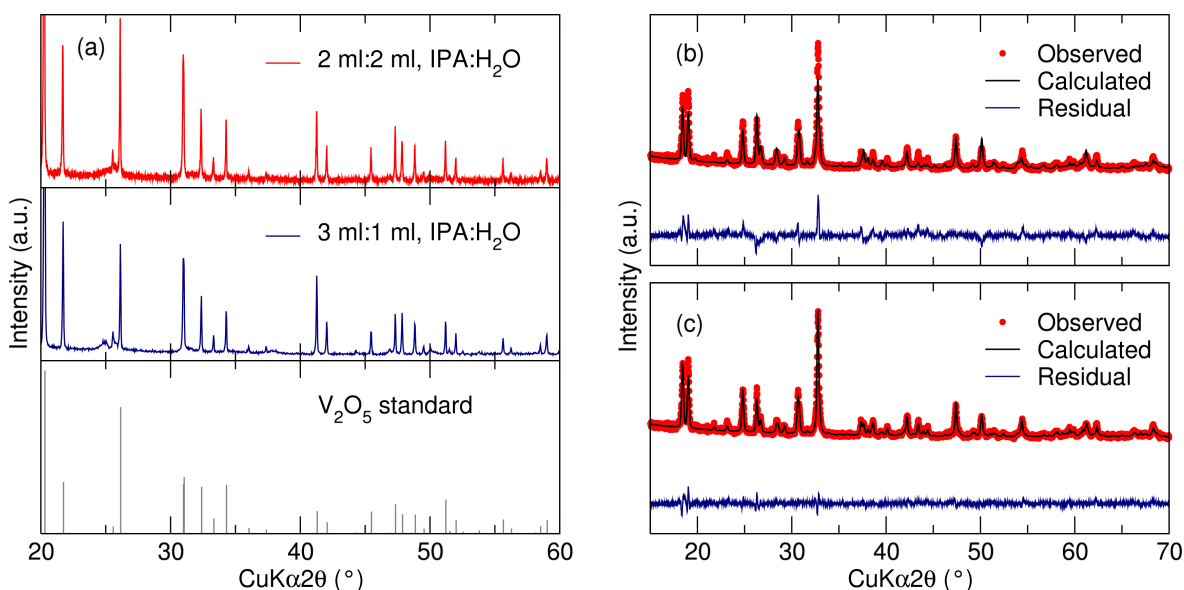


**Figure 6.6:** (a) Microwave-assisted reactions carried out in 2 ml:2 ml and 3 ml:1 ml IPA:H<sub>2</sub>O showing no reduction of the V<sub>2</sub>O<sub>5</sub> reagent. The reference pattern for *Pmmnz* structured V<sub>2</sub>O<sub>5</sub> is taken from Reference 253. (b) Rietveld refinement of H<sub>2</sub>V<sub>3</sub>O<sub>8</sub> prepared in 1 ml:3 ml, H<sub>2</sub>O:IPA and (c) with preferential orientation applied along the [0 0 1] direction. Refinement was performed using H<sub>2</sub>V<sub>3</sub>O<sub>8</sub> diffraction data from Reference 243.

revealed a large discrepancy in peak intensity (Figure 6.6 b). Applying preferred orientation along the [0 0 1] direction (Figure 6.6 c) gave a much better fit to H<sub>2</sub>V<sub>3</sub>O<sub>8</sub> ( $R_p = 25\%$ ,  $R_{wp} = 24\%$ ,  $R_{exp} = 16.47$ ,  $\chi^2 = 2.12$ ). The preferential orientation was identified along [0 0 1] is in good agreement with previous TEM studies of H<sub>2</sub>V<sub>3</sub>O<sub>8</sub> where growth along this direction was also observed.<sup>127</sup> Numerical parameters for the Rietveld refinement of H<sub>2</sub>V<sub>3</sub>O<sub>8</sub> can be seen in Table 6.1.

SEM images taken of the H<sub>2</sub>V<sub>3</sub>O<sub>8</sub> sample revealed ultra-long nanowires, several tens of  $\mu\text{m}$  in length (Figure 6.7 a). The morphology observed agrees with the preferential growth inferred from the Rietveld refinement. Figure 6.7 (b) shows a structural representation of growth of the nanowires along the *b*-axis in the direction of the [0 0 1] direction. Figure 8.1 shows a histogram of measured particle width of 100 H<sub>2</sub>V<sub>3</sub>O<sub>8</sub> nanowires. An average width of 124 nm is observed with a standard deviation of 44 nm.

Space group	<i>Pnam</i>	<b>U</b>	0.24(3)	<b>Atom</b>	<b>x</b>	<b>y</b>	<b>z</b>	<b>Atom</b>	<b>x</b>	<b>y</b>	<b>z</b>
<b>a</b> (Å)	16.8473(7)	<b>V</b>	-0.18(2)	<b>V1</b>	0.0478(6)	0.1213(9)	0.25	<b>O4</b>	0.940(2)	0.213(2)	0.25
<b>b</b> (Å)	9.3154(5)	<b>W</b>	0.078(2)	<b>V2</b>	0.8506(6)	0.0746(8)	0.25	<b>O5</b>	0.772(1)	0.190(2)	0.25
<b>c</b> (Å)	3.6333(3)	<b>R<sub>p</sub></b>	25.0 %	<b>V3</b>	0.4453(5)	0.0850(9)	0.25	<b>O6</b>	0.775(1)	0.896(2)	0.25
		<b>R<sub>wp</sub></b>	24.0 %	<b>O1</b>	0.960(2)	0.917(2)	0.25	<b>O7</b>	0.521(1)	0.924(2)	0.25
		<b>R<sub>exp</sub></b>	16.47 %	<b>O2</b>	0.102(1)	0.284(2)	0.25	<b>O8</b>	0.354(1)	0.030(2)	0.25
		<b>χ<sup>2</sup></b>	2.12	<b>O3</b>	0.136(2)	0.965(2)	0.25	-	-	-	-

**Table 6.1:** Calculated Rietveld refinement parameters from the powder XRD pattern of  $\text{Li}_{0.4}\text{H}_2\text{V}_3\text{O}_8$  prepared by chemical lithiation of  $\text{H}_2\text{V}_3\text{O}_8$  with reference to the pattern taken from Reference 243.

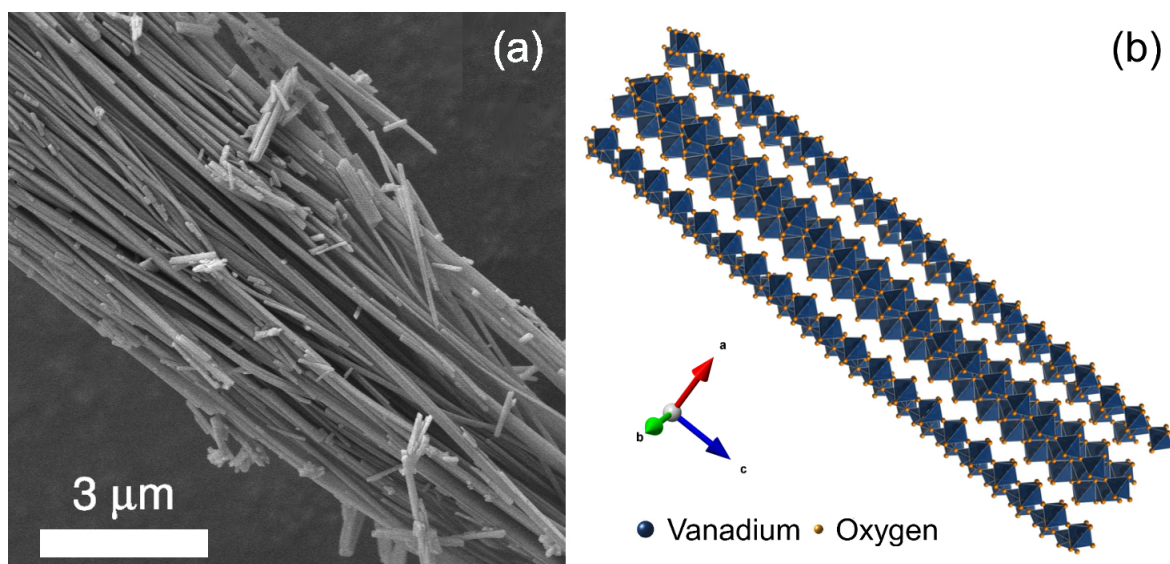


**Figure 6.7:** (a) SEM image of H<sub>2</sub>V<sub>3</sub>O<sub>8</sub> nanowires and (b) the H<sub>2</sub>V<sub>3</sub>O<sub>8</sub> crystal structure showing the preferential growth along the *b*-axis ([0 0 1] direction) from Rietveld analysis.

### 6.3.2 Electrochemical analysis of $\text{H}_2\text{V}_3\text{O}_8$

To analyse the electrochemical behaviour of the  $\text{H}_2\text{V}_3\text{O}_8$  nanowires, CV was conducted in a 0.01 V to 4 V range. On the first cycle there are several features present from the reduction of  $\text{V}^{5+}$  to lower oxidation states and reversible oxidation back to  $\text{V}^{5+}$  at  $0.1 \text{ mV s}^{-1}$ . However, there are not simply two defined peaks for  $\text{V}^{5+}$  to  $\text{V}^{4+}$  and  $\text{V}^{4+}$  to  $\text{V}^{3+}$  suggesting there is a complex structural evolution during cycling responsible for lowering the redox couple after a change in  $[\text{Li}^+]$ .

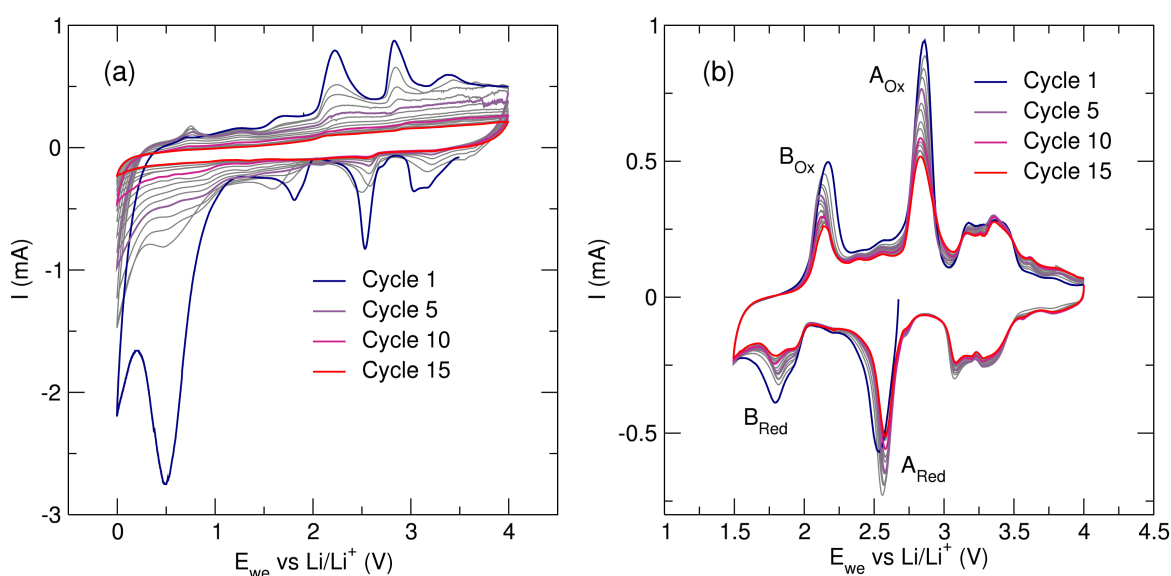


**Figure 6.8:** (a) CV of  $\text{H}_2\text{V}_3\text{O}_8$  between 4 V and 0.1 V showing irreversible loss of redox features and close to no electrochemical activity after 15 cycles. The large peak at 0.5 V corresponds to the formation of the SEI layer. (b) CV of  $\text{H}_2\text{V}_3\text{O}_8$  between 1.5 V and 4 V showing good reversibility of the redox behaviour.

The large peak at 0.5 V is due to the formation of a solid-electrolyte interface (SEI) due to slow electrochemical decomposition of the electrolyte in competition with the half cell redox reaction occurring. The tail close to 0 V corresponds to accommodation of  $\text{Li}^+$  into the carbon additive in the electrode pellet. As cycling of the half-cell continues, the redox peaks from the  $\text{H}_2\text{V}_3\text{O}_8$  diminish rapidly. It has previously been observed that theoretical capacity cannot be reached in  $\text{H}_2\text{V}_3\text{O}_8$  as full reduction to  $\text{V}^{3+}$  causes an irreversible capacity loss, occurring below 1.5 V versus  $\text{Li}/\text{Li}^+$ .<sup>217</sup> The mechanism for this behaviour is likely to be from the substitution of hydrogen in  $\text{H}_2\text{V}_3\text{O}_8$  at low voltages with  $\text{Li}^+$ .<sup>254</sup> In agreement with this

observation,  $\text{Li}_x\text{H}_{2-x}\text{V}_3\text{O}_8$  previously prepared electrochemically exhibits lower reversible discharge capacity than  $\text{H}_2\text{V}_3\text{O}_8$ .<sup>255</sup> The peak from the carbon additive also diminishes rapidly indicating this process is also not fully reversible. Here, after 15 cycles there is no significant redox behaviour occurring indicating reduction to 0.1 V is detrimental to the performance of the material.

Increasing the minimum voltage of the CV to 1.5 V, a similar profile to the first cycle of  $\text{H}_2\text{V}_3\text{O}_8$  is observed between 0.1 V and 4 V over many cycles. CV conducted on other samples of  $\text{H}_2\text{V}_3\text{O}_8$  in the literature have been unsuccessful at assigning the specific peaks to any particular redox potential. However, classical electrochemistry demands that higher voltages are indicative of higher order oxidation state changes. Similar to the 0.1 V to 4 V CV, many redox features appear in the 1.5 V to 4 V CV. These observations are in good agreement with the literature, indicating a multi-step intercalation process with good reversibility.<sup>136,219,256</sup> The multi-step process likely arises from the structural complexity exhibited by  $\text{H}_2\text{V}_3\text{O}_8$ . In addition, the position of redox peaks  $A_{\text{Ox}}$  increases by +0.03 V and  $A_{\text{Red}}$  decreases by -0.02 V respectively. This implies the  $\text{Li}^+$  insertion and extraction is becoming more energetically efficient by decreasing the overpotential of this redox couple. Peak  $B_{\text{Ox}}$  shifts to lower and then higher voltage ultimately ending at a difference of +0.03 V versus the initial value further indicating a change in the electronic environment in this redox couple with increasing cycle number. The intensity of the peaks (I, mA) all decrease with increasing cycle number which is indicative of diminishing capacity. After the 15th cycle, the intensity of the two main peaks at 2.83 V ( $A_{\text{Ox}}$ ) and 2.58 V  $A_{\text{Red}}$  have decreased by 0.424 mA and 0.218 mA respectively. The rate of change of I is slower in the reduction step, converging after the 10th cycle. This indicates that irreversible insertion of  $\text{Li}^+$  is mainly responsible for capacity loss during the first 10 cycles in this redox step.

$\text{H}_2\text{V}_3\text{O}_8$  was mixed with 30 % carbon black and 10 % PTFE binder and pressed into pellets at 1.2 T for all further experiments. Galvanostatic cycling of the  $\text{H}_2\text{V}_3\text{O}_8$  nanowires between 1.5 V and 3.8 V at 100 mA  $\text{g}^{-1}$  reveals an initial discharge capacity of 334 mAh  $\text{g}^{-1}$  (Figure 6.9 a) and the cycling profile exhibits several pseudo-plateaus due to the reversible reduction and oxidation of vanadium from  $\text{V}^{5+}$  to  $\text{V}^{4+}$  in good agreement with previous studies.<sup>217</sup> After 20 cycles this capacity decreases to 316 mAh  $\text{g}^{-1}$  giving an excellent Col-

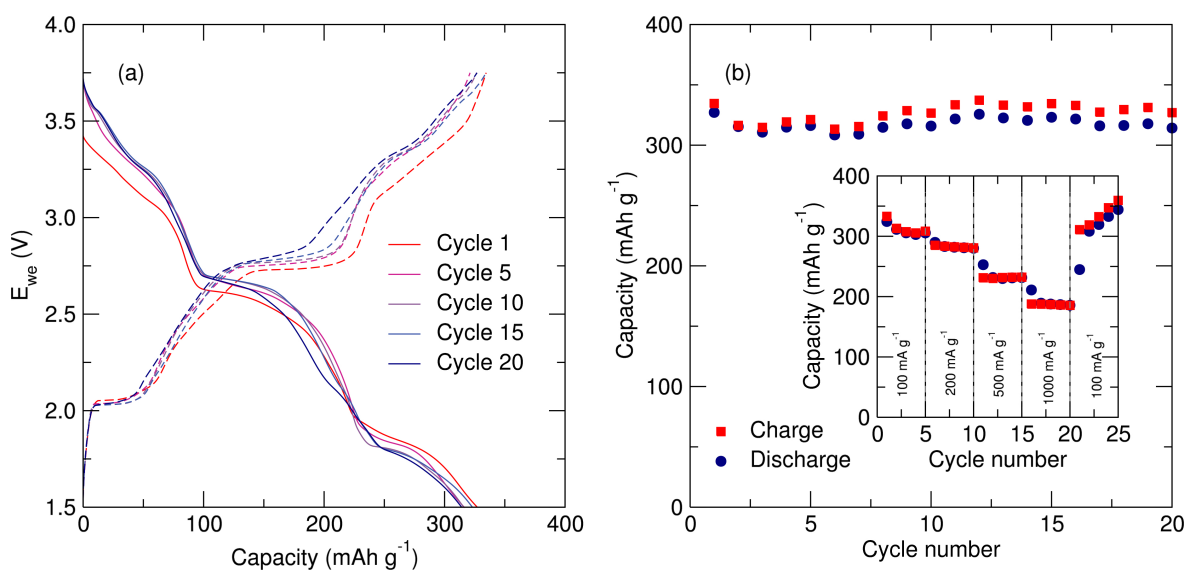


**Figure 6.9:** (a) Galvanostatic cycling of  $\text{H}_2\text{V}_3\text{O}_8$  between 1.5 V and 3.75 V versus  $\text{Li/Li}^+$  at  $100 \text{ mA g}^{-1}$ . (b) Excellent stability of the charge and discharge capacities is observed after 20 cycles, with a retention of 98 % and 95 % respectively, inset shows the cycling performance at faster rates.

ombic efficiency of 95 % (Figure 6.9 b). The observed capacities are similar to previous reports for  $\text{H}_2\text{V}_3\text{O}_8$  but still below the theoretical capacity. Other investigations have found that the full capacity is only realised by cycling the material down to 1 V to reduce  $\text{V}^{4+}$  to  $\text{V}^{3+}$ , but cannot be sustained upon extended cycling leading to a detrimental loss in capacity.<sup>217</sup> A sequential loss of capacity is observed when cycling at faster rates (Figure 6.9 b inset) with a modest capacity of approximately  $180 \text{ mAh g}^{-1}$  observed at the fastest rate of  $1000 \text{ mA g}^{-1}$ . This is the highest reported capacity to date in a MET capable vanadium based electrode at this rate. A full recovery of the initial capacity is observed on returning to  $100 \text{ mA g}^{-1}$ . It has been suggested that the narrow width of the  $\text{H}_2\text{V}_3\text{O}_8$  particles may reduce the  $\text{Li}^+$  diffusion distances, leading to increased performance observed.<sup>257</sup>

These electrochemical results parallel those observed from the highest, first discharge capacity of  $\text{H}_2\text{V}_3\text{O}_8$  reported to date, which was prepared by a hydrothermal route at  $180^\circ\text{C}$  for 7 days. Additionally, superior cycling stability (95 %) is observed after 20 cycles at  $100 \text{ mA g}^{-1}$  in the microwave prepared  $\text{H}_2\text{V}_3\text{O}_8$ , compared to the former study (66 %). Furthermore studies of  $\text{H}_2\text{V}_3\text{O}_8$  that do achieve a commensurate stability to our findings do

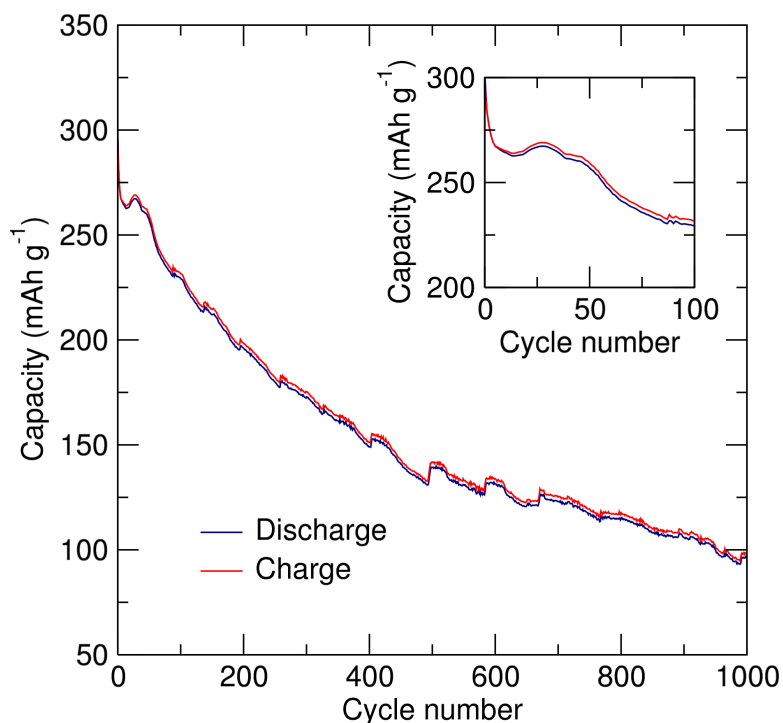


**Figure 6.10:** GCPL of  $\text{H}_2\text{V}_3\text{O}_8$  nanowires between 3.75 V and 1.5 V at a constant current of  $1000 \text{ mA g}^{-1}$

so at lower rates and/or yield significantly lower discharge capacities.<sup>127,219,245,246,255</sup> The electrochemical performance also exceeds that of composite materials of  $\text{H}_2\text{V}_3\text{O}_8$  prepared with  $\text{AlO}_x\text{OH}_y$  or reduced graphene oxide in an attempt to improve capacity by increasing the electrical conductivity.<sup>256,258,259</sup> These reports also required multistep synthetic processes, compared to the single step microwave-assisted route presented here.

To further understand the rate capability at high rates GCPL at  $1000 \text{ mA g}^{-1}$  was conducted over 1000 cycles (Figure 6.10). An initial capacity of  $285 \text{ mAh g}^{-1}$  quickly decays to  $230 \text{ mAh g}^{-1}$  (80 % capacity retention) and  $98 \text{ mAh g}^{-1}$  after 1000 cycles (capacity retention of 34 %).

## 6.4 $\text{Li}^+$ diffusion in $\text{Li}_{0.4}\text{H}_2\text{V}_3\text{O}_8$

It has been shown that  $\text{H}_2\text{V}_3\text{O}_8$  exhibits excellent electrochemical performance as a  $\text{Li}^+$  insertion electrode. Electrochemical performance of  $\text{Li}^+$  insertion electrodes is ultimately governed by the diffusion of  $\text{Li}^+$ . High diffusion coefficients ( $D_{\text{Li}}$ ) and low activation energies

(E<sub>a</sub>) for Li<sup>+</sup> diffusion allow insertion electrodes to perform more efficiently, and may contribute to the outstanding performance observed in H<sub>2</sub>V<sub>3</sub>O<sub>8</sub>. To investigate the local Li<sup>+</sup> diffusion properties of Li<sub>x</sub>H<sub>2</sub>V<sub>3</sub>O<sub>8</sub>  $\mu$ SR studies were performed.

#### 6.4.1 Chemical lithiation of H<sub>2</sub>V<sub>3</sub>O<sub>8</sub>

To measure Li<sup>+</sup> diffusion in a material, it must contain lithium. As H<sub>2</sub>V<sub>3</sub>O<sub>8</sub> does not contain Li<sup>+</sup> after synthesis, it must a sample of H<sub>2</sub>V<sub>3</sub>O<sub>8</sub> was chemically lithiated by a solution based method. H<sub>2</sub>V<sub>3</sub>O<sub>8</sub> prepared by a microwave-assisted approach was reduced using LiOH, employing ascorbic acid as an anti-oxidant to ensure no oxidation of the V<sup>4+</sup> occurred. The Li<sub>x</sub>H<sub>2</sub>V<sub>3</sub>O<sub>8</sub> nanowires were washed with water and dried in air overnight and their Li<sup>+</sup> concentration was analysed using flame photometry, giving a stoichiometry of Li<sub>0.4</sub>H<sub>2</sub>V<sub>3</sub>O<sub>8</sub>. Flame photometry of the water used to wash the nanowires was performed to quantify the amount remaining LiOH and accounted for only 0.3 % of the concentration in the sample, showing that there was minimal (if any) contamination from residual LiOH.

Rietveld refinement of the Li<sub>0.4</sub>H<sub>2</sub>V<sub>3</sub>O<sub>8</sub> nanowires was performed using H<sub>2</sub>V<sub>3</sub>O<sub>8</sub> as the reference pattern gave no indication of impurity phases or side products. Similar to the microwave prepared H<sub>2</sub>V<sub>3</sub>O<sub>8</sub>, Li<sub>0.4</sub>H<sub>2</sub>V<sub>3</sub>O<sub>8</sub> exhibited preferred orientation along the [0 0 1] direction, although the magnitude was lower in the lithiated sample. This is likely due to the shortening of the particles after chemical lithiation. Furthermore, the unit cell shows a contraction of the *a* (0.08 Å) and *b* (0.03 Å) directions in Li<sub>0.4</sub>H<sub>2</sub>V<sub>3</sub>O<sub>8</sub>, suggesting that the H<sub>2</sub>V<sub>3</sub>O<sub>8</sub> layers become closer upon lithiation.

SEM of the nanowires revealed a shortening in length. A histogram of the thickness of the nanowires is given in Figure 8.2. It is observed that the average thickness of the nanowires decreases upon lithiation from 124 nm in H<sub>2</sub>V<sub>3</sub>O<sub>8</sub> to 84 nm in Li<sub>0.4</sub>H<sub>2</sub>V<sub>3</sub>O<sub>8</sub>. A lower standard deviation is also observed in the lithated sample.

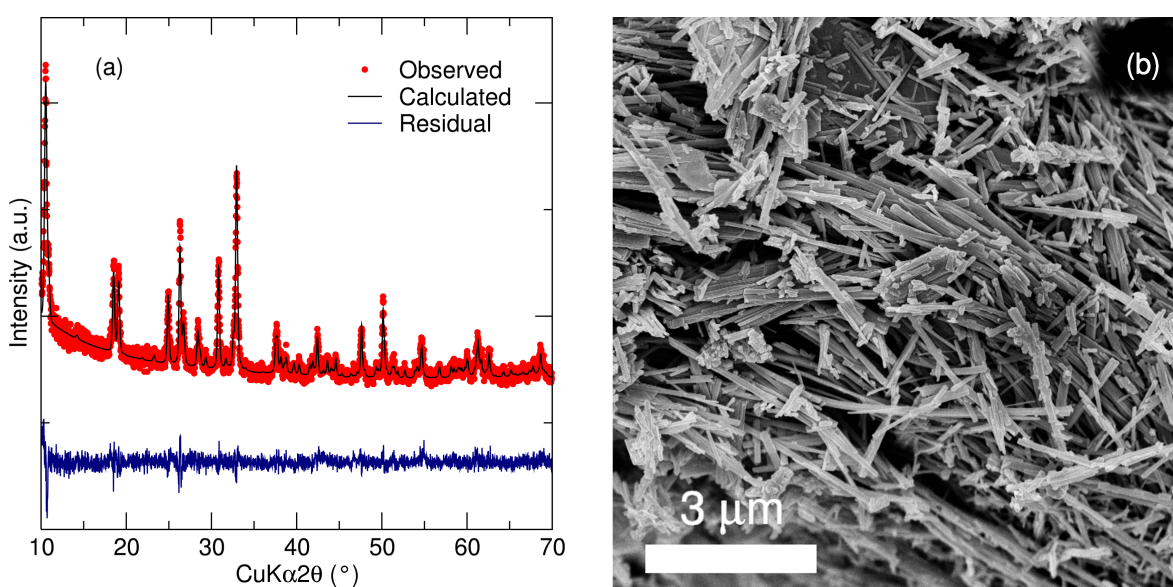


**Figure 6.11:** (a) Rietveld refinement of  $\text{Li}_{0.4}\text{H}_2\text{V}_3\text{O}_8$  prepared by chemical lithiation of  $\text{H}_2\text{V}_3\text{O}_8$  nanowires using  $\text{H}_2\text{V}_3\text{O}_8$  diffraction data from Reference 243. Numerical parameters for the refinement can be seen in Table 8.2. (b) SEM image of  $\text{Li}_{0.4}\text{H}_2\text{V}_3\text{O}_8$  showing that the overall nanowire morphology is preserved but with a reduction length due to grinding in a pestle and mortar.

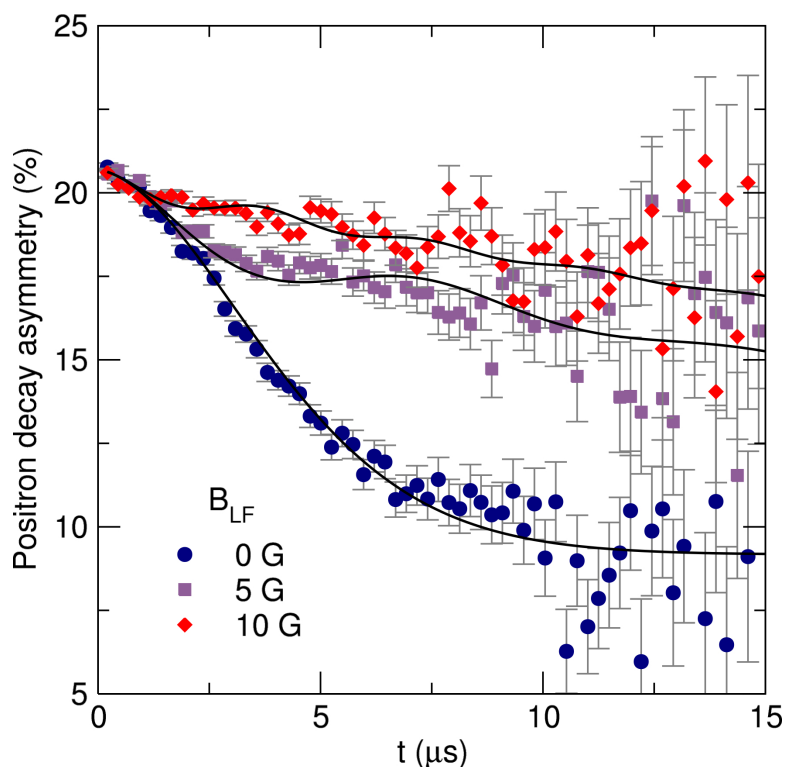


**Figure 6.12:** Raw muon data collected at 300 K showing a relaxation in the positron decay asymmetry with increasing time. Applying larger longitudinal fields sequentially decouples the muon decay from paramagnetic  $V^{4+}$ .

#### 6.4.2 Investigation of $Li^+$ diffusion in $Li_{0.4}H_2V_3O_8$ by muon spin relaxation

$\mu$ SR studies were performed on  $Li_{0.4}H_2V_3O_8$  by applying fields of 0 G, 10 G and 20 G to decouple the muon from any local paramagnetic influences from  $V^{4+}$  in  $H_2V_3O_8$  and to add more constraints when fitting the data simultaneously. An example of these fits to the raw data at 300 K can be seen in Figure 6.12.

The data were fit using a combination of the analytical Keren function, which models the temperature dependent fluctuations in muon decay due to  $Li^+$  was employed and multiplied by a Lorentzian component to account for temperature independent contributions from randomly fluctuating magnetic moments. This can be expressed as:

$$P_z(t) = \exp[-\Gamma(\Delta, \nu, \omega_L, t)t] \exp(-\lambda t) \quad (6.1)$$

where  $P_z(t)$  is the probability a muon will decay in a given direction at a given time,  $\Delta$

is the quasielastic distribution of local magnetic fields at the muon stopping site,  $\nu$  is the temperature dependent fluctuation rate in muon decay,  $\omega_L = \gamma\mu B$  is the Larmor precession frequency of the muon in a given magnetic field and  $\lambda$  is the contribution from temperature independent, randomly fluctuating magnetic moments.<sup>172</sup> The data collected for  $B_{LF} = 0$  G, 10 G and 20 G at a given temperature were fit simultaneously to introduce more constraint to the model, with a constant  $\lambda$  of 0.0239 MHz. It is observed that  $\nu$  (Figure 6.13 a) shows thermally activated behaviour between 180 °C and 230 °C, after which there is a steep decline which can be attributed to the ionic diffusion process occurring faster than the muon decay.  $\mu$ SR does not discriminate diffusing species, and has been used to detect the diffusion of  $H^+$  as well as  $Li^+$ .<sup>260</sup> However, theoretical calculations of  $H_2V_3O_8$  have suggested that the hydrogen atoms in the structure bond covalently to O forming hydroxyl groups.<sup>261</sup> The bond strength of O-H in the structure is therefore thought to be great enough to prevent mobilisation of  $H^+$ .<sup>243</sup> Furthermore, it has previously been reported from experimental observations that there is no  $Li^+/H^+$  exchange mechanism that occurs in the voltage range studied.<sup>254</sup> Outside of this range the exchange can occur but becomes irreversible. Thus, any diffusive behaviour observed in  $Li_{0.4}H_2V_3O_8$  must be attributed to the  $Li^+$  not  $H^+$ .

The  $\Delta$  (Figure 6.13 b) remains a relative constant at all temperatures indicating the behaviour of  $\nu$  is not due to any changes in the local magnetic environment of the muon. Using the values of  $\nu$  an Arrhenius plot can be constructed (Figure 6.13 c) to calculate the  $E_a$  for the  $Li^+$  hopping process, giving an estimated value of 99 meV at 300 K. These muon studies show competitive dynamic behaviour, on a local scale, compared to previously reported lead commercial materials such as  $\alpha$ - $LiFePO_4$ .<sup>71</sup>

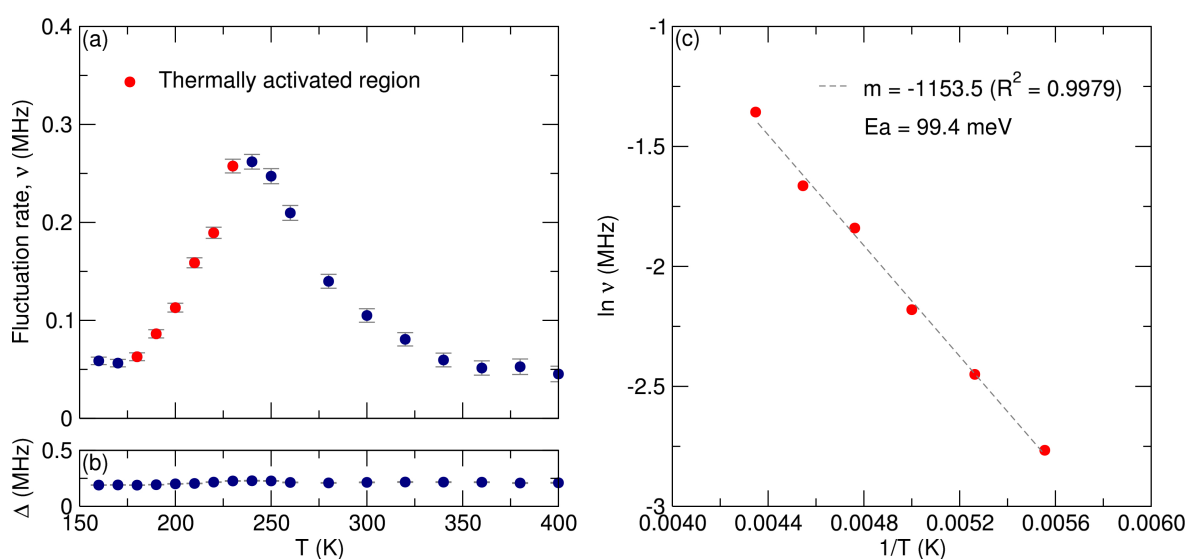


**Figure 6.13:** (a) Muon spin relaxation measurements performed on  $\text{Li}_x\text{H}_2\text{V}_3\text{O}_8$  show temperature dependence of the fluctuation rate,  $\nu$ , beginning at 180 °C. (b) The field distribution width,  $\Delta$ , remains a relative constant suggesting the behaviour of  $\nu$  can be wholly attributed to the diffusion of  $\text{Li}^+$ . (c) Activation energy calculated from an Arrhenius plot over the thermally activated region.

## 6.5 *In situ* XAS of $\text{H}_2\text{V}_3\text{O}_8$

Although *ex situ* studies have been performed to evaluate the oxidation state changes in  $\text{H}_2\text{V}_3\text{O}_8$  such as XPS, these do not represent the behaviour of the electrode during operation, as electrochemical relaxation may occur.<sup>6.1</sup> To give further insight into the evolution of the oxidation state changes within  $\text{H}_2\text{V}_3\text{O}_8$ , *in situ* XAS studies were performed to allow a local investigation of redox behaviour.

*Ex situ* vanadium K-edge XAS of several vanadium standards in oxidation states 3+ to 5+ ( $\text{V}_2\text{O}_3$ , VC,  $\text{V}_2\text{O}_5$ ) and  $\text{H}_2\text{V}_3\text{O}_8$  can be seen in Figure 6.14.

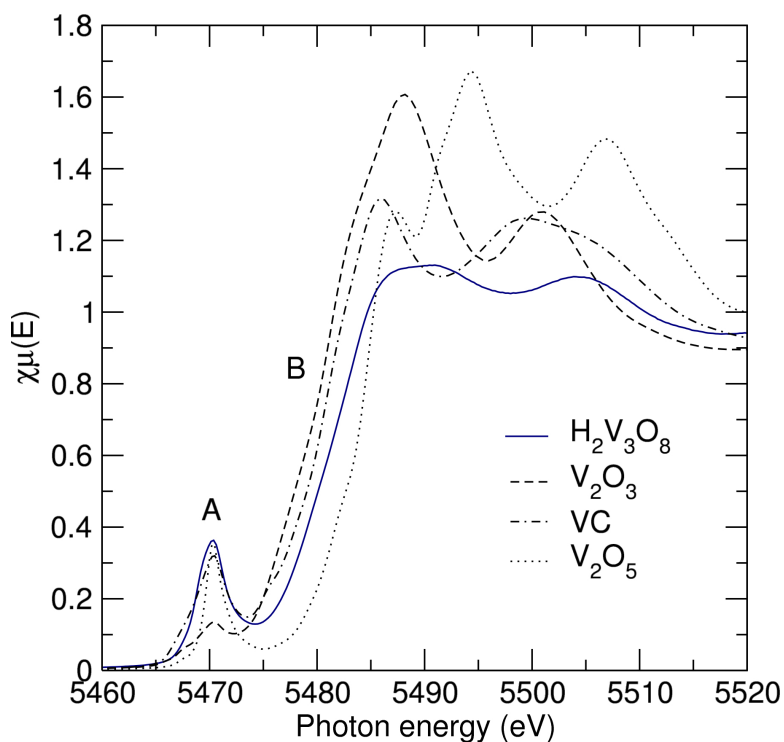


**Figure 6.14:** *Ex situ* XAS of  $\text{H}_2\text{V}_3\text{O}_8$  prepared by a microwave-assisted route and vanadium standards  $\text{V}_2\text{O}_3$  ( $\text{V}^{3+}$ ), VC ( $\text{V}^{4+}$ ) and  $\text{V}_2\text{O}_5$  ( $\text{V}^{5+}$ )

The spectra exhibit two features of notable interest, the pre-edge (A) which arises from the quadrupole excitation of a core 1s electron to the 3d states, and the rising edge (B) arising from a core level 1s dipole transition to  $4+np$  states where  $n$  is an integer.<sup>228</sup> It is observed that as the oxidation state of the vanadium atoms decreases the photon energy also decreases leading to a shift in the spectrum, consistent with Kunzl's law, due to the

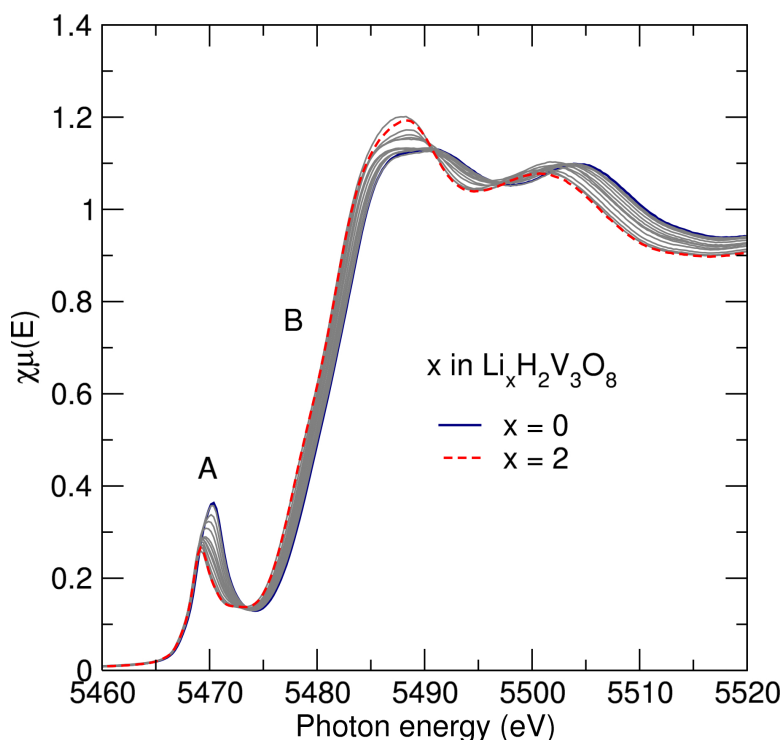


**Figure 6.15:** *In situ* normalised XAS spectra over the XANES region of  $\text{H}_2\text{V}_3\text{O}_8$  during electrochemical lithiation showing an increasing shift in the edge energy to lower eV with increasing  $\text{Li}^+$  concentration due to the reduction of  $\text{V}^{5+}$  in  $\text{H}_2\text{V}_3\text{O}_8$ .

relative destabilisation of the core  $1s$  electron with respect to the  $3d$  (pre-edge) and  $4+np$  (rising edge) levels. The rising edge of the  $\text{H}_2\text{V}_3\text{O}_8$  sample lies between the  $4+$  and  $5+$  standards due to the mixed oxidation state (two  $\text{V}^{5+}$  and one  $\text{V}^{4+}$ ) as expected. Figure 6.15 shows the *in situ* XAS data collected for  $\text{H}_2\text{V}_3\text{O}_8$  with increasing concentrations of intercalated  $\text{Li}^+$ . It is observed that as the concentration of  $\text{Li}^+$  increases the spectra shift to lower photon energy due to the reduction of the vanadium species present. Recent *in situ* studies of  $\text{V}_2\text{O}_5$  have found that upon reduction to  $\text{V}^{3+}$  a new shoulder is formed on the pre-edge at lower energy.<sup>262</sup> The absence of this shoulder implies that no reduction to  $\text{V}^{3+}$  has occurred in our sample in our sample upon lithiation.

B3LYP DFT calculations of the  $\text{H}_2\text{V}_3\text{O}_8$  asymmetric unit (Figure 6.16) give a close profile to that observed experimentally. V1 (blue) and V2 (lilac) both adopt the  $\text{V}^{5+}$  oxidation state and the DFT photon energies are larger than those of V3 (red) which adopts the  $\text{V}^{4+}$  state by approximately 1.3 eV in good agreement with previously reported vanadate studies of 1.1

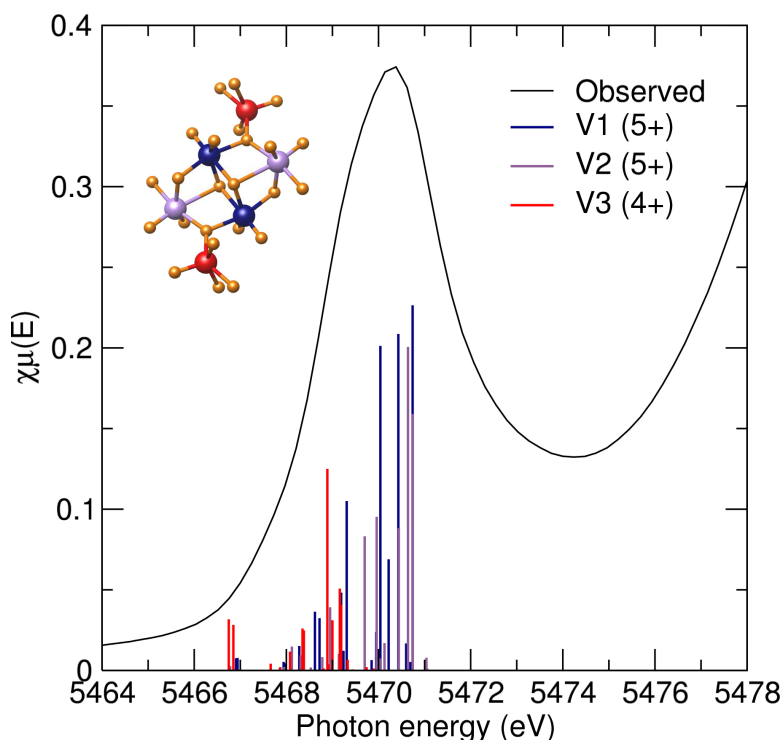


**Figure 6.16:** B3LYP pre-edge calculation for the  $\text{H}_2\text{V}_3\text{O}_8$  asymmetric unit and experimental data showing the expected energies for the 3 V sites. Both  $\text{V}^{5+}$  environments overlap at high energy while  $\text{V}^{4+}$  is at lower energy.

eV (literature) to 1.2 eV (Chapter 5).<sup>229</sup>

By taking the second derivative over the pre-edge region (Figure 6.17), four features of interest can be seen. The first two low energy minima (A) can be assigned to separate contributions from  $\text{V}^{5+}$  (5470.4 eV) and  $\text{V}^{4+}$  (5469.2 eV) with an energy gap of approximately 1.2 eV, consistent with previously reports on vanadium oxides.<sup>229</sup> As the concentration of  $\text{Li}^+$  is increased, a simultaneous increase of  $\text{V}^{4+}$  and decrease of  $\text{V}^{5+}$  is observed, confirming the selective reduction of  $\text{V}^{5+}$  in the first stage of lithiation as no contribution from  $\text{V}^{3+}$  is present. This implies a two-step mechanism for  $\text{Li}^+$  intercalation where  $\text{V}^{5+}$  is first fully reduced to  $\text{V}^{4+}$  before reduction of the  $\text{V}^{4+}$  population begins, in good agreement with other *in situ* XAS studies on other intercalation cathode materials.<sup>263</sup>

The minima at 5479.8 eV in the  $\text{H}_2\text{V}_3\text{O}_8$  (non-lithiated) scan, feature (B), is from ligand-metal charge transfer (LMCT) by the transfer of one electron from the oxygen 2p orbital to fill the  $1s^0$  core-hole. In the normalised data, the LMCT forms a lower energy shoulder to

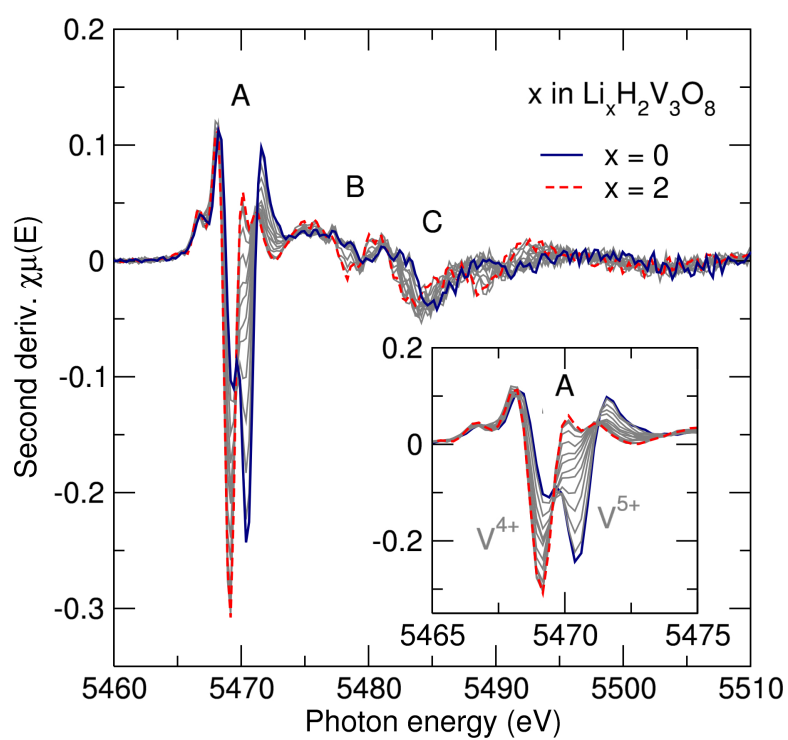


**Figure 6.17:** Second derivative of the pre-edge feature for  $\text{H}_2\text{V}_3\text{O}_8$  as an increasing concentration of  $\text{Li}^+$  is inserted showing separate contributions from  $\text{V}^{5+}$  (5470.4 eV) and  $\text{V}^{4+}$  (5469.2 eV).

the higher energy edge feature, represented by a minima in the second derivative at 5484.8 eV, since filling the core-hole screens the nucleus making the excitation of the core electron less energetically costly. As  $\text{Li}^+$  is inserted into  $\text{H}_2\text{V}_3\text{O}_8$ , a decrease in energy is observed for the LMCT and edge energy to 5478.8 eV and 5483.3 eV respectively. This is due to the destabilisation of the  $1s$  orbital with respect to the  $V 4+np$  excited state. Lastly, the minima at 5480.4 eV (C) is the rising edge. As with the normalised spectra, a shift to lower energy is observed due to the reduction of  $\text{V}^{5+}$  to  $\text{V}^{4+}$ .

The pre-edge features of the *in situ* XAS were modeled with a combination of two Lorentzian functions (one for each of the oxidation states  $\text{V}^{4+}$  and  $\text{V}^{5+}$ ) an arctangent function to account for the contribution in intensity from the rising edge. The centroids of the Lorentzian functions were fixed at 5470.4 eV for  $\text{V}^{5+}$  and 5469.2 for  $\text{V}^{4+}$ , taken from the minima in the second derivative plot. The widths and height of the Lorentzian peaks were allowed to vary to account for the change in local coordination and relative oxidation state concentration during lithiation. The magnitude and width of the arctangent was fixed while the centroid was allowed to vary to account for the change in the  $1s$  to  $4+np$  excitation energy in vanadium with changing oxidation state. Figure 6.18 shows fits to the pre-edge feature at (a)  $\text{H}_2\text{V}_3\text{O}_8$  and (b)  $\text{Li}_2\text{H}_2\text{V}_3\text{O}_8$ .

Upon lithiation it is observed that the peak attributed to  $\text{V}^{5+}$  diminishes in intensity while the peak attributed to  $\text{V}^{4+}$  grows due to the reduction of vanadium during lithiation. Extracting the peak areas from these fits allows the study of relative concentration of  $\text{V}^{4+}$  and  $\text{V}^{5+}$  in the sample with increasing  $\text{Li}^+$  concentration. It is observed that as the scan number increases (increase in  $\text{Li}^+$  concentration) the area of the  $\text{V}^{5+}$  peak consistently diminishes while the area of the  $\text{V}^{4+}$  peak increases. It is interesting to note that the rate of change in area is not constant implying that there may be other contributions involved such as changes in geometry of the  $\text{VO}_x$  polyhedra.

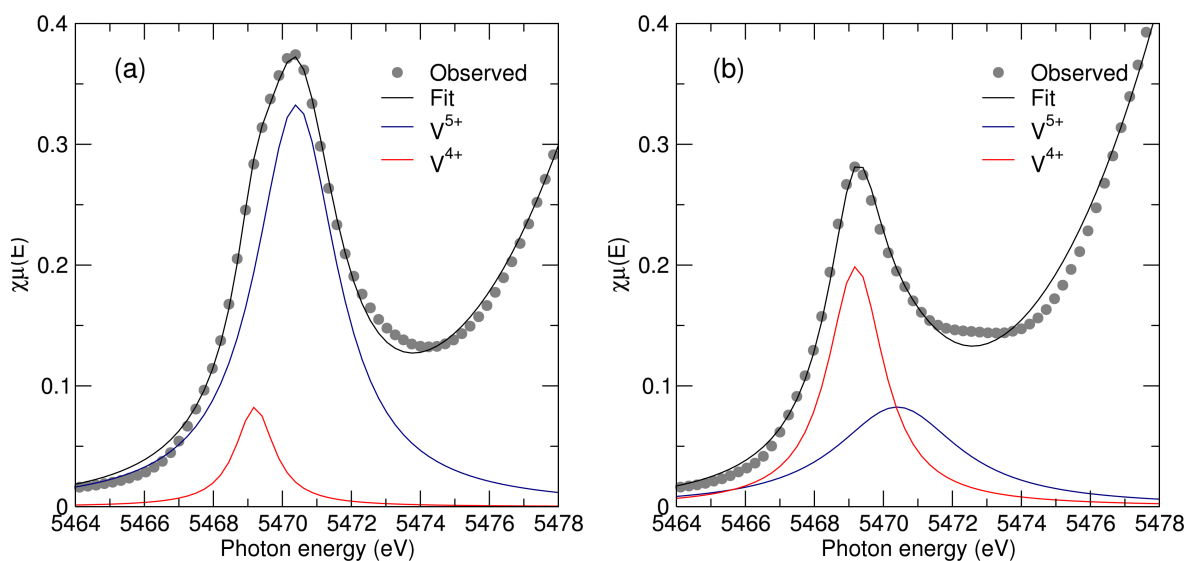


**Figure 6.18:** Pre-edge fits using two Lorentzian functions with centroids fixed at 5470.4 eV ( $\text{V}^{5+}$ ) and 5469.2 eV ( $\text{V}^{4+}$ ) and an arc tangent function to account for contributions from the rising edge of (a)  $\text{H}_2\text{V}_3\text{O}_8$  and (b)  $\text{Li}_2\text{H}_2\text{V}_3\text{O}_8$ .

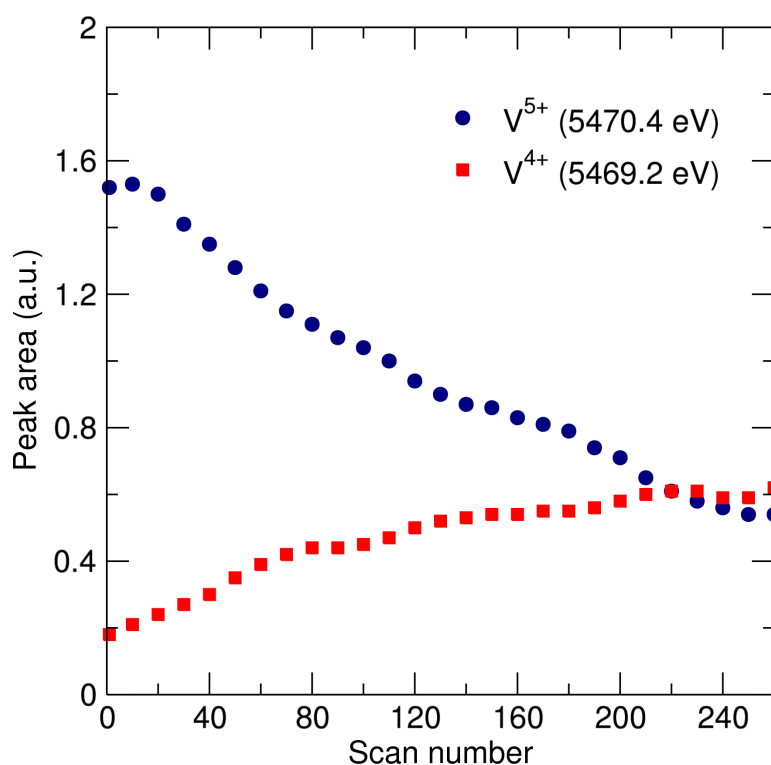


**Figure 6.19:** Scan number versus peak area for the two contributions to the pre-edge from  $\text{V}^{5+}$  and  $\text{V}^{4+}$  in  $\text{H}_2\text{V}_3\text{O}_8$ . It is observed that  $\text{V}^{5+}$  decreases while  $\text{V}^{4+}$  increases indicating a change in the relative concentration upon  $\text{Li}^+$  insertion.

## 6.6 Conclusions

These studies show that vanadium oxyhydroxides are viable candidates for Li-ion insertion electrodes. Häggite has been synthesised for the first time by a microwave-assisted route, and it has also been confirmed by XAS that the vanadium exists only in the  $V^{4+}$  oxidation state, confirming the stoichiometry cannot be the formerly reported  $V_4O_4(OH)_6$  (which has a mixed oxidation state), but  $V_4O_6(OH)_4$  proposed in more recent reports.<sup>248</sup> Although this means that Häggite can not be considered as a MET capable insertion cathode (as it contains no  $V^{5+}$ ), it shows a promising theoretical capacity of  $292 \text{ mAh g}^{-1}$ , and an experimental maximum discharge capacity of  $200 \text{ mAh g}^{-1}$ , at  $100 \text{ mA g}^{-1}$ . This exceeds the obtainable capacity in lead cathode materials such as  $\text{LiCoO}_2$  ( $140 \text{ mAh g}^{-1}$ ) and  $\text{LiFePO}_4$  ( $170 \text{ mAh g}^{-1}$ ).

MET capable  $\text{H}_2\text{V}_3\text{O}_8$  nanowires have also been prepared using a microwave-assisted approach. The  $\text{H}_2\text{V}_3\text{O}_8$  nanowires exhibit a large capacity after 20 cycles of  $316 \text{ mAh g}^{-1}$  at  $100 \text{ mA g}^{-1}$  and  $180 \text{ mAh g}^{-1}$  at  $1000 \text{ mA g}^{-1}$ . These capacities are competitive to previous reports of  $\text{H}_2\text{V}_3\text{O}_8$  prepared by multi-step reactions, long heat treatments and composite  $\text{H}_2\text{V}_3\text{O}_8$  materials. Furthermore the rate capability of the  $\text{H}_2\text{V}_3\text{O}_8$  nanowires prepared here offer capacities  $1000 \text{ mA g}^{-1}$  exceeding the obtainable capacities of  $\text{LiFePO}_4$  and  $\text{LiCoO}_2$ . For the first time the lithium diffusion has been probed in  $\text{H}_2\text{V}_3\text{O}_8$ , using a lithiated sample ( $\text{Li}_{0.4}\text{H}_2\text{V}_3\text{O}_8$ ) showing a reasonable activation energy for lithium diffusion of  $99 \text{ meV}$ , robust electrochemical performance of the material. These measurements have been made possible by state-of-the art  $\mu\text{SR}$  analyses, allowing investigation of  $\text{Li}^+$  diffusion on a local level.

Lastly, for the first time the oxidation state change in  $\text{H}_2\text{V}_3\text{O}_8$  has successfully been monitored with insitu XAS. XAS has shown it can offer highly accurate measurements of the oxidation state of vanadium during operation of the battery cell. This type of information is rarely obtainable from other techniques, such as solid-state NMR. During electrochemical lithiation of  $\text{H}_2\text{V}_3\text{O}_8$  the population of the  $V^{4+}$  species increases at the expense of  $V^{5+}$ . It has also been shown that upon reduction to  $\text{Li}_2\text{H}_2\text{V}_3\text{O}_8$  there is no appearance of the  $V^{3+}$  species suggesting that the intercalation process proceeds through reducing all of the  $V^{5+}$

to  $V^{4+}$  before the reduction of  $V^{4+}$  to  $V^{3+}$  occurs.

To conclude, vanadium oxyhydroxides obtained by microwave-assisted routes have successfully been shown to operate as insertion cathodes. Hopefully, these observations may revive investigation of other transition metal oxyhydroxide materials as potential insertion cathodes.

## Chapter 7: Conclusions and Future Work

### 7.1 Summary of conclusions

Microwave-assisted synthesis has been presented as an alternative route to nanostructured insertion electrodes. Routes to several materials,  $\alpha$ -LiFePO<sub>4</sub>, VO<sub>2</sub> (B), V<sub>3</sub>O<sub>7</sub>, H<sub>2</sub>V<sub>3</sub>O<sub>8</sub> and V<sub>4</sub>O<sub>6</sub>(OH)<sub>4</sub> have all been successfully developed by careful alteration of reaction time, reaction temperature and synthesis media. Polyol and IL media have both show excellent microwave heating properties, and vastly different products when employed in the synthesis of  $\alpha$ -LiFePO<sub>4</sub>. While phase pure  $\alpha$ -LiFePO<sub>4</sub> can be obtained with EMIM-TFMS as the solvent media, a significant amount of  $\beta$ -LiFePO<sub>4</sub> is obtained when employing EG. Electrochemical analyses have shown that  $\beta$ -LiFePO<sub>4</sub> is almost electrochemically inert, and has been attributed to the lack of Li<sup>+</sup> diffusion in the  $\beta$  polymorph observed with  $\mu$ SR measurements.

Investigation of DES media as an alternative ionic media to ILs has provided the first studies of these solvents in microwave-assisted synthesis. Several DESs were prepared using different hydrogen bond donors and ammonium salts. The polyol based DESs, employing ChCl or TMAC as the ammonium salt, gave the most promising synthesis results, showing thermal stability between 150 °C and 250 °C and competitive power consumption compared to IL based syntheses. Moreover, phase pure  $\alpha$ -LiFePO<sub>4</sub> was obtained at lower times and/or temperatures with DESs compared to ILs with no indication of the  $\beta$ -LiFePO<sub>4</sub>, even at the lowest temperature of 200 °C. Electrochemical analyses of the DES prepared  $\alpha$ -LiFePO<sub>4</sub> have shown an excellent capacity of 168 mAh g<sup>-1</sup> is achievable, approaching the theoretical capacity of  $\alpha$ -LiFePO<sub>4</sub> (170 mAh g<sup>-1</sup>).<sup>19</sup> These results are the highest reported capacities to date for microwave prepared  $\alpha$ -LiFePO<sub>4</sub>, and present DESs as highly attractive media for microwave assisted approaches, compared to more expensive, air and moisture sensitive ILs.

Electrochemical performance of VO<sub>2</sub> (B) nanorods has also been improved by employing microwave-assisted routes, allowing the intercalation of more Li<sup>+</sup> when compared to solvothermally prepared VO<sub>2</sub> (B). This has been attributed to smaller particles, easing intercalation and decreasing the miscibility gap. These processes were investigated using *in situ* XAS studies, also showing increased reduction in microwave prepared VO<sub>2</sub> (B) compared

to solvothermally prepared VO<sub>2</sub> (B) nanorods. The electrochemical performance can also be further improved by employing binary solvent systems and adding a PVP additive to alter the morphology of the VO<sub>2</sub> (B) nanorods. The best results for these nanostructures show similar electrochemical properties to the best reported results of particles with a similar morphology, which were prepared using extended synthesis times.<sup>207</sup> These results emphasise that microwave-assisted synthesis can produce commensurate materials to conventional solvothermal methods, with no detriment to electrochemical performance.

It has also been possible to access MET capable materials, V<sub>3</sub>O<sub>7</sub> and H<sub>2</sub>V<sub>3</sub>O<sub>8</sub>. Of these H<sub>2</sub>V<sub>3</sub>O<sub>8</sub> has shown outstanding, stable discharge capacity of 325 mAh g<sup>-1</sup> over 20 cycles at 100 mAh g<sup>-1</sup>. Chemical lithiation has also allowed the investigation of E<sub>a</sub> of Li<sup>+</sup> diffusion in Li<sub>0.4</sub>H<sub>2</sub>V<sub>3</sub>O<sub>8</sub> (99 meV), calculated using  $\mu$ SR. The values obtained are on the same order of magnitude as  $\alpha$ -LiFePO<sub>4</sub> (19 meV). It has also been possible to investigate the redox behaviour of H<sub>2</sub>V<sub>3</sub>O<sub>8</sub> during cell operation using insitu XAS showing a clear transformation of the V<sup>5+</sup> to 4<sup>+</sup> as the first lithiation step.

For the first time V<sub>4</sub>O<sub>6</sub>(OH)<sub>4</sub> was prepared by a microwave-assisted route, and studied as a Li<sup>+</sup> insertion electrode showing a moderate capacity of 150 mAh g<sup>-1</sup> at 100 mA g<sup>-1</sup>. XANES analysis of V<sub>4</sub>O<sub>6</sub>(OH)<sub>4</sub> has also confirmed the stoichiometry as all of the vanadium atoms remain in the +4 oxidation state, rather than the V<sup>4+</sup>/V<sup>3+</sup> V<sub>4</sub>O<sub>4</sub>(OH)<sub>6</sub> postulated in the literature.<sup>251</sup> This confirms that microwave-assisted synthesis can be successfully employed to access new phases by changing the solvent media, and that further oxyhydroxide materials may be obtained in this manner.

In summary, microwave-assisted syntheses have shed light on the synthesis of materials, morphology, structure, electrochemistry and fundamental local properties of positive insertion electrodes.

## 7.2 Future work

The research presented here provides many new opportunities for extended future studies. Firstly, the evidence of microwave-assisted phase transformation may prove useful to access new morphologies of  $\alpha$ -LiFePO<sub>4</sub> by conversion from  $\beta$ -LiFePO<sub>4</sub>. This morphological templating may provide new nanostructures unobtainable through solid-state phase conversion.

Deep eutectic solvents (DES) offer a huge opportunity for further research, by substituting either the hydrogen bond donor or the salt to tailor the morphology of nanostructured electrodes and alter their electrochemical performance. More study should also be invested in the microwave absorption properties of DES based media using microwave absorption spectroscopy to understand their dielectric properties, and their competitive behaviour to ILs. Furthermore, microwave-assisted preparation of other inorganic materials could be investigated using DESs as syntheses media, such as metal oxides and polyanionic insertion cathodes other than  $\alpha$ -LiFePO<sub>4</sub>. This would support the competitive use of DESs over ILs in microwave-assisted syntheses.

Although MET capable materials were successfully synthesised, there remains a plethora of MET capable vanadate phases that may be accessible using microwave-assisted routes. This would require careful consideration of the reducing media employed, but may give access to high capacity, nanostructured insertion cathodes. Additionally, the MET capable phases that have been obtained could be investigated as insertion cathodes for divalent ions, such as in Mg<sup>2+</sup> cells, as their multiple electron reactions are ideal for this application.

Finally, the promising electrochemical properties of V<sub>4</sub>O<sub>6</sub>(OH<sub>4</sub>) and H<sub>2</sub>V<sub>3</sub>O<sub>8</sub> inspires investigation of routes to more metal oxyhydroxides. One remaining challenge with these materials is the exact role of the hydroxyl groups during electrochemical cycling. Although studies have suggested that they increase the stability by interlayer bonding, more work could be conducted with in situ techniques such as XRD, NPD, NMR and XAS to understand their role during cell operation.

## **Chapter 8: Appendices**

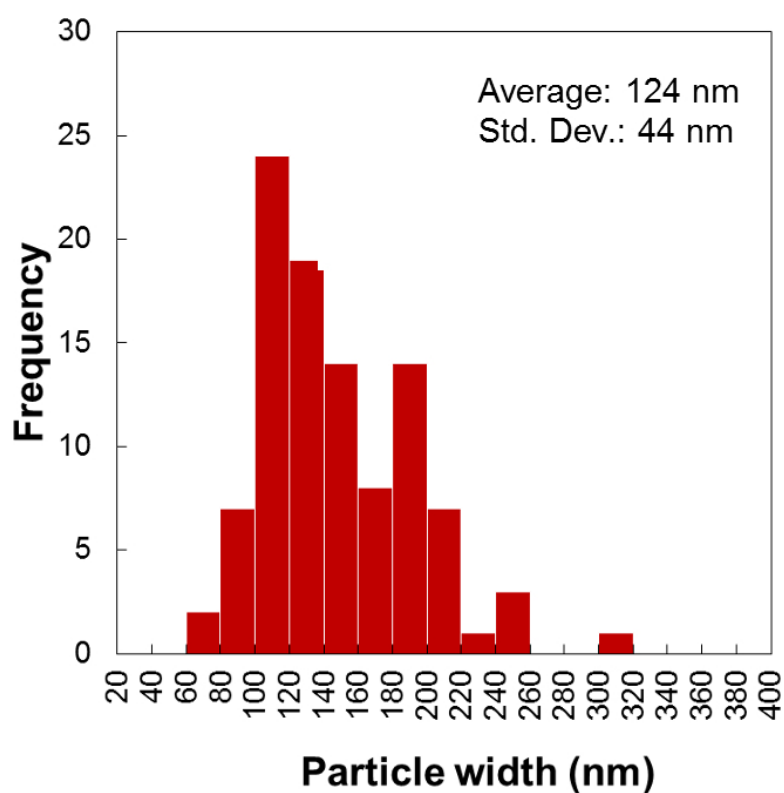


**Figure 8.1:** Histogram of particle width for  $\text{H}_2\text{V}_3\text{O}_8$  prepared by a microwave-assisted solvothermal route.

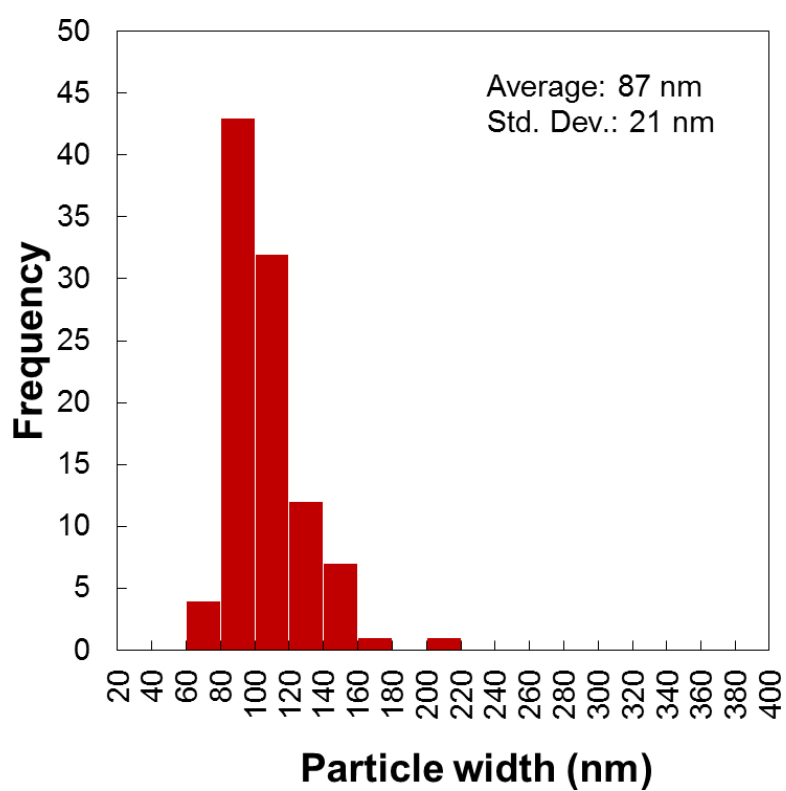


**Figure 8.2:** Histogram of particle width for chemically lithiated  $\text{Li}_{0.4}\text{H}_2\text{V}_3\text{O}_8$  prepared by a microwave-assisted solvothermal route.

$\alpha$ -LiFePO <sub>4</sub>			Fraction			5.6505		
	a	b	c					
	10.31059	5.986945	4.968954					

$\beta$ -LiFePO <sub>4</sub>			Fraction			1.0987		
	a	b	c					
	5.534955	8.241218	6.177624					

Atom	x	y	z	Atom	x	y	z
Li1	0.000000	0.000000	0.000000	Li1	0.000000	0.676000	0.250000
Fe1	0.282297	0.250000	0.968887	Fe1	0.000000	0.000000	0.000000
P1	0.087761	0.250000	0.414997	P1	0.000000	0.320668	0.250000
O1	0.101647	0.250000	0.746064	O1	0.000000	0.267172	0.015239
O2	0.451655	0.250000	0.212016	O2	0.206454	0.438479	0.250000
O3	0.194418	0.524850	0.273789				

GU	8.18E+03	LX	1.36E+01	GU	1.66E+03	LX	0.00E+00
GV	-4.00E+02	LY	0.00E+00	GV	-4.08E+00	LY	0.00E+00
GW	-2.78E+02			GW	1.38E+02		

Fit		Background	
wRp	Rp	wRp	Rp
0.0179	0.0115	0.435	0.0236

DWd	Chi <sup>2</sup>	Zero	Scale
0.164	1.77E+01	2.24065	61.708

**Table 8.1:** Rietveld refinement parameters for the dual-phase refinement in Figure 3.15 from Figure 3.15.

Space group	<i>Pnam</i>	<b>U</b>	0.39(5)	<b>Atom</b>	<b>x</b>	<b>y</b>	<b>z</b>	<b>Atom</b>	<b>x</b>	<b>y</b>	<b>z</b>
<b>a</b> (Å)	16.764(1)	<b>V</b>	-0.37(4)	<b>V1</b>	0.0516(9)	0.124(1)	0.25	<b>O4</b>	0.936(3)	0.216(5)	0.25
<b>b</b> (Å)	9.281(8)	<b>W</b>	0.133(7)	<b>V2</b>	0.8488(9)	0.065(1)	0.25	<b>O5</b>	0.762(2)	0.181(3)	0.25
<b>c</b> (Å)	3.636(3)	<b>R<sub>p</sub></b>	39.3 %	<b>V3</b>	0.448(1)	0.090(1)	0.25	<b>O6</b>	0.783(1)	0.889(3)	0.25
		<b>R<sub>wp</sub></b>	34.6 %	<b>O1</b>	0.958(4)	0.928(5)	0.25	<b>O7</b>	0.527(2)	0.924(4)	0.25
		<b>R<sub>exp</sub></b>	27.69 %	<b>O2</b>	0.098(2)	0.283(4)	0.25	<b>O8</b>	0.357(2)	0.0182(3)	0.25
		<b>χ<sup>2</sup></b>	1.56	<b>O3</b>	0.129(3)	0.954(5)	0.25	-	-	-	-

**Table 8.2:** Calculated Rietveld refinement parameters from the powder XRD pattern of  $\text{Li}_{0.4}\text{H}_2\text{V}_3\text{O}_8$  prepared by chemical lithiation of  $\text{H}_2\text{V}_3\text{O}_8$  with reference to the pattern taken from Reference .

## Bibliography

- [1] J. Tarascon and M. Armand, *Nature*, 2001, **414**, 359–367.
- [2] N. Oreskes, *Science*, 2004, **306**, 1686–1686.
- [3] N. Wan, X. Lu, Y. Wang, W. Zhang, Y. Bai, Y.-S. Hu and S. Dai, *Sci. Rep.*, 2016, **6**, 18978.
- [4] C. Wang, A. Appleby and F. Little, *J. Electroanal. Chem.*, 2001, **497**, 33–46.
- [5] J. Y. Huang, L. Zhong, C. M. Wang, J. P. Sullivan, W. Xu, L. Q. Zhang, S. X. Mao, N. S. Hudak, X. H. Liu, A. Subramanian, H. Fan, L. Qi, A. Kushima and J. Li, *Science*, 2010, **330**, 1515–1520.
- [6] L. Li, Z. Guo, A. Du and H. Liu, *J. Mater. Chem*, 2012, **22**, 3600–3605.
- [7] K. Mizushima, P. C. Jones, P. J. Wiseman and J. B. Goodenough, *Mater. Res. Bull.*, 1980, **15**, 783–789.
- [8] S. Laubach, S. Laubach, P. C. Schmidt, D. Ensling, S. Schmid, W. Jaegermann, A. Thiszen, K. Nikolowski and H. Ehrenberg, *Phys. Chem. Chem. Phys.*, 2009, **11**, 3278–3289.
- [9] R. Hausbrand, G. Cherkashinin, H. Ehrenberg, M. Gräßling, K. Albe, C. Hess and W. Jaegermann, *Mater. Sci. and Eng., B*, 2015, **192**, 3 – 25.
- [10] J. D. Donaldson and D. Beyersmann, in *Cobalt and Cobalt Compounds*, Wiley-VCH Verlag GmbH Co. KGaA, 2000.
- [11] A. A. Yaroshevsky, *Geochem. Int.*, 2006, **44**, 48–55.
- [12] W. Xu, J. Wang, F. Ding, X. Chen, E. Nasybulin, Y. Zhang and J.-G. Zhang, *Energy Environ. Sci.*, 2014, **7**, 513–537.
- [13] L. Zhang, K. Zhao, W. Xu, J. Meng, L. He, Q. An, X. Xu, Y. Luo, T. Zhao and L. Mai, *R. Soc. Chem. Adv.*, 2014, **4**, 33332–33337.

- 
- [14] J. M. Clark, C. Eames, M. Reynaud, G. Rousse, J.-N. Chotard, J.-M. Tarascon and M. S. Islam, *J. Mater. Chem. A*, 2014, **2**, 7446–7453.
- [15] T. Sarkar, M. D. Bharadwaj, U. V. Waghmare and P. Kumart, *J. Phys. Chem. C.*, 2015, **119**, 9125–9133.
- [16] R. Tripathi, G. Popov, X. Sun, D. H. Ryan and L. F. Nazar, *J. Mater. Chem. A*, 2013, **1**, 2990–2994.
- [17] M. Ati, B. Melot, J.-N. Chotard, G. Rousse, M. Reynaud and J.-M. Tarascon, *Electrochemistry Communications*, 2011, **13**, 1280 – 1283.
- [18] L. Liu, B. Zhang and X. jie Huang, *Prog. Nat. Sci.*, 2011, **21**, 211 –215.
- [19] A. Padhi, K. Nanjundaswamy and J. Goodenough, *J. Electrochem. Soc.*, 1997, **144**, 1188–1194.
- [20] S.-i. Nishimura, G. Kobayashi, K. Ohoyama, R. Kanno, M. Yashima and A. Yamada, *Nat. Mater.*, 2008, **7**, 707–711.
- [21] M. Islam, D. Driscoll, C. Fisher and P. Slater, *Chem. Mater.*, 2005, **17**, 5085–5092.
- [22] A. Padhi, K. Nanjundaswamy, C. Masquelier, S. Okada and J. Goodenough, *J. Electrochem. Soc.*, 1997, **144**, 1609–1613.
- [23] J. Wang and X. Sun, *Energy Environ. Sci.*, 2012, **5**, 5163–5185.
- [24] C. Delmas, M. Maccario, L. Croguennec, F. Le Cras and F. Weill, *Nat. Mater.*, 2008, **7**, 665–671.
- [25] J. Goodenough and V. Manivannan, *Denki Kagaku*, 1998, **66**, 1173–1181.
- [26] J. Liu, Z. Wang, G. Zhang, Y. Liu and A. Yu, *Int. J. Electrochem. Sci.*, 2013, **8**, 2378–2387.
- [27] G. Chen, X. Song and T. Richardson, *Electrochem. Solid St.*, 2006, **9**, A295–A298.
- [28] D. Morgan, A. Van der Ven and G. Ceder, *Electrochem. Solid St.*, 2004, **7**, A30–A32.
-

- 
- [29] A. Ait-Salah, J. Dodd, A. Mauger, R. Yazami, F. Gendron and C. M. Julien, *Z. Anorg. Allg. Chem.*, 2006, **632**, 1598–1605.
- [30] L.-X. Yuan, Z.-H. Wang, W.-X. Zhang, X.-L. Hu, J.-T. Chen, Y.-H. Huang and J. B. Goodenough, *Energy Environ. Sci.*, 2011, **4**, 269–284.
- [31] A. Andersson, B. Kalska, L. Haggstrom and J. Thomas, *Solid State Ionics*, 2000, **130**, 41–52.
- [32] A. Andersson and J. Thomas, *J. Power Sources*, 2001, **97-8**, 498–502.
- [33] J. Yao, S. Bewlay, K. Konstantionv, V. A. Drozd, R. S. Liu, X. L. Wang, H. K. Liu and G. X. Wang, *J. Alloy Compd.*, 2006, **425**, 362–366.
- [34] A. Yamada, Y. Takei, H. Koizumi, N. Sonoyama, R. Kanno, K. Itoh, M. Yonemura and T. Kamiyama, *Chem. Mater.*, 2006, **18**, 804–813.
- [35] T. Muraliganth and A. Manthiram, *J. Phys. Chem. C*, 2010, **114**, 15530–15540.
- [36] H. Liu, F. C. Strobridge, O. J. Borkiewicz, K. M. Wiaderek, K. W. Chapman, P. J. Chupas and C. P. Grey, *Science*, 2014, **344**, 1252817.
- [37] G. Hautier, A. Jain, S. P. Ong, B. Kang, C. Moore, R. Doe and G. Ceder, *Chem. Mater.*, 2011, **23**, 3495–3508.
- [38] A. Yu, N. Kumagai, Z. Liu and J. Lee, *J. Solid State Electrochem.*, 1998, **2**, 394–400.
- [39] P. Christian, J. Carides, F. DiSalvo and J. Waszczak, *J. Electrochem. Soc.*, 1980, **127**, 2315–2319.
- [40] Y. Takeda, R. Kanno, Y. Tsuji, O. Yamamoto and H. Taguch, *J. Power Sources*, 1983, **9**, 325–328.
- [41] O. Yamamoto, Y. Takeda, R. Kanno, Y. Oyabe and Y. Shinya, *J. Power Sources*, 1987, **20**, 151–156.
- [42] P. Zavalij and M. Whittingham, *Acta Cryst. B*, 1999, **55**, 627–663.
- [43] N. Kumagai and K. Tanno, *Denki Kagaku*, 1980, **48**, 432–437.
-

- [44] D. Chao, X. Xia, J. Liu, Z. Fan, C. F. Ng, J. Lin, H. Zhang, Z. X. Shen and H. J. Fan, *Adv. Mater.*, 2014, **26**, 5794–5800.
- [45] H.-B. Wu, A. Pan, H. H. Hng and X. W. D. Lou, *Adv. Funct. Mater.*, 2013, **23**, 5669–5674.
- [46] H. Fei, Y. Lin and M. Wei, *J. Colloid Interface Sci.*, 2014, **425**, 1–4.
- [47] K. West, B. Zachaustriansen, T. Jacobsen and S. Atlung, *J. Power Sources*, 1985, **14**, 235–245.
- [48] Y. Zhang, M. Zhou, M. Fan, C. Huang, C. Chen, Y. Cao, H. Li and X. Liu, *Curr. Appl. Phys.*, 2011, **11**, 1159–1163.
- [49] M. Takahashi, S. Tobishima, K. Takei and Y. Sakurai, *Solid State Ionics*, 2002, **148**, 283–289.
- [50] D. Y. W. Yu, C. Fietzek, W. Weydanz, K. Donoue, T. Inoue, H. Kurokawa and S. Fujitani, *J. Electrochem. Soc.*, 2007, **154**, A253–A257.
- [51] C. Delacourt, L. Laffont, R. Bouchet, C. Wurm, J. Leriche, M. Morcrette, J. Tarascon and C. Masquelier, *J. Electrochem. Soc.*, 2005, **152**, A913–A921.
- [52] S. Shi, L. Liu, C. Ouyang, D. Wang, Z. Wang, L. Chen and X. Huang, *Phys. Rev. B*, 2003, **68**, year.
- [53] P. Prosini, M. Lisi, D. Zane and M. Pasquali, *Solid State Ionics*, 2002, **148**, 45–51.
- [54] J. Molenda, W. Ojczyk, K. Swierczek, W. Zajac, F. Krok, J. Dygas and R.-S. Liu, *Solid State Ionics*, 2006, **177**, 2617–2624.
- [55] S. Franger, F. Le Cras, C. Bourbon and H. Rouault, *Electrochem. Solid. St.*, 2002, **5**, A231–A233.
- [56] A. V. Churikov, A. V. Ivanishchev, I. A. Ivanishcheva, V. O. Sycheva, N. R. Khasanova and E. V. Antipov, *Electrochim. Acta*, 2010, **55**, 2939–2950.
- [57] B. Ellis, L. K. Perry, D. H. Ryan and L. F. Nazar, *J. Am. Chem. Soc.*, 2006, **128**, 11416–11422.

- 
- [58] R. Amin, J. Maier, P. Balaya, D. P. Chen and C. T. Lin, *Solid State Ionics*, 2008, **179**, 1683–1687.
- [59] J. Cabana, J. Shirakawa, G. Chen, T. J. Richardson and C. P. Grey, *Chem. Mater.*, 2010, **22**, 1249–1262.
- [60] A. S. Powell, J. S. Lord, D. H. Gregory and J. J. Titman, *J. Phys. Chem. C*, 2009, **113**, 20758–20763.
- [61] A. S. Powell, Z. Stoeva, J. S. Lord, R. I. Smith, D. H. Gregory and J. J. Titman, *Phys. Chem. Chem. Phys.*, 2013, **15**, 816–823.
- [62] P. Gubbens, M. Wagemaker, S. Sakarya, M. Blaauw, A. Yaouanc, P. de Reotier and S. Cottrell, *Solid State Ionics*, 2006, **177**, 145–147.
- [63] J. Sugiyama, Y. Ikedo, K. Mukai, H. Nozaki, M. Mansson, O. Ofer, M. Harada, K. Kamazawa, Y. Miyake, J. H. Brewer, E. J. Ansaldo, K. H. Chow, I. Watanabe and T. Ohzuku, *Phys. Rev. B*, 2010, **82**, year.
- [64] J. Sugiyama, K. Mukai, H. Nozaki, M. Harada, M. Mansson, K. Kamazawa, D. Andreica, A. Amato and A. D. Hillier, *Phys. Rev. B*, 2013, **87**, 024409.
- [65] J. Sugiyama, K. Mukai, M. Harada, H. Nozaki, K. Miwa, T. Shiotsuki, Y. Shindo, S. R. Giblin and J. S. Lord, *Phys. Chem. Chem. Phys.*, 2013, **15**, 10402–10412.
- [66] M. Ariza, D. Jones, J. Roziere, J. Lord and D. Ravot, *J. Phys. Chem. B*, 2003, **107**, 6003–6011.
- [67] K. Mukai, J. Sugiyama, Y. Ikedo, H. Nozaki, K. Shimomura, K. Nishiyama, K. Ariyoshi and T. Ohzuku, *J. Power Sources*, 2007, **174**, 711–715.
- [68] J. Sugiyama, H. Nozaki, M. Harada, K. Kamazawa, Y. Ikedo, Y. Miyake, O. Ofer, M. Mansson, E. J. Ansaldo, K. H. Chow, G. Kobayashi and R. Kanno, *Phys. Rev. B*, 2012, **85**, year.
- [69] M. Ariza, D. Jones, J. Roziere and J. Lord, *J. Phys. Chem. Solids*, 2004, **65**, 597–602.
-

- 
- [70] J. Sugiyama, H. Nozaki, M. Harada, K. Kamazawa, O. Ofer, M. Mansson, J. H. Brewer, E. J. Ansaldo, K. H. Chow, Y. Ikedo, Y. Miyake, K. Ohishi, I. Watanabe, G. Kobayashi and R. Kanno, *Phys. Rev. B*, 2011, **84**, 054430.
- [71] P. J. Baker, I. Franke, F. L. Pratt, T. Lancaster, D. Prabhakaran, W. Hayes and S. J. Blundell, *Phys Rev B*, 2011, **84**, 174403.
- [72] J. Lord, S. Cottrell and W. Williams, *J. Phys.-Condens. Mat.*, 1998, **10**, 7975–7982.
- [73] J. Lord, S. Cottrell and W. Williams, *Physica B*, 2000, **289**, 491–494.
- [74] H. Nozaki, M. Harada, S. Ohta, I. Watanabe, Y. Miyake, Y. Ikedo, N. H. Jalarvo, E. Mamonov and J. Sugiyama, *Solid State Ionics*, 2014, **262**, 585–588.
- [75] C. Kaiser, V. Verhoeven, P. Gubbens, F. Mulder, I. de Schepper, A. Yaouanc, P. de Reotier, S. Cottrell, E. Kelder and J. Schoonman, *Phys. Rev. B*, 2000, **62**, R9236–R9239.
- [76] J. Sugiyama, K. Mukai, Y. Ikedo, H. Nozaki, M. Mansson and I. Watanabe, *Phys. Rev. Lett.*, 2009, **103**, 147601.
- [77] T. Shodai, S. Okada, S. Tobishima and J. Yamaki, *Solid State Ionics*, 1996, **86-8**, 785–789.
- [78] P. G. Bruce, B. Scrosati and J.-M. Tarascon, *Angew. Chemie Int. Ed.*, 2008, **47**, 2930–2946.
- [79] M. Winter, J. Besenhard, M. Spahr and P. Novak, *Adv. Mater.*, 1998, **10**, 725–763.
- [80] A. Arico, P. Bruce, B. Scrosati, J. Tarascon and W. Van Schalkwijk, *Nat. Mater.*, 2005, **4**, 366–377.
- [81] L. Nazar, G. Goward, F. Leroux, M. Duncan, H. Huang, T. Kerr and J. Gaubicher, *Int. J. Inorg. Mater.*, 2001, **3**, 191–200.
- [82] B. Scrosati, *Nature*, 1995, **373**, 557–558.
- [83] N. Meethong, H.-Y. S. Huang, W. C. Carter and Y.-M. Chiang, *Electrochem. Solid State Lett.*, 2007, **10**, A134–A138.
-

- 
- [84] A. Robertson, A. Armstrong and P. Bruce, *Chem. Mater.*, 2001, **13**, 2380–2386.
- [85] P. Bruce, A. Armstrong and R. Gitzendanner, *J. Mater. Chem.*, 1999, **9**, 193–198.
- [86] Y. Shao-Horn, S. Hackney, A. Armstrong, P. Bruce, R. Gitzendanner, C. Johnson and M. Thackeray, *J. Electrochem. Soc.*, 1999, **146**, 2404–2412.
- [87] S. Kang, J. Goodenough and L. Rabenberg, *Chem. Mater.*, 2001, **13**, 1758–1764.
- [88] W. Tang, X. J. Wang, Y. Y. Hou, L. L. Li, H. Sun, Y. S. Zhu, Y. Bai, Y. P. Wu, K. Zhu and T. van Ree, *J. Power Sources*, 2012, **198**, 308–311.
- [89] N. Ravet, Y. Chouinard, J. Magnan, S. Besner, M. Gauthier and M. Armand, *J. Power Sources*, 2001, **97-8**, 503–507.
- [90] H. Huang, S. Yin and L. Nazar, *Electrochem. Solid State Lett.*, 2001, **4**, A170–A172.
- [91] F. Croce, A. D'Epifanio, J. Hassoun, A. Deptula, T. Olczac and B. Scrosati, *Electrochem. Solid State Lett.*, 2002, **5**, A47–A50.
- [92] C. Kim, M. Noh, M. Choi, J. Cho and B. Park, *Chem. Mater.*, 2005, **17**, 3297–3301.
- [93] D. Le, S. Passerini, J. Guo, J. Ressler, B. Owens and W. Smyrl, *J. Electrochem. Soc.*, 1996, **143**, 2099–2104.
- [94] W. Dong, D. Rolison and B. Dunn, *Electrochem. Solid State Lett.*, 2000, **3**, 457–459.
- [95] M. Jo, Y.-S. Hong, J. Choo and J. Cho, *J. Electrochem. Soc.*, 2009, **156**, A430–A434.
- [96] R. Malik, D. Burch, M. Bazant and G. Ceder, *Nano Lett.*, 2010, **10**, 4123–4127.
- [97] F. Du, X. Ren, J. Yang, J. Liu and W. Zhang, *J. Phys. Chem. C*, 2014, **118**, 10590–10595.
- [98] A. Liu, Y. Liu, Z. Hu, G. Gao, Y. Xu and L. Lei, *J. Phys. Chem. Solids*, 2011, **72**, 831–835.
- [99] P. Nithyadharseni, M. Reddy, K. I. Ozoemena, R. G. Balakrishna and B. Chowdari, *Electrochim. Acta*, 2015, **182**, 1060–1069.
-

- 
- [100] M. Rahman, J.-Z. Wang, M. F. Hassan, S. Chou, D. Wexler and H.-K. Liu, *J. Power Sources*, 2010, **195**, 4297–4303.
- [101] K. Hsu, S. Tsay and B. Hwang, *J. Mater. Chem.*, 2004, **14**, 2690–2695.
- [102] M. Gao, N. Liu, Z. Li, W. Wang, C. Li, H. Zhang, Y. Chen, Z. Yu and Y. Huang, *Solid State Ionics*, 2014, **258**, 8 – 12.
- [103] X. Qin, X. Wang, H. Xiang, J. Xie, J. Li and Y. Zhou, *J. Phys. Chem. C*, 2010, **114**, 16806–16812.
- [104] D. Bhuvanewari and N. Kalaiselvi, *Phys. Chem. Chem. Phys.*, 2014, **16**, 1469–1478.
- [105] F. Wang, Z. Fang and Y. Zhang, *J. Electroanal. Chem.*, 2016, **775**, 110 – 115.
- [106] S. Yang, M. Hu, L. Xi, R. Ma, Y. Dong and C. Y. Chung, *ACS Appl. Mater. Interfaces*, 2013, **5**, 8961–8967.
- [107] P. Vaishnava, A. Dixit, K. Bazzi, M. B. Sahana, C. Sudakar, M. Nazri, V. Naik, V. K. Garg, A. C. Oliveira, G. A. Nazri and R. Naik, APS Meeting Abstracts, 2012.
- [108] K. Rao, B. Vaidhyanathan, M. Ganguli and P. Ramakrishnan, *Chem. Mater.*, 1999, **11**, 882–895.
- [109] R. Gedye, F. Smith, K. Westaway, H. Ali, L. Baldisera, L. Laberge and J. Rousell, *Tetrahedron Lett.*, 1986, **27**, 279–282.
- [110] S. Galema, *Chem. Soc. Rev.*, 1997, **26**, 233–238.
- [111] C. O. Kappe, *Chem. Soc. Rev.*, 2008, **37**, 1127–1139.
- [112] M. Bhattacharya and T. Basak, *Energy*, 2016, **97**, 306 – 338.
- [113] J.-S. Schanche, *Mol. Diver.*, 2003, **7**, 293–300.
- [114] D. M. P. Mingos and D. R. Baghurst, *Chem. Soc. Rev.*, 1991, **20**, 1–47.
- [115] A. KUMAR, *Int. J. Electron.*, 1979, **47**, 531–536.
- [116] D. S. Jacob, I. Genish, L. Klein and A. Gedanken, *J. Phys. Chem. B*, 2006, **110**, 17711–17714.
-

- 
- [117] P. Chen, Y. Su, H. Liu and Y. Wang, *ACS Appl. Mater. Interfaces*, 2013, **5**, 12073–12082.
- [118] J. Yin, H. Cao, Z. Zhou, J. Zhang and M. Qu, *J. Mater. Chem.*, 2012, **22**, 23963–23970.
- [119] Y. Wang and J. Lee, *J. Power Sources*, 2005, **144**, 220–225.
- [120] V. Subramanian, W. W. Burke, H. Zhu and B. Wei, *J. Phys. Chem. C*, 2008, **112**, 4550–4556.
- [121] S. Chen, Y. Wang, H. Ahn and G. Wang, *J. Power Sources*, 2012, **216**, 22–27.
- [122] C. Zhong, J. Wang, Z. Chen and H. Liu, *J. Phys. Chem. C*, 2011, **115**, 25115–25120.
- [123] Y. Lu, Y. Wang, Y. Zou, Z. Jiao, B. Zhao, Y. He and M. Wu, *Electrochem. Comm.*, 2010, **12**, 101–105.
- [124] Y. Ding, L. Xu, C. Chen, X. Shen and S. L. Suib, *J. Phys. Chem. C*, 2008, **112**, 8177–8183.
- [125] S. Q. Chen and Y. Wang, *J. Mater. Chem.*, 2010, **20**, 9735–9739.
- [126] T. Muraliganth, A. V. Murugan and A. Manthiram, *Chem. Comm.*, 2009, 7360–7362.
- [127] Y. Zhang, X. Liu, G. Xie, L. Yu, S. Yi, M. Hu and C. Huang, *Mater. Sci. and Eng. B*, 2010, **175**, 164–171.
- [128] Y. Zou, J. Kan and Y. Wang, *J. Phys. Chem. C*, 2011, **115**, 20747–20753.
- [129] X. Hu, J. C. Yu and J. Gong, *J. Phys Chem. C*, 2007, **111**, 11180–11185.
- [130] S.-H. Lee, V. Sridhar, J.-H. Jung, K. Karthikeyan, Y.-S. Lee, R. Mukherjee, N. Koratkar and I.-K. Oh, *ACS Nano*, 2013, **7**, 4242–4251.
- [131] Y. Sun, X. Hu, W. Luo and Y. Huang, *J. Mater. Chem.*, 2012, **22**, 19190–19195.
- [132] W. Luo, X. Hu, Y. Sun and Y. Huang, *ACS Appl. Mater. Interfaces*, 2013, **5**, 1997–2003.
- [133] C. T. Cherian, M. V. Reddy, S. C. Haur and B. V. R. Chowdari, *ACS Appl. Mater. Interfaces*, 2013, **5**, 918–923.
-

- 
- [134] L. Q. Lu and Y. Wang, *J. Mater. Chem.*, 2011, **21**, 17916–17921.
- [135] L. Noerochim, J.-Z. Wang, D. Wexler, Z. Chao and H.-K. Liu, *J. Power Sources*, 2013, **228**, 198–205.
- [136] J. Li, Y.-L. Jin, X.-G. Zhang and H. Yang, *Solid State Ionics*, 2007, **178**, 1590–1594.
- [137] S.-L. Chou, J.-Z. Wang, H.-K. Liu and S.-X. Dou, *J. Mater. Chem. C*, 2011, **115**, 16220–16227.
- [138] K. Kim, Y.-H. Cho, D. Kam, H.-S. Kim and J.-W. Lee, *J. Alloy Compd.*, 2010, **504**, 166–170.
- [139] S.-M. Bak, K.-W. Nam, C.-W. Lee, K.-H. Kim, H.-C. Jung, X.-Q. Yang and K.-B. Kim, *J. Mater. Chem.*, 2011, **21**, 17309–17315.
- [140] P. Whitfield and I. Davidson, *J. Electrochem. Soc.*, 2000, **147**, 4476–4484.
- [141] S. Yang, J. Jia, L. Ding and M. Zhang, *Electrochim. Acta*, 2003, **48**, 569–573.
- [142] G. Yang, G. Wang and W. Hou, *J. Phys. Chem. B*, 2005, **109**, 11186–11196.
- [143] J. Pan, L. Zhong, M. Li, Y. Luo and G. Li, *Chem. Eur. J.*, 2016, **22**, 1461–1466.
- [144] J. Pan, M. Li, Y. Luo, H. Wu, L. Zhong, Q. Wang and G. Li, *Mater. Res. Bull.*, 2016, **74**, 90–95.
- [145] S. Beninati, M. Fantuzzi, M. Mastragostino and F. Soavi, *J. Power Sources*, 2006, **157**, 483–487.
- [146] X.-H. Liao, Y. Liu, Z. Xu, X. Chen and R. Wang, *Material sciences and technology*, Pts. 1 & 2, 2012, pp. 191–201.
- [147] M. Higuchi, K. Katayama, Y. Azuma, M. Yukawa and M. Suhara, *J. Power Sources*, 2003, **119**, 258–261.
- [148] K. Park, J. Son, H. Chung, S. Kim, C. Lee and H. Kim, *Electrochem. Comm.*, 2003, **5**, 839–842.
- [149] L. Wang, Y. Huang, R. Jiang and D. Jia, *Electrochimica Acta*, 2007, **52**, 6778–6783.
-

- [150] M.-S. Song, Y.-M. Kang, J.-H. Kim, H.-S. Kim, D.-Y. Kim, H.-S. Kwon and J.-Y. Lee, *J. Power Sources*, 2007, **166**, 260–265.
- [151] I. Bilecka, A. Hintennach, I. Djerdj, P. Novak and M. Niederberger, *J. Mater. Chem.*, 2009, **19**, 5125–5128.
- [152] A. V. Murugan, T. Muraliganth, P. J. Ferreira and A. Manthiram, *Inorg. Chem.*, 2009, **48**, 946–952.
- [153] I. Bilecka, A. Hintennach, M. D. Rossell, D. Xie, P. Novak and M. Niederberger, *J. Mater. Chem.*, 2011, **21**, 5881–5890.
- [154] S. Beninati, L. Damen and M. Mastragostino, *J. Power Sources*, 2008, **180**, 875–879.
- [155] A. V. Murugan, T. Muraliganth and A. Manthiram, *Electrochemistry Communications*, 2008, **10**, 903–906.
- [156] Y. Shi, S.-L. Chou, J.-Z. Wang, D. Wexler, H.-J. Li, H.-K. Liu and Y. Wu, *J. Mater. Chem.*, 2012, **22**, 16465–16470.
- [157] S. A. Corr, M. Grossman, Y. Shi, K. R. Heier, G. D. Stucky and R. Seshadri, *J. Mater. Chem.*, 2009, **19**, 4362–4367.
- [158] A. Stokes and A. Wilson, *Proc. Phys. Soc.*, 1944, **56**, 174–181.
- [159] B. Toby, *Powder Diffr.*, 2006, **21**, 67–70.
- [160] NIST, *NIST Standard Reference Database 123*, 2016, <http://physics.nist.gov/cgi-bin/cuu/Value?f>, Accessed: 2016-06-17.
- [161] E. E. Alp, G. L. Goodman, L. Soderholm, S. M. Mini, M. Ramanathan, G. K. Shenoy and A. S. Bommanavar, *J. Phys. Condens. Matter*, 1989, **1**, 6463.
- [162] D. E. Sayers, E. A. Stern and F. W. Lytle, *Phys. Rev. Lett.*, 1971, **27**, 1204–1207.
- [163] L. Reining, J. J. Rehr, J. J. Kas, M. P. Prange, A. P. Sorini, Y. Takimoto and F. Vila, *C. R. Physique*, 2009, **10**, 548 – 559.

- [164] J. J. Rehr, J. J. Kas, F. D. Vila, M. P. Prange and K. Jorissen, *Phys. Chem. Chem. Phys.*, 2010, **12**, 5503–5513.
- [165] B. Ravel and M. Newville, *J. Synchrotron. Radiat.*, 2005, **12**, 537–541.
- [166] O. J. Borkiewicz, B. Shyam, K. M. Wiaderek, C. Kurtz, P. J. Chupas and K. W. Chapman, *J. Appl. Cryst.*, 2012, **45**, 1261–1269.
- [167] M. Conversi, E. Pancini and O. Piccioni, *Phys. Rev.*, 1945, **68**, 232.
- [168] M. Conversi, E. Pancini and O. Piccioni, *Phys. Rev.*, 1947, **71**, 209–210.
- [169] M. Månsson and J. Sugiyama, *Phys. Scr.*, 2013, **88**, 068509.
- [170] S. Blundell, *Contemp. Phys.*, 1999, **40**, 175–192.
- [171] R. Hayano, Y. Uemura, J. Imazato, N. Nishida, T. Yamazaki and R. Kubo, *Phys. Rev. B*, 1979, **20**, 850–859.
- [172] A. Keren, *Phys. Rev. B*, 1994, **50**, 10039–10042.
- [173] W.-J. Zhang, *J. Power Sources*, 2011, **196**, 2962 – 2970.
- [174] C. Delacourt, P. Poizot, S. Levasseur and C. Masquelier, *Electrochem. Solid-State Lett.*, 2006, **9**, A352–A355.
- [175] C. Nan, J. Lu, C. Chen, Q. Peng and Y. Li, *J. Mater. Chem.*, 2011, **21**, 9994–9996.
- [176] Q. Wang, W. Zhang, Z. Yang, S. Weng and Z. Jin, *J. Power Sources*, 2011, **196**, 10176–10182.
- [177] N. G. Patil, E. V. Rebrov, K. Eranen, F. Benaskar, J. Meuldijk, J.-P. Mikkola, V. Hessel, L. A. Hulshof, D. Y. Murzin and J. C. Schouten, *J. Microwave Power E. E.*, 2012, **46**, 83–92.
- [178] C. Gabriel, S. Gabriel, E. H. Grant, E. H. Grant, B. S. J. Halstead and D. Michael P. Mingos, *Chem. Soc. Rev.*, 1998, **27**, 213–224.
- [179] Y. Chen, Y. Ozaki and M. A. Czarnecki, *Phys. Chem. Chem. Phys.*, 2013, **15**, 18694–18701.

- [180] P. B. Undre, P. W. Khirade, V. S. Rajenimbalkar, S. N. Helambe and S. C. Mehrotra, *J. Korean Chem. Soc.*, 2012, **56**, 416–423.
- [181] O. Garcia-Moreno, M. Alvarez-Vega, F. Garcia-Alvarado, J. Garcia-Jaca, J. Gallardo-Amores, M. Sanjuan and U. Amador, *Chem. Mater.*, 2001, **13**, 2455.
- [182] B. Voss, J. Nordmann, A. Kockmann, J. Piezonka, M. Haase, D. H. Taffa and L. Walder, *Chem. Mater.*, 2012, **24**, 633–635.
- [183] G. Zeng, R. Caputo, D. Carriazo, L. Luo and M. Niederberger, *Chem. Mater.*, 2013, **25**, 3399–3407.
- [184] X. Huang, X. He, C. Jiang and G. Tian, *RSC Adv.*, 2014, **4**, 56074–56083.
- [185] P. Axmann, C. Stinner, M. Wohlfahrt-Mehrens, A. Mauger, F. Gendron and C. M. Julien, *CHEMISTRY OF MATERIALS*, 2009, **21**, 1636–1644.
- [186] D. Y. W. Yu, K. Donoue, T. Kadohata, T. Murata, S. Matsuta and S. Fujitani, *J. Electrochem. Soc.*, 2008, **155**, A526–A530.
- [187] N. Recham, L. Dupont, M. Courty, K. Djellab, D. Larcher, M. Armand and J. M. Tarascon, *Chem. Mater.*, 2009, **21**, 1096–1107.
- [188] J.-M. Tarascon, N. Recham, M. Armand, J.-N. Chotard, P. Barpanda, W. Walker and L. Dupont, *Chem. Mater.*, 2010, **22**, 724–739.
- [189] A. Deb, U. Bergmann, E. Cairns and S. Cramer, *J. Phys. Chem. B*, 2004, **108**, 7046–7049.
- [190] G. Assat and A. Manthiram, *Inorg. Chem.*, 2015, **54**, 10015–10022.
- [191] S.-H. Wu, A. R. Caparanga, R. B. Leron and M.-H. Li, *Thermochimica Acta*, 2012, **544**, 1 – 5.
- [192] A. Yadav and S. Pandey, *J. Chem. Eng. Data*, 2014, **59**, 2221–2229.
- [193] E. L. Smith, A. P. Abbott and K. S. Ryder, *Chemical Reviews*, 2014, **114**, 11060–11082.
-

- 
- [194] P. M. Schaber, J. Colson, S. Higgins, D. Thielen, B. Anspach and J. Brauer, *Thermochimica Acta*, 2004, **424**, 131–142.
- [195] J. Zhu, J. Fiore, D. Li, N. M. Kinsinger, Q. Wang, E. DiMasi, J. Guo and D. Kisailus, *Cryst. Growth Des.*, 2013, **13**, 4659–4666.
- [196] Z. Ma, G. Shao, Y. Fan, G. Wang, J. Song and T. Liu, *ACS Appl. Mater. Interfaces*, 2014, **6**, 9236–9244.
- [197] L. Laffont, C. Delacourt, P. Gibot, M. Y. Wu, P. Kooyman, C. Masquelier and J. M. Tarascon, *Chem. Mater.*, 2006, **18**, 5520–5529.
- [198] *Sigma-Aldrich*, <https://www.sigmaaldrich.com/united-kingdom.html>, Accessed: 2016-04-30.
- [199] A. Zylbersztejn and N. F. Mott, *Phys. Rev. B*, 1975, **11**, 4383–4395.
- [200] F. J. Morin, *Phys. Rev. Lett.*, 1959, **3**, 34–36.
- [201] C. Lampeonnerud, J. O. Thomas, M. Hardgrave and S. Ydeanderson, *J. Electrochem. Soc.*, 1995, **142**, 3648–3651.
- [202] A. Cao, J. Hu, H. Liang and L. Wan, *Angew. Chem. Int. Ed.*, 2005, **44**, 4391–4395.
- [203] Z. Zou, H. Cheng, J. He, F. Long, Y. Wu, Z. Yan and H. Chen, *Electrochim. Acta*, 2014, **135**, 175–180.
- [204] H. Liu, Y. Wang, K. Wang, Y. Wang and H. Zhou, *J. Power Sources*, 2009, **192**, 668–673.
- [205] S. G. Bratsch, *J. Phys. Chem. Ref. Data*, 1989, **18**, 1–21.
- [206] M. Qin, Q. Liang, A. Pan, S. Liang, Q. Zhang, Y. Tang and X. Tan, *J. Power Sources*, 2014, **268**, 700–705.
- [207] G. Armstrong, J. Canales, A. R. Armstrong and P. G. Bruce, *J. Power Sources*, 2008, **178**, 723–728.
-

- [208] X.-P. Yan, J. Chen, J.-M. Liu, P.-P. Zhou, X. Liu and Z.-X. Su, *Mater. Lett.*, 2010, **64**, 278–280.
- [209] F. Y. Kong, M. Li, X. Y. Yao, J. M. Xu, A. D. Wang, Z. P. Liu and G. H. Li, *CrystEngComm*, 2012, **14**, 3858–3861.
- [210] C. Niu, J. Meng, C. Han, K. Zhao, M. Yan and L. Mai, *Nano Lett.*, 2014, **14**, 2873–2878.
- [211] L. Mai, Q. Wei, Q. An, X. Tian, Y. Zhao, X. Xu, L. Xu, L. Chang and Q. Zhang, *Adv. Mater.*, 2013, **25**, 2969–2973.
- [212] C. Tsang and A. Manthiram, *J. Electrochem. Soc.*, 1997, **144**, 520–524.
- [213] M. Zhang and J. Dahn, *J. Electrochem. Soc.*, 1996, **143**, 2730–2735.
- [214] V. Subramanian, C. Chen, H. Chou and G. Fey, *J. Mater. Chem.*, 2001, **11**, 3348–3353.
- [215] T. E. Ashton, J. V. Laveda, D. A. MacLaren, P. J. Baker, A. Porch, M. O. Jones and S. A. Corr, *J. Mater. Chem. A*, 2014, **2**, 6238–6245.
- [216] J.-M. Li, K.-H. Chang, T.-H. Wu and C.-C. Hu, *J. Power Sources*, 2013, **224**, 59–65.
- [217] J. Prado-Gonjal, B. Molero-Sanchez, D. Avila-Brande, E. Moran, J. Carlos Perez-Flores, A. Kuhn and F. Garcia-Alvarado, *J. Power Sources*, 2013, **232**, 173–180.
- [218] C. Arbizzani, S. Beninati, L. Damen and M. Mastragostino, *Solid State Ionics*, 2007, **178**, 393–398.
- [219] Q. An, J. Sheng, X. Xu, Q. Wei, Y. Zhu, C. Han, C. Niu and L. Mai, *New J. Chem.*, 2014, **38**, 2075–2080.
- [220] K. Waltersson, B. Forslund, K.-A. Wilhelmi, S. Andersson and J. Galy, *Acta Cryst. B*, 1974, **30**, 2644–2652.
- [221] J. Cocciantelli, M. Menetrier, C. Delmas, J. Doumerc, M. Pouchard, M. Broussely and J. Labat, *Solid State Ionics*, 1995, **78**, 143–150.

- [222] Q. Liu, Z.-F. Li, Y. Liu, H. Zhang, Y. Ren, C.-J. Sun, W. Lu, Y. Zhou, L. Stanciu, E. A. Stach and J. Xie, *Nat. Commun.*, 2015, **6**, 6127.
- [223] F. Theobald, R. Cabala and J. Bernard, *J. Solid State Chem.*, 1976, **17**, 431–438.
- [224] W. Jiang, J. Ni, K. Yu and Z. Zhu, *Appl. Surface Sci.*, 2011, **257**, 3253 – 3258.
- [225] I. Mjejri, N. Etteyeb and F. Sediri, *J. Alloy Compd.*, 2014, **611**, 372–380.
- [226] C. S. Reddy, E. H. W. Jr., S. W. Sr., Q. L. Williams and R. R. Kalluru, *Curr. Appl. Phys.*, 2009, **9**, 1195 – 1198.
- [227] Q. Wang, J. Pan, M. Li, Y. Luo, H. Wu, L. Zhong and G. Li, *J. Mater. Sci. Technol.*, 2015, **31**, 630 – 633.
- [228] Z. Y. Wu, D. C. Xian, T. D. Hu, Y. N. Xie, Y. Tao, C. R. Natoli, E. Paris and A. Marcelli, *Phys. Rev. B*, 2004, **70**, 033104.
- [229] J. Wong, F. W. Lytle, R. P. Messmer and D. H. Maylotte, *Phys. Rev. B*, 1984, **30**, 5596–5610.
- [230] D. Li and S. Komarneni, *J. Am. Chem. Soc.*, 2006, **89**, 1510–1517.
- [231] E. Shangguan, Z. Chang, H. Tang, X.-Z. Yuan and H. Wang, *J. Power Sources*, 2011, **196**, 7791–7796.
- [232] Y. Guo-Xia, H. Ke-Long, L. Su-Qin and Z. Xiao-Ling, *J. Inorg. Mater.*, 2010, **25**, 1099–1104.
- [233] D. Guo, E. Shangguan, J. Li, T. Zhao, Z. Chang, Q. Li, X.-Z. Yuan and H. Wang, *Int. J. Hydrogen Energ.*, 2014, **39**, 3895–3903.
- [234] G. Caravaggio, C. Detellier and Z. Wronski, *J. Mater. Chem*, 2001, **11**, 912–921.
- [235] X. Lou, X. Wu and Y. Zhang, *Electrochem. Comm.*, 2009, **11**, 1696–1699.
- [236] T. Tabuchi, Y. Katayama, T. Nukuda and Z. Ogumi, *J. Power Sources*, 2009, **191**, 636–639.

- 
- [237] T. Tabuchi, Y. Katayama, T. Nukuda and Z. Ogumi, *J. Power Sources*, 2009, **191**, 640–643.
- [238] C. Xu, Y. Zeng, X. Rui, J. Zhu, H. Tan, A. Guerrero, J. Toribio, J. Bisquert, G. Garcia-Belmonte and Q. Yan, *J. Phys. Chem. C*, 2013, **117**, 17462–17469.
- [239] C. Zhang, J. Zhu, X. Rui, J. Chen, D. Sim, W. Shi, H. H. Hng, T. M. Lim and Q. Yan, *CrystEngComm*, 2012, **14**, 147–153.
- [240] G. X. Do, B. J. Paul, V. Mathew and J. Kim, *J. Mater. Chem. A*, 2013, **1**, 7185–7190.
- [241] I. Rodrigues, J. Wontcheu and D. D. MacNeil, *Mater. Res. Bull.*, 2011, **46**, 1878–1886.
- [242] Y. Xu, L. Zheng and Y. Xie, *Dalton Trans.*, 2010, **39**, 10729–10738.
- [243] Y. Oka, T. Yao and N. Yamamoto, *J. Solid State Chem.*, 1990, **89**, 372–377.
- [244] Y. Mettan, R. Caputo and T. Chatterji, *RSC Adv.*, 2015, **5**, 106543–106550.
- [245] H. Li, T. Zhai, P. He, Y. Wang, E. Hosono and H. Zhou, *J. Mater. Chem.*, 2011, **21**, 1780–1787.
- [246] V. S. R. Channu, R. Holze and B. Rambabu, *Curr. Appl. Phys.*, 2013, **13**, 237–240.
- [247] D. Wang, Q. Wei, J. Sheng, P. Hu, M. Yan, R. Sun, X. Xu, Q. An and L. Mai, *Phys. Chem. Chem. Phys.*, 2016, **18**, 12074–12079.
- [248] C. Wu, J. Dai, X. Zhang, J. Yang and Y. Xie, *J. Am. Chem. Soc.*, 2009, **131**, 7218+.
- [249] A. Pommer, *Geochim. Cosmochim. Ac.*, 1957, **13**, 20–27.
- [250] A. M. Pommer, *Geochim. Cosmochim. Ac.*, 1959, **17**, 148.
- [251] H. T. Evans, Jnr and M. E. Mrose, *Acta Cryst.*, 1958, **11**, 56–58.
- [252] H. Evans and M. Mrose, *Am. Mineral*, 1960, **45**, 1144–1166.
- [253] R. Enjalbert and J. Galy, *Acta Cryst. C*, 1986, **42**, 1467–1469.
- [254] V. Legagneur, A. La Salle, A. Verbaere, Y. Piffard and D. Guyomard, *J. Mater. Chem.*, 2000, **10**, 2805–2810.
-

- [255] V. Legagneur, A. La Salle, A. Verbaere, Y. Piffard and D. Guyomard, *Electrochim. Acta*, 2002, **47**, 1153–1161.
- [256] C. Zhang, H. Song, C. Zhang, C. Liu, Y. Liu and G. Cao, *J. Phys. Chem. C*, 2015, **119**, 11391–11399.
- [257] K.-H. Chang and C.-C. Hu, *Acta Mater.*, 2007, **55**, 6192–6197.
- [258] M. Simoes, Y. Mettan, S. Pokrant and A. Weidenkaff, *J. Phys. Chem. C*, 2014, **118**, 14169–14176.
- [259] K. Zhu, X. Yan, Y. Zhang, Y. Wang, A. Su, X. Bie, D. Zhang, F. Du, C. Wang, G. Chen and Y. Wei, *ChemPlusChem*, 2014, **79**, 447–453.
- [260] R. Hempelmann, M. Soetratmo, O. Hartmann and R. Wappling, *Solid State Ionics*, 1998, **107**, 269–280.
- [261] F. Theobald and R. Cabala, *C. R. Acad. Sci.*, 1970, **270**, 2138–&.
- [262] S. Passerini, W. Smyrl, M. Berrettoni, R. Tossici, M. Rosolen, R. Marassi and F. Decker, *Solid State Ionics*, 1996, **90**, 5–14.
- [263] W. Yoon, C. Grey, M. Balasubramanian, X. Yang and J. McBreen, *Chem. Mater.*, 2003, **15**, 3161–3169.